University of Alberta

MICROSEGREGATION STUDIES OF RAPIDLY SOLIDIFIED BINARY AL-CU ALLOYS

by

Arvind Prasad ©

A thesis submitted to the Faculty of Graduate Studies and Research in partial fulfillment of the requirements for the degree of **Doctor of Philosophy**.

in

Materials Engineering

Department of Chemical and Materials Engineering

Edmonton, Alberta
Spring 2006

Library and
Archives Canada

Published Heritage
Branch

395 Wellington Street
Ottawa ON K1A 0N4
Canada

Bibliothèque et
Archives Canada

Direction du
Patrimoine de l'édition

395, rue Wellington
Ottawa ON K1A 0N4
Canada

Your file Votre référence
ISBN: 0-494-14028-3
Our file Notre référence
ISBN: 0-494-14028-3

NOTICE:
The author has granted a non-exclusive license allowing Library and Archives Canada to reproduce, publish, archive, preserve, conserve, communicate to the public by telecommunication or on the Internet, loan, distribute and sell theses worldwide, for commercial or non-commercial purposes, in microform, paper, electronic and/or any other formats.

The author retains copyright ownership and moral rights in this thesis. Neither the thesis nor substantial extracts from it may be printed or otherwise reproduced without the author's permission.

AVIS:
L'auteur a accordé une licence non exclusive permettant à la Bibliothèque et Archives Canada de reproduire, publier, archiver, sauvegarder, conserver, transmettre au public par télécommunication ou par l'Internet, prêter, distribuer et vendre des thèses partout dans le monde, à des fins commerciales ou autres, sur support microforme, papier, électronique et/ou autres formats.

L'auteur conserve la propriété du droit d'auteur et des droits moraux qui protège cette thèse. Ni la thèse ni des extraits substantiels de celle-ci ne doivent être imprimés ou autrement reproduits sans son autorisation.

In compliance with the Canadian Privacy Act some supporting forms may have been removed from this thesis.

While these forms may be included in the document page count, their removal does not represent any loss of content from the thesis.

Conformément à la loi canadienne sur la protection de la vie privée, quelques formulaires secondaires ont été enlevés de cette thèse.

Bien que ces formulaires aient inclus dans la pagination, il n'y aura aucun contenu manquant.

Canada

Abstract

Most of the materials that we use in our day-to-day activities undergo solidification at some stage of manufacturing. Normal solidification of alloys can result in chemical inhomogeneity (microsegregation) and coarse structure that can make the material weak. Rapid solidification has been known to reduce microsegregation and produce materials with improved properties. To control the microstructure obtained from rapid solidification, and thus attain desired properties, requires an understanding of microstructure evolution and the resulting microsegregation.

We have studied microsegregation in rapidly solidified Al-Cu alloys using a combination of experiments and modeling. Rapidly solidified Al-Cu alloys were produced using Impulse Atomization. Microsegregation studies were performed on the droplets for different alloy chemistry (Al-4.3%Cu, Al-5%Cu, Al-10%Cu and Al-17%Cu), droplet sizes and gas type. The droplets produced were characterized using X-Ray Tomography, Neutron Diffraction, Electron Microscopy and Stereology. Using these techniques, nucleation and microstructure formation were studied and eutectic amount measured within the droplets. Modeling involved developing a microsegregation model for a droplet solidifying during Impulse Atomization. Rappaz-Thevoz microsegregation model was used coupled with LKT dendrite kinetic model with modification for off-center nucleation.

The results from the experiment and model show that the droplets undergo a nucleation undercooling of approximately 20K with a single, off-center, nucleation event. Individual droplets showed gradation in microstructure believed to be caused due to recalescence. The observed trend in microsegregation showed that the segregation decreases as the alloy composition is increased. Microsegregation also showed a slight decrease with increasing cooling rate, but the trend was not very clear. Based on the alloy composition, droplet size ranges studied and type of gas used (He or N_2), the estimated cooling rates were in the range of $10^2 - 10^3$ K/s. It was found that the final microsegregation in the droplet is effected by the phenomena taking place in the period between onset of nucleation and end of recalescence. While solute drag may be operative in this period, the nucleation undercooling was too low for solute trapping to take place. Evidence of macrosegregation was also found in the droplets.

Acknowledgements

It is often said that it is the journey that is more important than the final destination. After completing my degree requirements, I am at the vantage point to look at both, the journey as well as the destination. As I look back at all these years at the "grad school", a common usage for post graduation studies in universities, I realize that I have evolved and grew in ways more than I had imagined when I first started. I believe the journey presented me with the opportunity to observe, understand and grapple with the lessons of life than to merely grasp the technical concepts in the literature. And in so doing, I have changed and I am glad I was given this opportunity.

The journey of life is far from over and the destination of a Ph.D. degree is just, albeit an important, milestone. This short journey has been dotted with events and personals that have brought about the changes in me. Hence, a heartfelt acknowledgement, to both events and people, is more than due. Of course, no journey starts without parents. I would like to thank my mom, Vijayalakshmi, for her patience and, dad, Sheo Prasad, for his determination. I imbibed both of these qualities from them and these have come to my rescue more than once. My sister Alka, her fiancé Denis Jr., my dear friends Rahul and Ashutosh (and their family), have taught me about the different facets of life and I will, forever, be grateful to them. My sincere thanks to my advisor, Hani Henein, for giving me this opportunity to take this journey, and also showing me the advantages of being able to apply the knowledge from multiple disciplines to solve a problem. Support from friends has been the most important part of this journey and I have had the good fortune to have a long list of them. My special thanks to them – Manuel, Sirinda, Venkat, Sanket, Sujit, Tonya, Raghu, Ibrahim, Steve, Oscar and Jayant. A big "Thank you" is due to the AMPL members for de-stressing me ever so often. The technical support from Craig, Tina, Nathan and Peter is acknowledged. Finally, the contribution of the loads of non-technical books and the authors of those wonderful books, which kept me from going astray all these years, is deeply appreciated.

TABLE OF CONTENTS

List of Tables
List of Figures
List of Symbols

1. Introduction 1
    1.1 Thesis layout 7
    1.2 References 8

2. Literature Review 10
    2.1 Rapid solidification techniques 11
        2.1.1 Chill methods 11
        2.1.2 Spray techniques 12
        2.1.3 Weld methods 13
        2.1.4 Commercial applications 13
    2.2 Rapid solidification: Microstructure and Properties 15
        2.2.1 Fine grain 16
        2.2.2 Finer structure 18
        2.2.3 Morphologies 19
        2.2.4 Phases 21
        2.2.5 Extended solid solution 22
        2.2.6 Properties 23
            2.2.6.1 Yield Stress 23
            2.2.6.2 Corrosion resistance 25
            2.2.6.3 Electrical and Magnetic properties 25
    2.3 Microstructure formation 27
        2.3.1 Unconstrained solidification growth theory 29
            2.3.1.1 Controlled nucleation undercooling 32
                2.3.1.1.1 Microstructure 34
                2.3.1.1.2 Velocity 34
                2.3.1.1.3 Microsegregation 35
            2.3.1.2 Uncontrolled nucleation undercooling in droplets 38
                2.3.1.2.1 Experiments 42
                2.3.1.2.2 Characterization 43
                2.3.1.2.3 Modeling efforts 47
                2.3.1.2.4 Microsegregation models 51
            2.3.1.3 Undercooling measurements by Differential Scanning Calorimeter (DSC) 53
    2.4 Thesis objective 57
        2.4.1 Choice of rapid solidification technique 58

2.4.2 Choice of alloy system 59
2.5 References 60

3. Experimental Techniques **71**
3.1 Impulse Atomization 71
3.1.1 Melting and atomization 73
3.1.2 Powder washing, drying and sieving 75
3.1.3 Powder mounting and polishing 77
3.2 X-ray tomography 78
3.3 Neutron diffraction 79
3.4 Stereology 80
3.4.1 Cavalieri method 83
3.5 References 85

4. X-Ray Tomography study of atomized Al-Cu droplets **86**
4.1 Introduction 86
4.2 Experimental 87
4.3 Results 88
4.3.1 Nucleation 89
4.3.2 Recalescence 90
4.3.3 Porosity distribution 95
4.3.3 2-dimensional microscopic analysis 97
4.4 Discussion 99
4.4.1 Nucleation 99
4.4.2 Recalescence 103
4.4.3 Dendritic structure and scale of microstructure 105
4.4.4 Porosity distribution 105
4.5 Conclusions 107
4.6 References 108

5. Understanding the rapid solidification of Al-4.3Cu and Al-17Cu using X-Ray Tomography **111**
5.1 Introduction 111
5.2 Experimental 112
5.3 Results 114
5.3.1 Region I 114
5.3.1.1 Quantification of Region I 116
5.3.2 Region II 120
5.3.3 Region III 122
5.3.4 Porosity distribution 122
5.4 Discussion 125
5.4.1 Region I: Evidence of a single nucleation site 125
5.4.1.1 Region I: Probable mechanism of nucleation 126

        - 5.4.2 Region II: Microstructural features and Recalescence 127
        - 5.4.3 Region III: Effect of coarsening 129
        - 5.4.4 Coarsening: Effect of composition 129
            - 5.4.4.1Coarsening of different regions 132
        - 5.4.5 Porosity distribution 133
    - 5.5 Solidification of the atomized droplet 136
    - 5.6 Conclusions 137
    - 5.7 References 139

- 6. Quantification of microsegregation during rapid solidification of Al-Cu powders **142**
    - 6.1 Introduction 142
    - 6.2 Experiment and Results 145
        - 6.2.1 Quantitative metallography 146
        - 6.2.2 Neutron diffraction 151
    - 6.3 Mathematical formulation 153
        - 6.3.1 Average Cu content in the primary phase 157
    - 6.4 Results 158
    - 6.5 Discussion 164
        - 6.5.1 Solute solubility 164
    - 6.6 Conclusions 167
    - 6.7 References 168

- 7. Solidification modeling of Al-Cu Impulse Atomized droplets **172**
    - 7.1 Introduction 172
    - 7.2 Model formulation 174
        - 7.2.1 Macroscopic: Momentum balance 177
        - 7.2.2 Macroscopic: Heat loss from the droplet 180
        - 7.2.3 Microscopic: Latent heat generation 182
            - 7.2.3.1 Fraction solid formed during Stage I 184
                - 7.2.3.1.1 LKT model 187
            - 7.2.3.2 Fraction solid formed during Stage II 194
        - 7.2.4 Off-center nucleation 195
        - 7.2.5 Calculation of microsegregation 202
    - 7.3 Solution of heat balance equation 203
    - 7.4 Solving the set of equations 206
    - 7.5 References 210

- 8. Results and Discussion **214**
    - 8.1 Model validation and microsegregation results 216
        - 8.1.1 Model validation 223
            - 8.1.1.1 Stochastic position of nucleation 223
            - 8.1.1.2 Sensitivity analysis of nucleation position 225

8.1.1.3 Droplet undercooling analysis 226
8.1.1.4 Sensitivity analysis of nucleation undercooling and droplet size 229
8.1.1.5 Sensitivity analysis of phase diagram approximation 233
8.2 Comparison of weight percent eutectic 237
8.3 Comparison of average solute solubility 236
8.4 Microstructural features in an atomized droplet 239
8.5 Dendrite velocity and effective partition coefficient 246
8.5.1 Solute trapping 246
8.5.2 Solute drag 250
8.5.3 Dendrite remelting 257
8.6 Center-Surface nucleation 258
8.6.1 Effect on recalescence 258
8.6.2 Effect on eutectic 261
8.7 Effect of undercooling 262
8.7.1 Nucleation undercooling 262
8.7.1.1 Effect of cooling rate 263
8.7.1.1.1 Macrosegregation 269
8.8 Effect of alloy composition 273
8.9 References 275

9. Conclusions **278**
9.1 Summary 278
9.2 Observations 282
9.3 Future Work 285
9.3.1 A reliable parameter 285
9.3.2 Solute drag 287
9.3.3 Improvements in the model 287

Appendix A. Equations for growth of grain envelope during off-center nucleation **289**

Appendix B. Accuracy analysis of model results **293**

List of Tables

Table headings Page no.

Table 1.1: Categorization of solidification based on cooling rates [Flemings1981]. 4

Table 2.1: Extended solute solubilities of various elements in Cu base alloys [Srivatsan1993b] 22

Table 3.1: Summary of atomized alloys and the atomization run conditions used in tomography, neutron diffraction and stereology experiments. Number of images and the number of grid points per image used in stereological analysis for volume percent eutectic calculation are also given. 76

Table 4.1: Average recalescence volume fraction within the droplets. 93

Table 4.2: Cell spacing results for Al-5%Cu on 2-D SEM and 3-D tomography images. 98

Table 4.3: Cell spacing results for Al-5%Cu on different sections of a 3-D Tomography image. 98

Table 5.1: Volume percent results of Region I from Cavalieri method. 119

Table 5.2: Quantification results of Region II (primary trunks + ultra fine structure) from Cavalieri method. 121

Table 5.3: Porosity distribution in a Al-4.3%Cu droplet. The average droplet porosity was 0.6%. 124

Table 6.1: Summary of alloy compositions and droplet sizes for atomization, neutron diffraction and stereology experiments. 147

Table 7.1: Coordinates for evaluating the effective grain volume. 201

Table 7.2: Physical properties of gases used in the simulation [Wiskel2002a]. 204

Table 7.3: Properties of alloys used in the simulation^{a,b,c}. 206

Table 7.4: List of initial values used in the simulation. 209

Table 8.1: Summary of simulation results for the reference droplet for different nucleation positions. 227

Table 8.2: Effect of changing undercooling, droplet size and gas type on the eutectic formed with nucleation at the same position in all cases. Simulations are run for the reference droplet with nucleation at 0.75 R_p. 230

Table 8.3: Comparison of weight percent eutectic for Al-5%Cu droplet between the model and the experimental results. 232

Table 8.4: Partition coefficient values from the two different phase diagram approximations. 234

Table 8.5: Comparison of average Cu solubility obtained from the different approximations and the experiment. 235

Table 8.6: Average dendrite velocities in initial growth and recalescence periods for Al-5%Cu, Al-10%Cu and Al-17%Cu atomized droplets. 250

Table 8.7: Solute Drag parameter calculated (from Hillert et al [Hillert1976]) for dendrite velocities obtained from LKT dendrite kinetics for Al-5%Cu atomized droplets. 254

Table 8.8: Solute Drag parameter calculated (from Hillert et al [Hillert1976]) for dendrite velocities obtained from LKT dendrite kinetics for Al-10%Cu atomized droplets. 254

Table 8.9: Solute Drag parameter calculated (from Hillert et al [Hillert1976]) for dendrite velocities obtained from LKT dendrite kinetics for Al-17%Cu atomized droplets. 255

List of Figures

Figure Captions Page no.

Figure 1.1: Schematic of a) constrained and b) unconstrained growth during solidification [Fisher2000]. 5

Figure 2.1: Change in morphology in bulk-undercooled Fe-25%Ni alloy. As the undercooling is increased from a) 0 K to d) 300 K, the structure changes from dendritic to fine equiaxed grains [Kattamis1966]. 17

Figure 2.2: Figure showing the change in scale of the structure as the cooling rates are increased. The results are a compilation of the work of several researchers on the Al-Cu alloy [Hatch1984]. 19

Figure 2.3: Change in morphology in Al-Mn binary alloy as a function of interface growth rate and alloy composition [Juarez1988]. 21

Figure 2.4: Yield Strength versus grain size for a Mg-Al-Zn alloy [Nussbaum1989]. 24

Figure 2.5: Increase in dendrite growth rate as a function of undercooling for Ni-Sn alloy. The results are from Emulsion technique experiments. Model results are also reported for comparison [Wu1987]. 35

Figure 2.6: Decrease in microsegregation as a function of undercooling for different alloys. The results are from bulk undercooled experiments [Kattamis and co workers]. 37

Figure 2.7: Schematic for a change in undercooling during recalescence in a droplet solidification which results in a change in the interface velocity [Trivedi2003]. 40

Figure 2.8: Decrease in cell spacing with decreasing droplet size during rapid solidification of Al-4.5%Cu atomized powders [Wiskel2002b]. 44

Figure 2.9: Schematic of thermograph from a DSC experiment. Arrows indicate the heating/cooling cycle. 54

Figure 3.1: Schematic of the Impulse Atomization unit. The numerical labels describe the different parts of the unit. 72

Figure 3.2: A 15mm grid is randomly superimposed on the photomicrograph of a droplet taken from SEM. 81

Figure 3.3: Principle of the Cavalieri technique. The volume of interest is divided into several sections and the volume of each section is evaluated. The summation of these volumes for each section is the total volume of the feature [Howard1998]. 83

Figure 3.4: Figure explaining the $\frac{a_r}{p}$ ratio in stereology [Howard1998]. 84

Figure 4.1: Images showing the progressive movement of multiple equiaxed pattern (white dotted lines) converging to a nucleation site in Al-5%Cu droplet. Note the movement of the pattern across the droplet. The encircled region in figure 1d shows the nucleation site. Image numbers 430(1a), 460(1b), 495(1c) and 520(1d) out of a stack of 660 for a 660μm Al-5%Cu droplet viewed along the Axial direction. 91

Figure 4.2: Simulated temperature and fraction solid profile for a 660μm Al-5%Cu droplet solidified with 30^0C nucleation undercooling. Point A is the nucleation temperature, AB is the initial dendrite growth region, BC is the recalescence region and DE is the eutectic solidification. 92

Figure 4.3: Images showing the recalescence structure in Al-17%Cu (center-left triangular region in Figure 3a) and Al-5%Cu droplet (encircled region in Figure 3b). The recalescence region has much finer structure than the rest of the droplet. Also note the overall coarser structure of Al-5% Cu droplet. 93

Figure 4.4: Porosity distribution in Al-5%Cu 660μm droplet. Axial image # 210.95

Figure 4.5: Figure 4.5a shows the axial view of image # 40 with porosity across the entire section. A porosity free section (image # 250) from the same droplet along the same axis is shown in Figure 4.5b. Al-17%Cu, 492 μm droplet. 96

Figure 4.6: Elongated peripheral porosity in an Al-17%Cu droplet. The triangular recalescence region can be seen in the center of the droplet. Al-17%Cu, 456 μm droplet. Image # 262, Frontal axis. 97

Figure 4.7: Figure 4.7a shows the external and internal fluid flow for a liquid droplet. 4.7b shows the same for a lower Re number [Pruppacher1970]. 102

Figure 4.8: Surface pressure variation on a sphere for different Re numbers [Weber1978]. X-axis represents the polar angle from the front to the rear of the sphere. 102

Figure 5.1: 2D images of Region I in (a) Al-4.3%Cu and (b) Al-17%Cu droplet obtained from Tomography. The circle in (a) and the triangular region in (b) are the ultra fine structure region in Al-4.3%Cu and Al-17%Cu respectively. These images are just one of the several images in a Tomography generated stack. The thicker white arrows in (a) show the approximate direction of the droplet falling during atomization. Region I is at 120^0 from either arrow. Because of the bigger size of Region I in (b), such trajectory pointing arrows cannot be placed with accuracy. 115

Figure 5.2: Four slices taken from the stack of images along axial direction of Al-4.3%Cu droplet. Dotted lines are drawn to help see the movement of equiaxed site forming the vertices of a polygon. These vertices move towards one point in figure (d). 117

Figure 5.3: Four slices taken from the stack of images along axial direction of Al-17%Cu droplet. Black lines are drawn to help see the movement of equiaxed site forming the vertices of a polygon. Just as in Al-4.3%Cu, these vertices move towards one zone (Region I) in (d). 118

Figure 5.4: Primary Trunks emanating from Region I of Ultra Fine structure. Region II is defined as Region I and the primary trunks surrounding Region I. Region III is the rest of the area in the droplet. 120

Figure 5.5: 3-D porosity distribution for (a) Al-4.3%Cu and (b) Al-17%Cu droplets. The homogeneous distribution in Al-4.3%Cu droplet is markedly different from the peripheral distribution in the Al-17%Cu droplet. 123

Figure 5.6: Tubular shaped porosity in a Al-17%Cu droplet. The porosity is at the boundary of the solidifying droplet thereby suggesting the role of nucleation and recalescence in pushing the porosity away towards the periphery. 124

Figure 5.7: Cell spacing of Al-5%Cu and Al-17%Cu droplets atomized under He and N_2. Spacing measurements done on SEM images. Spacing measurements done on tomographic 2-D image for

Al-4.3%Cu is also included in the figure. Random Line intercept method was used for all cell spacing calculations. 131

Figure 5.8: Porosity distribution calculation in a Al-4.3%Cu droplet. The calculation was done by calculating the porosity within a cube of side 50 μm. This cube was moved from the nucleation point towards the periphery along <111> direction. 135

Figure 6.1: Schematic of the thermal history and fraction solid formed during the solidification of an atomized droplet. 144

Figure 6.2: Volume percent of eutectic for droplets of different (a) sizes and (b) compositions obtained from Stereology. 150

Figure 6.3: Weight percent of $CuAl_2$ for droplets of different (a) sizes and (b) compositions obtained from ND experiments. The error bars are the estimated standard deviation which comes from the Rietveld analysis used for phase quantification. 152

Figure 6.4: Weight percent of eutectic for droplets of different (a) sizes and (b) compositions. The weight percent was obtained by using volume percent eutectic and weight percent $CuAl_2$. 159

Figure 6.5: Figure showing the eutectic structure with a halo in an Al-17%Cu, 850–710 μm droplet, atomized in N_2 (Run no. 021021). The halo is the light band surrounding the primary phase and is an evidence of eutectic undercooling. 160

Figure 6.6: Ratio of weight percent $CuAl_2$ and weight percent eutectic plotted as a function of droplet composition. The amount of $CuAl_2$ in the eutectic decreases steadily as the alloy composition is increased. 161

Figure 6.7: Total Cu content in the primary phase plotted for droplets of the three alloy compositions. 161

Figure 6.8: Cu solubility in the primary phase plotted for droplets of the three alloy compositions. The strong effect of alloy composition in the solubility is clearly seen. 162

Figure 7.1: Schematic of a droplet during atomization with different forces acting on it. The heat loss due to convection and radiation and latent heat generated due to phase transformation is also shown. 178

Figure 7.2: Schematic representation of the R-T model with nucleus at the center. The change in grain radius δR_g in one time step is exaggerated for illustration purposes. 182

Figure 7.3: Possible undercoolings in front of a growing dendrite [Lipton1984]. The sum of the three undercoolings is the driving force for the dendrites to grow. 188

Figure 7.4: Schematic showing the dendrite growth in a droplet with off-center nucleation N. 195

Figure 7.5: Schematic showing the progressive growth of a grain from an off-center nucleation point N within the droplet with center denoted as C_n. The shaded circle is the spherical grain envelope whose radius, R_g, increases with time. Part a) of the figure shows the off-center nucleation site N. This is followed by growth of grain with passing time. In b) the grain is still within the droplet. However with increasing time the grain envelope will grow beyond the droplet as shown in c). Finally, as shown in d) the grain completely covers the original droplet ABCD. The part of the grain envelope outside the droplet does not take part in the latent heat release. 196

Figure 7.6: Figure showing the schematic of grain growth from off-center nucleation. The effective volume of the grain, EDGF, within the droplet is calculated using calculus. 200

Figure 7.7: Schematic of a linearized phase diagram with straight line approximation of the liquidus and the solidus. Solid lines indicate the actual phase diagram, and the dotted lines are the approximations. 205

Figure 7.8: Plot for the convergence test for choosing appropriate time step. Test results for Al-4.3%Cu shown with the chosen time step. 209

Figure 8.1: Representative thermal history plot for the reference atomized droplet with two undercoolings of 5K and 30K. Higher undercooling (lighter line) results in delayed nucleation and more recalescence. 217

Figure 8.2: Plot for the model results for the same reference droplet as in Figure 8.1 showing the time history profile for fraction solid formed at two different undercoolings. Solid line indicates 5K of undercooling and dotted line indicates 30K of undercooling. 218

Figure 8.3: Dendrite velocities in Al-4.3%Cu and Al-17%Cu droplets as a function of undercooling calculated from the LKT model. 220

Figure 8.4: Dendrite velocity in the reference droplet for two undercoolings. The change in velocity results in a corresponding change in temperature. 222

Figure 8.5: Schematic of the volume within an atomized droplet that represents the highest heat transfer region in an atomized droplet. S is the stagnation point and ABS represents the volume covering the range of highest heat transfer. 225

Figure 8.6: Comparison between experimental and model results for volume percent of Region I in the Al-4.3%Cu droplet. As explained in the text, an increase in the nucleation undercooling results in a decrease in the volume of initial growth regime. 228

Figure 8.7: Schematic of two different linearization schemes that can be used for approximating the phase diagram. The figure in (a) has been called Approximation I and that in (b) has been called Approximation II. 234

Figure 8.8: Figure comparing the weight percent eutectic from experiments and model. The model was run with eutectic assumed to occur at equilibrium. 236

Figure 8.9: Comparison of Cu solubility in the primary phase from experimental calculations and model. 238

Figure 8.10: FESEM images of the droplet cross-section for the Al-17%Cu droplet. The white lines indicate the enclosed recalescence region. which has a different morphology than the post-recalescence region outside the white lines. 241

Figure 8.11: Magnified FESEM images of the (a) region within white lines and (b) region outside white lines for the Al-17% Cu droplet. The images are inverted for clarity so that the lighter regions are primary phase and the darker regions are the $CuAl_2$ phase. 242

Figure 8.12: Microstructure gradation in a Al-10%Cu droplet very similar to that seen in the Al-17%Cu droplets. 243

Figure 8.13: The three calculated undercoolings, capillary, solutal and thermal, presented in a dimensionless temperature-composition diagram. Data taken from Boettinger et al [Boettinger1985] with k=0.1 and $\alpha/D = 10000$. 245

Figure 8.14: Variation in partition coefficient with dendrite velocity from velocity-dependant partition coefficient LKT model [Lipton1987c]. 248

Figure 8.15: Variation in partition coefficient with dendrite velocity attained in the droplets during atomization [Trivedi1987b]. 249

Figure 8.16: Solute Drag Parameter for Al-Cu system following the analysis of Hillert et al [Hillert1976]. 252

Figure 8.17: Thermal history for a Al-17%Cu droplet atomized in He. Undercooling is 20K and the nucleation position is chosen to be at the center (bold line) and the surface (lighter lines). 259

Figure 8.18: Fraction solid history for the same droplet as shown in Figure 8.17. The lighter lines represent surface nucleation while the darker lines represent center nucleation. 261

Figure 8.19: Effect of cooling rate on the weight percent eutectic. The cooling rates were evaluated from the model. 264

Figure 8.20: Effect of cooling rate on the average Cu content of the primary phase. The cooling rates were evaluated from the model. 265

Figure 8.21: Q-Q plot for an Al-10%Cu alloy 1000μm droplet atomized in He gas. The slope of the line is not equal to 1, indicating the deviation from normalcy as a result of macrosegregation. 271

Figure 8.22: Time history of the supersaturation term f_l. 273

Figure A.1: Schematic of the grain envelope growing from an off-center nucleation. Solid semi-circle represents the actual droplet and the dashed semi-circle is the grain envelope. 290

Figure B.1: Simulation results for droplet velocity calculated and compared using Milne's and 4th order R-K techniques. The straight line at 45^0 shows that the two techniques give same results with both the time steps used. 295

List of Symbols

Symbol	Description	Units
A	*Base area of cylinder*	m^2
A_i	*Area of ith intersect in the volume of interest*	m^2
A_A	*Area fraction from Stereology*	-
a	*Thermal diffusivity*	m^2/s
a_r	*Area per point in Cavalieri method*	m^2
B	*Parameter in modified Whitaker correlation*	-
b	*Exponential factor in SDAS-Solidification time correlation*	
$\overline{C}$	*Dimensionless alloy composition*	$C_0 \mid m_l \mid C_p / L$
C_0	*Original alloy Solute concentration*	%
$\overline{C}_0$	*Average Cu in the droplet*	%
C_d	*Drag coefficient*	-
C_p	*Specific heat per unit volume*	J/K/m^3
C_{lliq}	*Liquid composition at liquidus temperature*	%
C_{le}	*Liquid composition at eutectic temperature*	%
$C_{s\,ave}$	*Average composition of the primary phase*	%
C_{se}	*Solid composition at eutectic temperature*	%
C_{sliq}	*Solid composition at liquidus temperature*	%

Cu_{α_P}	*Copper in primary α-Al*	%
Cu_{α_E}	*Copper in α-Al in eutectic*	%
$\overline{C}u_{\alpha_P}$	*Average copper in primary α-Al*	%
Cu_{CuAl_2}	*Copper in $CuAl_2$*	%
C^*	*Solute concentration at the interface*	%
C_l^*	*Instantaneous liquidus solute concentration*	%
C_s^*	*Instantaneous solidus solute concentration*	%
D	*Solute diffusion in liquid*	m^2/s
D_{gn}	*Diffusion of a species appearing in general Peclet number*	m^2/s
D_p	*Droplet Diameter*	m
d_0	*Interatomic jump distance*	m
df_g	*Change in grain envelope fraction*	-
df_s	*Change in fraction solid*	-
dR_g	*Change in grain envelope radius*	m
dT	*Change in temperature in one time-step*	K
dt	*One time step*	s
dy	*Thickness of strip for volume of revolution*	m
$E_1(P)$	*Exponential integral function of Peclet number*	-
F	*Pre-exponential parameter in the cooling rate arm spacing expression*	-

f_g	*Ratio of grain envelope volume and droplet volume*	-
$f_{g_{eff}}$	*Effective grain volume fraction for off-center nucleation*	-
f_t	*Supersaturation*	-
f_s	*Fraction solid within the droplet*	-
$\overline{G}$	*Dimensionless thermal gradient*	$-\frac{P_t L}{C_p R_{dend}}$
$\overline{G_c}$	*Dimensionless concentration gradient*	$-\frac{P_c C^*(1-k_0)}{R_{dend}}$
g	*Acceleration due to gravity*	m/s^2
$g(P)$	*Peclet number of growing grain envelope*	-
H	*Pre-exponential parameter in the cooling rate arm spacing expression*	-
$\hbar$	*Planck's Constant*	Js
h_c	*Convective heat transfer coeff.*	W/m^2/K
Iv	*Ivantsov solution to diffusion equation*	-
K	*Conductivity of Al-Cu alloy*	W/m/K
k_0	*Equilibrium partition coefficient*	-
k_1, k_2, k_3, k_4	*Calculated slopes in the Runge-Kutta method*	-
k_s	*Conductivity of atomization gas*	W/m/K
L	*Latent heat of fusion per unit volume*	J/m^3
L_L	*Lineal fraction from Stereology*	-
M	*Coarsening factor*	-

M_n	*Mass of neutrons*	kg
m	*Exponential coefficient in modified Whitaker correlation*	-
m_l	*Equilibrium liquidus slope*	K/%
m_s	*Equilibrium solidus slope*	K/%
Nu	*Nusselt number*	-
n	*Exponential power in the cooling rate arm spacing expression*	-
n_b	*Number of points falling on eutectic-primary phase boundary*	-
n_e	*Number of points falling on eutectic*	-
n_t	*Total* number *of points falling on eutectic*	-
P	*Number of points falling on the feature of interest*	-
Pr	*Prandtl number*	-
P_c	*Solutal Peclet number*	$\frac{VR}{2D}$
P_{dend}	*Peclet number of the dendrite*	$\frac{V_{dend} R_{dend}}{2D}$
P_{gn}	*General Peclet number*	-
$\overline{P}_p$	*Point fraction from Stereology*	-
P_t	*Thermal Peclet number*	$\frac{VR}{2a}$

p	*Number of points in Cavalieri method*	-
$\dot{Q}_c$	*Rate of convective heat loss*	W/K/m^2
$\overline{R}$	*Dimensionless radius of curvature*	$\frac{R_{dend}}{d_0}$
Re	*Reynolds number*	-
R_{gn}	*Radius of a species appearing in general Peclet number*	m
R_{dend}	*Dendrite Radius of curvature*	m
R_g	*Grain envelope radius*	m
R_p	*Droplet radius*	m
R_{p_0}	*Distance from off-center nucleation to droplet center*	m
SDAS	*Secondary dendrite arm spacing*	m
T	*Thickness of an individual intersect in the volume of interest*	m
T_E	*Eutectic temperature*	K
T_f	*Fluid temperature at droplet surface*	K
T_l	*Alloy equilibrium liquidus temperature*	K
T_t	*Instantaneous droplet temperature*	K
T_m	*Melting temperature of pure metal*	K
T_s	*Droplet temperature at droplet surface*	K
T_x	*Droplet melting temperature in DSC heating cycle*	K

T_y	*Droplet nucleation temperature in DSC cool. cycle*	K
$\overline{\Delta T_r}$	*Dimensionless capillary undercooling*	$\frac{2}{\overline{R}}$
$\overline{\Delta T_s}$	*Dimensionless solutal undercooling*	$\overline{C}\left(\frac{1}{1-(1-k_0)Iv(P_c)}-1\right)$
$\overline{\Delta T_t}$	*Dimensionless thermal undercooling*	$Iv(P_t)$
V	*Volume of feature of interest*	m^3
V_{gn}	*Velocity of a species appearing in general Peclet number*	m/s
V_1	*Volume of first segment in effective grain volume calc.*	m^3
V_2	*Volume of second segment in effective grain volume calc.*	m^3
$V_1' ... V_4'$	*Simplified volume expression for effective volume calc.*	m^3
V_{cyl}	*Volume of cylinder*	m^3
V_{dend}	*Velocity of dendrite*	m/s
$V_{g_{eff}}$	*Effective grain volume for off-center nucleation*	m^3
V_V	*Volume fraction from Stereology*	-
$\bar{V}$	*Dimensionless dendrite velocity*	$\frac{V_{dend} d_0}{2a}$
v	*Droplet velocity in the atomizer*	m/s

v_{α_P}	*Volume percent a-Al in primary phase*	%
v_{α_P}	*Volume percent a-Al in eutectic*	%
v_{α_P}	*Volume percent $CuAl_2$*	%
v_{CuAl_2}	*Volume percent $CuAl_2$*	%
v_E	*Volume percent eutectic*	%
$\hat{v}_e$	*Estimated average volume of eutectic from Stereology*	%
W_{α_E}	*Weight of α-Al in the eutectic*	kg
W_{α_P}	*Weight of primary α-Al*	kg
W_{CuAl_2}	*Weight of $CuAl_2$*	kg
w_{α_P}	*Weight percent primary α-Al*	%
w_{α_P}	*Weight percent α-Al in eutectic*	%
$\hat{w}_{CuAl_2}$	*Weight percent of $CuAl_2$*	%
w_E	*Weight percent eutectic*	%
Δx	*Linear dimension along Y-axis of the Stereology grid spacing*	m
Y_D	*Coordinates of point D along Y-axis in effective grain volume calculation*	-
Δy	*Linear dimension along Y-axis of the Stereology grid spacing*	m
Z	*Inverse function of Peclet number*	-

Greek Symbols

δt	*Discretized time step*	s
Γ	*Gibbs-Thomson coefficient*	*mK*
ξ_c	*Stability parameter - concentration*	-
ξ_t	*Stability parameter – thermal*	-
υ_d	*Dimensionless dendrite velocity*	-
η	*Ratio of thermal and solutal diffusivity*	-
ε	*Ratio of interatomic jump distance and capillary length*	-
μ_∞	*Viscosity of gas at free stream gas temperature*	Pa.s
μ_f	*Kinematic viscosity of atomization fluid*	Pa.s
μ_s	*Viscosity of gas at droplet surface temperature*	Pa.s
λ	*Wavelength of neutron wave*	m
υ	*Velocity of neutron beam*	m/s
ρ_a	*Density of a-Al*	kg/m^3
ρ_{CuAl_2}	*Density of* $CuAl_2$	kg/m^3
ρ_f	*Density of atomization fluid*	kg/m^3
ρ_p	*Density of droplet*	kg/m^3
σ^*	*Stability constant*	-

Introduction

The properties of the materials that we use in our day-to-day activities are governed by their structures. For example, a finer structure results in a stronger material and a coarser structure results in a weaker material. Similarly, chemical inhomogeneity (or segregation) within the material can also result in weaker materials. Segregation in alloys results from the difference in solute solubility between the liquid and the solid phases. Therefore, to accommodate this difference during phase transformation, the solute has to be redistributed between the solid and the liquid phase. When this segregation is considered in the vicinity of solid-liquid interface, it is termed microsegregation. On the other hand, segregation within different regions of the solidifying system is called macrosegregation. In an ingot casting, for example, the center of the ingot may have a different chemical composition than the periphery. Such a difference in chemistry across the solidifying volume is called macrosegregation. However, a localized heterogeneity of the composition at the center (or surface) of the casting is called microsegregation. Although both involve the redistribution of solute between the solid and liquid phases, macrosegregation is a result of additional factors like density differences, convection currents etc. within the solidifying volume. Thus segregation is a result of solidification processing, which most metals and alloys undergo at some stage of manufacturing.

It is often possible to refine the structure and to chemically homogenize a segregated alloy obtained from solidification by using heat treatment operations. But it is usually very expensive both in terms of time and energy. For example, the homogenization time for a material is proportional to the square of the scale of the microstructure [Kurz2000]. Therefore, it will take four times longer to homogenize a structure that is twice the scale of a finer one. Furthermore, even with post-processing, it may not be possible to completely eliminate the ill-effects of segregation resulting from solidification. Therefore, the final structure of these materials is largely governed by solidification phenomena. Thus, controlling the structure formation and the degree of segregation during the solidification process itself is very important [Kurz2000]. Hence, research has been directed towards generating finer structures with increased chemical homogeneity.

Towards this end, one of the important breakthroughs in solidification is rapid solidification. Conventionally, the process is termed rapid solidification when the cooling rate of the system is very high resulting in vast deviations from equilibrium. Although cooling rate is a very commonly used parameter in describing a solidification process, it is a less stringently defined parameter in the solidification literature. Eskin et al [Eskin2005] have provided three different definitions of cooling rate: i) rate of heat extraction, ii) slope of the thermal history (i.e. time-temperature graph) at the melting point of the material and the most commonly used definition iii) the ratio of temperature and time as the material passes from melting temperature to the temperature when the solidification is complete. In equation form this is given as,

$$\dot{T} = \frac{\Delta T}{t_f} \tag{1.1}$$

Where $\dot{T}$ is the cooling rate, ΔT is the solidification range and t_f is the total solidification time.

Solidification processes can be classified on the basis of cooling rate, as shown in the definitions presented in Table 1.1 [Flemings1981]. The very low and low cooling rate solidification processes in the table are also referred to as "normal" solidification. Medium rapid to ultra-rapid solidification occurs when one dimension of the system is very small with respect to other dimensions. Such a system in the presence of a large heat sink gives a very high cooling rate [Srivatsan1993]. However, deviation from equilibrium can also result when there is a high degree of undercooling. Undercooling is defined as the temperature difference between the equilibrium liquidus temperature and the nucleation temperature. For rapid solidification with high undercoolings, it has been shown that the nucleation undercooling achievable for pure liquid metals can be as high as $0.3T_m$ [Holloman1953], where T_m is the melting point of the metal in Kelvin.

With high cooling rates and nucleation undercooling, there is a significant deviation from equilibrium. Because of this deviation, rapid solidification processes can result in final products with microstructural and constitutional features much different from those obtained under near equilibrium conditions. Unique microstructural features arising from rapid solidification may include formation of microcrystalline structures, decreased grain size or dendrite spacing and coupled growth [Jones1983]. Constitutional features may include increased solute solubility beyond equilibrium, reduced microsegregation and metastable phases. These novel microstructural and constitutional features have exhibited improved mechanical properties, which in turn have generated strong interest in rapid solidification processes in recent years.

Table 1.1: Categorization of solidification based on cooling rates [Flemings1981].

Cooling Rate (K/s)	Designation
$10^{-6} - 10^{-3}$	Very Low
$10^{-3} - 10^{0}$	Low
$10^{0} - 10^{3}$	Medium Rapid
$10^{3} - 10^{6}$	Rapid
$10^{6} - 10^{9}$ and above	Ultra-rapid

During microstructure evolution, solute segregation takes place, along with the formation of the scales of microstructure. Therefore, in order to control the microstructural features and solute segregation during rapid solidification, it is very important to understand microstructural evolution. The microstructural evolution depends on the rate of motion of the solid-liquid interface, which in turn, depends on the mode of heat extraction amongst other factors. Solidification requires that the latent heat released during phase change be extracted, which can be done in two ways. When the heat is extracted through the solid phase, it is called constrained growth and when it is extracted through the liquid phase, it is called unconstrained growth. The difference in the direction of heat flow and the morphology obtained from the two processes is illustrated in Figure 1.1. The variables in the figure are as follows: q is the heat flow, T_E is the eutectic temperature, T_l is the alloy liquidus, T_q is the temperature in the liquid melt, ΔT is the undercooling ahead of the interface, V is the interface velocity and z is the distance from the cooling interface.

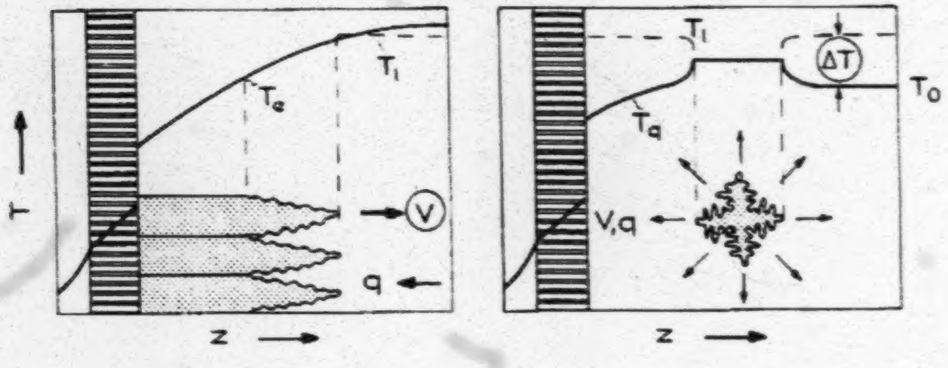

(a) (b)

Figure 1.1: Schematic of a) constrained and b) unconstrained growth during solidification [Kurz2000].

In constrained growth, Figure 1.1a, the solid-liquid interface grows in the opposite direction to that of the heat flow. In the unconstrained growth, the interface growth is in the same direction as the heat flow. Heat transfer through the solid phase is seen in casting walls, directional solidification situations and splat cooling whereas heat transfer through the liquid phase is seen in droplet solidification such as in atomization techniques, spray forming or drop-tube experiments. These differences in the modes of solidification result in different growth conditions and may result in different morphologies and/or microsegregation in the solid phases.

Theories have been developed describing the growth rate of interfaces under both constrained and unconstrained growth conditions. The theories for constrained growth have been experimentally verified. For example, using weld-techniques of rapid solidification on Al-Mn alloys, Juarez et al [Juarez1988] have shown that the morphology and microsegregation in the rapidly solidified product change with velocity of the solid-liquid interface. This is in good agreement with the theory. Similar results under constrained growth conditions have been reported by Boettinger et al [Boettinger1984] for Ag-Cu alloys.

Unconstrained growth, on the other hand, is largely dependent on nucleation undercooling since the solid grows from a nucleus into an undercooled melt (Figure 1.1b). Hence, studies of unconstrained growth have concentrated on determining undercooling, how the growth rate is affected by undercooling and the subsequent impact on recalescence, microsegregation and grain size. However, because of the practical difficulties, experimental verification is often not possible for the unconstrained growth conditions. For example, no experimental verification exists for the nucleation undercooling or interface growth rates attained in a droplet solidified during atomization. Likewise, no validation exists for the estimated cooling rates of droplets undergoing unconstrained solidification. The literature review in the next chapter discusses the limited availability of data for unconstrained growth conditions in more detail.

This project is therefore aimed at studying microstructure formation and microsegregation during rapid solidification under unconstrained conditions. The study has been conducted for an Al-Cu binary system for a range of alloy compositions and cooling rates. The current work has involved both experimental and modeling work. Experimental studies used atomization to generate rapidly solidified powders of binary Al-Cu alloy, on which. microstructural and microsegregational studies were performed. Microstructure was studied in terms of nucleation, morphology, scale of microstructure, etc., within the entire volume of the powders. Microsegregation was studied by measuring the volume of eutectic. In addition, the amount of second phase formed and the average amount of solute within the primary phase were also calculated for the entire powder volume. Modeling work involved developing a solidification model for the atomized droplet to study the microsegregation as a function of composition and cooling rates. The model was developed to also assess the role of solid-liquid interface growth rates on microsegregation for different alloy compositions.

1.1 Thesis layout

Chapter 2 describes the research efforts of other workers in the field of rapid solidification and the motivation and objective of this thesis work. Chapter 3 describes the experimental procedures utilized in this research. The experiments involved generating alloy powders using Impulse Atomization technique, followed by the study of microstructure and microsegregation using characterization techniques (X-Ray tomography, neutron diffraction and electron microscopy) on these powders. Following Chapter 3, the thesis is laid out according to the characterization technique used. Chapters 4 and 5 are devoted to X-Ray tomography. Nucleation, recalescence, morphology and porosity distribution are studied using this technique and described in these two chapters. Solute solubility and microsegregation were studied using neutron diffraction, SEM and stereology, as described in Chapter 6. Chapter 7 is devoted to modeling and error analysis of the model. In Chapter 8, results from the model and experiments are compared and discussed. Based on the comparison between the experiment and modeling results, the model is validated, nucleation undercooling in the atomized droplets is established and microsegregation in the droplets is analyzed with respect to solid-liquid interface growth rates and the variables that affect it. Finally, Chapter 9 outlines conclusions arising from this study and areas for further research.

1.2 References

[Boettinger1984]: "The effect of rapid solidification velocity on the microstructure of Ag-Cu alloys", Boettinger W.J., Schechtman D., Schaefer R.J. and Biancaniello F.S., Metallurgical Transactions A, v. 15A, 1984, pp 55-66.

[Eskin2005]: "Experimental study of structure formation in binary Al–Cu alloys at different cooling rates", Eskin D., Du Q., Ruvalcaba D. and Katgerman L., Materials Science and Engineering A, v. 405, 2005, pp 1–10.

[Flemings1981]: "Segregation and structure of rapidly solidified cast metals", Flemings M.C., Metallurgical Treatises, Metallurgical Society of AIME, 1981, pp 291-300.

[Holloman1953]: "Solidification of lead-tin alloy droplets", Holloman J.H. and Turnbull D., AIME – Journal of Metals, v. 3, n. 9, 1951, pp 803-805.

[Jones1983]: "Rapid Solidification of Metals and Alloys", Jones H., The Institute of Metallurgists, London, 1983, pp 35.

[Juarez1988]: "Effect of solidification front velocity on the characteristics of Al-rich Al-Mn alloy solutions extended by rapid solidification", Juarez Islas J.A., Jones H. and Kurz W., Materials Science and Engineering, v. 98, 1988, pp 201-205.

[Kurz2000]: "Fundamentals of Solidification", Kurz W. and Fisher D., Trans Tech Publications Ltd., Switzerland, 2000, pp 64,292.

[Srivatsan1993]: "Rapid Solidification Technology: An Engineering Guide", Srivatsan T.S. and Sudarshan T.S. (eds.): Technomic Publishing Company Inc., U.S.A., 1993, pp 3-6.

Chapter 2

Literature Review

As mentioned in the previous chapter, rapid solidification processes can result in microstructures with improved properties. The attractive features of rapid solidification were first demonstrated in 1960 by Duwez [Duwez1960a,b], who reported an increase in the solubility of solute in the solid phase in the Cu-Ag system and the formation of a metastable phase in the Ag-Ge system. The experimental technique consisted of impinging a small volume of liquid on a cold substrate. The thin liquid layer formed subsequently lost heat rapidly to the substrate. Since then, rapid solidification technology has advanced tremendously. The vast body of knowledge now available on the subject can be categorized into three areas:

- development of rapid solidification techniques,
- research on the microstructures possible with these techniques and
- understanding the microstructure formed during rapid solidification.

This chapter divides the relevant literature on the research done on rapid solidification according to these three categories. These are described in Sections 2.1 – 2.3. Following this, the thesis objective is outlined in Section 2.4, which also describes the rationale for using Impulse Atomization as the rapid solidification technique for the current work and for the choice of Al-Cu as the alloy system for this study.

2.1 Rapid solidification techniques

Duwez' observations demonstrated that rapid solidification processes can produce new phases not found in conventional solidification structures. The unique feature of Duwez' experiment was a small liquid volume from which heat was extracted rapidly. The resulting product was a phase not obtained from conventional solidification processes. Following this experiment, new techniques were developed with the aim of generating a small volume of liquid and extracting heat very rapidly from this volume. Consequently, over the years, several rapid solidification techniques have been developed. These processes can be classified according to the technique used to generate a small liquid volume and the subsequent mode of heat extraction from this liquid. These processes are described in greater detail in the literature. For example, Savage and Froes [Savage1984] review and compare more than 25 different rapid solidification techniques. However, only the basic principles of some of these processes are described in the following sections.

2.1.1 Chill methods

A very common rapid solidification technique, similar to Duwez' initial experimental set-up, is what is called the Chill method [Jones1983]. In this process, a thin layer of liquid metal is deposited on a colder substrate, loses heat through the chilled substrate and solidifies. Some examples of processes falling under this category are Splat Cooling, Melt Spinning, the Twin Roll process, the Two-Piston method and the Hammer-Anvil technique.

In the Single Splat technique, a molten mass of metal is propelled towards a cold substrate. A variation of this is the Continuous Splat process where a stream of liquid metal is directed on the surface of a rapidly moving cold substrate. The mode of heat transfer in the two processes is the same. When the cold substrate is a spinning wheel, the process is called Chill-Block Melt-Spinning, which has become a widely popular technique for studying rapid solidification. When the liquid is pinched between two rotating wheels it is called a Twin-Roll process; the liquid in this case loses heat to the two rotating wheels. Similar to this are the Two-Piston method and the Hammer-Anvil technique. These techniques produce a very thin layer of liquid as a result of high impact between two surfaces with the liquid volume in between.

2.1.2 Spray techniques

The spray method represents another class of rapid solidification technique [Jones1983]. The central idea in these techniques is to destabilize a stream of metal to form a small liquid volume in the shape of tiny droplets that are then made to lose heat rapidly by some means. Atomization is one of the most popular spray methods. In the atomization process, a liquid metal jet is made unstable by mechanical means (Impulse Atomization, Centrifugal Atomization, etc.) or by blowing gas at the liquid jet (Gas Atomization), and it then disperses into fine droplets. These droplets are made to fall through a much colder fluid medium, wherein they lose heat and consequently solidify. Other spray methods include Spray Deposition, the Rotating Electrode Process and Drop Tube tower. Spray Deposition is atomizing a liquid stream into droplets that subsequently fall in a semi-solid form onto a substrate.

2.1.3 Weld methods

Weld methods make up a third rapid solidification technique [Jones1983]. In chill methods, the contact between the solid layer and the substrate may not be uniform which could compromise the heat extraction. Weld methods rectify this situation. In weld methods, melting and solidification occurs in situ at the chill surface which itself is partially melted. To generate a partially melted pool, a high flux of localized energy is used to melt a shallow layer of bulk metal. This thin layer of liquid metal loses heat to the bulk substrate and rapidly solidifies. The localized beam of heat can be produced by Laser, Plasma or Electron beams.

2.1.4 Commercial applications

Initially, the rapid solidification techniques were aimed towards producing materials in forms such as powders, wires, flakes, etc [Jones1983]. Since Duwez' discovery of the metallurgical benefits of rapid solidification techniques, the focus shifted towards developing processes that would yield products offering these benefits. Among the techniques mentioned in the previous section, powder production has become one of the most commercially used routes of material production [Srivatsan1993d]. This is a result of the ease in manufacturing products of different shapes from different alloys while retaining the properties of the rapidly solidified microstructure. The atomization process is the most common powder production technique. Using atomization, the given alloy is produced in the form of powders that have the microstructural features found in materials that are rapidly solidified. These features are described later in the following sections. Subsequent to powder production, these powders are cold pressed and consolidated to form bulk materials [Srivatsan1993d]. These consolidated parts can then be extruded or forged to get the desired shape while still retaining the characteristics of a rapidly solidified material. Although considerable research has been directed towards optimizing the consolidation processes of the rapidly solidified powders, that area of research will not be discussed here. Some of the commercially important alloy systems currently using the atomization technique of powder production include – Iron base alloys (304SS stainless steel, Precipitation hardenable steel grades), Ni-base superalloys, Al-base alloys and Cu-base alloys. These alloys in powder form are manufactured using different atomization techniques. These techniques essentially differ in the way the liquid melt stream is dispersed into small droplet.

It is well known that the final properties of a material have an important relationship to its microstructure. To attain a desired property from alloy powder, the microstructure of the powder has to be controlled. Thus the focus of research has been on understanding the rapid solidification of the atomized droplets. It should be noted that Chill Block Melt Spinning technique is also used in commercial manufacturing of ribbons [Jech1984]. However, atomization is more popular since powders can be consolidated to form a final product of the desired shape.

2.2 Rapid solidification: Microstructure and Properties

The microstructure obtained from these processes and the enhanced properties associated with these structures have been extensively studied using the techniques described in the previous section. Indeed, the literature contains an enormous volume of publications on this subject. Only a limited number of observations are presented here, with the aim of illustrating that rapid solidification techniques can generate novel microstructures with improved properties.

Typically, the rapidly solidified structure differs from a conventional normal solidified structure in fineness of the scale, difference in morphologies, presence of non-equilibrium phases and extended solute solubility. The properties evaluated include mechanical (Yield Stress, Ultimate Tensile Strength, Ductility, etc), electro-chemical (corrosion resistance), magnetic (ease of magnetization) and electrical (resistivity, superconductivity, etc). Studies on structure and concomitant properties have been performed on various alloy systems. However, for the purposes of the current chapter, an example of the advantages of rapid solidification is given for each of the sub-categories (e.g., morphology, non-equilibrium phases, UTS, superconductivity, etc) falling under the broader categories of "structure" and "property". The microstructures possible from rapid solidification techniques are described first. The properties arising from these microstructures will then be considered.

2.2.1 Fine grain

Using bulk-undercooling experiments, the Fe-25%Ni alloy was undercooled to different temperatures and solidified [Kattamis1966]. The experiment consisted of placing the alloy (approximately 100 g) in an alumina crucible placed between layers of crushed glass. The mixture of metallic alloy and glass was melted several times until a glass coating was formed surrounding liquid alloy. The glass separated the melt from the crucible wall thus reducing the possibility of nucleation in the liquid alloy starting from the crucible wall. The melt temperature was measured by using a thermocouple. At the desired undercooling temperature, nucleation was triggered by inserting iron wire into the molten charge. The undercooling was varied from 0 K to as high as 300 K and the structure of the solidified material was studied using optical microscopy.

Metallographic examination of the solidified alloy revealed that as the undercooling changed, the microstructure also changed. On increasing the undercooling, the structure changed from dendritic to fine dendritic to multiple equiaxed grains, as shown in Figure 2.1. The finer equiaxed grains in Figure 2.1(d) were thought to have developed from multiple nucleation events, arising from dendrite remelting during recalescence of the original single crystal dendrites.

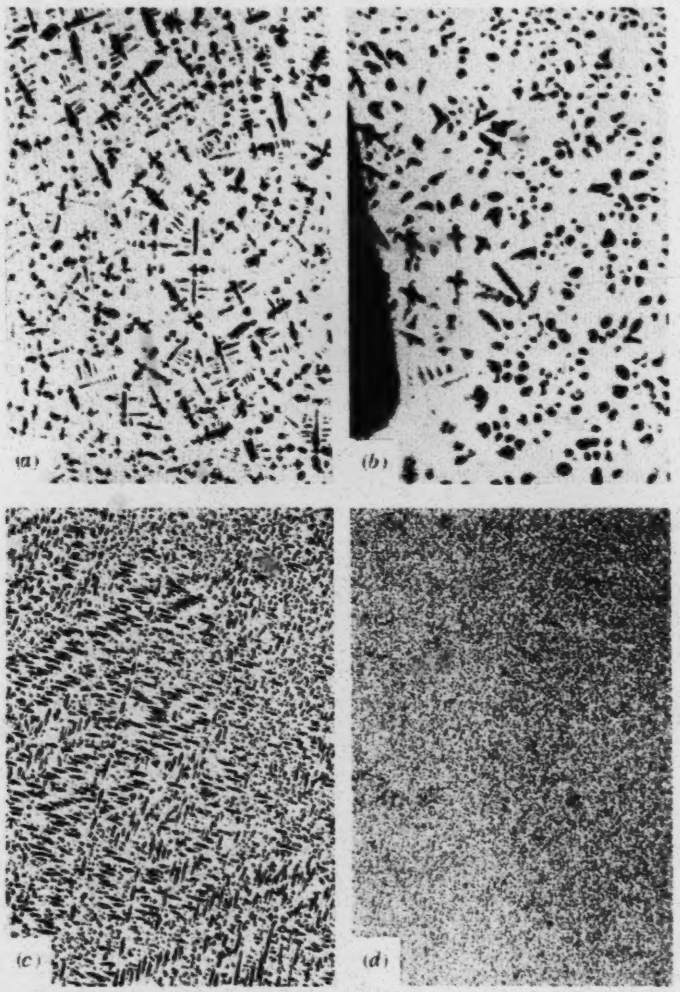

Figure 2.1: Change in morphology in bulk-undercooled Fe-25%Ni alloy. As the undercooling is increased from a) 0 K to d) 300 K, the structure changes from dendritic to fine equiaxed grains [Kattamis1966].

2.2.2 Finer structure

Rapid solidification can also generate finer structures without multiple grains forming from dendrite remelting or inoculation. An example of inoculation to get finer grain size is seen in Al alloys, where Al-Ti-B inoculators are used to increase the number of potential nucleating sites in the melt [Kearns1996]. The casting that results has a finer structure owing to the increased number of grains. Figure 2.2 shows a summary of work done on Al-Cu system for a very wide range of cooling rates [Hatch1984]. The secondary dendrite arm spacing, measured as the distance between the center of two dendrite arms [Lavernia1989], is shown as a function of cooling rates. The cooling rates shown in Figure 2.2 are measured/estimated for a variety of rapid solidification techniques. As seen from Figure 2.2, as the cooling rate increases, the dendrite arm spacing decreases. The axis label on the right hand side of the plot shows the dendrite arm spacing as “mils”, which is a unit of length. One mil is equivalent to 25.4 microns. Figures 2.1 and 2.2 thus show that a decrease in scale of the microstructure can result from either increasing the undercooling or the cooling rate.

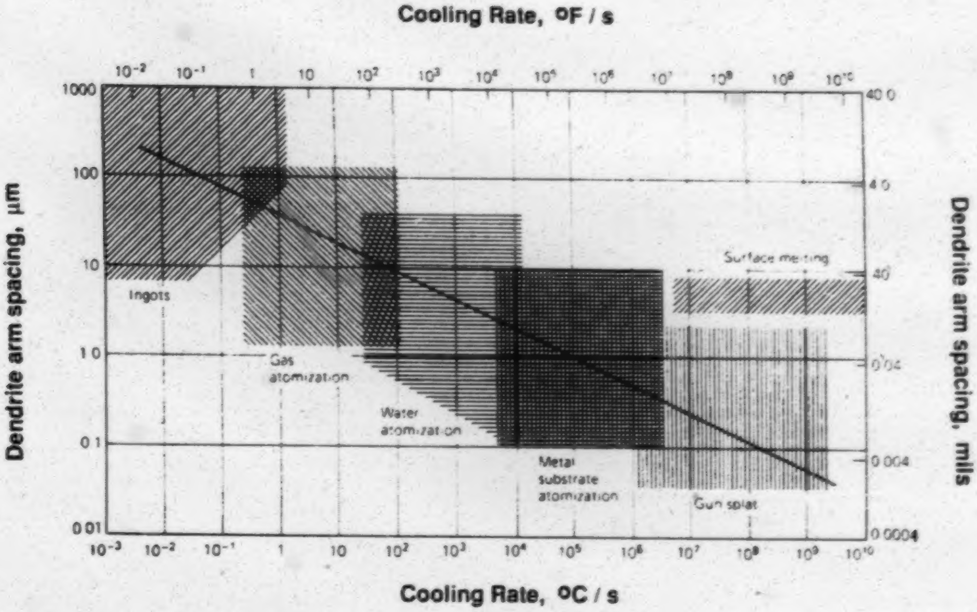

Figure 2.2: Figure showing the change in scale of the structure as the cooling rates are increased. The results are a compilation of the work of several researchers on the Al-Cu alloy [Hatch1984].

2.2.3 Morphologies

The driving force for solidification is the undercooling present in the liquid. This undercooling also dictates the thermal gradient ahead of the growing interface, since heat needs to be extracted from the interface. Therefore, by changing the undercooling or the thermal gradient, the rate of growth of the solid-liquid interface can be changed. Using Electron beam welding techniques, growth rates up to as high as 4 m/s have been attained [Schechtman1984]. At such high growth rates, the shape of the dendrite becomes important since the heat and solute rejection has to be accommodated. Using different experiments (Tungsten Inert Gas welding - TIG, Laser Surface Melting - LSM, Unidirectional Bridgeman Solidification - UDS) on

Al-Mn alloys, Juarez et al [Juarez1988] demonstrated that different morphologies can be obtained as the growth velocity is increased. Their results are reproduced in Figure 2.3. For a given composition of the alloy, as the growth velocity is increased, different morphologies of the same phase were seen. The dark squares represent Al6Mn needles, dark triangles represent eutectic structure, dark circles represent primary dendrite cellular α-Al solid solution, partial circles represent primary elongated cellular α-Al solid solution and hollow circles represent microsegregation free α-Al solid solution. Similar results were shown by Boettinger et al [Boettinger1984] for the Ag-Cu system. These examples demonstrate the effect of the growth velocity on morphology and hence on microsegregation under constrained growth conditions.

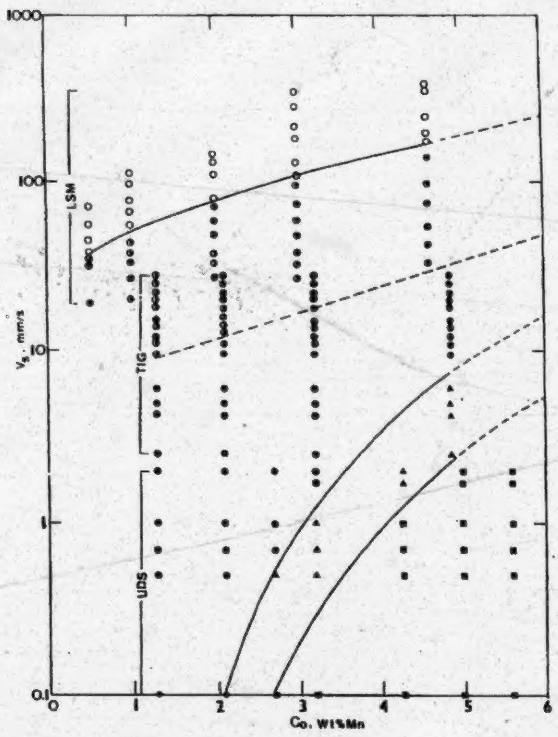

Figure 2.3: Change in morphology in Al-Mn binary alloy as a function of interface growth rate and alloy composition [Juarez1988].

2.2.4 Phases

Even when the morphologies of the solid are similar, the solid formed could be composed of different phases. Rapid solidification is known to produce non-equilibrium phases. Several alloy systems have shown phases that are not found with conventional solidification processes. Al-Fe and Al-Mn are the most commonly found Al-based binary systems that give metastable phases upon rapid solidification [Srivatsan1993a]. Al_6Fe is the metastable phase found in Al-Fe system whereas, Al_4Mn is the metastable phase found in the Al-Mn system. Al_4Cr

and Al_3Cu_2 non-equilibrium phases have also been reported in the literature [Srivatsan1993a]. Furthermore, non-crystalline or amorphous phases have been reported by Suzuki [Suzuki1989] in Al-Fe-Si alloys. Likewise, Al-Y-Ni-Mg glassy phase have also been found in this quaternary system.

2.2.5 Extended solid solution

Part of the reason for the presence of a non-equilibrium phase in rapidly solidified alloys is the now well known extension in solute solubility in the solid phase. As an example, results from the Cu-base alloy system are reproduced here [Srivatsan1993b]. Table 2.1 shows the extended solute solubilities for various elements in Cu-base alloys.

Table 2.1: Extended solute solubilities of various elements in Cu base alloys [Srivatsan1993b].

Element	Equilibrium Solubility (at%)	Extended Solubility (at%)
Ag	4.9	100.0
Be	16.4	19.0
Co	5.5	15.0
Cr	0.8	1.8
Fe	4.5	20.0
Pb	0.09	1.3
Rh	18.5	100.0

2.2.6 Properties

The advantages of rapid solidification processing can be illustrated by evaluating the properties of the microstructure it produces. Examples of improvements in mechanical strength, corrosion resistance, superconductivity and magnetic properties are given next.

2.2.6.1 Yield Stress

Nussbaum et al [Nussbaum1989] report the yield stress of Mg-Al-Zn alloy as a function of grain size. The different grain sizes were obtained from rapid solidification process (atomization) as well as conventionally cooled ingot samples of the same chemical composition. Figure 2.4 shows their result as a function of grain size. The data points for conventionally cast ingots are shown by arrows in the figure. The grain sizes from rapidly solidified processing are smaller than those obtained by conventional processes. The figure shows that as the grain size decreases, the yield strength of the alloy increases. This clearly demonstrates the increase in strength obtainable through rapid solidification.

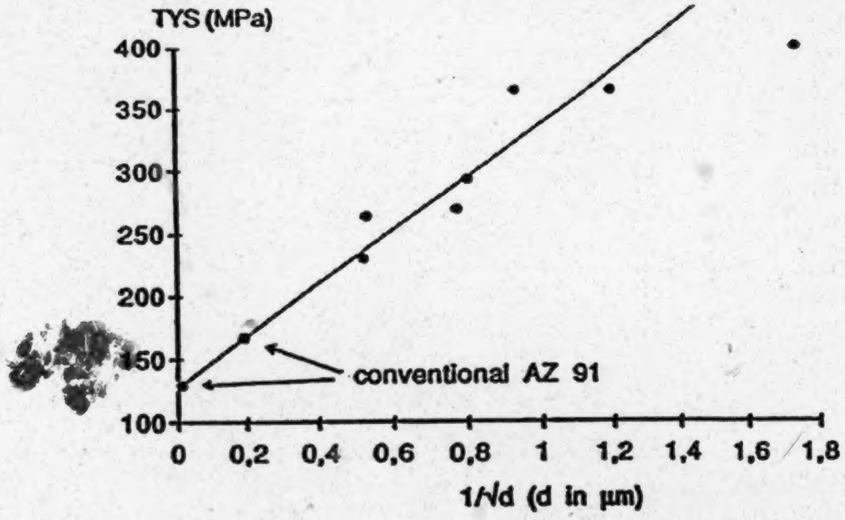

Figure 2.4: Yield Strength versus grain size for a Mg-Al-Zn alloy [Nussbaum1989].

Similarly, Albarran and coworkers [Albarran1991] worked on melt-spun rapidly solidified nickel-based superalloys - Inconel 718 and Nimonic 80A. Near the chilled surface, the alloys showed finer microstructure with superior mechanical properties. Also, melt-spun Nimonic 80A, with faster cooling rates, showed a higher yield strength - 775MPa compared to the conventionally cast Nimonic 80A which showed a yield strength value of only 611 MPa.

Undercooled $Cu_{70}Ni_{30}$ alloy obtained from emulsion droplet technique showed a gradation in structure when the degree of undercooling was changed [Jinfu2000]. The emulsion droplet technique can be used to generate droplets with different magnitudes of nucleation undercooling. This technique and the measurement of undercooling in such experiments are described briefly later in the chapter. Jinfu et al reported different microstructure, microsegregation and corresponding mechanical properties of droplets obtained under different undercooling conditions. The droplets showed a dendritic structure with an undercooling of 13K, while the structure changed to fine equiaxed grains at 200K of undercooling. The microsegregation was also reduced with increasing undercooling. They also reported improved mechanical properties with increasing undercooling. For example, they obtained 160% increase in maximum elongation at 180K of undercooling as compared to samples with no undercooling. Likewise, there was an 88% increase in UTS at 200K of undercooling.

2.2.6.2 Corrosion resistance

Microstructural refinement due to rapid solidification and increase in Al content has been reported as causing an increase in corrosion resistance of Mg alloy [Cotton1991].

2.2.6.3 Electrical and Magnetic properties

Electrical and magnetic properties are also improved as a result of microstructures obtained from rapid solidification processing. Superconducting materials with higher mechanical strength that cannot be produced from conventional processes, can obtained from rapid solidification techniques [Srivatsan1993c]. For example, rapidly solidified superconducting Cu-Nb-Hf and Cu-Nb-Ti alloys form metallic glasses with superior mechanical properties. These materials have good ductility with tensile strength ranging from 1600 to 1800 MPa [Srivatsan1993c].

Similarly, the coercivity of melt-spun Fe-Nd-B alloys has been known to vary from 2e-2 to 2e+4 Oe depending upon the interface growth velocity attained during the solidification process. Coercivity increases with cooling rate (governed by the solid-liquid interface velocity) up to a critical value and then drops drastically beyond that point [Hilsher1986]. It has been hypothesized [Hilsher1986] that the increase in coercivity with the interface growth velocity is due to the decrease in grain size with increasing velocity up to a critical diameter. This critical diameter is equal to the dimensions of a single magnetic domain. Typically, the magnetic domain size is in the range of 0.2-2 μm. Thus, the nanosized grains possible with rapid solidification can easily be single magnetic domains.

The above examples clearly show that the use of rapid solidification on a given alloy system can generate microstructures with improved properties. The formation of several new phases with different scales of morphologies illustrates the enormous potential of rapid solidification processing. These microstructures are obtained directly after the solidification. The focus of research has therefore been directed towards understanding the formation of microstructure so that better control can be obtained through the manipulation of appropriate process parameters.

2.3 Microstructure formation

Microstructure formation has been studied by developing theories as to how it forms and by performing experiments to verify the theory. The theory states that, following nucleation, the interface will grow if there is an undercooling ahead of it. During the interface growth, heat and solute (for alloys) are rejected. The heat and solute rejection are diffusion processes that are driven by gradients in the liquid. In turn, these gradients are due to differences in temperature and concentration ahead of the growing interface, respectively. Furthermore, since the solid phase grows into the liquid phase, surface tension between the two phases also plays a role in microstructure formation. Thus, the undercooling, growth rate, morphology and solute rejection (microsegregation) are intricately linked. The theoretical aspect of microstructure formation deals with developing equations that describe the relationship between undercooling, scale of structure and growth rate. Equations describing a unique relationship between the scale of the structure and undercooling and between the scale of structure and growth rate has been possible through morphological stability analysis. As pointed out in Chapter 1, solidification can be classified as either constrained or unconstrained depending upon whether the released latent heat is extracted through the solid or dissipated into the liquid. Thus, depending upon the system, the aforementioned equations may differ. For example, the slope of the thermal gradient in front of the interface is positive in the case of constrained growth and negative in the case of unconstrained growth. Thus, in comparing constrained and unconstrained growths, differences in the growth rate, morphology, scale of morphology and microsegregation can be expected for a given degree of undercooling. The unconstrained growth theory is described in more detail in Section 2.3.1 and the equations for the same are provided in Chapter 7 with the description of the model development.

The experimental verification of the theory developed, requires measurement of temperature and interface velocity. Because of the relative ease of measuring temperature and interface velocity, melt-spinning and welding techniques have been the main tools used for studying rapid solidification, such as in research by Juraez et al [Juarez1989] and Boettinger et al [Boettinger1986]. While melt-spinning and welding techniques result in constrained growth conditions, atomization and spray-deposition result in unconstrained solidification conditions.

Experimental studies have also been performed for solidification under unconstrained growth conditions. Early work has shown that differences in undercooling can result in different structures, which is evident in Figure 2.1. Therefore, depending upon the undercooling achieved, a wide variety of microstructures are possible. Also, since the morphology as well as the scale of the structure depends on the growth rate (Figure 2.2), it is important to understand the growth kinetics. Thus, research under unconstrained growth conditions has been aimed at generating droplets with some undercooling, and subsequently measuring the undercooling and growth rate and performing a metallographic analysis. The theory of unconstrained solidification and the description of the research done in this area are described next.

2.3.1 Unconstrained solidification growth theory

Unconstrained solidification microstructure has been studied with the help of models that quantitatively describe the velocity of the interface, the radius of curvature of the growing interface and the interface solute concentration. These three parameters describe the morphology, scale of the microstructure and chemical segregation. In general, the driving force for the growth of the solid-liquid interface for an alloy is the undercooling ahead of the interface. In an atomized droplet (assumed isothermal), for example, this undercooling is the difference between the alloy equilibrium liquidus temperature and the actual droplet temperature. This undercooling is also called the total undercooling and is the sum of individual undercoolings caused by heat, by solute transport (for alloys) from the interface and by the interface curvature. The individual undercooling is a result of the differences in temperature (thermal gradient), solute (solutal gradient) ahead of the interface and the surface tension between the solid and liquid phase. As the planar interface is perturbed (due to local fluctuations in thermal and solutal fields [Kurz2000]) in the presence of this total undercooling, it becomes unstable and grows in the form of cells or dendrites. The radius of curvature of the interface for the growing cells/dendrites is given by marginal stability theory, which states that the radius of curvature is equal to the wavelength of the perturbation. This perturbation wavelength is the minimum wavelength that can result in a cellular/dendritic growth [Langer1977]. Thus, the rate of growth and morphology (and scale of morphology) are related. A fast growth rate of the interface will have a smaller radius of curvature while a slower growing interface will have a larger radius of curvature. This can be understood by realizing that a faster growth rate of the interface requires rejecting the heat and/or solute at a faster rate. Thus, the system will grow with a smaller radius of curvature that facilitates easier rejection.

Combining the equations developed for the driving force of the growth of the interface and the marginal stability criteria, it is possible to calculate the interface growth rate and interface radius of curvature. Using this approach, Lipton et al [Lipton1984] formulated the equations for calculating the velocity of dendrites under unconstrained growth conditions for low total undercoolings at near equilibrium conditions (LGK model). Trivedi and coworkers [Lipton1987a] extended the dendrite kinetics for unconstrained growth to the more general case of a wider range of undercooling (LKT model).

A very important aspect of microstructure formation is the segregation of solute during the phase transformation. Because of the difference in solute solubilities between the solid and liquid phases, the solute has to be rejected during the phase transformation. The interface velocity and the solute rejection are coupled and govern the microsegregation in the solidifying system. The partition coefficient gives the magnitude of solute segregation between the solid and the liquid phases and is given by $k_0 = {C_s^*}/{C_l^*}$, where C_s^* and C_l^* are solute concentration in the solid and liquid phases respectively at a given temperature. Under equilibrium conditions, the value of the partition coefficient is determined from the equilibrium phase diagram of the system under study. The C_s^* and C_l^* values are obtained from the liquidus and solidus lines and no reference is made to the effect of interface velocity on the partition coefficient. However, one of the consequences of rapid solidification is the extremely high interfacial velocities that result in deviation from equilibrium at the interface. Because of very high dendrite velocity, there is not enough time for the solute to diffuse out of the solid phase and therefore there is a modification of the solute transfer across the interface. Under such conditions, it becomes necessary to take into account the effect of interface velocity on partition coefficient. Aziz [Aziz1982] developed a correlation that takes this effect into account. Since the solute is unable to escape the rapidly growing solidifying front, the theory is popularly termed the solute-trapping theory. Aziz [Aziz1982] developed a model for the modification in partition coefficient as a function of interface growth velocity and this has been experimentally confirmed [Smith1993] for directional solidification of germanium and silicon. The model states that, as the velocity increases, the partition coefficient also increases monotonously and eventually reaches a value of 1, suggesting no solute transfer. Thus the model predicts segregation free (diffusionless or partitionless) solidification at very high growth rates. Trivedi and coworkers [Lipton1987b] extended their unconstrained growth model (LKT model) for higher undercoolings to include Aziz's solute trapping model.

In summary, the theory states that undercooling, growth rate, morphology and microsegregation are coupled. Moreover, the theory is based on the undercooling-growth rate relationship and suggests that growth rate plays an important role in microstructure formation and microsegregation. Therefore, attempts have been made to confirm experimentally the theory of growth in an undercooled melt and to understand growth rates as a function of undercooling. The following section gives the major experimental efforts in this area and is divided into two categories based on growth under constant undercooling or changing undercooling. In addition, reference is made to undercooling experiments conducted by Perepezko and coworkers.

2.3.1.1 Controlled nucleation undercooling

One of the foci of the studies on unconstrained growth conditions has been towards fixing the initial nucleation undercooling and measuring the velocities of growth, recalescence and microsegregation during recalescence for that particular undercooling. By changing this initial undercooling, the rapid solidification characteristics of velocity, recalescence etc. can be estimated as a function of undercooling. The experimental challenge has been in achieving undercooling, since the presence of heterogeneous agents can trigger nucleation. One way to achieve a desired undercooling is the bulk-undercooling technique used by Kattamis et al [Kattamis1966], as briefly described in a previous section (Section 2.2.1). However, undercooling – growth rate relationships cannot be ascertained by this technique and in addition the solidified product from such experiments is not in a droplet form. Thus, techniques are required to produce a droplet in which undercooling can be attained and growth rates can be measured.

One of the most effective ways to obtain a desired undercooling in a droplet is the levitation melting technique [Schleip1988]. The technique involves electromagnetically levitating a metallic droplet of a given size and composition. The induction coil, which helps in levitating the droplet, also heats and melts the droplet to above the melting temperature of the droplet. The droplet is flooded in a cross-flow of inert gas which cools the droplet. The nucleation is prevented by ensuring that the droplet does not come into contact with any external contamination that might trigger heterogeneous nucleation. The temperature of the droplet is measured by an optical pyrometer or by photosensing diodes. When the desired undercooling is reached in the droplet, the nucleation is induced at the surface by touching the droplet surface with a ceramic pin (Al_2O_3) or a plate. Thus, a controlled nucleation undercooling is achieved in the droplets. A variation of the levitation technique is the emulsion technique. In this technique the metal droplet is enveloped in a glass or slag coating thus preventing the heterogeneous nucleation from external impurities that can act as potential nuclei. A number of experiments based on the levitation melting technique and the emulsion technique have been performed. The microstructure, degree of recalescence, microsegregation and dendrite velocity measurements from bulk-undercooled, levitated droplets and emulsion droplet experiments are summarized next.

2.3.1.1.1 Microstructure

Kattamis and Flemings [Kattamis1966] performed experiments on several alloy systems (Fe-Ni, Fe-Ni-S, Ni-Ag and Ni-Cu) using the bulk-undercooling technique. They showed that increasing the undercooling results in a change in morphology that occurs at some critical undercooling temperature specific to the alloy system. This change in morphology was believed to be the result of dendrite remelting at the end of recalescence [Kattamis1966]. The example of the change in microstructure given in Figure 2.1 is from this study.

2.3.1.1.2 Velocity

The growth rate of dendrites during recalescence has been measured by high speed photography. These have been carried out for various alloy systems such as, Ni-25%Sn [Wu1982, Wu1987], Fe-Ni [Zhao1989], Fe-P [Suzuki1989], Cu-Ni [Schleip1988] and Ni-Si [Cochrane1991]. While Wu et al and Zhao et al performed experiments on emulsion droplets, Schleip and Cochrane performed experiments on those formed by the levitation technique. In the case of the emulsion technique, the velocity was measured by tracking the thermal change in the droplets (optical pyrometer) using high speed photography. In the levitation technique photosensing diodes were used for measuring the temperature at different parts of the droplet and the interface velocity was measured by correlating the time lag in the temperature profile at the two points. Irrespective of the method of measuring the velocity, the trend that emerges for all the alloy systems studied is an increase in growth rate with increase in undercooling. This is consistent with the model formulation assumptions that the growth rate is proportional to the undercooling. A typical result from the Ni-Sn [Wu1987] alloy system is presented in Figure 2.5.

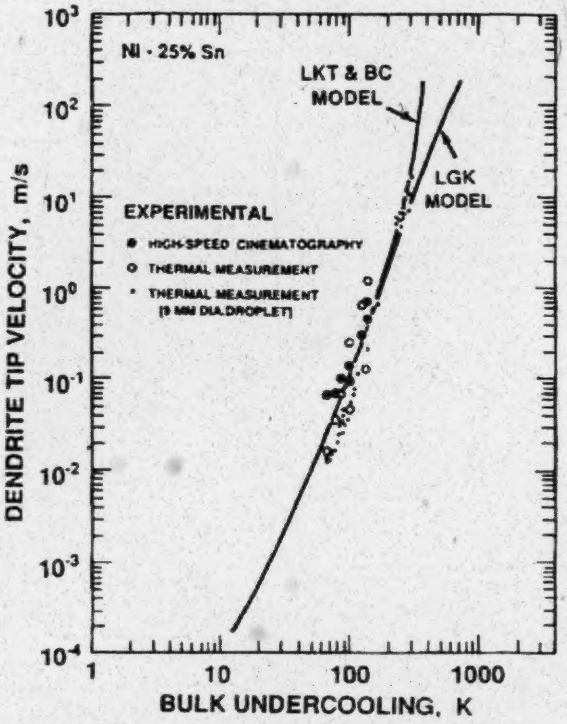

Figure 2.5: Increase in dendrite growth rate as a function of undercooling for Ni-Sn alloy. The results are from Emulsion technique experiments. Model results are also reported for comparison [Wu1987].

2.3.1.1.3 Microsegregation

Reduced microsegregation was seen in bulk undercooled samples, as shown in experiments on Fe-25%Ni [Kattamis1970], Ni-25%Cu [Kattamis1967] and

VM300 Maraging steel [Kattamis1974] samples. The results for Fe-Ni, Ni-Cu and 4330 Steel are given in Figure 2.6, which clearly shows that increasing the undercooling decreases the microsegregation in these alloys. Microsegregation in these alloys is defined by segregation ratios, defined as the ratio between the maximum solute concentration of the primary phase and the equilibrium solute concentration. For a given alloy, as the undercooling increases, the segregation ratio decreases. Energy dispersive X-ray analyses were performed to measure the solute concentrations on 2-D sections of dendrite arms. The increase in segregation ratio was believed to be due to increased recalescence with higher undercooling. Increased recalescence results in a higher fraction of solid with solute trapping. Recalescence is defined as an increase in temperature of the system even as the system is solidifying. It results when the latent heat released during phase transformation is greater than the heat lost to the surroundings. The high rate of latent heat release is a consequence of very fast growth rates of the interface.

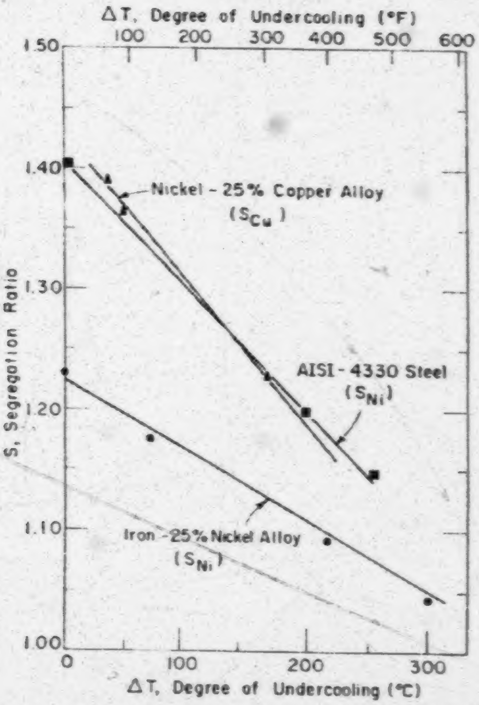

Figure 2.6: Decrease in microsegregation as a function of undercooling for different alloys. The results are from bulk undercooled experiments [Kattamis and co workers].

The bulk-undercooled specimens also exhibited higher solute content in the dendrite core (thereby lower interdendritic solute content) as compared to normal solidification specimens. This has been explained by the fact that the core of the dendrite is formed in the initial stages of solidification during the recalescence regime. Solute trapping during recalescence results in higher solute content. As the recalescence ends, normal solidification takes place at near equilibrium conditions and solute rejection takes place. Therefore, the solute content is lower at the edges of the dendrite.

The research on controlled nucleation undercooling suggests that growth rate is proportional to undercooling. Furthermore, high growth rates can result in reduced segregation during recalescence and can also produce finer structure. Thus, it confirms the role of growth rates on microstructure formation and microsegregation for constant undercooling condition.

2.3.1.2 Uncontrolled nucleation undercooling in droplets

As noted in Section 2.1.4, the atomization route of powder production has become commercially important. From a rapid solidification perspective, the advantage of producing small liquid droplets from a relatively larger liquid volume is that, the finite number of potent heterogeneous nucleation sites present in the larger liquid volume is distributed in a very small number of the liquid droplets. Thus, a majority of the liquid droplets are free of nucleating agents, allowing a high degree of undercooling to be achieved in them. Moreover, the small size of the droplets helps in increasing the ratio of surface area to volume, thus resulting in faster heat loss. Furthermore, since the latent heat released is dissipated into the droplet volume, the solidification occurs under unconstrained conditions. Thus, the solidification of the atomized droplet falls under the category of unconstrained growth.

The experiments performed with the levitation melting and emulsion techniques are based on controlled undercooling at a certain known temperature, achieved with the help of surface induced nucleation. However, most of the industrial rapid solidification processing has been based on powder metallurgy techniques which use atomization or the spray deposition. Solidification of the droplets during atomization (or spray deposition) starts with nucleation at some undercooled temperature, which is uncontrolled. Following nucleation, the solidification occurs, dissipating heat first to the solidifying droplet volume and then to the surrounding atomization fluid. This may result in recalescence within the droplet. As the recalescence proceeds, the time dependant undercooling continuously changes. Such a change in undercooling in front of the growing interface would affect the interface velocity during recalescence; consequently the microstructure formation and microsegregation may be affected. Recall that the recalescence in the droplet is a result of heat balance between the latent heat generated and the heat lost to the surrounding. Since growth rate affects the microstructure and microsegregation, it is worth noting that a changing growth rate of the interface with time can result in a gradation in microstructure and microsegregation. These events may also occur under controlled nucleation undercooling conditions during levitation melting or emulsion droplet experiments. However, the foci of these experiments were not to study the gradation of microstructure and microsegregation within individual droplets.

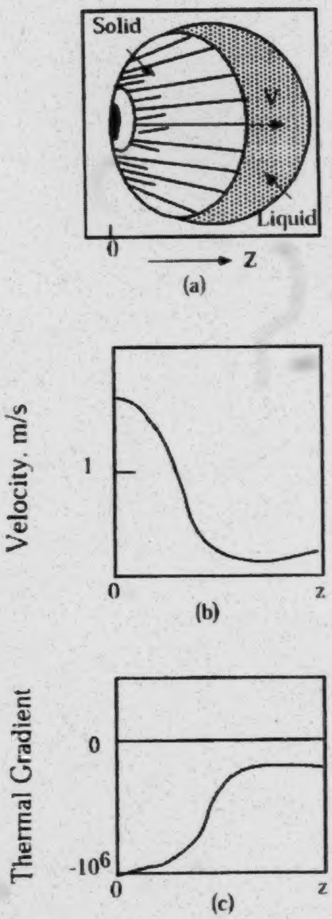

Figure 2.7: Schematic for a change in undercooling during recalescence in a droplet solidification which results in a change in the interface velocity [Trivedi2003].

Figure 2.7 [Trivedi2003] provides a schematic of changes in thermal gradient and interface velocity (interface growth rate) within a droplet. The figure shows the spatial variation of the interface velocity within the droplet when recalescence varies the undercooling and subsequently the thermal gradient within the droplet. Such a situation exists within a non-isothermal droplet when temperature differences exist within the droplet. Recalescence can also cause a temporal change in temperature within the droplet and thus vary the interface velocity. Therefore, both spatial and temporal change in temperature within the droplet can cause changes in interfacial velocity. The temporal change in temperature can also exist within an isothermal droplet. Since interface velocity affects the microstructure and microsegregation, thus a variation in undercooling within the droplet can result in a gradation in microstructure and microsegregation within the droplet volume.

The variation in undercooling and interface velocity within the droplet may also differ depending upon the position of the nucleus within the droplet. For example, in Figure 2.7, if the nucleus is shifted from droplet surface to droplet center, the thermal gradient profile within the droplet may change. This, in turn, will affect the growth rate profile. Moreover, alloy composition can also affect the interface growth rate within the droplet because interface growth rate and chemical composition in the interface vicinity are interrelated. Thus, the alloy composition, time dependent thermal profile and nucleation position can all affect the microstructure and microsegregation within the atomized droplet. Therefore, studies on these issues are critical to understanding the microstructure and microsegregation in the droplets.

To study solidification under unconstrained growth conditions with changing undercooling, atomization and drop-tube experiments have been carried out. However, majority of the work done on atomization has been concentrated on characterizing the microstructure and correlating it with a processing parameter, cooling rate being the most commonly used parameter. Moreover, with a lack of a suitable 3–dimensional characterization tool, the microstructure characterization has been 2-dimensional. This microstructural characterization work is described next.

2.3.1.2.1 Experiments

As mentioned earlier, during droplet solidification, the droplets may experience a change in undercooling. Most of the work on atomization powders has been concentrated towards either determining powder size distribution or microstructural characterization of the powders. Powder size distribution has been studied by Henein and co workers [Morin1996] and Flinn [Srivatsan1993c], amongst others. Such research typically involves generating log-normal plots for estimating the mean droplet size and standard deviation of the droplet diameter. By relating the size distribution to process parameters, the size-distribution information can be used as a means of assessing a given powder production technique. For example, Salgado et al [Salgado1991] have reported different powder size distributions for water and air atomization of Ni-Cu alloy, with more spherical particles obtained in the case of air atomization. They have also shown that by using a higher overheating temperature, smaller mean powder size results from both techniques. Moreover, smaller particle size was obtained by increasing the atomization fluid pressure.

2.3.1.2.2 Characterization

Microstructural characterization work is essential to studying the rapid solidification characteristics of powders obtained from these experiments since powders from atomization and drop-tube experiments do not yield themselves to real-time temperature measurements or growth front velocity measurements. The entire microstructural characterization work can be divided into either finding the kind of phases and morphology formed or finding the scale of the morphology as a measure of the refinement of the structure.

One example of characterization of the first kind is the work done by Flinn [Srivatsan1993e] on the effect of atomization process parameters on Fe-based alloys. The atomization techniques used were Vacuum Gas (VGA) and Centrifugal Atomization (CA). For Fe-40Ni alloys, he showed that VGA powders showed dendritic structure, whereas the CA powders showed a predominantly cellular structure. The effects of small additions of Nb (0.3wt%) and C (0.05wt%) on the Fe-Ni alloy were also studied. The results showed that these additions did not result in any differences in the morphology. Microstructures for a series of stainless steel powders processed by Inert Gas Atomization showed differences in morphologies. While 304SS and PH 13-8 steel showed dendritic morphology, Fe-16Ni-9Cr-0.04C was cellular. Likewise, gas atomization experiments on Al-Ti alloys by Lavernia and coworkers [Gupta1992] have experimentally shown dendrite/cell free zones in very small droplets (less than 10 μm) and dendritic microstructure in 100 μm droplets. Similarly, Samuels [Samuels1986] has shown that atomization melt temperature and type of alloying elements can result in different morphologies in the droplets. These examples show that the atomization process can yield different morphologies for a given alloy.

The scale of the structure, traditionally plotted as a function of droplet size, is usually given in terms of the spacing of the secondary arms in a dendritic microstructure. It has been shown that as the droplet size decreases, the secondary dendrite arm spacing decreases too, thus showing the effect of cooling rate on the refinement of the structure. An example of such research done on Al-Cu binary alloys (Al4.5%Cu) is given in Figure 2.8 reproduced from Wiskel et al [Wiskel2002b].

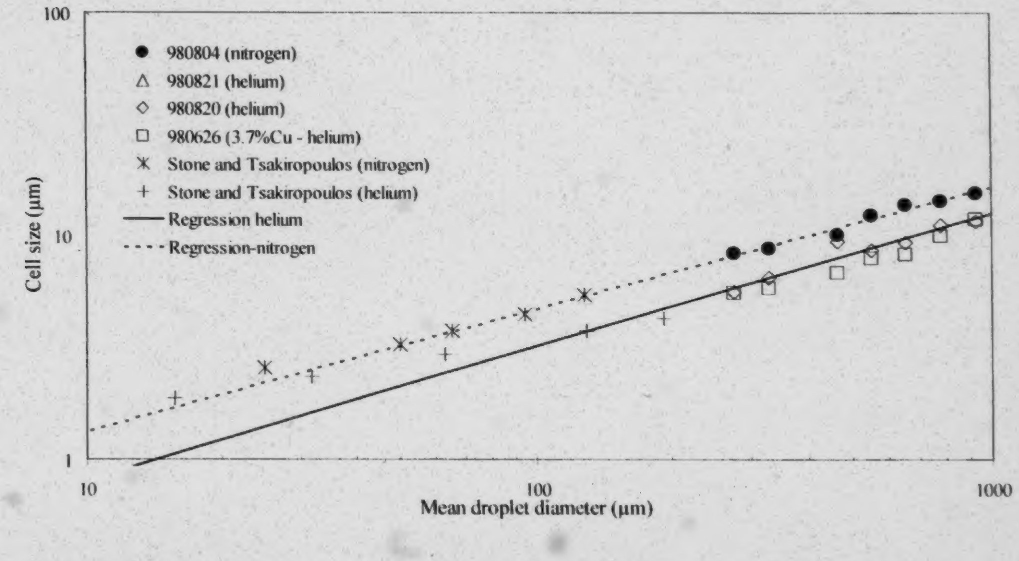

Figure 2.8: Decrease in cell spacing with decreasing droplet size during rapid solidification of Al-4.5%Cu atomized powders [Wiskel2002b].

The figure shows the decrease in cell spacing as the droplet size decreases. The figure also shows the effect of gas type on the fineness of the structure. Because of the better conductivity of He gas compared to N_2, the cooling rate is faster for droplets atomized in He as compared to N_2. Thus, a droplet of a given size in He would show finer structure compared to the same droplet size atomized in N_2. These results, reported as a function of droplet size and gas type, provide important information on the kind of microstructure to expect if the processing parameters, like droplet size or gas type, are changed.

It has been shown mathematically that the cooling rate attained by a droplet depends on its size [Lavernia1989]. For the same convective heat transfer condition of same gas type smaller droplets have faster cooling rates. Therefore, the scale of the structure has also been reported in terms of cooling rates. The cooling rates reported in these results are obtained from empirical formulas of the type,

$$SDAS = F\dot{T}^{-n} \tag{2.1}$$

Equation 2.1 states that faster cooling rates result in smaller arm spacings or a finer scale of microstructure. SDAS is the secondary dendrite arm spacing, $\dot{T}$ is the cooling rate, F is the pre-exponential constant and n is the exponential power whose values depend on the alloy. For example, Jones [Jones1983] proposes F=18 to 47 and n=0.25 to 0.39 for Al4.5Cu in the cooling rate range of 10^{-5} to 10^{+4} K/s. Based on the Rotating Electrode Process of atomization, Dube et al [Dube1996] have proposed F = 61.1 and n = 0.348 for Al-4.5Cu alloy for 10^2 to 10^4 K/s range of cooling rates. The cooling rates were obtained from atomization modeling whereas the values of F and n were obtained empirically from experimental SDAS values.

Note that according to the definition of cooling rates given in Section 1.1 (Equation 1.1), the cooling rate can be converted into solidification time, t_f. Therefore, the secondary dendrite arm spacing or the scale of the structure can also be correlated with the total solidification time. Since the cooling rate is inversely proportional to the solidification time, the secondary arm spacing is directly proportional to the length of the time taken for complete solidification. Therefore, the longer the time required for solidification, the coarser the structure would be. This has indeed been observed experimentally by Kattamis and Flemings [Kattamis1966b]. The coarseness of the scale of the structure is explained by a phenomenon called "Coarsening". Derivations based on first principles, which include solute diffusion, indicate that the scale of the structure is proportional to one-third the power of the solidification time t_f.

$$SDAS = Ht_f^{\,b} \tag{2.2}$$

Where H will assume a different value compared to the pre-exponential factor F in Eqn. 2.1 and b = 1/3.

2.3.1.2.3 Modeling efforts

The 2-D characterization work does not give information on the change in structure within a droplet. Depending upon the droplet section analyzed, the change in structure may or may not be identified. Also, the microstructure characterization does not give growth rate-microstructure or growth rate-microsegregation information. To complement the experimental results, modeling attempts have been made. As noted earlier, cooling rate has been extensively used to describe a given process. However, because of practical difficulties, cooling rates cannot be measured in situ while the droplets are being produced. Hence, models have been used to estimate cooling rates.

The effects of process parameters like droplet size and gas type on cooling rates have been extensively studied by modeling the atomization process. Models of isothermal droplet solidification are based on solving the heat energy equation for the droplet as follows:

$$C_p \frac{dT}{dt} = -\dot{Q}_c + L\frac{df_s}{dt} \tag{2.3}$$

where $L\frac{df_s}{dt}$ is the latent heat released due to droplet solidification and $\dot{Q}_c$ is the convective heat loss from the droplet surface.

Cooling rate is a result of the heat balance between predominantly convective heat loss and latent heat generation. In atomization models, these two parameters are evaluated independently. Convective heat transfer is calculated by evaluating the heat transfer coefficient, which is either assumed to be constant or calculated by using empirical correlations. Levi et al [Levi1982] have assumed constant heat transfer coefficient, which does not simulate the conditions during an actual atomized droplet cooling process. During atomization the relative velocity between the droplet and the atomizing fluid constantly changes; thus the heat transfer coefficient would assume a transient value. The Whitaker and Ranz-Marshall correlations are the most popular expressions used to evaluate the transient heat transfer coefficient during atomization. The equation for the Whitaker correlation (in its modified form) is given in Chapter 7. These expressions help in evaluating the Nusselt number for a sphere placed in the cross-flow of a fluid. The Nusselt number is defined as follows:

$$Nu = \frac{h_c D_p}{k_s} \tag{2.4}$$

where Nu is the Nusselt number, h_c is the convective heat transfer coefficient, k_s is the conductivity of the gas and D_p is the droplet diameter. Combining the definition of Nusselt number and the correlation (Whitaker or Ranz-Marshall), the heat transfer coefficient is evaluated. The mathematical forms of these correlations have Re number, which takes into account the relative velocity between the droplet and the fluid. Thus transient heat transfer coefficients can be calculated. Lee and Ahn [Lee1994] have used the Whitaker correlation to calculate the heat transfer, whereas Yang and Lavernia [Yang1997] have used the Ranz-Marshall correlation.

The rate of latent heat released depends on the rate of solid formation, which in turn depends upon the interface growth rate. Also, the interface growth rate would result in the solid-liquid interface traversing the volume of the droplet. Since the interface growth rate depends on the nucleation undercooling, two pieces of information are required; i) a nucleation temperature and ii) a position where nucleation may occur.

To calculate the nucleation temperature in the droplets during atomization, droplet solidification models are often coupled with transient nucleation models. By coupling these two models, the instantaneous cooling rate can be fed into the nucleation model and the cooling rate dependent droplet nucleation temperature can be calculated. This nucleation temperature is then used to estimate the undercooling required for calculating the interface growth rates. Both, transient homogeneous [Liu1995, Yang1997] and transient heterogeneous nucleation models [Lee1994, Tsao1995] have been used.

The position of the nucleation site is often assumed in such models. It is typically chosen to be one point on the surface [Lee1994, Levi1982] or even the whole surface itself [Yang1997]. These assumptions have not been verified experimentally. Likewise, there is no experimental evidence of number of nucleation sites within a solidifying droplet.

Once the nucleation undercooling and the nucleation site are fixed, the interface is allowed to grow into the melt, releasing latent heat. The literature proposes several growth rate - undercooling relationships, that have been used. These relationships include linear and exponential laws for planar continuous growth at small and large undercoolings [Levi1982, Clyne1984, Lavernia1988] as well as the power laws for dendrite growth [Zhang1992]. Thus, by combining the latent heat generation from dendrite growth rates and the droplet heat loss due to the convective heat transfer, the temperature of the atomized droplet can be calculated as a function of time. This provides the cooling rate estimation. By changing gas type, droplet size, melt super-heat and other parameters or a combination thereof, their effects on cooling rate can be assessed. Moreover, the evaluation of temperature profile within the droplet gives information about the change in undercooling in the droplet.

Almost all of the models that have been developed are for Gas Atomization. These models have been developed to study cooling rates only. In Gas Atomization, gases at high pressure travel at supersonic speed, which not only helps to break the liquid jet into droplets, but also transfers heat out of the droplets through convection, thus cooling them. The relative velocity between the droplet and the gas is required for evaluating the Re number for evaluating the convective heat transfer coefficients. The relative velocity is evaluated using models [Su1997], which have not been validated to date owing to the practical difficulties of experimentation. Furthermore, it has been shown that thermal coupling may exist in Gas Atomization that further complicates the modeling of droplet cooling [Freyberg2003]. Thermal coupling is the phenomena where the cooling droplets heat the surrounding gas and subsequently, the heat removal ability of the heated surrounding gas in turn is affected. For all these reasons, the cooling rate predictions from these gas atomized droplet solidification models have not been experimentally validated.

2.3.1.2.4 Microsegregation models

The literature presents a number of standalone microsegregation models that have been developed based on solidification theories only. Some important microsegregation models are the Gulliver and Scheil model [Scheil1942], Brody-Flemings [Brody1966] model and the Clyne-Kurz [Clyne1981] model. The Gulliver-Scheil model assumes zero solute diffusion in the solid and infinite solute diffusion in the liquid. The Brody-Flemings and Clyne-Kurz models assume finite diffusion in the solid and infinite diffusion in the liquid. These models do not take into account the interface growth rate. According to theory, the growth rates can affect microsegregation. Some of the models that do take into account the cell/dendrite growth rate (or cell/dendrite tip undercooling) are the Palacio-Solari-Biloni [Palacio1985] and Tong-Beckermann [Tong1984] models. The Palacio-Solari-Biloni model takes into account the tip undercooling as a result of a solute gradient ahead of the tip. Likewise, considering a solute boundary layer analysis in the liquid and taking finite solute diffusion in the solid and liquid phases, Tong and Beckermann [Tong1984] also developed a microsegregation model. However, all of these models, and others, are based on a local mass balance of solute in the vicinity of the individual cells or dendrites. Hence, these models are based on a scale that corresponds to the scale of cell/dendrite arm spacing.

To model microsegregation in atomized droplets with a moving interface, any one of the models mentioned above (e.g. Palacio-Solari-Biloni) can be used with the condition that solute (or mass) needs to be conserved for the entire droplet volume and not just at the local dendrite tip region. Furthermore, interface growth rate also needs to be considered to assess its effect on microsegregation. Rappaz-Thevoz [Rappaz1987] developed a microsegregation model (R-T model) for equiaxed solidification of a grain in a casting. They have considered a spherical grain and have predicted microsegregation within the grain by taking into account both micro and macroscopic solute balance. Moreover, they have used the LGK model [Lipton1984] for dendrite kinetics, which gives fraction solid and latent heat released. Thus, considering the solute balance and dendrite kinetics in a spherical grain, presents an opportunity to model the solidification of the atomized droplets, provided that conditions of heat loss from the droplets are taken into account. In the current work, the R-T model has been modified for the external heat loss conditions to model the microsegregation in the atomized droplets. The model development is described in Chapter 7.

2.3.1.3 Undercooling measurements by Differential Scanning Calorimeter (DSC)

Using Differential Scanning Calorimeter (DSC), nucleation undercooling measurements have been made on powders by Perepezko and coworkers. These measurements have been made to assess the effects of variables such as powder size, cooling rate, surface coating, etc, on nucleation undercooling [Mueller1987] and to correlate the type of phase found with a certain undercooling [Allen1991]. The technique involves, first, producing metal droplets in a carrier medium. Droplets are typically generated by shearing a liquid stream. The role of the carrier medium is twofold, which is usually inorganic salts. The carrier medium supports the droplets formed and also forms a non-catalytic surface coating on the droplets. These droplets are then subjected to heating and cooling cycles in a DSC. A schematic of a heating and cooling cycle is shown in Figure 2.9. The endothermic peak in the heating cycle, T_X, represents the melting temperature of the droplet. T_Y represents the exothermic peak corresponding to the nucleation temperature of the liquid droplet. The cooling cycle can be carried out at a certain rate, with the difference between T_X and T_Y being the nucleation undercooling.

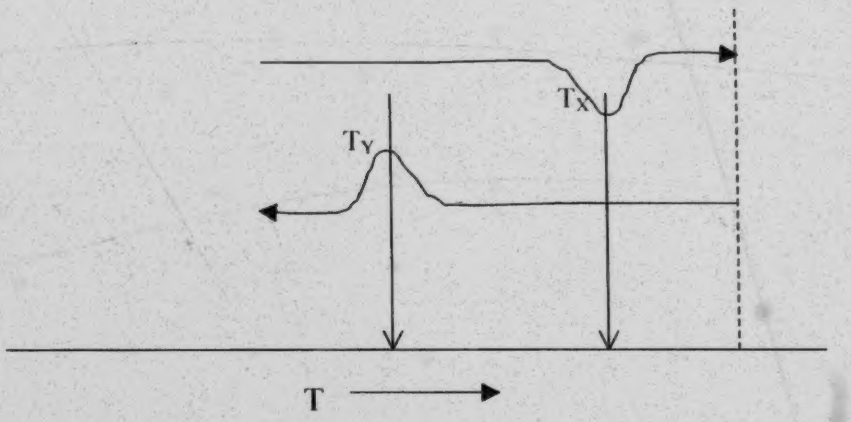

Figure 2.9: Schematic of thermograph from a DSC experiment. Arrows indicate the heating/cooling cycle.

Experiments were performed on pure Al powder [Mueller1987] in the size ranges between 150 μm and -20 μm. The cooling rates were varied between 0.33 K/s to 25 K/s. It was shown that smaller particles and higher cooling rates result in higher undercooling. Furthermore, the choice of salt and melt superheat also plays a role in determining the undercooling.

While the results from this technique are informative, the technique has the following shortcomings. The technique requires a carrier medium, which needs to be non-catalytic to the droplet material as well as be stable in the melting temperature range of the droplet. These two conditions place stringent constraints on the choice of the medium. Secondly, the DSC technique cannot be used on as-atomized powders, which are produced without a suitable surface coating.

Furthermore, the cooling rate attainable in DSC is very small compared to the cooling rates experienced by the atomized droplets. Lastly, the dendrite growth velocity cannot be measured to correlate with the undercooling.

The studies cited so far are deficient in the following areas. On account of changing undercooling during recalescence, the interface growth velocity changes across the droplet (Figure 2.7) and therefore a change in morphology would be expected. The change in interface velocity can be a result of time dependant change in undercooling, spatial variation of undercooling, alloy composition or a combination of these. The study of the variation in microstructure during spatial change of undercooling has been studied to some extent by Boettinger [Boettinger1986] and very recently by Trivedi et al [Trivedi2003]. Boettinger reported and quantified the different morphologies present in an atomized Al-Fe droplet. Both the droplet size and alloy composition were fixed. Similar analysis was done on Al-Si alloy droplets for different sizes by Trivedi et al. These results confirm the possibility of microstructure gradation in atomized droplets. However, the effect of alloy composition and the effect of temporal changes in undercooling on microstructures have not been studied experimentally. Furthermore, there is no knowledge of the number of nucleation sites or position of nucleation sites within the atomized droplets. Recall that induced nucleation for the emulsion and levitation techniques were externally carried out on the droplet surface. Thus, the study of changes in growth rate, and therefore microstructures, within a droplet is not complete.

Though microsegregation is inherently coupled to microstructure formation, a very limited experimental/modeling work has been carried out to study microsegregation in atomized droplets. In the most notable work of this kind, Lavernia and coworkers have shown experimental evidence of the extension of solute solubility as a function of decreasing droplet size in several systems - Rh in Pd-Rh alloys [Li2000], Mn in Al-Mn alloys, Al and Zn in Mg-Al-Zr and Mg-Zn-Zr alloys [Ruhr1990] respectively. They have shown that as the droplet size decreases (in the size range of 10-400 μm) the solute solubility of the primary phase increases. These results are based on the change in lattice parameter values of the solvent as a result of the presence of solute atoms in the alloy phase. However, the effect of alloy composition on microsegregation has not yet been studied.

While microsegregation can be experimentally determined, however, experimental measurement of interface growth rate during powder production is not possible. Thus, experimentation has to be complemented by modeling so that the growth rate–microstructure–microsegregation relationship can be assessed. No microsegregation model exists for the atomized droplets. The importance of such a model is that it can provide valuable microsegregation data as a function of nucleation undercooling and interface growth rate. Furthermore, the effect of droplet size, gas type and cooling rates on microsegregation can also be studied. Moreover, in the absence of a microsegregation model for the atomized droplets, it has not been possible to validate the cooling rate values for the droplets while taking into account microsegregation within the droplets.

2.4 Thesis objective

In summary, previous work has led to the development of a theory for dendrite growth under unconstrained growth conditions. This theory states that the growth velocity is proportional to the undercooling. This has been confirmed experimentally for controlled nucleation undercooling. As the undercooling changes, the growth rate changes, consequently changing the morphology. Furthermore, for atomized droplets, it has been hypothesized that gradation in morphology may exist as a result of spatial changes in undercooling that result from recalescence. However the issues of the effect of variation in alloy composition and nucleation (single or multiple, position) on microstructure formation and microsegregation have not been addressed experimentally. These deficiencies raise the following questions:

- How would a change in alloy composition change the microstructural evolution and microsegregation?
- What role does growth rate play in microstructure formation and microsegregation?
- How many nucleation sites are present in an atomized droplet?
- How would recalescence and microsegregation be affected if the nucleation position changes?
- How does microsegregation change with undercooling and cooling rates during rapid solidification?

The objective of this thesis is to attempt to answer the above questions. The aim was to perform experiments as well as modeling. Rapidly solidified powders of different compositions of a given alloy system were generated using atomization. Following the powder generation, 3-D characterization was performed on these powders to study nucleation sites, microstructure evolution and microsegregation. This gave information on the nucleation position, spatial microstructure variation within the droplet and volume information on the microsegregation in the droplet.

A microsegregation model was developed for an individual droplet solidifying during atomization. By taking dendrite kinetics and nucleation position into account, the effects of changing the alloy chemistry and interface growth rate on microsegregation could be studied. With an isothermal droplet model, the role of interface growth rate on microsegregation was assessed in terms of microsegregation in the droplet volume.

2.4.1 Choice of rapid solidification technique

The Impulse Atomization process was developed and patented [Ding1997] at University of Alberta, Canada. It is a single fluid atomization process that results in rapidly solidified metallic (or non-metallic) droplets and powders. It has been shown [Morin1996, Ding1997, Wiskel2000a] that this process can reproducibly yield powders of uniform size-distribution with cooling rates as high as 10^4 K/s. The cooling rate was estimated from a droplet solidification model developed for droplets solidifying during Impulse Atomization [Ding1997]. This model only calculates the thermal changes within an iso-thermal droplet without taking microsegregation into account. Heat loss from the droplet is determined by calculating the transient convective heat transfer coefficient as described earlier with respect to other models (Section 2.3.1.2.3). Since a stagnant gas is used in this process (process described in detail in Chapter 3), modeling the relative velocity between the droplet and gas is straight forward. Moreover, extensive experimental work on the Al-Cu system has provided experimental validation of the cooling rate from this model [Wiskel2002a]. Therefore, given its advantages as an experimental tool for producing rapidly solidified powders and ease of developing droplet solidification model, Impulse Atomization was chosen to perform the experiments for this study.

2.4.2 Choice of alloy system

Rapidly solidified Al-alloys have resulted in a variety of microstructures that have led to a significant jump in Al-alloy application. Specifically, the aerospace and automotive industries have benefited immensely from the rapid solidification research on Al-alloys. The microstructural features that have brought about such changes are metastable phase formation, amorphous phase formation and refined grain formation. The precipitation hardenable series of Aluminum alloys, called the 2XXX and 7XXX series, are commercially very important, as can be gauged from the fact that these two alloys constitute 80% of the structural weight in an aircraft [Srivatsan1993e]. In view of the industrial significance of Al-alloys, the binary Al-Cu alloy (2XXX series) was chosen for this study. Also, the Al-Cu system is amenable to Impulse Atomization experiments and metallographic preparation for post-experimental analysis of the rapidly solidified product. Moreover, since no microsegregation experiments have been performed on atomized Al-Cu alloys, this work also contributes in the area of segregation under unconstrained growth conditions.

2.5 References

[Albarran1991]: "Some preliminary results on the microstructure and mechanical properties of rapidly solidified nickel-based superalloys", Albarran J.L., Campillo B. et al, Scripta Metallurgica et Materialia, v. 25, iss. 7, July 1991, pp 1611-1616.

[Allen1991]: "Solidification of undercooled Sn-Sb peritectic alloys: Part I. Microstructural evolution", Allen W.P. and Perepezko J.H., Metallurgical Transactions A, v. 22, is. 3, 1991, pp 753-764.

[Aziz1982]: "Model for solute redistribution during rapid solidification", Aziz, M.J., Journal of Applied Physics, v. 53, 1982, pp 1158-1168.

[Boettinger1984]: "Effect of rapid solidification velocity on microstructure of Ag-Cu alloy", Boettinger W.J., Shechtman D., Schaefer R.J.

and Biancanielo F.S., Metallurgical Transactions A, v. 15A, 1984, pp 55-66.

[Boettinger1986]: "An analysis of the microstructure of rapidly solidified Al-8wt percent Fe powder", Boettinger W.J., Bendersky L. and Early G., Metallurgical Transactions A, v. 18A, 1986, 781-790.

[Brody1966]: "Solute redistribution in dendrite solidification", Brody H.D. and Flemings M.C., Transactions of AIME, v. 236, 1966, pp 615-623.

[Clyne1981]: "Solute redistribution during solidification with rapid solid state diffusion", Clyne T.W. and Kurz W., Metallurgical Transactions A, v. 12A, 1981, pp 965-971.

[Clyne1984]: "Numerical treatment of rapid solidification", Clyne T.W., Metallurgical Transactions B, v. 15B, 1984, pp 369-381.

[Cochrane1991]: "Dendrite growth velocities in undercooled Ni-Si alloys", Cochrane R. F. et al, Material Science and Engineering A, v. A133, 1991, 698-701.

[Cotton1991]: "The sensitivity to Iron impurity content of the corrosion rate of extrusions of rapidly solidified Mg-15wt%Al alloy powder", Cotton J. D. and Jones H., International Journal of rapid solidification, v. 6, 1991, pp 55-76.

[Ding1997]: "Impulse Atomization", PhD Thesis, Ding Y., University of Alberta, 1997.

[Dube1996]: “Cooling rates of REP Al-4.5%Cu particles”, Dube D., Angers R. and Adnot A., Powder Metallurgy Institute, v. 23, n. 1, 1991, pp 22-25.

[Duwez1960a]: “Continuous series of metastable solid solutions on Ag-Cu alloys”, Duwez P., Willens, R.H. and Klement W., Journal of Applied Physics, v. 31, 1960, pp 1136-1137.

[Duwez1960b]: “Metastable electron compound in Ag-Ge alloys”, Duwez P., Willens, R.H. and Klement W., Journal of Applied Physics, v. 31, 1960, pp 1137.

[Freyberg2003]: “Droplet solidification and gas-droplet thermal coupling in the atomization of a Cu-6Sn alloy”, Freyberg A.V., Henein H., Uhlenwinkel V. and Buchholz .M, Materials and Metallurgical Transactions B, v. 34, n. 2, 2003, pp 243-253.

[Gupta1992]: “Solidification characteristics of atomized Al-Ti powders”, Gupta M., Mohamed F.A. and Lavernia E.J., Scripta Metallurgica et Materialia, v. 26, 1992, pp 697-702.

[Hatch1984]: “Aluminum, Properties and physical Metallurgy”, Hatch J.E. (ed.), American Society for Metals, Warrendale, 1984, pp 37.

[Hilsher1986]: “Magnetic and anisotropy studies of Nd-Fe-B based permanent magnets”, Hilsher et al, Journal of Magnetism and Magnetic Materials, v. 54-57, 1986, pp 577-578.

[Jech1984]: “Rapid solidification via Melt-Spinning: Equipment and Techniques”, Jech R.W., Moore T.J., Glasgow T.K. and Orth N.W., Journal of Metals, v. 36, n. 4, 1984, pp 41-45.

[Jinfu2000]: "Mechanical properties of undercooled $Cu_{70}Ni_{30}$ alloy", Jinfu L., Yaohe Z. and Yang G., Journal of Materials Science, v. 35, is. 22, 2000, pp 5581-5585.

[Jones1983]: "Rapid Solidification of Metals and Alloys", Jones H., Institution of Metallurgists, London, 1983, pp 8-14, 40-47.

[Juarez1988]: "Effect of solidification front velocity on the characteristics of Al rich Al-Mn alloy solutions extended by rapid solidification", Juarez Islas R.A., Jones H. and Kurz W., Material Science and Engineering, v. 98, 1988, pp 201-205.

[Kattamis1966]: "Dendrite structure and Grain Size of Undercooled melts", Kattamis T.Z. and Flemings M.C., Transactions of TMS-AIME, 236, 1966, 1523-1532.

[Kattamis1966b]: "Influence of coarsening on dendrite arm spacing of aluminum-copper alloys", Kattamis T.Z., Coughlin J.C. and Flemings M.C., Transactions of TMS-AIME, v. 239, n. 10, 1967, 1504-1511.

[Kattamis1967]: "Solidification of highly Undercooled castings", Kattamis T.Z. and Flemings M.C., Transactions of American Foundrymen's society, 75, 1967, pp 191-198.

[Kattamis1970]: "Redistribution of solute in Highly Undercooled Iron-Nickel alloy", Kattamis T.Z., Zeitschrift fur Metallkunde, v. 61, 1970, pp 856-860.

[Kattamis1974]: "Undercooling during Atomization of VM300 Maraging Steel", Kattamis T.Z. and Mehrabian R., Journal of Material Science, v. 9, 1974, pp 1040-1043.

[Kearns1996]: "Recent advances in understanding the mechanism of Al grain refinement by TiBAl master alloys", Kearns M.A., Thistletwaith S.R. and Cooper P.S., Light Metals 1996, The Minerals, Metals and Materials Society, 1996, pp 713-720.

[Kurz2000]: "Fundamentals of Solidification", Kurz W. and Fisher D., Trans Tech Publications, Switzerland, 2000, pp 45-61.

[Langer1977]: "Stability effects in dendritic crystal growth", Langer J.S. and Muller-Krumbhaar H., Journal of Crystal Growth, v. 42, 1977, pp 11-14.

[Lavernia1988]: "A mathematical model of the liquid dynamic compaction process. Part 1: Heat flow in gas Atomization", Lavernia E.J., Gutierrez E.M., Szekely J. and Grant N.J., International Journal of Rapid solidification, v. 4, 1988, pp 89-124.

[Lavernia1989]: "On quenching rates, secondary dendrite arm spacings and particle size in gas atomization", Lavernia E.J. and Baram J.C., Journal of Materials Science Letters, v. 8, 1989, pp 612-614.

[Lee1994]: "Solidification progress and heat transfer analysis of gas-atomized alloy droplets during spray forming", Lee E-S. and Ahn S., Acta Metallurgica et Materialia, v. 42, n. 9, 1994, pp 3231-3243.

[Levi1982]: "Heat Flow during Rapid Solidification of Undercooled Metal Droplets", Levi C.G. and Mehrabian R., Metallurgical Transactions A, v. 13, 1982, pp 221-234.

[Li2000]: "Factors affecting solute segregation behavior in Spray Atomized Pd alloy powders", Li B., Yang N., and Lavernia E.J., Metallurgical and Materials Transactions A, v. 31A, 2000, pp 2681-2686.

[Lipton1984]: "Dendritic growth into Undercooled Alloy Melts", Lipton J., Glicksmann M.E. and Kurz W., Material Science and Engineering, 65, 1984, pp 57-63.

[Lipton1987a]: "Rapid Dendrite growth in Undercooled Alloys", Lipton J., Kurz W. and Trivedi R., Acta Metallurgica, 35, n. 4, 1987, pp 957-964.

[Lipton1987b]: "Effect of growth rate dependant partition coefficient on the Dendrite growth in Undercooled Melts", Lipton J., Kurz W. and Trivedi R., Acta Metallurgica, 35, n. 4, 1987, pp 965-970.

[Liu1995]: "Modeling of droplet-gas interactions in spray atomization of Ta-2.5W alloy", Liu H. Rangel R.H. and Lavernia E.J., Materials Science and Engineering, v. A191, 1995, pp 171-184.

[Luo2003]: "The corrosion resistance of 0Cr19Ni9 stainless steel arc welding joints with and without arc surface melting", Luo W., Materials Science & Engineering A, v. A345, is. 1-2, 2003, pp 1-7.

[Morin1996]: "The Impulse Atomization Process: an economical and flexible process for producing powders with a tailored size distribution", Morin L.C., Rieder M., Meja J. and Henein H., Proceedings of the Int. Symposium on Light Metals 1996, Metallurgical Society of CIM, Montreal, pp 293-304.

[Mueller1987]: "The undercooling of Aluminum", Mueller B.A. and Perepezko J.H., Metallurgical Transactions A, v. 18, is. 6, 1987, pp 1143-1150.

[Nussbaum1989]: "Strengthening Mechanisms in the rapidly solidified AZ91 Mg alloy", Nussbaum G., Sainfort P., Regazzoni G. and Gjestlund H., Scripta Metallurgica, v. 23, 1989, pp 1079-1084.

[Palacio1985]: "Microsegregation in cellular dendritic growth in binary alloys of Al-Cu", Palacio H.A., Solari M. and Biloni H., Journal of crystal growth, v. 73, n. 2, 1985, pp 369-378.

[Prasad2004]: "X-Ray Tomography study of atomized Al-Cu droplets", Prasad A., Henein H., Maire E. and Gandin Ch.A., Canadian Metallurgical Quarterly, v. 43, n. 2, 2004, pp 273-282.

[Prasad2005]: "Understanding the rapid solidification of Al-4.3Cu and Al-17Cu using X-Ray Tomography", Prasad A., Henein H., Maire E. and Gandin Ch.A., Metallurgical Transactions A, v. 37, n. 1, 2006, pp 249-257.

[Rappaz1987]: "Solute diffusion model for equiaxed dendritic growth", Rappaz M. and Thevoz P., Acta Metallurgica, v. 35, 1987, pp 1487-1497.

[Ruhr1990]: "Extended Al(Mn) solution in a rapidly solidified Al-Li-Mn-Zr alloy", Ruhr M., Lavernia E.J. and Baram J.C., Metallurgical Transactions A, v. 21A, 1990, pp 1785-1789.

[Salgado1991]: "Characterization of Ni-Cu powders produced by the atomization process", Salgado L. et al, Materials Science and Engineering, v. A133, 1991, pp 692-697.

[Samuels1997]: "Microstructural characterization of rapidly solidified Al-Li-Co powders", Samuels F.H., Materials and Metallurgical Transactions A, v. 17A, 1986, pp 73-91.

[Savage1984]: "Production of rapidly solidified metals and alloys", Savage S.J. and Froes F.H., Journal of Metals, v. 36, n. 4, 1984, pp 20-33.

[Scheil1942]: "Bemerkungen zur Schichtkristallbildung", Scheil E., Zeitschrift fur Metallkunde, vol. 236, 1942, pp 70-72.

[Schleip1988]: "Measurements of Ultrarapid Solidification Rates in greatly undercooled bulk Melts with a high speed photo sensing device", Schleip E. et al, Material Science and Engineering, v. 98, 1988, pp 39-42.

[Shechtman1984]: "Precipitation in rapidly solidified Al-Mn alloy", Shechtman D., Schaefer R.J. and Biancaniello F.S., Metallurgical Transactions A, v. 15A, n. 11, Nov. 1984, pp 1987-1997.

[Smith1993]: "Solute trapping in metals", Smith P.M., Reitano R. and Aziz M.J., Beam Solid interactions: Fundamentals and Applications Symposium, 1993, pp 749-754.

[Srivatsan1993a]: "Rapid Solidification Technology: An engineering approach", (eds.) Srivatsan T.S. and Sudarshan T.S., Technomic Publishing Company Inc., Pennsylvania, 1993, pp 321-324.

[Srivatsan1993b]: "Rapid Solidification Technology: An engineering approach", (eds.) Srivatsan T.S. and Sudarshan T.S., Technomic Publishing Company Inc., Pennsylvania, 1993, pp 412.

[Srivatsan1993c]: "Rapid Solidification Technology: An engineering approach", (eds.) Srivatsan T.S. and Sudarshan T.S., Technomic Publishing Company Inc., Pennsylvania, 1993, pp 426.

[Srivatsan1993d]: "Rapid Solidification Technology: An engineering approach", (eds.) Srivatsan T.S. and Sudarshan T.S., Technomic Publishing Company Inc., Pennsylvania, 1993, pp 127-561.

[Srivatsan1993e]: "Rapid Solidification Technology: An engineering approach", (eds.) Srivatsan T.S. and Sudarshan T.S., Technomic Publishing Company Inc., Pennsylvania, 1993, pp 127-155.

[Su1997]: "Modeling of solidification of molten metal droplet during atomization", Su Y.H. and Tsao C.-T.A., Metallurgical and Materials Transactions B, v. 28B, 1997, pp 1249-3108.

[Suzuki1989]: “Solidification of Highly Undercooled Fe-P alloys”, Suzuki M. et al, Metallurgical Transactions A, v. 22A, 1991, pp 2761-2768.

[Tong1984]: “A boundary diffusion layer model of microsegregation”, Tong X. and Beckermann C., Journal of crystal growth, v. 187, 1998, pp 289-302.

[Trivedi2003]: “Dynamical evolution of microstructure in finely atomised droplets of Al-Si alloys”, Trivedi R., Jin F. and Anderson I.E., Acta Materialia,v. 51, 2003, pp 289-300.

[Wiskel2002a]: “Solidification study of aluminum alloys using Impulse Atomization: Part I: Heat transfer analysis of an atomized droplet”, Wiskel J.B., Henein H. and Maire E., Canadian Metallurgical Quarterly, v. 41, n. 2, January 2002, pp 97-110.

[Wiskel2002b]: “Solidification study of aluminum alloys using Impulse Atomization: PartII: Effect of cooling rate on microstructure”, Wiskel J.B., Navel K., Henein H. and Maire E., Canadian Metallurgical Quarterly, v. 41, n. 2, April 2002, pp 193-204.

[Wu1987]: “Dendritic growth of undercooled Nickel-Tin: Part I”, Wu Y., Piccone T.J., Shiohara Y. and Flemings M.C., Metallurgical Transactions A, v. 18A, 1987, pp 915-924.

[Wu1987]: “Dendritic growth of undercooled Nickel-Tin: Part II”, Wu Y., Piccone T.J., Shiohara Y. and Flemings M.C., Metallurgical Transactions A, v. 18A, 1987, pp 925-932.

[Yang1997]: “Solidification behavior of Pd-Rh droplets during Spray Atomization”, Yang N., Guthrie S.E., Ho S. and Lavernia E.J., Journal of Materials Science, v. 32, 1997, pp 6589-6594.

[Zhang1992]: “Thermokinetic model for rapid solidification”, Zhang X. and Atrens A., International Journal of Rapid Solidification, v. 7, 1992, pp 83-107.

[Zhao1989]: “Rapid Dendritic growth of Highly Undercooled Iron-Nickel alloys”, Zhao Q. et al, MRS Meeting on Advanced Materials, v. 3, 1989, pp 597-602.

Experimental Techniques

The study of the rapid solidification of Al-Cu system under free growth conditions involved experimental as well as modeling work. The experimental work included generating rapidly solidified Al-Cu powders of the desired composition, sieving the powders into the appropriate size range and analyzing them, either in the as-atomized form (for tomography and neutron diffraction) or mounting and polishing them, for the SEM and stereology work. This chapter describes these experimental procedures in details. The powder generation is described first followed by sieving. Following this, the details on tomography, neutron diffraction and SEM plus stereology are described.

3.1 Impulse Atomization

Impulse Atomization is a single-fluid atomization process developed at the Advanced Material and Processing Laboratory, University of Alberta, Canada. Figure 3.1 shows a schematic of the atomization unit. It consists of a cylindrical chamber that is 4m tall and 0.5m in diameter. The entire chamber is atmospherically sealed and can be filled with the gas of choice. For this study, He and N_2 gases were used for the atomization experiments. The top portion of the chamber consists of the Impulse unit where the material is melted and subsequently pushed through small orifices. The ensuing discontinuous melt streams break down into small droplets that fall through the atomization chamber.

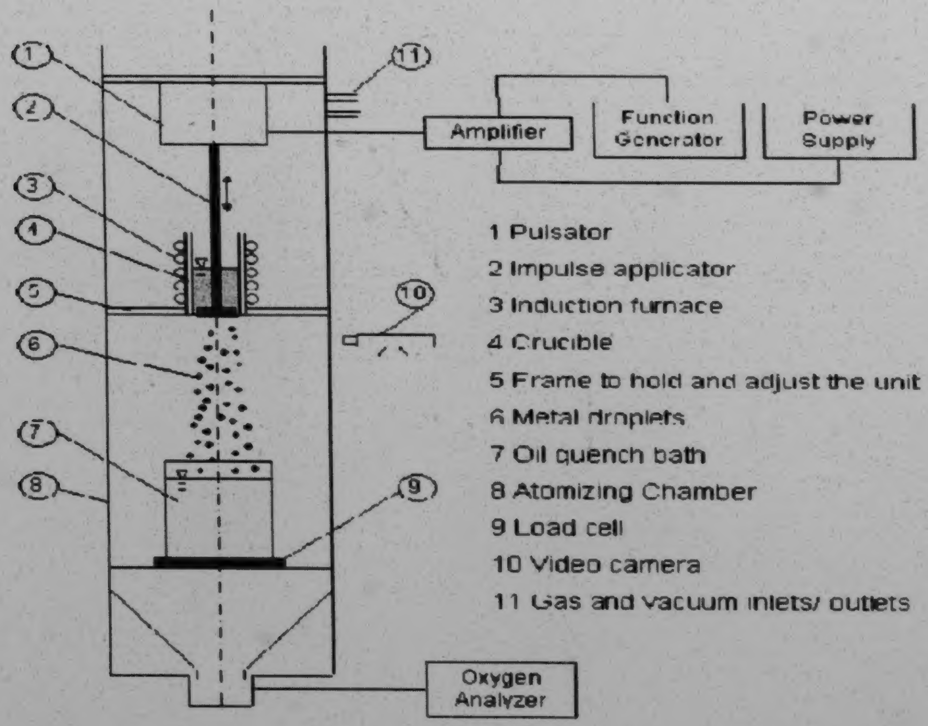
1
2
3
4
5
6
7
8
9
10
11
Amplifier
Function Generator
Power Supply
Oxygen Analyzer
1 Pulsator
2 Impulse applicator
3 Induction furnace
4 Crucible
5 Frame to hold and adjust the unit
6 Metal droplets
7 Oil quench bath
8 Atomizing Chamber
9 Load cell
10 Video camera
11 Gas and vacuum inlets/ outlets

Figure 3.1: Schematic of the Impulse Atomization unit. The numerical labels describe the different parts of the unit.

As the liquid droplets fall, the atomization fluid takes the heat from these droplets by convection, whereby the droplets cool and solidify. Since the atomization temperature is close to 1100K, the liquid droplets may lose heat to radiation as well. However, since the droplets cool rapidly, the radiation heat loss component decreases drastically, and subsequently, has a small effect on the total heat loss. The primary function of the gas is to withdraw the heat from the liquid droplets, although the surface tension between the gas and liquid metal does play a part in breaking the liquid stream into droplets. The droplets completely solidify as they fall through 3.5m of the gas filled chamber and are collected in glass beakers filled with oil. The glass beaker is kept on a load cell, which is connected to a computer. This instrumentation captures the rate of mass of the powder produced.

3.1.1 Melting and atomization

The atomization runs for the experiments were carried out to generate binary alloys of Cu with four different nominal compositions: Al-4.3wt%Cu, Al-5wt%Cu, Al-10wt%Cu and Al-17wt%Cu. These compositions will be written as Al-X%Cu in the rest of the thesis, where X% is the weight percent of Cu. Commercially pure Al and Cu shot was used in the experiments. The set-up for an atomization run consisted of placing the melt material in the crucible (label 4 in Figure 3.1). A clay-graphite crucible was used to prevent reaction between the melt material and the crucible. For a desired alloy composition and total weight, the appropriate weights of Al and Cu were added. 99.9% pure Al granules (8-10 mm supplied by AlfaAesar) and 99.9% pure Cu shot (1-10mm supplied by AlfaAesar) were used. Typically, 250 grams of melt material were used in one run. Therefore, an Al5%Cu alloy would have 12.5 gm of Cu and 237.5 gm of Al added to the crucible. The nozzle plate at the bottom of the crucible was drilled with the desired number of holes of a specific size (see Table 3.1 for the exact number of holes and hole dimensions), all hole sizes being equal. The nozzle plate was made of high-quality graphite. The crucible was wrapped with a hollow Cu tube, which was connected to the induction leads from an Induction Generator, thus providing the induction field for melting (label 3 in Figure 3.1). The induction generator used was an Inducto20 generator. The plungers used in the experiments were made of alumina. The plunger (label 2 in Figure 3.1) was attached to a vibrating unit which is controlled by a function generator (label 1 in Figure 3.1). Setting the function generator on a sinusoidal function (100 Hz) produced an oscillating plunger motion. The amplitude of these oscillations was controlled by using a variable voltage. C-type thermocouples were placed inside the crucible for monitoring the melt temperature.

After this initial set-up, the chamber was completely sealed and the chamber was evacuated till vacuum (-15mmHg pressure) was attained. The chamber was then filled with the desired gas (label 11 in Figure 3.1) and then evacuated again. This was followed by refiling the chamber with the gas. This cycle was repeated till a very low O_2 content (less than 20 ppm) was left within the chamber. At this point, the induction generator was turned on and the crucible was heated at a rate of approximately 400 K/hr. The heating was carried out till a superheat of approximately 50K above the melting temperature of the higher melting point metal, Cu in this case, was attained. The induction power required to raise the temperature of the melt to 1325K was 8-10 KW. The melt was held at this temperature for about 15 minutes. The induction power was then turned down to 2-3 KW at this stage so that the alloy in the crucible could cool and reach the pre-set atomization temperature (Table 3.1). At this point, the vibration unit was activated, whereupon the plunger was set into motion. The oscillation of the plunger results in ligaments of molten alloy ensuing from the nozzle plate. These ligaments break into small droplets that cool and solidify as they fall through the chamber. The solidified droplets are collected in oil-filled beakers (label 7 in Figure 3.1). A high temperature oil (Galden perflourinated fluid – HT230 supplied by Ausimont) was used to minimize vaporization of the oil, as such vapors can possibly alter the cooling characteristics of the atomization gas. The oil used could withstand up to 230 ^{0}C temperature without vaporizing. Table 3.1 gives the atomization run conditions.

3.1.2 Powder washing, drying and sieving

The powder from the oil beaker was washed in Toluene + Ethanol. To ensure that all the oil was removed from the surface of the powder, several cycles of washing were employed. The powder was then placed on a Whatman filter paper 2 (125mm diameter) to dry. The dried powder was weighed and sieved. A RO-TAP sieving machine (model number RX-29) was used to sieve the powders according to ASTM E-11 specifications. A Gilson sieve set, with stainless steel frame and steel wire grid, was placed in the RO-TAP for 20 minutes. After the sieving, powders of different size ranges from the sieves were weighed and placed in separate glass vials.

Table 3.1: Summary of atomized alloys and the atomization run conditions used in tomography, neutron diffraction and stereology experiments. Number of images and the number of grid points per image used in stereological analysis for volume percent eutectic calculation are also given.

Atomization Run #	Atomization Gas / Temp.	Actual Alloy comp. (wt%)	Number of Holes, Nozzle dia. (μm)	Average droplet size (μm)	# of Images	# of grid points/image
980804	N_2 / 1123K	4.3	1, 363	660	-	-
020313	He / 1123K	4.98	37, 250	196	31	156
020313	He / 1123K	4.98	37, 250	925	31	156
020315	N_2 / 1123K	4.92	37, 250	196	31	156
020315	N_2 / 1123K	4.92	37, 250	925	31	154
021029	He / 1123K	10	37, 250	196	31	156
021029	He / 1123K	10	37, 250	925	39	164
020320*	N_2 / 1123K	9.96	37, 250	196	-	-
020320	N_2 / 1123K	9.96	37, 250	234	31	161
020320	N_2 / 1123K	9.96	37, 250	925	40	164
021024	He / 1123K	16.8	37, 250	196	34	157
021024	He / 1123K	16.8	37, 250	925	30	160
021021*	N_2 / 1123K	16.8	37, 250	196	-	-
021021	N_2 / 1123K	16.8	37, 250	234	31	159
021021	N_2 / 1123K	16.8	37, 250	780	31	159
021021*	N_2 / 1123K	16.8	37, 250	925	-	-
960604	He / 1115K	17	37, 337	490	-	-

* - Not tested by neutron diffraction

3.1.3 Powder mounting and polishing

Powders of the size range of interest were either used as-atomized (for tomography/neutron diffraction experiments) or were mounted in epoxy for SEM imaging. Cold mounting was carried out for these powders in plastic molds 31.75mm in diameter. Epoxy resin (West systems 105A) and hardener (West Systems 205A) were poured in a ratio of 2.5:1 into a paper cup containing the powder of interest. The two were stirred and mixed slowly so that minimal gas bubbles were formed. This mix, along with the powder, was then poured into the plastic molds. This was left for 6 hours for the epoxy mount to set.

The mounted samples were appropriately labeled using an engraving pen or a felt pen. The mounted samples were ground using 400 grit and 600 grit SiC paper on a manual polisher. After grinding with the 600 grit paper, the samples were polished using 10μm & 6μm diamond slurry on nylon cloth. The final polishing with 0.5μm Al_2O_3 slurry was carried out on soft cloth. Both, an auto (Buehler Automat) as well as a manual polishing machine were used, depending on the number of mounted samples to be polished at any given time. The polished samples were not etched. A model S-2700 Hitachi Scanning electron microscope was used for the microstructural imaging of the droplets. An accelerating voltage of 20kV with back scattered electron imaging mode was used.

3.2 X-ray tomography

The working principle of tomography is based on X-ray radiography. The contrast observed in a simple X-ray projection is associated with local fluctuations of the absorbance of the beam when passing through a sample. A number of radiographs taken under different viewing angles are combined to reconstruct a 3-dimensional map of the local attenuation coefficient of the X-rays. This allows a non-destructive image of the sample. A very high resolution from this technique is obtained by using an intense and highly energetic source. The experiments used in this work were performed on the ID19 beam line at the European Synchrotron Radiation Facility (ESRF) in Grenoble (France). The setup consisted of a double crystal monochromator, selecting the white beam in a narrow energy range, i.e., 30 keV +/-0.001 keV. The samples used were as-atomized droplets of Al-4.3%Cu (660μm size) and Al-17%Cu (490μm size).

Individual droplets were encased in cylindrical glass tubes of 1mm internal diameter. Both ends of the hollow glass tubes were sealed with epoxy to prevent the droplets from falling out. For each droplet, three orthogonal angles were used to generate 2-D radiographs. The radiographs were converted to volume information of the droplet using an in-house program developed at ESRF [Maire1999]. The volume information was in the form of .RAW format, which could be further converted into stacks of images using commercial software. The software used in this case was Volume Graphics (Germany). Three stacks of images were generated, corresponding to each angle. These stacks of images were then used to construct movies also using the Volume Graphics software. Table 3.1 lists the atomized droplets that were imaged using 3-D X-ray tomography and then analyzed.

3.3 Neutron diffraction (ND)

Neutron diffraction works on the same principle as X-ray diffraction where the energy waves experience diffraction from the lattice points, which are separated by distances similar to the wavelength of the wave. Neutrons are produced in a nuclear reactor and made to move at relativistic speeds. At such speeds the neutron beam acts as a wave whose magnitude is given by DeBroglie's equation,

$$\lambda = \frac{\hbar}{M_n \upsilon} \tag{3.1}$$

where $\hbar$ is the Planck's constant, M_n is the mass of the neutrons and υ is the neutron velocity. When the neutron beam is focused on the samples, diffraction results from the atomic arrangements in the phases constituting the sample. Therefore, such diffraction patterns obtained from the neutron beam can be analyzed to give information on the phases present in the sample. ND experiments were performed on the atomized droplets to gather information on the weight fraction of the second phase (θ or $CuAl_2$ phase) in the Al-Cu binary alloy system. Further details about the experiment, for example, spectrometer type, detector function, etc, are given in the published article that forms Chapter 6. Therefore, to prevent repetition, these details are not included in this section.

3.4 Stereology

Quantitative microscopy is the procedure of quantifying the microstructural features. The quantifying technique used is called stereology. It consists of a set of equations from which 3-D information can be obtained from 2-D images [DeHoff1968, Howard1998]. One of the basic equations of stereology is given by the following [DeHoff1968],

$$V_V = A_A = L_L = \overline{P}_p \tag{3.2}$$

where the letters and subscripts are volume, area, line intercept and point count of a feature of interest. Eqn. 3.2 states that the volume fraction of the feature of interest can be obtained by either doing the Volume Fraction calculation, Area Fraction calculation, Lineal analysis or Point Count analysis. The equation $V_V = \overline{P}_p$ is based on the concept that if a point is placed randomly within a volume, then the probability that it will fall within the feature of interest is equal to the volume fraction of that feature. This makes the procedure inherently statistical in nature. To calculate the volume percent eutectic in the atomized powders, a manual point count technique was employed on the eutectic areas on 2-D SEM images of the atomized droplets. The analyzed powders were for Al-5%Cu, Al-10%Cu and Al-17%Cu of different sizes obtained by atomizing under different gas conditions. For neutron diffraction, a significant detailed procedure of the stereological technique in terms of number of samples used is outlined in Chapter 5 and therefore will not be repeated here, but the grid that was used for the volume percent analysis and the relative error to be expected from this procedure will be described.

A stereological grid of 15mm spacing was used on the images. The grid (number G2802) was obtained from Agar Scientific and conforms to the ASTM standard E562 - 01. The grid was randomly placed on the image photograph, as shown in Figure 3.2, and the points falling in the eutectic region were counted manually. Each point falling within the eutectic region was taken as 1, whereas each point falling on the boundary of the eutectic and α-Al dendrite was taken as 0.5. Based on this, the volume percent eutectic in each image was calculated as,

Figure 3.2: A 15mm grid is randomly superimposed on the photomicrograph of a droplet taken from SEM.

$$\hat{v}_e = \overline{P}_p = \frac{n_e + 0.5n_b}{n_t} * 100 \qquad (3.3)$$

Here, n_e, n_b and n_t are the number of points falling within the eutectic region, on the eutectic-dendrite boundary and the total number of grid points on the image, respectively. The average of volume percent eutectic data was calculated by taking the mean of 30+ images on which the volume percent eutectic measurement was performed. The volume percent eutectic thus obtained for the droplet set is denoted by $\hat{v}_e$. Since the set is an unbiased representation of the population, the eutectic percent obtained represents the average of the sample and is also known as Estimated True Mean.

For a given volume fraction of the feature of interest, the ASTM standard E562-01 report data on the relative accuracy that is to be expected when a certain number of grid points are used on certain number of images. Using this information on a 5% volume eutectic, a grid with 100 points used on 80 images would give a relative accuracy of 10%, provided that the eutectic is randomly distributed in each powder particle. Similarly, for a 20% volume eutectic, a 10% relative accuracy would require only 20 images with a 100 point grid. The 15mm grid used in this research offered a minimum of 150 points on the images. Therefore, for a 5% volume eutectic microstructure, about 54 images would be needed. Table 3.1 gives the number of grid points and the number of images used for each droplet set. Based on this, the relative accuracy to be expected for the eutectic data should be around 10% or lower, assuming a random distribution of eutectic in the particles.

3.4.1 Cavalieri method

The Cavalieri method, a stereological technique, was used to evaluate the volume fraction of certain microstructural features of interest from the tomographic images. This technique is widely used in medical field [Howard1998] and is useful in obtaining the volume fraction, for example, of the organ of a mammal. The principle of the technique is explained in Figure 3.3.

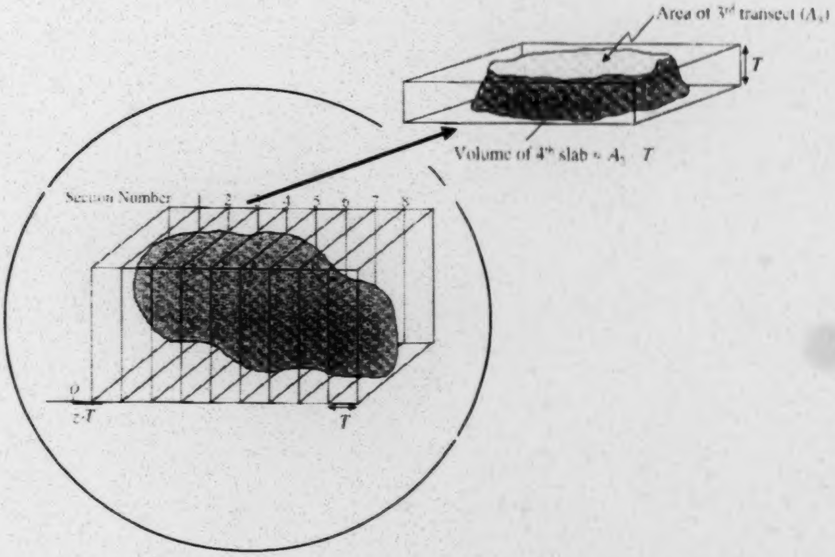
Area of 3rd transect (A_3)
T
Volume of 4th slab ≈ $A_3 \cdot T$
Section Number
1
2
3
4
5
6
7
8
0
z·T
T

Figure 3.3: Principle of the Cavalieri technique. The volume of interest is divided into several sections, and the volume of each section is evaluated. The summation of these volumes for each section is the total volume of the feature [Howard1998].

The volume was randomly divided into several parallel sections, each of thickness T. Note that the thickness can be non-uniform as well, but for the sake of explanation, a uniform slice thickness was taken. The volume of each section is given by $(T.A_i)$, where A_i is the area of cross-section of the i$^{\text{th}}$ slice. The total volume of the feature is then given by,

$$V = (T.A_1) + (T.A_2) + ... + (T.A_m) = T.\sum_{i=1}^{m} A_i \qquad (3.4)$$

where m is the total number of slices.

The area of cross-section of each slice can be calculated using any of the stereological techniques for Areal fraction. In our case, a manual point count was used, as explained in Section 3.4. The area of each slice is given by,

$$A_i = \frac{a_r}{p} P = \Delta x.\Delta y.P \qquad (3.5)$$

where $\frac{a_r}{p}$ denotes the area occupied by a given point on a grid and P is the total number of points falling on the area of interest. Both these terms are also explained schematically in Figure 3.4.

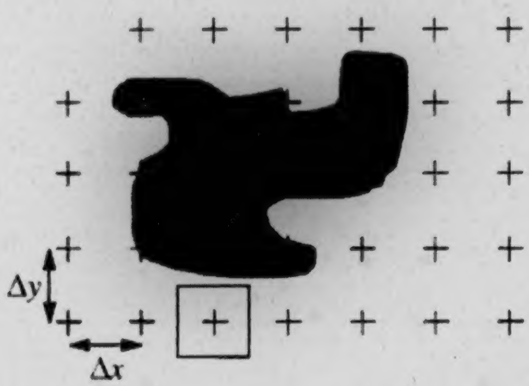

Figure 3.4: Figure explaining the $\frac{a_r}{p}$ *ratio in stereology [Howard1998].*

From tomography, we obtained the 3-D microstructural information and therefore the Cavalieri technique was useful in this case as well. The 3-D images showed gradation in the scale of the microstructure within the individual droplets. This formed the volume of interest, as shown in Figure 3.3. This was then divided into an appropriate number of sections, keeping the section thickness constant. The area fraction of each section was then manually evaluated using the point count technique. The $\frac{a_r}{p}$ ratio in this case depends not only upon the grid spacing used, but also on the magnification of the images on which the point count is performed. The details of direction, slice thickness and $\frac{a_r}{p}$ ratio are provided in Chapters 4 and 5, where the volume fraction results are reported.

3.5 References

[DeHoff1968]: "Quantitative Microscopy", DeHoff R.T. and Rhines F. N., 1st ed., McGraw-Hill Book Company, New York, 1968.

[Howard1998]: "Unbiased Stereology: 3-Dimensional measurement in microscopy", Howard C.V. and Reed M.G., BIOS scientific Publishers Limited, 1998.

[Maire1999]: "Characterization of internal damage in a MMC$_p$ using X-ray synchrotron phase contrast microtomography", Maire E. et al, Acta Materialia, v. 47, n. 5, 1999, pp 1613-1625.

X-Ray Tomography study of atomized Al-Cu droplets[1]

4.1 Introduction

Rapid solidification techniques have grown in importance in recent years because of their ability to generate a variety of structures [Jones1983], which are not possible with conventional solidification processes. Impulse atomization is a relatively new rapid solidification technique, which can generate rapidly solidified powders [Morin1996]. Microscopy can be used to gather information about solidification characteristics like cell spacing and microsegregation (using quantitative metallography), but is constrained by the small number of sections that can be viewed from a given sample, more so for a droplet. To understand rapid solidification from a physical phenomena point of view, the important rapid solidification characteristics like nucleation, recalescence etc, need to be physically viewed and analyzed. Therefore one needs a 3D visualization technique, which can provide information about the entire solidified volume.

---

[1] Published as, "X-Ray Tomography studies of Al-Cu droplets", Prasad A. et al, Canadian Metallurgical Quarterly, v. 43, n. 2, 2004, pp 273-282. Reformatted according to thesis requirements.

X-ray tomography is one such non-destructive technique that allows information from the entire volume to be gathered [Maire2001]. X-ray beams from a synchrotron facility were used to carry out computer tomography work. This paper describes the Tomography technique using the synchrotron and results obtained therefrom. The results are discussed vis-à-vis the rapid solidification of the droplets.

4.2 Experimental

Nominal Al-5%Cu and Al-17%Cu (weight %) were produced using Impulse Atomization. The details of the atomization conditions are described elsewhere [Prasad2002]. The powders obtained from the atomization runs were sieved and only one size range was analyzed for tomography, 600 - 710 μm for Al-5 %Cu, and 400 - 500 μm powders for Al-17%Cu. The experimental tomography is described briefly in the following.

X-ray radiography is a widespread imaging technique. The contrast observed in a simple X-ray projection is associated to local fluctuations of the attenuation of the beam when pathing through a sample (think of the radiographs used in medicine). On the same physical basis, the recent improvement of the power of the computers has allowed the three dimensional version of radiography, i.e. tomography (or scanner in medicine), to emerge. A high number of radiographs taken under different viewing angles are combined to reconstruct the three dimensional map of the local attenuation coefficient of the X-rays. This allows a non destructive image representing the microstructure to be calculated. The very high resolution of this technique is obtained by using an intense and highly energetic source, such as a third generation synchrotron.The experiments used in this paper were performed on the ID19 beam line at the European Synchrotron radiation facility (ESRF) in Grenoble (France). The setup consisted of a double crystal monochromator, selecting the white beam in a narrow energy range i.e. 30 keV +/-0.001 keV.

4.3 Results

Observations were made on the droplet using X-ray beams of 1 μm resolution. This non-destructive technique generated RAW files for the 3-Dimensional section of the droplet. This 3-D data collected in VOXELS (short form for volume pixels) was converted into stacks of images using Volume Graphics Software (see http://www.volumegraphics.com), which is commercially available. The stacks of images were further converted to movies using the same software. Nucleation, recalescence and porosity distribution in the entire volume of the droplet could be seen with the help of these images and movies, and are described in the following.

4.3.1 Nucleation

The stacks and the movies were prepared for three directions, Axial (X-Y plane), Frontal (Z-X plane), and Saggittal (Y-Z plane). The following observations were made based on the movies of both 5% Cu and 17% Cu particles. Figure 4.1 shows the sequence of images of the moving equiaxed structures meeting at a single point for a 5% Cu droplet. Both particle types showed multiple equiaxed sites move across the droplet and converge at a point. For a better view the white dotted lines are drawn parallel to the dendrite arms in the images (see Figure 4.1). This was seen along all the three axes in all the droplets. The point where they meet also shows an equiaxed structure. Furthermore, the region close to this converging point shows an even finer microstructure. Since a nucleation point cannot be mobile within the droplet and the presence of the fine microstructure near this point, suggests that this region of very fine microstructure contains the nucleation site of the droplet. The fine structure in this region is believed to be the initial growth region occurring immediately after nucleation. The 17%Cu droplet showed larger areas of this fine structure compared to the 5%Cu droplet. This is explained in more details under the recalescence section.

The nucleation site was found to be within the droplet for all cases. Since the thickness of each image was 1μm, the image number in a stack could be determined. Using this scheme, nucleation centers were approximately calculated for each of the droplet. The average distance between the droplet center and the nucleation site was 0.63 R_p for the Al-17%Cu droplet and 0.75 R_p for the Al-5%Cu droplet, where R_p is the radius of the individual droplet. No evidence of multiple nucleation sites was found on any of the droplets examined.

4.3.2 Recalescence

Figure 4.2 shows the simulated temperature and fraction solid profile as a function of time for a 660μm Al-5%Cu droplet atomized under N_2. The results are based on the Rappaz-Thevoz model for microsegregation, described in an earlier paper [Prasad2002][2]. The model requires a user defined nucleation undercooling. For the present case a nucleation undercooling of 30^0C was selected. Point A is the nucleation temperature and points B and C mark the start and end of recalescence period respectively. As soon as nucleation occurs, the dendrites grow into an undercooled melt, at a rate governed by the degree of undercooling [Lipton1984].

The higher the undercooling, the faster is the rate of growth. Associated with this rapid growth rate is a high rate of latent heat generation within the droplet. If this rate of heat generation is greater than the rate of heat loss of the droplet at the surface to the surrounding gas, an increase in temperature of the droplet occurs. This is recalescence. During the recalescence period in the droplet, the rate of dendrite growth decreases. Points A to C represent this initial growth and recalescence period.

---

[2] The model is also described in Chapter 7 in the thesis.

Because of the faster growth rate during this period, the microstructure is finer compared to the rest of the droplet microstructure in region C to D. However, coarsening of some of the structure may occur between regions B and C. For purposes of this paper, region A to C will be referred to as the complete recalescence region. D to E is the eutectic region in Figure 4.2.

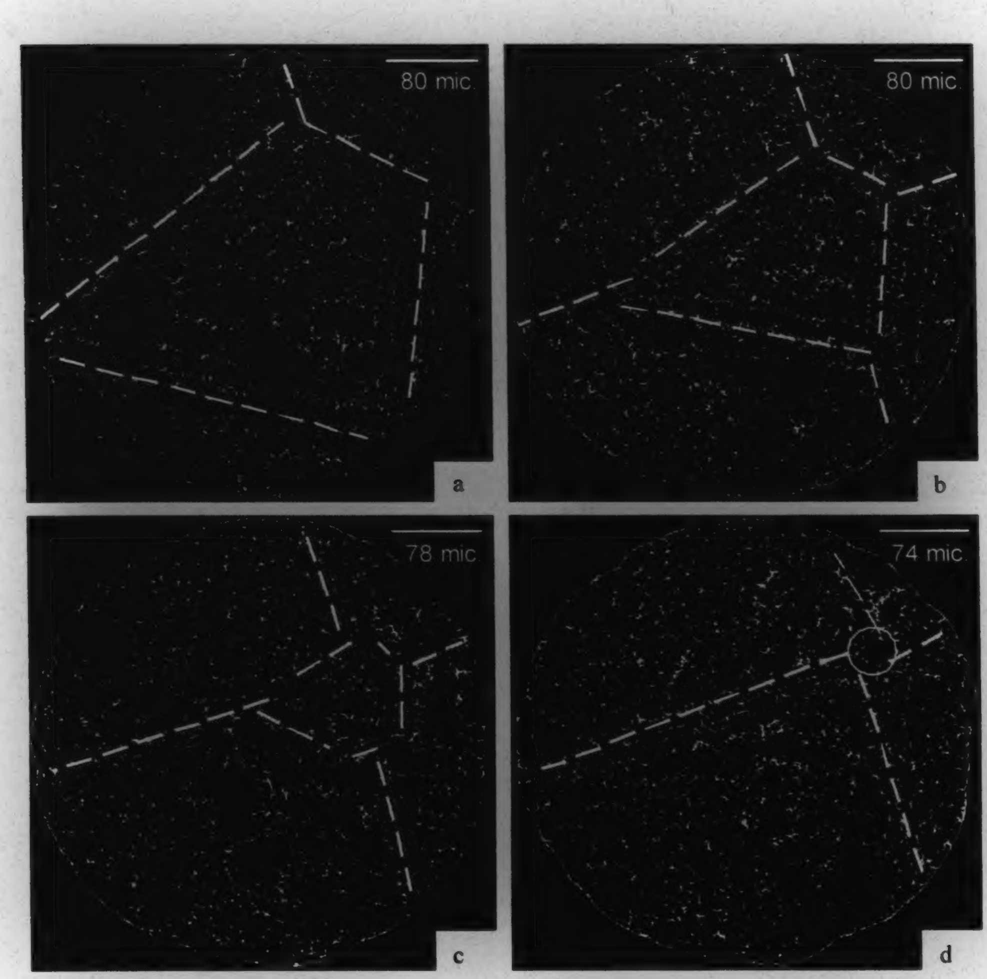

Figure 4.1: Images showing the progressive movement of multiple equiaxed pattern (white dotted lines) converging to a nucleation site in Al-5%Cu droplet. Note the movement of the pattern across the droplet. The encircled region in Figure 4.1d shows the nucleation site. Image numbers 430(a), 460(b), 495(c) and 520(d) out of a stack of 660 for a 660μm Al-5%Cu droplet viewed along the Axial direction.

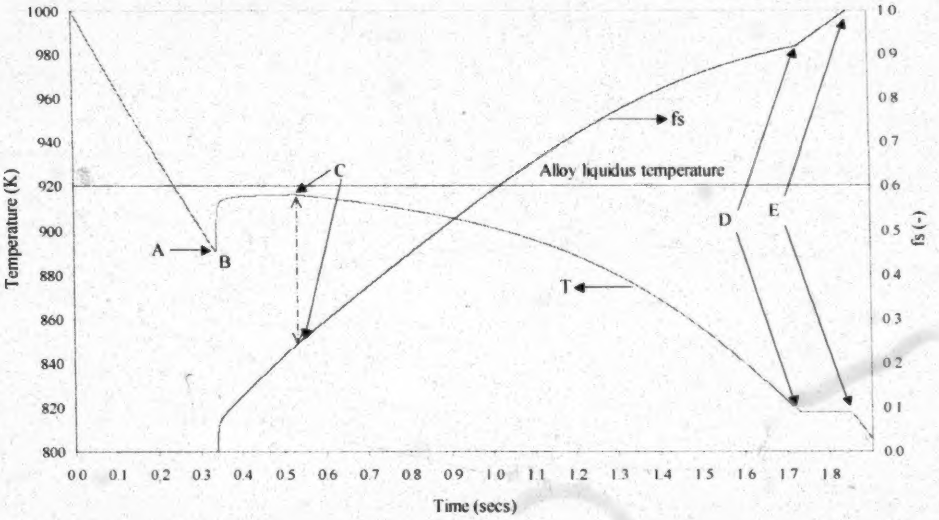

Figure 4.2: Simulated temperature and fraction solid profile for a 660µm Al-5%Cu droplet solidified with 30^{0}*C nucleation undercooling. Point A is the nucleation temperature, AB is the initial dendrite growth region, BC is the recalescence region and DE is the eutectic solidification.*

From the 3-D tomography images, in and around the nucleation site (Figure 4.1), which show growth of initial dendrites, there is a change in the scale of microstructure. The fine dendrites are surrounded by coarser dendrite structure. The details of the fine structures, in both Al-5%Cu and Al-17%Cu particles, are not clearly visible as their scale is below the resolution limit of the X-ray beam in the synchrotron. Figures 4.3a and 4.3b show a typical recalescence structure in a Al-17%Cu and Al-5%Cu droplet respectively.

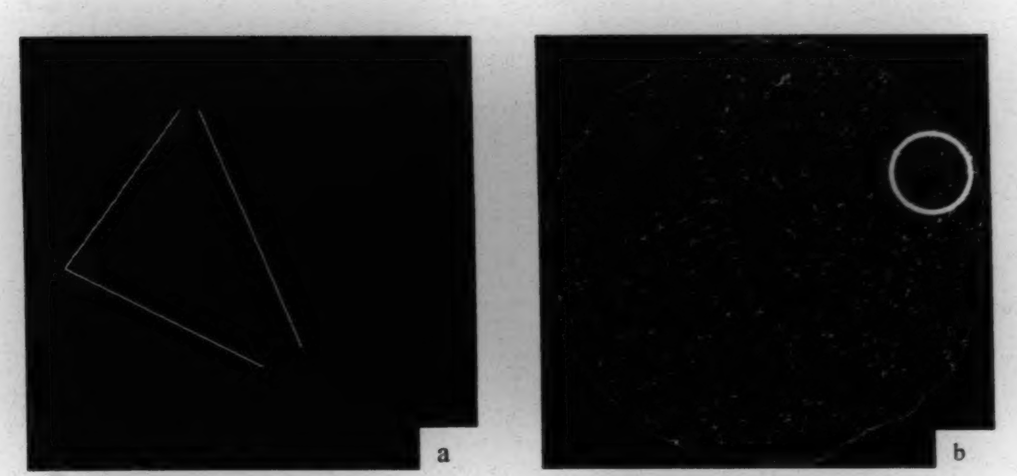

Figure 4.3: Images showing the recalescence structure in Al-17%Cu (center-left triangular region in part a) and Al-5%Cu droplet (encircled region in part b). The recalescence region has much finer structure than the rest of the droplet. Also note the overall coarser structure of Al-5% Cu droplet.

Table 4.1: Average recalescence volume fraction within the droplets.

S. N.	Nom. % Cu in the Droplet	Vol. % Recalescence (upper limit)	Vol. % Recalescence (lower limit)
1.	5	0.09 (±9E-3)	0.06 (±6E-3)
2.	17	14.8 (±1.5)	9.7 (±1)
3.	17	20 (±2)	15.9 (±1.6)
4.	17	8.9 (±0.9)	7.8 (±0.8)

As can be seen, the fraction of droplet area on the 2-D stack of images, covered by the fast growing fine dendrite structure, is larger for the Al-17%Cu than the Al-5%Cu droplets. Using stereological analysis [DeHoff1968] on these images, the average volume fraction of the recalescence within the particle was evaluated for one Al-5%Cu droplet and three Al-17%Cu droplets. The calculation was done on the axial stack of images. Note that any one of the three stacks (Axial, Frontal, Sagittal) would suffice to do the volume fraction calculation. The results are summarized in Table 4.1.

The calculation was done using Cavalieri method [Howard1998]. It is based on point counting scheme and the absolute volume fraction of a feature can be evaluated using stereological relationships. In this method the total volume of the feature of interest is randomly divided into slices of known thickness. On each slice, a uniform point grid is placed, whose magnification is known a priori. The point count on the region of interest then gives the area covered by the feature and the thickness of the slice gives the volume of the feature in that particular slice. Summation of this volume over all the sections yields the absolute volume of the feature. For the present calculation, images that showed region of recalescence were selected. The slice thickness for the analysis was the images chosen at regular intervals from the stack. It was different for the different droplets depending on the number of images showing recalescence. The volume fraction of recalescence was calculated from the known droplet diameter. Note that this requires demarcating the recalescence region from the rest of the droplet. With the current resolution of images it was difficult to exactly locate the boundary. Therefore, there are two values of recalescence volume reported, one as the upper limit and the other the lower limit. The error shown is that introduced by the stereological calculations.

There are differences in the upper and lower values between the same particle and also between the different particles. Moreover, the fraction solid value in Figure 4.2 does not match with the experimental result. It is therefore unlikely that the region AC corresponds exclusively to the calculated volume in Table 4.1.

However, for this work we will base our discussion of recalescence based on the tomographic images. This will be further discussed in a later section.

4.3.3 Porosity distribution

Al-5%Cu droplet showed an even distribution of porosity over the entire droplet volume. A typical distribution is shown in Figure 4.4. Al-17%Cu droplets, on the other hand, show difference not only in porosity distribution but also in the shape of the porosity formed (see Figures 4.5 and 4.6).

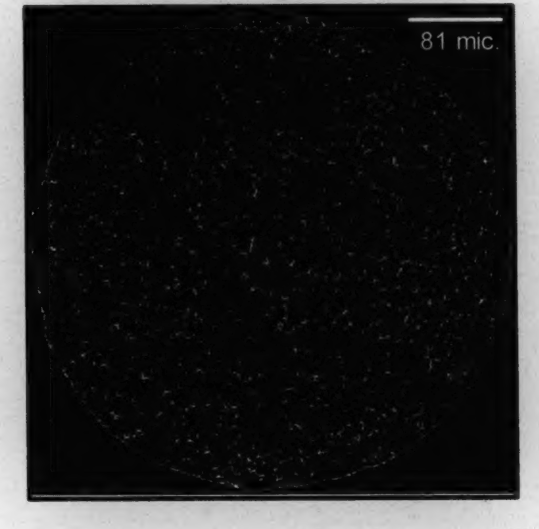

Figure 4.4: Porosity distribution in Al-5%Cu 660µm droplet. Axial image # 210.

The porosity formed in the four Al-17%Cu droplets can be summarized as follows. The droplets show extensive porosity in one half of the droplet with porosity spread across the entire droplet section in the 2-D images. Figure 4.5a shows such a droplet section. The other half of the droplet is relatively porosity free. This is shown in

Figure 4.5b. Sections between the heavy porosity and negligible porosity show porosity distributed mainly along the droplet periphery. A lot of these porosities are oriented along the dendrite growth direction. Figure 4.6 shows a peripheral elongated porosity aligned along the dendrite growth direction. The fine structure corresponding to recalescence was porosity free and small amount of porosity was seen either at the periphery when the recalescence region extended till the end of the droplet, or at the boundary between the coarse and the fine structure. In some cases traces of porosity were observed within the recalescence region. Note that when viewing both the Al-5%Cu and Al-17%Cu droplets, the porosity in all samples were interconnected.

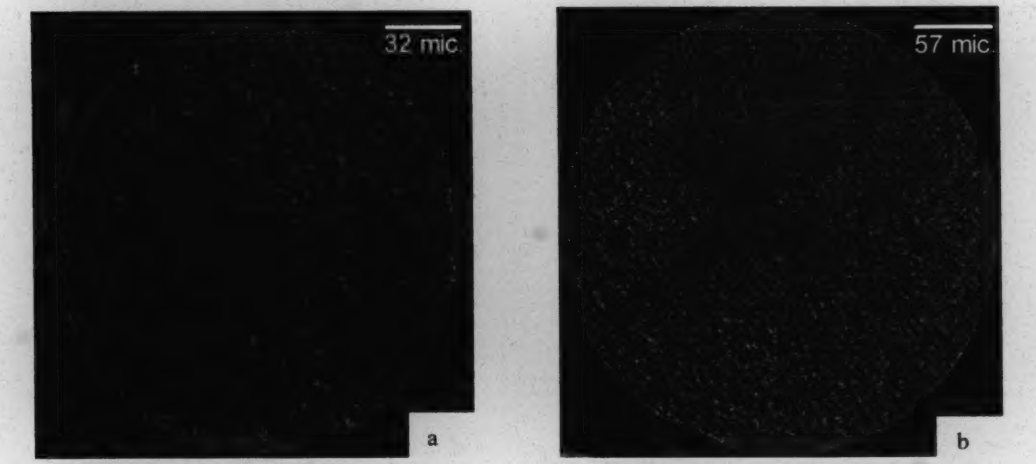

Figure 4.5: Figure 4.5a shows the axial view of image # 40 with porosity across the entire section. A porosity free section (image # 250) from the same droplet along the same axis is shown in Figure 4.5b. Al-17%Cu, 492 μm droplet.

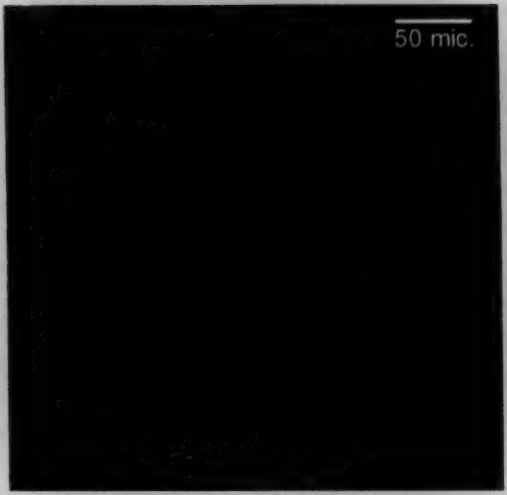

Figure 4.6: Elongated peripheral porosity in an Al-17%Cu droplet. The triangular recalescence region can be seen in the center of the droplet. Al-17%Cu, 456 μm droplet. Image # 262, Frontal axis.

4.3.4 2-dimensional microscopic analysis

The sieved powders were mounted on epoxy and polished and etched for microscopy work. SEM was then used to take images of both Al-5%Cu and Al-17%Cu droplets and cell spacing calculation was performed on Al-5%Cu 2-D images [Wiskel2002b]. Cell spacing was evaluated using random line intercept method. The results are summarized in Table 4.2.

The cell spacing was evaluated on stacks of images (Axial) generated by tomography as well. The spacing result from the entire droplet volume is also summarized in Table 4.2. The images were so chosen so that the entire spherical volume could be divided into three segments, top, middle and bottom. Four to five images from each segment were selected for spacing calculations. The average cell spacing from the three segments did not show any difference. The results from the three sections are shown in Table 4.3.

Table 4.2: Cell spacing results for Al-5%Cu on 2-D SEM and 3-D Tomography images.

Nom. wt. % Cu	Image Type	Droplet dia. (μm)	Cell Spacing (σ) - μm
4.3	SEM (2-D)	655	13.85(0.7)
5	Tomography (3-D)	660	12.4(1.5)

Table 4.3: Cell spacing results for Al-5%Cu on different sections of a 3-D Tomography image.

Droplet Section	Number of Images analyzed	Cell Spacing (σ) - μm
Top	5	12.2 (0.63)
Middle	4	12.7 (0.32)
Bottom	5	12.3 (0.64)

The results from the 2-D images show similar values for the cell spacing [Wiskel2002b] as the 3-D result. The slight difference can be attributed to the difference in the composition of the alloy. Higher solute concentration gives finer structure for the same size [Horwath1962, Wiskel2002b]. Based on the above, it seems that cell spacing results from the droplets is independent of the section, top, middle or bottom, on which the calculation is made. Clearly, more Tomography-SEM cell spacing results are required to confirm this. Cell spacing calculations on Al-17%Cu tomography images could not be performed because of the poor resolution.

Apart from cell spacing calculations, the 2-D images were also analyzed for microsegregation (amount of eutectic) using automated quantitative metallography.

The same principle can be applied to the 3-D images for validation of 2-D results. Unfortunately, the resolution of tomography images was not high enough for threshold contrast, which is absolutely necessary for computer aided quantitative microscopy.

The 2-D images also showed equiaxed structures with long dendrite arms traversing the entire droplet. Without the 3-D information such images can be misleading in terms of possibility of nucleation sites. The 2-D images also showed change in microstructure within the droplets, indicating differences in growth rates associated with the initial growth and recalescence, which takes place soon after nucleation. Although such information can be used qualitatively as evidence of recalescence, the 3-D images show the entire region of the finer structure that can be used for quantitative evaluation of recalescence.

4.4 Discussion

4.4.1 Nucleation

As the atomized liquid droplet falls through the stagnant fluid, there is interaction between the droplet and the fluid. As stated before, the nucleation site lies within the droplets. The nucleation sites are not at the center of the droplet nor at the droplet surface, but close to the periphery. In order to find a possible explanation for the position of the nucleation site found within the droplets, this interaction between the atomizing fluid and the liquid droplet was further investigated.

It is known that as the liquid droplets fall through a stagnant fluid, there is internal circulation within the droplet caused by the shear stress on the surface of the droplet [Pruppacher1970, Brant1969]. A typical internal circulation pattern [Pruppacher1970] is shown in Figure 4.7. The experimental work with water shows vortices of liquid around the equator. Apart from the inner circulation, the external fluid flow around the droplet shows a difference in velocity profile from the front to the rear end for Re = 20, as shown in Figure 4.7a [Clift1978]. There is also a third phenomenon that can possibly take place. With slow velocity flow, the internal vortices in Figure 4.7b are unidirectional. But at higher fluid velocities (Re = 300) there are reverse vortices near the rear [Clift1978].

The internal circulation is a function of the ratio of viscosities of the droplet and the surrounding fluid κ [Clift1978]. A high ratio, $\kappa \geq 55$ [Clift1978], inhibits the internal circulation. Taking the viscosity of pure Al at an atomizing temperature of 950K in a N_2 environment, $\kappa \approx 68$. Based on the high κ value, the internal circulation would be extremely limited. For an atomized droplet, e.g. 660μm Al5Cu, falling through N_2 at 2m/s, the typical Re number would be 90. With such low Re numbers and limited internal circulation, the formation of reverse vortices does not seem possible.

Re numbers for the droplet suggests that the surface pressure (and hence velocity) would change from the frontal stagnation point to the rear, shown in Figure 4.8 [Clift1978]. This would introduce a difference in heat transfer across the droplet surface since the convective heat transfer coefficient is a function of the relative velocity between the fluid and the droplet. Thus the presence of a nucleation site away from the center suggests the role of external fluid flow over the droplet and the consequent heat transfer from the droplet surface in deciding the nucleation site within the droplet.

Multiple nucleations can be caused by a) multiple homogeneous nucleation sites b) multiple substrates in the form of impurities within the melt or c) dendrite remelting during recalescence and providing multiple substrates for nucleation leading to grain multiplication. Both b) and c) results in heterogeneous nucleation. Multiple nucleation sites were not observed within any of the droplets analyzed. The multiple equiaxed sites forming the corners of the polygon in Figure 4.1 cannot be nucleation sites, as can be mistaken in an isolated 2-D image, as they change their position, also shown in Figure 4.1. They seem to be the primary dendrite trunks, with higher order arms, growing in the axial direction and when seen along the axis, exhibit equiaxed pattern. This should suggest a single nucleation site within the droplet and lack of multiple heterogeneous nucleation sites. Also, atomization is carried out under controlled conditions with 20ppm or less O_2 level in the atomization chamber. Hence the number of possible heterogeneous substrates in the form of Al_2O_3 particles can be considered to be negligible. Grain multiplication can be confirmed using EBSD technique. This technique determines the orientation of the crystals within the droplet. Several different orientations of crystals within the droplet would indicate grain multiplication. This is the subject of on-going research.

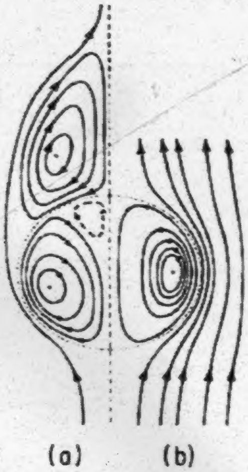

Figure 4.7: Figure 4.7a shows the external and internal fluid flow for a liquid droplet. 4.7b shows the same for a lower Re number [Pruppacher1970].

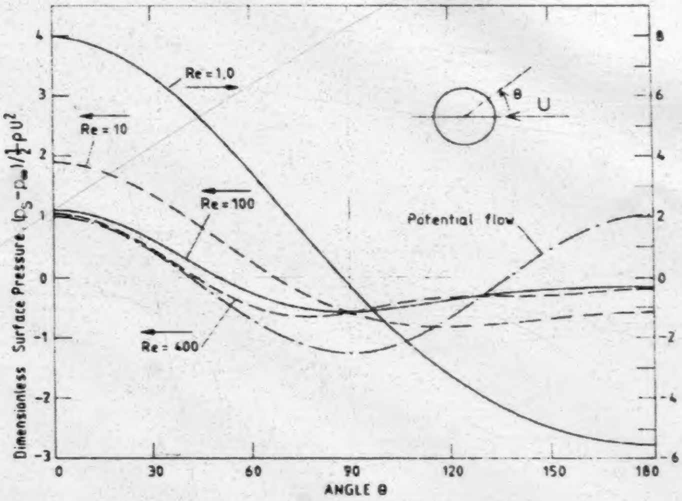

Figure 4.8: Surface pressure variation on a sphere for different Re numbers [Clift1978]. X-axis represents the polar angle from the front to the rear of the sphere.

4.4.2 Recalescence

The volume fraction recalescence calculations performed can be a useful guide for modeling purposes. For example based on the current data one can expect the Al-17%Cu droplet to have 10 to 15% volume percent recalescence. Given the number of particles for recalescence volume data, a rigorous error analysis is not possible. Nevertheless, it is extremely promising since it gives an estimate of the recalescence for the entire droplet, which is not possible with any other technique. To be able to perform a rigorous error analysis, more tomography work is required on more droplets.

There is a substantial difference between the recalescence volume between droplets 1 & 3 and 2. Qualitatively, the extent of recalescence found in droplet 2 was more than in droplets 1 and 3. The difference between the upper and lower values for a given particle is a measure of the difficulty encountered in demarcating the recalescence region from the rest of the particle. Such variation in the experimental result can make modeling a difficult task. For confirmation of the results, the present calculations are being performed again. Nevertheless, for modeling purposes also, more tomography work is required so that the experimental results can be reported after appropriate standard deviation calculations.

Error notwithstanding, the different amounts of recalescence in the Al-17%Cu and Al-5%Cu (confirmed by qualitative visual observation as well), can be explained by the fact that the growth velocities, for a given total undercooling, would be different for the two different compositions [Lipton1984, Lipton1987a, b, c]. This is owing to the different constitutional supercooling between the different compositions. At low total undercooling, the velocity increases on very slight increase of solute to a pure melt and then steadily decreases as the solute percentage is increased [Lipton1984, Lipton1987a]. For intermediate or high total undercooling, on adding solute into a pure melt, the velocity first decreases and then increases as the solute percentage is increased. On further addition of solute to the melt, the velocity continuously decreases [Lipton1987a, b]. Thus, there is an effect of total undercooling on velocity-composition profile. For the case of Al-5%Cu and Al-17%Cu droplets, the higher recalescence volume in Al-17%Cu droplet would correspond to higher growth velocities for Al-17%Cu droplet compared to the Al-5%Cu droplet. Therefore, solidification is believed to have taken place at intermediate to high total undercooling with the droplet compositions placed in the local minima (Al-5%Cu) and local maxima (Al-17%Cu) in the velocity-composition curve. Bearing this in mind, the fraction solid result given in Figure 4.2 is based on LKG model which is suitable for low undercoolings. It is believed that the change in dendrite kinetics at higher undercoolings, which is not taken into account by the LKG model, is the reason for the poor comparison between the experiment and the model results. Calculations based on LKT model [Lipton1987a, b] are being carried out to confirm this.

4.4.3 Dendritic structure & scale of microstructure

The Al-5%Cu droplet shows an overall coarser structure than the Al-17%Cu. Clearly, the growth rate for Al-17%Cu alloy is more than Al-5%Cu. This is based on the results of Howrath & Mondolfo [Horwath1962] that smaller solidification time (faster growth) would result in finer structure. The aforementioned mathematical model is being tried out to ascertain the liquid solid interface velocities for the Al-5%Cu and Al-17%Cu droplets for intermediate to high total undercooling. A higher velocity for Al-17%Cu would explain not only the higher volume fraction of recalescence, but also the coarser structure of Al-5%Cu droplet. This difference in scale of microstructure can also be useful for modeling since the total undercooling can be varied to get simulation results consistent with the experimental results. It should also be noted that the bigger size of the Al-5%Cu droplet, which results in slower cooling rates, also adds towards the coarser structure [Wiskel2002b].

4.4.4 Porosity distribution

The different regions of heavy and negligible porosity in Al-17%Cu droplets, Figures 4.5 and 4.6, show the region of last liquid to solidify. Also, recall that the recalescence microstructure does not show any porosity within the region and the porosity seen is restricted to either the droplet periphery or the fine-coarse structure boundary. The absence of porosity within the recalescence structure and the presence of porosity at the end of recalescence near the edge of the droplet indicate that the last liquid to solidify was away from the nucleation and that no porosity was formed during the recalescence. The porosity at the edge of recalescence region close to the droplet periphery suggests pore formation at the end of recalescence when the dendrites reached the physical limit of the solidifying boundary. This also explains the elongated shape of the porosity aligned along the growth direction. The porosity found at the boundary between the coarse and the fine structure also indicates that the recalescence region indeed was the initial growth region and the porosity was formed after the coarse region had solidified. The traces of porosity found within the fine structure were probably caused by the lack of liquid to pass through the fine dendrite spacing. The Al-5%Cu droplet also shows no porosity formation within the recalescence region. Also, there is even distribution of porosity over the entire droplet volume with no different regions of heavy and negligible porosity. Recall that the recalescence region in Al-5%Cu droplets was much smaller. Therefore, it seems that the nucleation site and early recalescence growth affects the porosity distribution in the droplets and since porosity is not formed during recalescence, the extent of recalescence decides the position of porosity formation as well. The higher amount of recalescence in Al-17%Cu droplets resulted in regions of last liquid to solidify with high porosity. The much smaller amount of recalescence in Al-5%Cu did not concentrate the porosity to one end of the droplet.

4.5 Conclusions

Tomography technique is extremely promising because of the extra information obtained about solidification features. These were not possible with the conventional 2-D techniques. Tomography images showed details of solidification features like nucleation, recalescence and porosity distribution, which are summarized below.

1) Nucleation site could be clearly seen and approximately located within the droplet.
2) Multiple nucleation was not observed within any of the droplets
3) Recalescence boundaries were seen in all the droplets. It was possible to evaluate the volume fraction of recalescence in the droplets.
4) Porosity distribution was different for the two alloys. The porosity distribution within the droplets, especially 5%Cu, could not be explained.

The current work has also shown the similarities between the 2-D microscopy and 3-D tomography work in that the cell spacing results showed similar results for 2-D as well as 3-D tomography images. Based on the current results, it seems that the cell spacing calculation is independent of the section of the droplet on which the spacing calculation is performed.

The major shortcoming of the 3-D tomography work was the limit of resolution of the synchrotron X-ray beam. Accurate recalescence volume calculation and quantitative image analysis could not be performed on the images because of the resolution. In view of the advantages of this technique, more tomography needs to be done on the atomized droplets to gather useful information about solidification for modeling purposes.

Some of the results obtained from this work need further confirmation by experimentation. For example, absence of grain multiplication still needs to be confirmed using EBSD. The rate of growth of dendrites for the Al-17%Cu and Al-5%Cu droplets seem to play an important role in determining both the scale of the microstructure as well as the amount of recalescence. Further modeling of the rate of growth of dendrites for high nucleation undercooling need to be done to confirm these.

4.6 References

[Brant1969]:	"On the internal circulation and shape of large raindrops", Brant F.G., Journal of Atmospheric Sciences, v. 26, 1969, pp.179-181.
[Clift1978]:	"Bubbles, drops and particles", Clift R., Grace J.R. and Weber M.E., New York, Academic Press, 1978.

[DeHoff1968]: “Quantitative Microscopy”, DeHoff R.T. and Rhines F.N., Materials Science and Engineering Series, McGraw Hill, 1968.

[Horwath1962]: “Dendritic Growth”, Horwath J.A. and Mondolfo L.F., Acta Metallurgica, v. 10, 1962, pp.1037-1042.

[Howard1998]: “Unbiased Stereology: Three Dimensional measurement in Microscopy”, Howard C.V. and Reed M.G.; BIOS Scientific Publishers Limited, Oxford, 1998, pp 39-54.

[Jones1983]: “Rapid solidification of Metals and Alloys”, Jones H., The Institution of Metallurgists, London, 1983, pp 8-14.

[Lipton1984]: “Dendrite growth into Undercooled Alloy Melts”, Lipton J., Glicksmann M. E. and Kurz W., Materials Science and Engineering, v. 65, 1984, pp 57-63.

[Lipton1987a]: “Equiaxed Dendrite growth at small Supercooling”, Lipton J., Glicksmann M. E. and Kurz W., Metallurgical Transactions A, v. 18A, 1987, pp 341-345.

[Lipton1987b]: “Rapid Dendrite Growth In Undercooled Alloys”, Lipton J., Kurz W. and Trivedi R., Acta Metallurgica, v. 35, n. 4, 1987, pp 957-964.

[Lipton1987c]: “Effect of growth rate dependant partition coefficient on the dendritic growth in undercooled melts”, Lipton J., Kurz W. and Trivedi R., Acta Metallurgica, v. 35, n. 4, 1987, pp 965-970.

[Maire2001]: "On the application of X-ray microtomography in the field of materials science", Maire E. et al, Advanced Engineering Materials, v.3, no. 8, 2001, pp 539 - 546.

[Morin1996]: "The Impulse Atomization Process: an economical and flexible process for producing powders with a tailored size distribution", Morin L.C., Rieder M., Meja J., Henein H., Proceedings of the Int. Symposium on Light Metals 1996, Metallurgical Society of CIM, Montreal, pp. 293-304.

[Prasad2002]: "A Study of Microsegregation in Al-Cu alloys Using Impulse Atomization as an RSP", Prasad A, Henein H. and Gandin C-A., Light Metals 2002 Métaux Légers, T. Lewis, Editor, MetSoc of CIM, 2002, pp. 101-114.

[Pruppacher1970]: "A wind tunnel investigation of the internal circulation and shape of water droplets falling at a terminal velocity in air", Pruppacher H.R. and Beard K.V., Quarterly Journal of the Royal Meteorological Society, v. 96, 1970, pp 247-256.

[Wiskel2002b]: "Solidification study of aluminum alloys using Impulse Atomization: Part II. Effect of cooling rate on microstructure", Wiskel J.B., Navel K., Henein H., Maire E., Canadian Metallurgical Quarterly, v. 41, n. 2, 2002, pp 193-204.

Chapter 5

Understanding the rapid solidification of Al-4.3Cu and Al-17Cu using X-Ray Tomography[1]

5.1 Introduction

Rapid solidification techniques have grown in importance because of their ability to generate a variety of structures [Jones1983], which are not possible with conventional solidification processes. The difference between conventional processes and rapid solidification lies in the extreme high cooling rates 10^3-10^6 K/s involved [Flemings1981]. As such, the physics of rapid solidification deviates from that of a normal solidification process. This results in additional solidification regimes during rapid solidification and a consequent difference in the morphology and scale of the microstructure. Conventional microstructural characterization involves 2-D microscopy to gather information about solidification characteristics such as cell spacing and microsegregation (using quantitative metallography). These approaches are constrained by the small number of sections that can be viewed from a given sample. A 3-D visualization technique offers obvious advantages over 2-D microscopy. We have used X-ray tomography for gathering 3-D information on rapidly solidified atomized Al-Cu droplets.

---

[1] Published as, "Understanding the rapid solidification of Al-4.3Cu and Al-17Cu using X-Ray Tomography", Prasad A. et al., Met. Trans. A, v. 37, n. 1, 2006, pp 249-257. Reformatted according to thesis requirements.

5.2 Experimental

The experimental details of atomization and tomography have been described in an earlier paper [Prasad2002, Prasad2004], however, a summary of these issues will be outlined here. The alloys were prepared using commercially pure Al and Cu to prepare Al-4.3%Cu and Al-17%Cu aluminum alloys. The actual chemistry of the alloys was analyzed from the atomized powders using an Inductively Coupled Plasma (ICP) mass spectroscopy. The powders were atomized [MPIF09] using a single fluid atomization process – Impulse Atomization [Prasad2002, Morin1996]. The alloy melt, atomized at about 200K superheat, was sprayed into a stagnant gas atmosphere of either N_2 or He. The impulse action of the plunger held in the melt during atomization pushed the melt through fine orifices, forming liquid jets of finite length in the atomization chamber. The jets broke up into small droplets due to Raleigh instability [Henein2001]. The droplets solidified while falling under gravity through the gas atmosphere and were fully solidified after a 4 m falling height of the atomizing tower. No secondary atomization was observed during any of the atomization runs and no satellites were observed on any particle.

X-ray beams from a synchrotron facility were used to carry out computer tomography work. Observations were made on the droplet using X-ray beams of 1 μm resolution at the European Synchrotron Radiation Facility (ESRF), Grenoble. One Al-4.3%Cu droplet (660 μm, N_2 gas) and four Al-17%Cu droplets ≅500 μm, He gas) were analyzed. Details of generating stacks of images and subsequently converting them into solidification movies are described in Prasad et al [Prasad2004] and reported three microstructural features: the evidence of a single grain, an Ultra-Fine structure during initial growth and the porosity distribution in Al-4.3%Cu and Al-17%Cu droplets. It was shown that the site from which the single grain evolves is not affected by internal fluid circulation and consequently the site is immobile within the droplet during solidification. The size of the Ultra-Fine structure associated with this initial growth was quantified and the difference in porosity distribution between the two compositions was also reported in that paper.

More work has since been done in terms of image analysis on the tomography images to better understand the rapid solidification process. This paper describes additional microstructural features. These features are differentiated as Region I, Region II and Region III. Region I is the initial growth with very fine microstructure. Region II is the primary dendrite growth region surrounding Region I. The rest of the droplet area is termed Region III. These three regions have different scales of microstructures, and therefore, in relative terms they are ultra-fine (Region I), fine (Region II) and coarse (Region III) microstructures. This paper also describes the mechanism of single grain formation and reasons for porosity distribution differences. Combining all the information, the rapid solidification process taking place as a droplet solidifies under a given atomizing condition is outlined.

5.3 Results

In this section, the quantification of the three regions of microstructures in the droplet will be presented. In addition, the amount of porosity and its distribution in the droplet will be identified. This will be followed, in the next section, by a discussion of these results in the context of rapid solidification of these droplets.

5.3.1 Region I

The stacks and the movies were prepared for three directions, Axial (X-Y plane), Frontal (Z-X plane), and Sagittal (Y-Z plane). It was possible to see an Ultra-Fine grained region, along all three directions, termed Region I in Figure 5.1. The figure shows one image (image number 540 out of a stack of 660 images) for Al-4.3%Cu along the axial direction and one image for Al-17%Cu along the saggittal direction. This region is encircled in Figure 5.1a and enclosed within a triangle in Figure 5.1b. The arrows seen in Figure 5.1a will be addressed in the Discussion section.

Figure 5.2 shows a sequence of images from Al-4.3%Cu droplet (660 µm, N_2 gas atomized) movie taken along the axial direction. Figure 5.2a shows four points A, B, C & D from which dendrites seem to grow. These dendrite growths are made clearer with the help of dotted lines. These points delineate a structure of dendrites forming a polygon. Noteworthy is that, as the movie is played these four points converge to a single region. This sequence is shown in images b) through d). Such a sequence was seen along all the three axes and in all the droplets observed. Where they meet is a small region of a very fine structure. This is Region I shown in Figure 5.1. The image in Figure 5.2 was inverted for a better view. The light areas are therefore primary pro-eutectic alpha-Al phase. The Al-17%Cu droplet showed a similar structure as in Al-4.3%Cu droplet, but polygonal in shape and larger areas of this fine structure. A similar sequence is shown for Al-17%Cu in Figure 5.3.

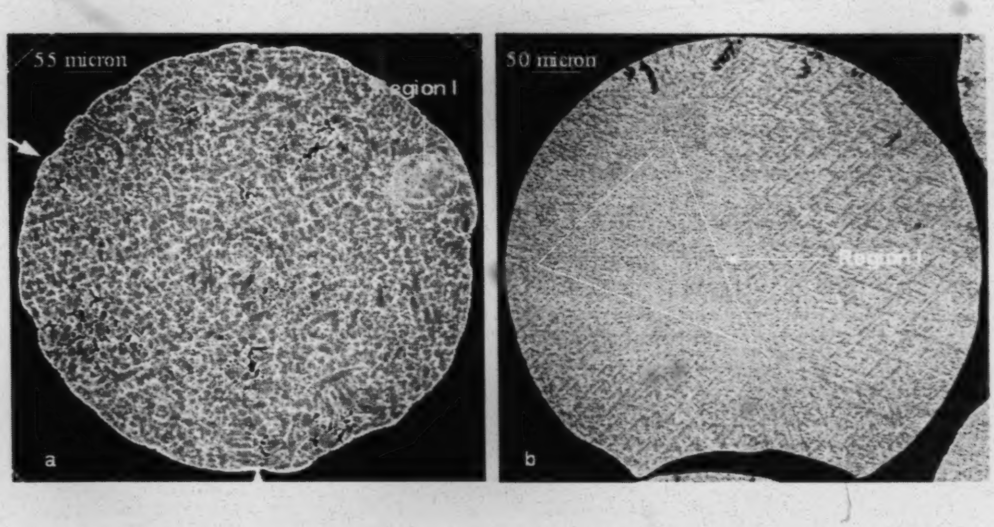

Figure 5.1: 2D images of Region I in (a) Al-4.3%Cu and (b) Al-17%Cu droplet obtained from Tomography. The circle in (a) and the triangular region in (b) are the Ultra-Fine structure region in Al-4.3%Cu and Al-17%Cu respectively. These images are just one of the several images in a Tomography generated stack. The thicker white arrows in (a) show the approximate direction of the droplet falling during atomization. Region I is at 120^0 from either arrow. Because of the bigger size of Region I in (b), such trajectory pointing arrows cannot be placed with accuracy.

5.3.1.1 Quantification of Region I

Region I was found to be within the droplet for all cases. Since the thickness of each image was 1 μm (beam resolution of 1 μm), the image number in a stack could be determined from the frame speed of the movies. Thus the image number in a stack provides information about the depth of penetration of the X-ray beam.

From the depth of penetration information along all three axes, the position of the site from where Region I emanates, could be measured. The average distance between the droplet center and Region I was $0.75\,R_p$ for the Al-4.3%Cu and $0.63\,R_p$ for the Al-17%Cu droplet, where R_p is the radius of the individual droplet and $R_p = 0$ is the center of the particle. From the full set of 2-D stack of images featuring the Ultra-Fine structure, it could be visually seen that the area fraction of Region I was larger for the Al-17%Cu than the Al-4.3%Cu droplets. The details of the fine structures, in both Al-4.3%Cu and Al-17%Cu particles, are not clearly visible as their scale is below the resolution limit of the X-ray beam in the synchrotron.

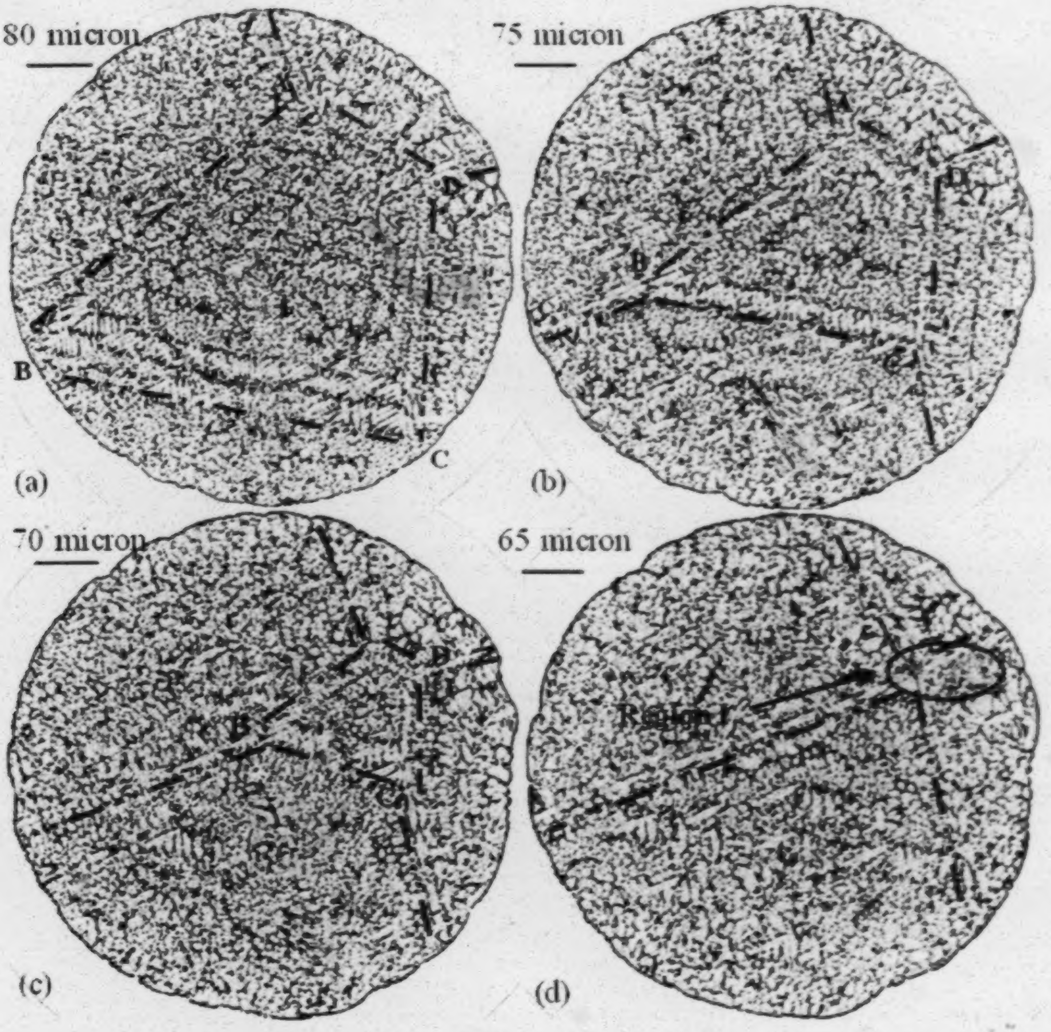
80 micron
75 micron
70 micron
65 micron
A
B
C
D
Region 1
(a)
(b)
(c)
(d)

Figure 5.2: Four slices taken from the stack of images along axial direction of Al-4.3%Cu droplet. Dotted lines are drawn to help see the movement of equiaxed site forming the vertices of a polygon. These vertices move towards one point in figure (d).

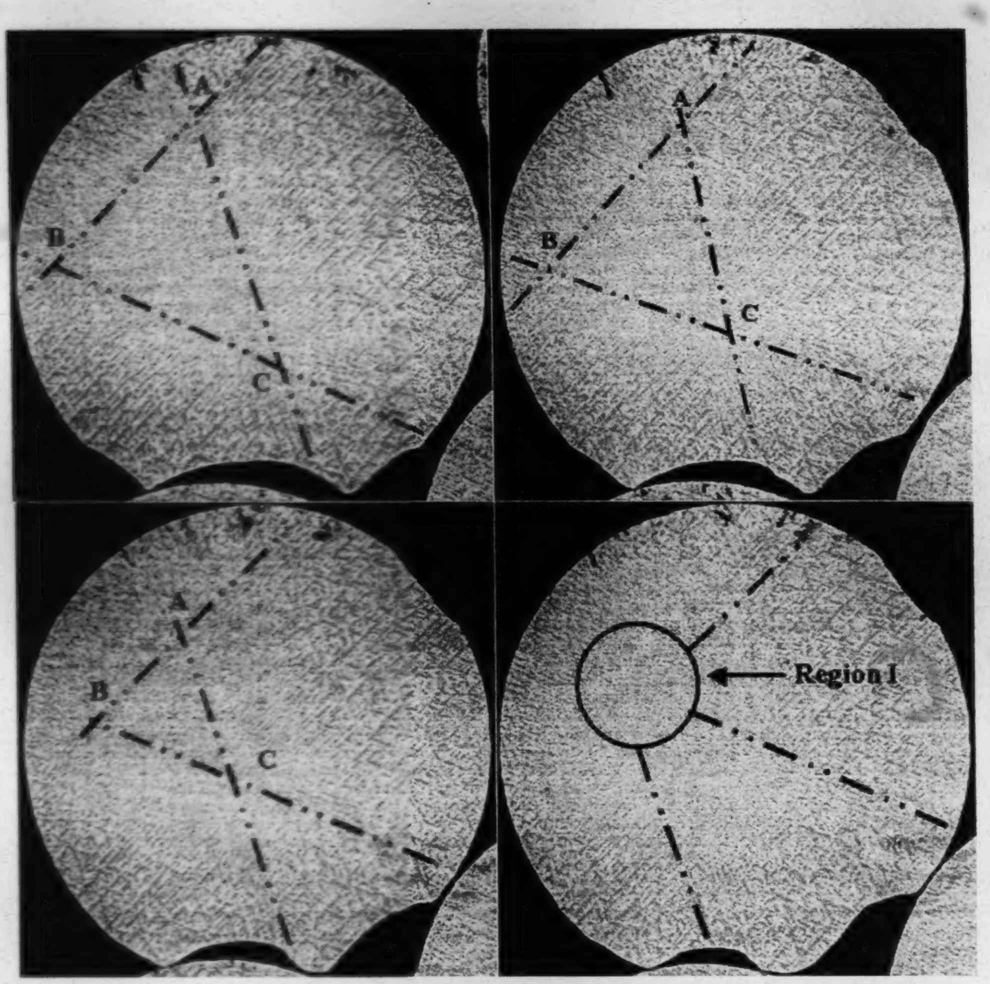

Figure 5.3: Four slices taken from the stack of images along axial direction of Al-17%Cu droplet. Black lines are drawn to help see the movement of equiaxed site forming the vertices of a polygon. Just as in Al-4.3%Cu, these vertices move towards one zone (Region I) in (d).

Using stereological analysis [DeHoff1968] on these images, the average volume fraction of Region I within the particle was quantified for all the droplets (one Al-4.3%Cu droplet and four Al-17%Cu droplets). The calculation was done using Cavalieri method, described in Howard and Reed [Howard1998]. It basically involves selecting the volumetric region containing Region I within the droplet and dividing that region into a fixed number of slices of known thickness. The area fraction of the feature of interest on each slice is then measured and the volume of Region I for each slice is given by the product of area fraction and the slice thickness. A manual point count technique was employed for measuring the area fraction on each slice. The summation of the volume fraction for each slice gives the total volume fraction of Region I for the entire droplet. Table 5.1 shows the results of volume fraction of Region I marked as a circle in Figure 5.1a and white lined triangle in Figure 5.1b. Also shown in Table 5.1, is the number of slices containing Region I and the slice thickness (i.e. measurement accuracy).

Table 5.1: Volume percent results of Region I from Cavalieri method.

Droplet details	4.3%Cu - Ball1	17%Cu –Ball2	17%Cu –Ball3	17%Cu –Ball4
Nom. Comp.	4.3	17	17	17
Drop. Diameter	660μm	490μm	450μm	420μm
Drop. Volume	1.5e8μm^3	6.2e7μm^3	4.8e7μm^3	3.8e7μm^3
Direction	Axial	Axial	Axial	Axial
# of Slices	17	15	16	15
Slice thickness	3μm	19μm	22μm	11μm
a/p, [mm^2]	122.5	122.5	122.5	122.5
Reg. I vol.%	0.09±0.01	14.8±2.9	20.0±4.24	8.9±0.63

5.3.2 Region II

From the 3-D tomography images, it is clear that outside of Region I, there is a change in the scale of the microstructure. The grain structure outside of Region I is considerably coarser. It is apparent that there are Primary Trunks of dendrites emanating from Region I as shown by labels in Figure 5.4. This is the same structure which was delineated with the help of lines in Figures 5.2 and 5.3.

As one observes the stack of images in all three axial orientations, it is evident that these Primary Trunks develop into an equiaxed dendritic region (see Figure 5.1a for Al-4.3%Cu). The microstructure of the Primary Trunks is evidently coarser than in Region I for both the Al-4.3%Cu and Al-17%Cu droplets. The coarser Primary Trunks plus the Ultra-Fine structure (Region I) it surrounds is defined as Region II.

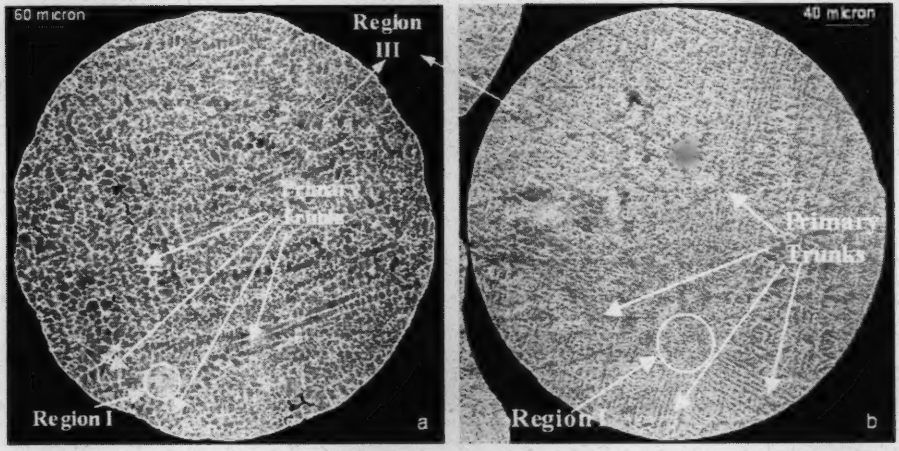

Figure 5.4: Primary Trunks emanating from Region I of Ultra-Fine structure. Region II is defined as Region I and the Primary Trunks surrounding Region I. Region III is the rest of the area in the droplet.

Since the Primary Trunks emanate from Region I and surround it, it is believed that Region I and Primary Trunks represent the early solid growth. Quantification of this Region II was similarly carried out using Cavalieri method described in the previous section. The directional morphology of the Primary Trunks was used for demarcating the calculation region (see Figure 5.4). Recall that these Primary Trunks grow to form an equiaxed polygon structure (Figures 5.2 and 5.3). Results of the quantification of Region II are presented in Table 5.2.

Table 5.2: Quantification results of Region II (Primary Trunks + Ultra-Fine structure) from Cavalieri method.

Droplet details	4.3%Cu - Ball1	17%Cu - Ball1	17%Cu – Ball2	17%Cu – Ball3	17%Cu – Ball4
Nom. Comp.	5	17	17	17	17
Drop. Diameter	660μm	480μm	490μm	450μm	420μm
Drop. Volume	1.5e8μm^3	5.8e7μm^3	6.16e7μm^3	4.77e7μm^3	3.88e7μm^3
Direction	Axial	Sagittal	Sagittal	Sagittal	Axial
# of Slices	38	35	35	35	33
Slice thickness	10μm	10μm	10μm	10μm	10μm
a/p, [mm^2]	122.5	122.5	122.5	122.5	122.5
Reg. II vol.%	19.4±0.6	27.8±2.4	33.3±2.3	44.1±2.2	32.1±3.1

5.3.3 Region III

The rest of the region in the droplet is termed Region III (Figure 5.4). This region shows uniform equiaxed growth which is non-directional. This region has the coarsest microstructure (see Al-17%Cu) and as coarse as the Primary Trunks of Region [illegible] in Al-4.3%Cu droplet. This region also contains porosity as seen in both Al-4.3%Cu and Al-17%Cu samples.

5.3.4 Porosity distribution

As reported in [Prasad2004], the porosity distribution in the Al-4.3%Cu and Al-17%Cu droplets are very different. A 3-D porosity distribution within the droplet was generated using the Volume Graphics software. Figure 5.5 shows this porosity distribution in two droplets. The Al-4.3%Cu has porosity throughout the droplet volume whereas Al-17%Cu has a highly heterogeneous porosity distribution polarized in the periphery. There are also some regions in Al-17%Cu droplet which shows a tubular shaped porosity, shown in Figure 5.6. This tubular porosity is only seen at the droplet periphery where the boundary of the solidifying system is reached. Such tubular porosity was not seen in Al-4.3%Cu droplet.

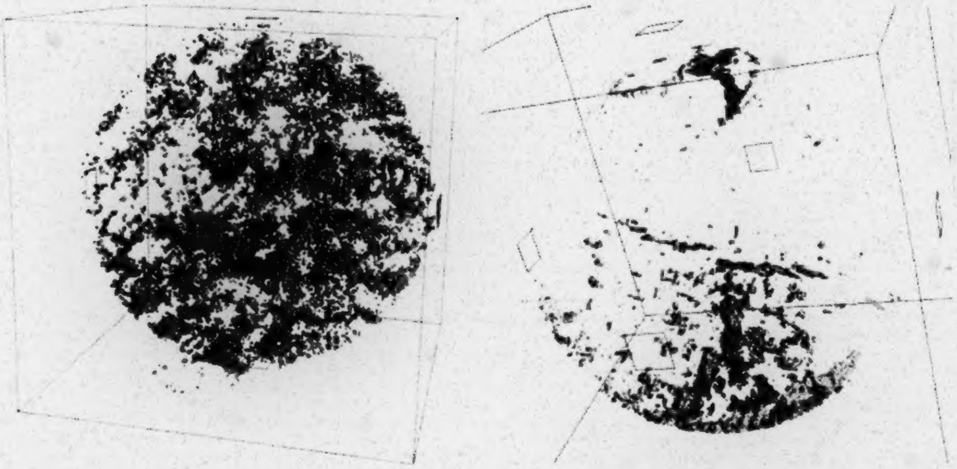

Figure 5.5: 3-D porosity distribution for (a) Al-4.3%Cu and (b) Al-17%Cu droplets. The homogeneous distribution in Al-4.3%Cu droplet is markedly different from the peripheral distribution in the Al-17%Cu droplet.

The average volume fraction of porosity, V_f, was also quantified. The procedure involves calculating the number of pixels with gray scale levels matching that of porosity (say 0-10) within the entire droplet volume. Note that in the Al-4.3%Cu droplet, pro-eutectic α-Al, the interdendritic regions and the interdendritic porosity would have different gray scale values. The V_f calculated was 0.60%.

In Al-17%Cu droplets, the tubular porosity opens up to the droplet surface and the gray scale value of the porosity and the area surrounding the droplet is similar. Hence a volume fraction analysis of the Al-17%Cu droplets was not possible. The detection limit of the porosity was same as the X-ray tomography beam resolution of 1 μm.

Table 5.3: Porosity distribution in a Al-4.3%Cu droplet. The average droplet porosity was 0.6%..

Radial distances (μm)	Volume fraction porosity
0	0.36
86	0.18
172	0.34
258	1.69
344	1.56

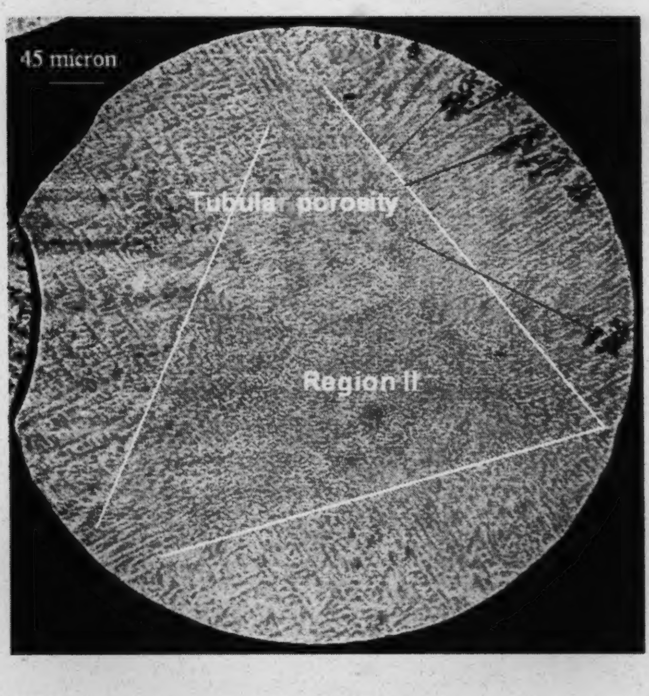

Figure 5.6: Tubular shaped porosity in a Al-17%Cu droplet. The porosity is at the boundary of the solidifying droplet thereby suggesting the role of nucleation and recalescence in pushing the porosity away towards the periphery.

5.4 Discussion

As the droplet falls through the atomization gas, it loses heat and begins to solidify. The solidified structure, based on the morphology and scale, can be differentiated into three distinct regions. The Ultra-Fine structure of initial growth (Region I) are surrounded by the directional Primary Trunk. Together they are termed Region II. The rest of the zone outside of Region II is the equiaxed zone called Region III. Porosity is seen mainly in Region III although for Al-4.3%Cu droplet some porosity is seen within Region II as well. The three regions and the porosity distribution can be understood in terms of nucleation, initial growth, recalescence and coarsening. These are explained in the following.

5.4.1 Region I: Evidence of a single nucleation site

The points A to D in Figures 5.2 and 5.3, which form the corners of the polygon, cannot be nucleation sites, as can be mistaken in an isolated 2-D image. This is so because these equiaxed sites change their position from one frame to the next while continuously maintaining the vertices of the polygon. These four points converge at a single site which also has a presence of Ultra-Fine microstructure near this site. This convergence to a single site and the presence of Ultra-Fine structure near this convergence site suggests that this region of very fine microstructure contains the nucleation site of the droplet. This is so because a nucleation point cannot be mobile within the droplet and it has already been pointed out in the previous work [Prasad2004] that a nucleation site in an Impulse Atomized droplet is immobile within the droplet. Since there is only one such point within the entire droplet, the solid could grow only from this site and therefore, it is believed that the droplet undergoes a single nucleation event. Moreover, the presence of Ultra-Fine structure near this site indicates that this initial growth took place from this nucleation site. The fine structure of Region I is the evidence of very fast growth rates and since the rate of growth is proportional to the undercooling, the nucleation seems to have taken place at some undercooling. Since nucleation in atomized droplets cannot be observed in real time, the estimation of this undercooling requires numerical modeling work. This is explored in a future publication devoted to modeling aspects of droplet solidification during atomization.

5.4.1.1 Region I: Probable mechanism of nucleation

Atomization is carried out under controlled conditions with 200 ppm or less O_2 level in the atomization chamber. The Al, with the present O_2, forms Al_2O_3 on the surface of the droplets. This is a highly exothermic reaction and the heat liberated during this exothermic reaction heats up the surface of the droplet. Even as the liquid droplet has an available nucleation substrate in the form of Al_2O_3, no nucleation occurs on the surface of the droplet because of the heat generated by the oxidation reaction. This is confirmed by the calculation of the coordinates of the nucleation site which shows nucleation sites (Region I) to be within the droplet volume. The droplet interior on the other hand is undercooled and colder than the surface. The presence of any impurity within this undercooled bulk results in nucleation. Since no TEM work was done on the droplets, the impurities acting as nucleating agents could not be characterized.

An understanding of the convective heat losses from a droplet under conditions of low Reynolds number (≅100, [Prasad2004]) can be used to infer the orientation of the droplet in flight during solidification. As the maximum heat transfer rate occurs in a droplet at an angle of 120^0 from the path of the fall, it thus appears likely that the stagnation point in heat transfer of the Al-4.3%Cu is either one of the locations indicated by the arrows in Figure 5.1. This stagnation point represents the bottom position of the droplet in free fall. This estimate of the stagnation point cannot be done for Al-17%Cu as the Region I in these particles are not as well defined as in the Al-4.3%Cu particles.

5.4.2 Region II: Microstructural features and Recalescence

When nucleation occurs at some bath undercooling, there is, subsequently, a fast rate of growth of dendrites. Due to the fast rate of growth of the dendrites, the latent heat of solidification generation is more than the rate of heat extraction from the system and therefore the temperature of the droplet actually increases resulting in recalescence. The dendrite growth rate during recalescence, while still fast, is clearly slower than before the onset of recalescence [Wu1987]. This change in growth rate before, during and after recalescence results in different scales of microstructure which demarcates recalescence from the rest of the solidification regimes.

From the tomography observations, the Ultra-Fine microstructure of Region I is found close to the nucleation event. Also, the Primary Trunks, outside Region I and surrounding it, has a distinct directionality. These directional trunks also emanate from the region containing the nucleation event. Since, in rapid solidification, nucleation event is followed by initial growth and recalescence, it is believed that Region II, as a whole, represents the initial growth and recalescence. Since the temperature of the system increases during recalescence, the driving force for solidification decreases, thus the structure in Region I is the finest in the droplet.

The quantification results show a difference between the volume of Region II in Al-4.3%Cu and Al-17%Cu droplets. This relates to a difference in the volume of initial growth and recalescence in the two compositions. Dendrite kinetic models developed by Kurz and coworkers, [Lipton1984,Lipton1987a,b,c] suggest that there would be a difference in dendrite growth velocities between the Al-4.3%Cu and Al-17%Cu droplets due to differences in constitutional undercooling. Since initial growth and recalescence microstructure reflects the effect of dendrite growth rate, it is expected that different growth rates would result in different volume fraction for Region II. The forthcoming publication on droplet solidification has dendrite kinetics coupled into it and this effect of dendrite growth velocity on initial growth and recalescence volume is explored in that paper.

5.4.3 Region III: Effect of coarsening

One of the major differences seen in the Al-4.3%Cu and Al-17%Cu microstructure is the difference in the coarseness of the structure. Note that Al-17%Cu shows a difference in scale between the Primary Trunks and Region III, while Al-4.3%Cu does not show any appreciable difference between the two. The difference in the scale of the microstructure between the two compositions is believed to be caused by different amounts of coarsening and is discussed next.

5.4.4 Coarsening: Effect of composition

The tomography image of Al-4.3%Cu droplet shows an overall coarser structure than the Al-17% Cu, which suggests that Al-4.3%Cu droplets undergo more coarsening than the Al-17%Cu droplets. Coarsening is essentially a mass diffusion phenomena and the difference in coarsening between the two compositions can be explained as follows.

Since solidification is likely to begin at a higher temperature in Al-4.3%Cu than in Al-17%Cu (the alloy liquidus is 50K higher for the lower Cu), the diffusivity of Cu in Al at higher temperatures would be higher, leading to greater coarsening. The higher alloy concentration showing finer secondary arm spacing has also been reported by Okamoto et al [Okamoto1975], on their directional solidification work on Al-Cu system. Furthermore, Kurz et al [Kurz2000], have proposed a coarsening parameter M given as,

$$M = -\frac{D\Gamma \ln(\frac{C_{le}}{C_0})}{m_l(1-k_0)(C_{le}-C_0)} \qquad (5.1)$$

Γ is the Gibbs-Thomson coefficient for liquid-solid surface energy, D is the solute diffusivity in the liquid, C_{le} is the liquid eutectic composition, C_0 is the original alloy composition, m is the slope of the liquidus and k_0 is the partition coefficient. This parameter M appears in the secondary arm spacing-solidification time equation. The value of this parameter was calculated for Al-5%Cu and Al-17%Cu. The ratio of this parameter for the Al-5%Cu and Al-17%Cu gives, $M_5/M_{17} = 1.8$. Hence one would expect Al5%Cu to coarsen more than the Al-17%Cu. Functionally from Eqn. 1 this is due primarily to the concentration terms C_{le} and C_0. In other words, lesser solute concentration, C_0, results in more coarsening. This was further confirmed by doing arm spacing calculations on 2-D SEM images of Al-5%Cu and Al-17%Cu droplets. The result is shown in Figure 5.7. The results are shown as a function of droplet size and gas types. Bigger particles show coarser structure than the smaller particles. Al-5%Cu with N_2 shows a coarser structure, while Al-17%Cu in He shows the finest structure. For a given particle size the He shows finer structure for both compositions. The difference in cell spacings in terms of particle size and gas reflects the effect of cooling rate on cell spacing. Also, for a given droplet size and gas type, lower alloy concentration show a higher arm spacing. Results from the tomography work are also included in the figure. In the earlier work [Prasad2004] it was shown that the spacing measurements on 3-D tomography and 2-D SEM images gave similar results. Also included is the cell spacing results done on 2-D SEM images, from Wiskel et al [Wiskel2002b], which shows the cell spacings for Al-4.3%Cu for different particle sizes. The result from the tomography and 2-D SEM images is for the same composition and gas type and show similar values. On the other hand, the Al-4.3%Cu shows an even coarser structure than the Al-5%Cu samples for the given range of particle sizes. This shows the effect of composition on cell spacing. Since the final cell spacing is controlled by coarsening, the effect of composition on coarsening is seen in Figure 5.7.

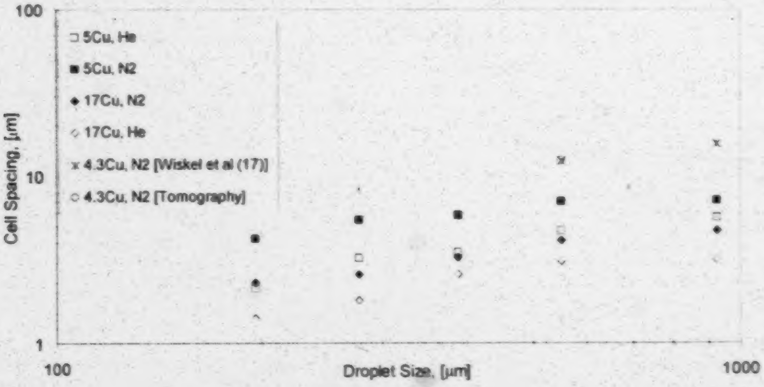

Figure 5.7: Cell spacing of Al-5%Cu and Al-17%Cu droplets atomized under He and N_2. Spacing measurements done on SEM images. Spacing measurements done on tomographic 2-D image for Al-4.3%Cu is also included in the figure. Random Line intercept method was used for all cell spacing calculations.

5.4.4.1 Coarsening of different regions

The above argument can be extended to explain the varying degree of coarseness observed in the three regions in Al-4.3%Cu and Al-17%Cu droplets. Al-4.3%Cu droplet shows an Ultra-Fine structure in Region I, while the Primary Trunks of Region II & non-directional equiaxed structure of Region III show similar coarseness. On the other hand Al-17%Cu droplet shows three different scales in these three regions. The Ultra-Fine structure in Region I in both Al-4.3%Cu and Al-17%Cu droplets is a result of the fastest growth rates and consequently the fastest cooling rates in agreement with what is widely reported in the literature, for example [Mondolfo1962, Bardes1966].

The similar coarseness between Primary Trunks in Region II and equiaxed structure in Region III in Al-4.3%Cu and dissimilar coarseness in these two regions in Al-17%Cu can be attributed to the difference in coarsening in the two compositions. Since there is more coarsening in the Al-4.3%Cu, the Primary Trunks of Region II have coarsened more and the scale of the microstructure of Primary Trunks and Region III are almost the same. In Al-17%Cu, since there is lesser coarsening, the two show different scales of microstructure. The similar scale of structure between Primary Trunks and Region III in Al-4.3%Cu droplet suggests that coarsening starts very early during the solidification. Note that the equilibrium freezing range T_l to T_E is larger for Al-4.3%Cu than Al-17%Cu. So there is more time at higher temperature leading to more coarsening. In fact, the Ultra-Fine structure may also have coarsened, though one cannot quantify it because of the limited resolution of the X-ray beam.

5.4.5 Porosity distribution

The porosity seen in the droplets is believed to be a result of the difference between the liquid and the solid density. The atomization process involves creating vacuum down to -1 atmosphere pressure followed by double purging with the atomization gas (He or N_2). Therefore, the atomization melt is not expected to contain any dissolved gas. A pore formed due to escape of gas (blow holes), typically, would have a smooth round structure. No such blow holes were seen in any of the droplets. The O_2 and N_2 will tend to form oxide/nitride with Al very quickly and will not remain dissolved in the melt. Also, the shape of the porosity conforming to the interdendritic space is an evidence of shrinkage cavities.

The major difference between the Al-4.3%Cu and Al-17%Cu porosity distribution was that the Al-4.3%Cu showed a homogeneous distribution throughout the droplet volume, whereas the Al-17%Cu showed a heterogeneous porosity distribution with porosity free and porosity concentrated regions (Figure 5.5). Region II, in general, does not show any porosity within it and the little porosity seen is restricted to the droplet periphery. Polarization in the porosity distribution in Al-17%Cu was believed to be the result of nucleation and extent of initial growth & recalescence and that the porosity was formed away from Region

II. This was confirmed by calculating the volume fraction, V_f, of porosity as a function of radial distance from the nucleation site for the Al-4.3%Cu alloy. As mentioned before, the porosity calculation could not be performed on the Al-17%Cu droplets. The porosity fraction was calculated in cubes of 100 μm size. For the calculation, the cube was initially centered on the nucleation site and then moved by 50 μm along each axis. Recall that it was mentioned in the Results section under sub-section Region I, that the coordinates of the nucleation site was calculated. This translates to a radial distance of 86 μm for each step along <111> direction of the cube enclosing the droplet, as shown in Figure 5.8. This was repeated till the droplet periphery was reached. Table 5.3 shows the results of this calculation. It can be seen that the porosity formation increases as the distance from the nucleus increases. Since Region II is believed to represent the recalescence microstructure, it seems that the extent of recalescence plays a role in defining the porosity distribution.

The different porosity distribution in the recalescence region between the Al-4.3%Cu and Al-17%Cu can be explained by the difference in dendrite growth rates in the two compositions. $V_{g4.3} > V_{g17}$ [Lipton1984,Lipton1987a,b,c] for a given undercooling, therefore the fine network of dendrites form more quickly in Al-4.3%Cu and the liquid does not get time to fill cavities caused by shrinkage. In Al-17%Cu, the growth is slower and therefore the liquid gets the time to reach the interdendritic regions where cavities are formed. Thus, no significant porosity is seen in Region II in Al-17%Cu. The traces of porosity found within the fine structure were caused by the lack of liquid to pass through the fine dendrite spacing.

The porosity found at the boundary between the coarse and the fine structure also indicates that Region II, indeed, was the early solid growth and the porosity was formed after the coarse region had solidified. The tubular porosity at the end of primary trunk growth, close to the droplet periphery, suggests pore formation at the end of primary trunk formation when the dendrites reached the physical limit of the solidifying boundary. This also explains the elongated shape of the porosity aligned along the growth direction. Thus, both the dendrite growth rates during recalescence and the extent of recalescence decides the position of porosity formation.

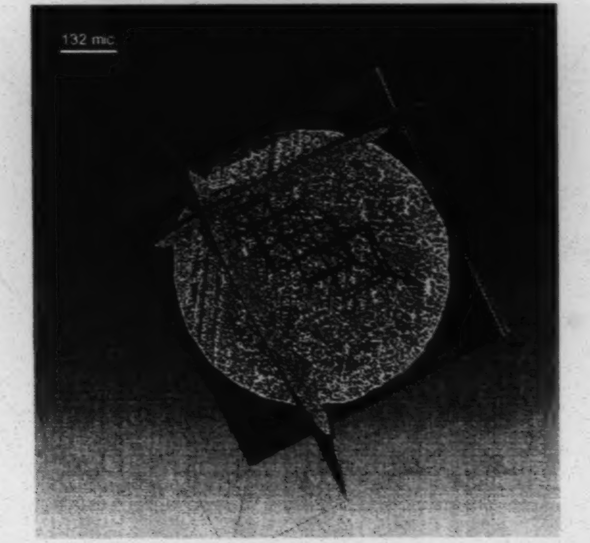

Figure 5.8: Porosity distribution calculation in a Al-4.3%Cu droplet. The calculation was done by calculating the porosity within a cube of side 50 μm. This cube was moved from the nucleation point towards the periphery along <111> direction.

5.5 Solidification of the atomized droplet

As the droplet falls through the stagnant gas atmosphere, it loses heat and begins to solidify. The Al reacts with the highly reactive O_2 in the atmosphere and forms a coating of Al_2O_3 at the droplet surface. The energy released from such a reaction makes the droplet surface hot. The bulk liquid is relatively colder and becomes the seat for the nucleation event to occur. The impurity present in the bulk results in heterogeneous nucleation at some undercooling. At this time the extent of undercooling in either Al-4.3%Cu or Al-17%Cu is not known and requires modeling work. Following nucleation there is a burst of solid growth. The extremely high growth rate results in Ultra-Fine structure. It is not clear whether the morphology is cellular or dendritic. This burst of initial growth results in some amount of solid fraction formed at a fast rate. As this solid fraction increases, because of the fast rate, recalescence sets in the droplet. As the temperature increases, the rate of growth decreases. At this time the morphology of the solid assumes the form of Primary Trunks growing in specific directions. This direction is controlled by the heat flow direction from the droplet. Such change in structure with undercooling has been reported by Kattamis et al [Kattamis1966]. Also, Cochrane et al [Cochrane1991] in their drop-tube experiments have even shown transition of microstructure within the same droplet. The Primary Trunks surround the initial growth of the solid. Note that some initial solid growth may take place during the early stages of recalescence before the temperature is high enough to cause the Primary Trunks to grow. The end of the Primary Trunk growth is marked by the end of recalescence. The volume of the recalescence is believed to depend on the dendrite growth rate, which is alloy composition dependent, other factors like nucleation undercooling being equal. After this point, the remaining liquid solidifies as secondary and tertiary growth from the Primary Trunk, probably in a Gulliver-Scheil type solidification path.

Coarsening also sets in, perhaps even during the early solid growth. Coarsening is alloy composition dependent and it also governs the final scale of the microstructure. In fact, the Ultra-Fine structure of Region I might also have coarsened. Porosity formation in the form of shrinkage cavity starts after the recalescence and its distribution is affected by the rate of dendrite growth and the volume of recalescence within the droplet.

5.6 Conclusions

Tomography technique is extremely promising because of the extra information obtained about solidification features. These were not possible with the conventional 2-D techniques. Tomography images showed microstructural details which point towards solidification phenomenon like nucleation, initial growth, recalescence, coarsening and porosity distribution. These are summarized below.

Based on the microstructure observed from the tomography images, evidence of nucleation site, initial growth and recalescence was seen. This nucleation site could be clearly seen and approximately located within the droplet. The nucleus did not move within the droplet. These were single nucleation sites and no evidence of multiple nucleation was found in any of the droplets.

Initial growth (Region I) and recalescence boundaries (Primary Trunks) were seen in all the droplets. It was possible to evaluate the volume fraction of these regions (Region I and Region II) in the droplets. There were differences in the volume fraction of these regions observed in the Al-4.3%Cu and Al-17%Cu. This was believed to be caused by the difference in growth rates between the two compositions for a given undercooling. This is based on dendrite models available in the literature.

It was shown that coarsening plays an important role in deciding the final scale of the microstructure. In general, Al-4.3%Cu showed a much coarser structure than the Al-17%Cu droplet and it was shown that Al-4.3%Cu would have higher coarsening than the Al-17%Cu. Coarsening probably starts during early solid growth.

Porosity distribution was different for the two alloys. The porosity distribution within the droplets could be explained by the amount of recalescence and dendritic growth rates. High growth rates during recalescence developed even distribution of porosity whereas lower growth rates but bigger recalescence volume segregated the porosity to one end of the droplet.

5.7 References

[Bardes1966]: “Dendritic arm spacing and solidification time in cast aluminum-copper alloy”, Bardes B.P. and Flemings M.C., Transactions of American Foundrymens’ Society, vol. 74, n. 2, 1966, pp 406-412.

[Cochrane1991]: “Grain refinement in drop-tube processed nickel based alloy”, Cochrane R.F., Herlach D.M. and Feuerbacher B., Materials Science and Engineering-A, vol. A133, n. 2, 1991, pp 706-710.

[DeHoff1968]: “Quantitative Microscopy”, DeHoff R.T. and Rhines F.N., 1st ed., McGraw-Hill Book Company, New York, 1968, pp 45-53.

[Flemings1981]: “Segregation and structure of rapidly solidified cast metals”, M.C. Flemings, Metallurgical Treatises, Metallurgical Society of AIME, 1981, pp 291-300.

[Henein2001]: “Single fluid atomization through the application of impulses to a melt”, Henein H., Materials Science and Engineering A, vol. 326, n. 1, 2001, pp 92-100.

[Horwath1962]: “Dendritic Growth”, Horwath J.A. and Mondolfo L.F., Acta Metallurgica, v. 10, 1962, pp 1037-1042.

[Howard1998]: “Unbiased Stereology: 3-Dimensional measurement in microscopy”, Howard C.V. and Reed M.G., BIOS Scientific Publishers Limited, Oxford, 1998, pp 39-44.

[Jones1983]: “Rapid Solidification of Metals and Alloys”, H. Jones, The Institution of Metallurgists, London, 1983, pp 77-81.

[Kattamis1966]: “Dendrite structure and grain size of undercooled melts”, Kattamis T.Z. and Flemings M.C., Transactions of AIME, vol. 236, n. 2, 1966, pp 1523-1532.

[Kurz2000]: “Fundamentals of Solidification”, Kurz W. and Fisher D.J., Trans Tech Publications, Switzerland, 2000, pp 257-259.

[Lipton1984]: “Dendritic growth into Undercooled Alloy Melts”, Lipton J., Glicksmann M.E. and Kurz W., Material Science and Engineering, 65, 1984, 57-63.

[Lipton1987a]: “Equiaxed Dendrite growth at small Supercooling”, Lipton J., Glicksmann M. E. and Kurz W., Metallurgical Transactions A, v. 18A, 1987, pp 341-345.

[Lipton1987b]: “Rapid Dendrite growth in Undercooled Alloys”, Lipton J., Kurz W. and Trivedi R., Acta Metallurgica, 35, n. 4, 1987, 957-964.

[Lipton1987c]: “Effect of growth rate dependant partition coefficient on the Dendrite growth in Undercooled Melts”, Lipton J., Kurz W. and Trivedi R., Acta Metallurgica, 35, n. 4, 1987, 965-970.

[MPIF09]: “MPIF09: Standard Test methods for Metal Powders and Powder Metallurgy Products”, Metal Powders Industries federation, 1992.

[Okamoto1975]: “Dendritic structure in unidirectionally solidified aluminum, tin, and zinc base binary alloys”, Okamoto T. and Kishitake K., Journal of Crystal Growth, vol. 29, 1975, pp 137-146.

[Prasad2002]: “A microsegregation model for studying rapidly solidified Impulse atomized Al-Cu droplet”, Prasad A., Henein H. and Gandin C-A., International Symposium of Light Metals, 2002, pp 101-114.

[Prasad2004]: “X-Ray Tomography study of atomized Al-Cu droplets”, Prasad A., Henein H., E. Maire and Gandin C-A., Canadian Metallurgical Quarterly, v. 43, n. 2, 2004, pp 273-282.

[Wiskel2002b]: “Solidification study of aluminum alloys using Impulse Atomization: Part II: Effect of cooling rate on microstructure”, Wiskel J.B., Navel K., Henein H. and Maire E., Canadian Metallurgical Quarterly, v. 41, n. 2, 2002, pp 193-204.

[Wu1987]: “Dendritic growth of undercooled Ni-Sn: Part I”, Wu Y., Piccone T.J., Shiohara Y. and Flemings M.C., Metallurgical Transactions A, vol. 18A, n. 2, 1987, pp 915-924.

Quantification of microsegregation during rapid solidification of Al-Cu powders[1]

6.1 Introduction

Conventional solidification processes of binary alloys follow a Scheil-Gulliver solidification path for the distribution of solute. The proportion of the primary pro-eutectic and eutectic that form during solidification as well as the solute content of these phases can be determined using the equilibrium phase diagram. However, during rapid solidification, the undercooling and/or high cooling rates attained by the liquid can result in a metastable situation for both the pro-eutectic phase as well as the eutectic solidification. Consequently, different microstructures can form which are not expected from the equilibrium diagram or the relative proportions of phases and their solute content will vary from the equilibrium state. Such deviations from equilibrium and formation of new microstructures are the motivation for rapid solidification processing. Reduced microsegregation and metastable extension of solute solubility are attractive features of rapid solidification processing. Microsegregation of the solute between the pro-eutectic phase and the liquid in rapid solidification processing can be studied in terms of the eutectic structures. The type and/or amount of eutectic is one measure of the extent of microsegregation under rapid solidification conditions. Wei et al have shown that coupled growth and divorced growth occurred in Co-Sb [Cao2000] and Co-Sn [Yao2002] systems, both produced from drop-tube experiments. Their results show that the nucleation undercooling during rapid solidification can affect the formation of eutectic. Sarreal et al [Sarreal1986] have shown a change in the amount of eutectic formed as cooling rates are varied in Al-Cu system. They studied Al-4.9%Cu alloy with cooling rates ranging from 10^{-1}-10^{4} K/s.

---

[1] In Press with Met. Trans. A as, "Quantification of microsegregation during rapid solidification of Al-Cu powders", Prasad A. et al. Reformatted according to the thesis requirements.

There is very little experimental data on the amounts of individual phases which constitute the eutectic under rapid solidification conditions. Such information can provide additional important information on solute distribution in rapid solidification processing such as strip casting. Some of the work done in this area has been limited to correlating eutectic morphology with the equilibrium amounts of individual phases constituting the eutectic [Scheil1954, Hunt1966, Croker1973, Dubey1982]. For the Al-Cu system, crystallographic growth characteristics of the eutectic phases [Chadwick1974a, Chadwick1974b], faceting behavior of $CuAl_2$ [Hamar1981] and morphological characterization [Mondolfo1965] have been reported.

In this work, we report a new technique to quantify the average solute solubility in the primary phase. The paper describes the average solute solubility studied as a function of cooling rate and alloy composition. Figure 6.1 shows the schematic of a cooling curve for a droplet solidified during atomization. The cooling rate is defined as the time required to solidify the droplet completely, starting from the solidification start temperature to the solidification end temperature; points A to E respectively in the figure. Points A-B represent the period of initial growth region and B-C is the recalescence, when the heat generated by crystal growth is greater than the heat loss to the surroundings. This results in an increase in droplet temperature. Points C-D is the Scheil-Gulliver type growth whereas D-E represents eutectic solidification.

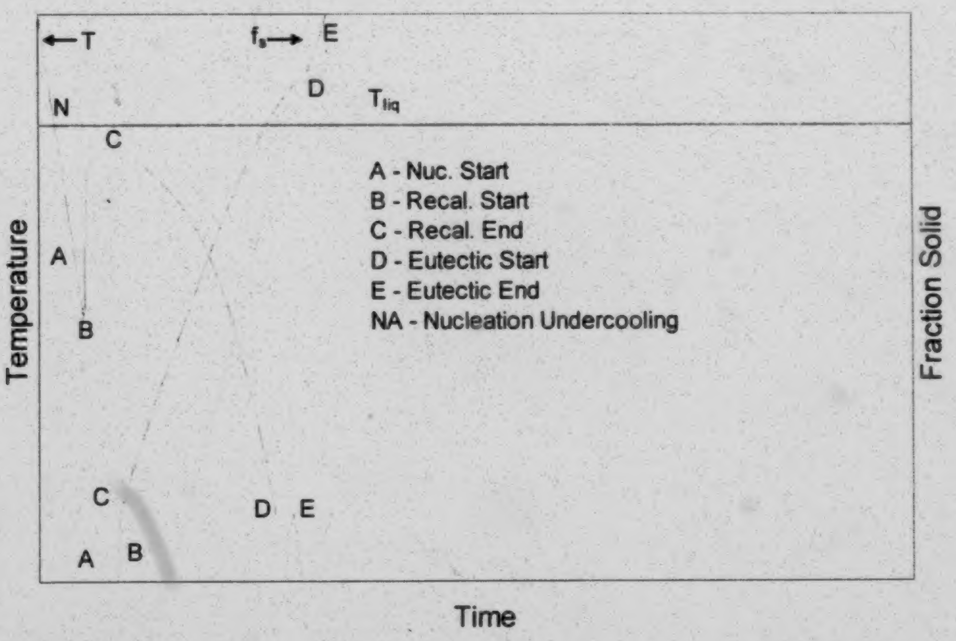

Figure 6.1: Schematic of the thermal history and fraction solid formed during the solidification of an atomized droplet.

The analysis presented here provides new knowledge to study the effect of metastability on the nucleation characteristics of the eutectic and microsegregation in Al-Cu system for Al-5%Cu, Al-10%Cu and Al-17%Cu compositions. The paper first presents the experimental generation of atomized Al-Cu powders. The characterization of the eutectic and the $CuAl_2$ portion of the eutectic are carried out using Neutron diffraction and microstructural examination in an SEM. Stereology calculations were done on SEM images of the atomized powders for volume percent eutectic information and the Rietveld analysis was used to determine the weight percent $CuAl_2$ in the powders. With this data the average Cu solubility in the primary α-Al phase is calculated.

6.2 Experiment and Results

Rapidly solidified samples were generated by atomizing Al-Cu alloys of different compositions (Al-5%Cu, Al-10%Cu and Al-17%Cu) under different gas atmospheres, N_2 and He. A single fluid atomization process, Impulse Atomization, was used to generate the powders. In this technique, which is a type of drop tower, atomization occurs when liquid metal is pushed through small orifices forming liquid jets which break up into small droplets by Rayleigh instability. The droplets lose heat to the stagnant gas and solidify as they fall through the atomization chamber. The details of the atomization experimental procedure is described in details elsewhere [Morin1996, Henein2001]. Briefly, however, the atomization run conditions were a melt temperature of 1120K for all alloy compositions atomized under He or N_2 gas. The solidified powders were collected at the bottom of the chamber and their composition was determined using the Inductively Coupled Plasma (ICP) mass spectroscopy technique. Following the chemical analysis, the powders were sieved into different size ranges according to MPIF standard 05 [MPIF92]. The droplets generated varied in size range from 100 to 1000 μm. The powders were then characterized using Neutron diffraction and stereology on SEM images. Table 6.1 shows the details of different alloy composition droplets atomized and characterized with Neutron diffraction and stereology. The details of the atomization process, particle size of samples used are also provided in the table.

6.2.1 Quantitative metallography

Quantitative microscopy is the procedure of quantifying the microstructural features. The quantifying technique used is called stereology. It consists of a set of equations wherefrom 3-D information can be obtained from 2-D images [DeHoff1968, Howard1998]. One of the basic equations of stereology is given by the following [DeHoff1968],

$$V_V = A_A = L_L = \overline{P}_P \tag{6.1}$$

where the letters and subscripts are volume, area, line intercept and point count of a feature of interest. Eqn. 6.1 states that the volume fraction of the feature of interest can be obtained by either doing the Volume Fraction calculation, Area Fraction calculation, Lineal analysis or Point Count analysis. In our case, the volume percent eutectic in the atomized powders was measured by doing a manual Point Count analysis on the eutectic areas on SEM images of Al-5%Cu, Al-10%Cu and Al-17

%Cu droplets of different sizes obtained by atomizing under different gas conditions.

Table 6.1: Summary of alloy compositions and droplet sizes for atomization, neutron diffraction and stereology experiments.

Atom. Run #	Gas Type	Holes & Nozzle dia.	Composition	Droplet Size (μm)
020313	He	37, 250 (μm)	4.98	196
020313	He	37, 250 (μm)	4.98	925
020315	N_2	37, 250 (μm)	4.92	196
020315	N_2	37, 250 (μm)	4.92	925
021029	He	37, 250 (μm)	10	196
021029	He	37, 250 (μm)	10	925
020320*	N_2	37, 250 (μm)	9.96	196
020320	N_2	37, 250 (μm)	9.96	234
020320	N_2	37, 250 (μm)	9.96	925
021024	He	37, 250 (μm)	16.8	196
021024	He	37, 250 (μm)	16.8	925
021021*	N_2	37, 250 (μm)	16.8	196
021021	N_2	37, 250 (μm)	16.8	234
021021	N_2	37, 250 (μm)	16.8	780
021021*	N_2	37, 250 (μm)	16.8	925

*** - Not tested by neutron diffraction**

The experimental procedure to obtain stereological data requires that unbiased random samples be selected. An unbiased random sample is that which is representative of the entire set of product and each sample (individual droplet in a set in our case) has an equal probability of being selected for stereological analysis. Here, the product is the atomized powders and we define a 'set' as a representative sample of droplets of specific size range atomized under specific gas type. The powders of a given size range of interest were mounted in epoxy and polished. The mounting and polishing was carried out using standard metallographic preparation techniques. The samples were not etched. The polished samples were placed in the SEM and viewed at the lowest magnification (so that details of local areas were not visible). The stage was randomly moved along the X and Y axes. The magnification was increased at this point and an image was taken of a random section of a random droplet. Statistics require that at least 30 data points be taken [Ott1985]. Therefore, 31-40 SEM images were taken for a given set of droplets. Note that the number of images correspond to the number of different droplets from the set. Stereological grid of 15mm spacing was placed randomly on the magnified pictures of these images. Typically, the linear magnification was such that the grid spacing of 15 mm translated to 2.5 – 3.0 μm. The grid was obtained from Agar Scientific and the grid number was G2802. The grid was randomly placed on the image photograph and points falling in the eutectic region were counted manually. Each point falling within the eutectic region was taken as 1 whereas each point falling on the boundary of eutectic and α-Al dendrite was taken as 0.5. Based on this, the volume percent eutectic is calculated as,

$$\hat{v}_e = \overline{P}_p = \frac{n_e + 0.5n_b}{n_t} * 100 \qquad (6.2)$$

Here, n_e, n_b and n_t are the number of points falling within the eutectic region, on the eutectic-dendrite boundary and total number of grid points on the image, respectively. The volume percent eutectic data thus obtained is denoted by $\hat{v}_e$. Since the set is an unbiased representation of the population, the eutectic percent obtained represents the average of the sample and is also known as Estimated True Mean.

The volume percent eutectic, $\hat{v}_e$, is plotted as a function of droplet size and alloy composition in Figure 6.2. The error bars indicate the standard deviation of the data. Figure 6.2a shows the volume percent eutectic as a function of droplet size for droplets atomized under both He and N_2 gas. Gas type and size determine the cooling rate of the droplets. For example, Wiskel et al [Wiskel2002b] have shown that droplets of a given size range atomized under He gives faster cooling rates as compared to droplets of the same size range atomized under N_2. Likewise, for a given gas type smaller droplets have faster cooling rates. Based on this, it can be seen that the cooling rate does not have significant effect on volume percent eutectic. Figure 6.2b shows the volume percent eutectic data as a function of composition. For any given composition, all the data for different size and gas are shown together along with Equilibrium and Scheil-Gulliver predictions. The Equilibrium and Scheil-Gulliver calculations were based on Lever Rule & Scheil-

Gulliver model respectively, applied to the equilibrium phase diagram. The volume percent eutectic is always below the Scheil-Gulliver line for all compositions and shows a steady decrease as the composition is increased. With respect to the Equilibrium line, low Cu composition (i.e. Al-5%Cu) shows more volume percent eutectic while the reverse holds for the larger Cu composition (i.e. Al-17%Cu). It appears that the intermediate Cu composition (i.e. 10wt%Cu) is in agreement with the Equilibrium line. This does not mean that the solidification in the Al-10%Cu occurs at equilibrium. Rather that the total effects of solidification and microsegregation events result in a volume percent eutectic coincident with the equilibrium value.

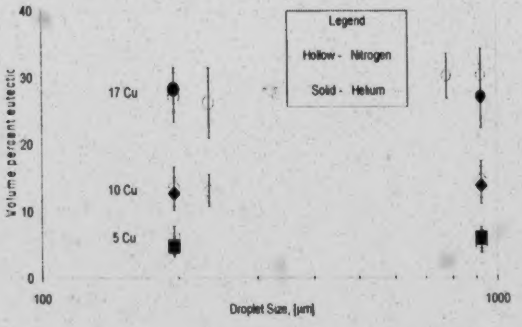

(a)

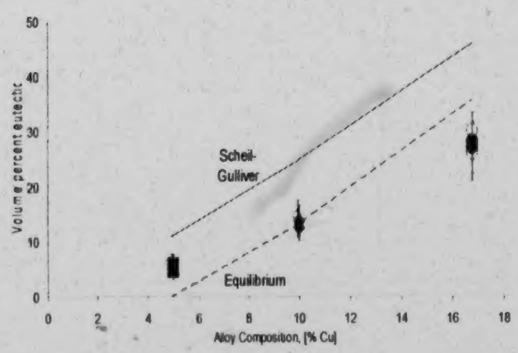

(b)

Figure 6.2: Volume percent of eutectic for droplets of different (a) sizes and (b) compositions obtained from Stereology.

6.2.2 Neutron diffraction (ND)

The ND experiments were carried out at the Atomic Energy of Canada Limited (AECL), Chalk River facilities using a collimated neutron beam of 1.33 A^0 wavelength. The neutron diffraction experiment in our case was used for phase identification and phase fraction analysis using Rietveld analysis using GSAS [Dreele1994]. Table 6.1 shows the alloy composition, gas type and droplet size for which Neutron diffraction experiments were performed. The samples were as atomized and were randomly chosen to form a droplet set. Each set consisted of 1-2 gm of powders. The ND results, therefore, give the sample (as opposed to population mean) mean value of the weight percent $CuAl_2$. This is denoted as, $\hat{w}_{CuAl_2}$. Figure 6.3a shows this weight fraction $CuAl_2$ as a function of droplet size. The droplets were atomized under the two different gases. The error bars represent the range of lattice parameters predicted by the Rietveld refinement method. This is called the Estimated Standard Deviation (ESD), [Young2000], since this calculation is based on peak height, peak width, intensity count etc. in the diffraction pattern. The result follows the same trend as volume percent eutectic data plots. A relatively large error bar is observed for the Al-17%Cu, however, the top of the error bars are still below the Equilibrium curve. Thus the trend observed for volume percent eutectic is maintained in the weight percent $CuAl_2$ results. For all the three compositions, the change in droplet size or gas type does not show any significant change in the amount of $CuAl_2$. The $CuAl_2$ weight percent is also plotted against the alloy composition in Figure 6.3b. For any given composition, all the data for different droplet size and gas are shown together. Also shown are Equilibrium and Scheil-Gulliver values for the respective compositions. There is a steady decrease in the amount of $CuAl_2$ below the equilibrium line as the alloy composition increases.

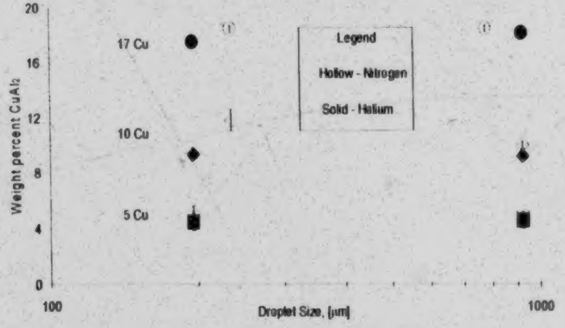

(a)

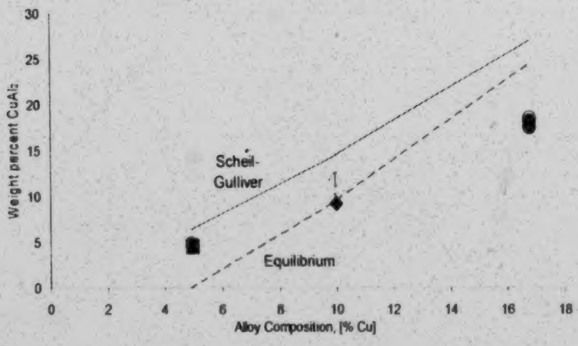

(b)

Figure 6.3: Weight percent of $CuAl_2$ for droplets of different (a) sizes and (b) compositions obtained from ND experiments. The error bars are the estimated standard deviation which comes from the Rietveld analysis used for phase quantification.

The plots of volume percent eutectic and weight percent $CuAl_2$ versus droplet size (Figures 6.2a and 6.3a respectively) show that, with the given range of cooling rates (droplet size and gas type), there is no significant change in microsegregation in the droplets for all compositions. Though there seems to be a tendency for more segregation in He gas (higher cooling rate). On the other hand, the plots as a function of composition (Figures 6.2b and 6.3b respectively) show a significant change. Scheil-Gulliver solidification predicts maximum segregation and the data points lie below the Scheil-Gulliver line. But the severity of segregation decreases dramatically as the alloy composition increases from 5%Cu to 17%Cu, with data points falling even below the Equilibrium value for 17%Cu. Since eutectic is formed by nucleation and growth of $CuAl_2$, therefore the formation of eutectic is determined by the concentration of solute available in the remaining liquid for the second phase nucleation. Therefore, to better interpret the eutectic amounts in the atomized droplets, as measured in SEM and Neutron data, we have attempted to calculate the average solute solubility in the primary phase. This is described next.

6.3 Mathematical formulation

This section describes the derivation for calculating the average solute solubility of primary α-Al in the rapidly solidified droplets. We have defined the average solute solubility as the total amount of solute (Cu) in the primary phase α-Al_P divided by the weight fraction of the primary phase. Therefore, the model derivation is based on calculating the weight fraction of primary phase and Cu content in the primary phase from known quantities. The known quantities are the alloy composition, volume percent eutectic (stereology on SEM images) and weight percent $CuAl_2$ (neutron diffraction).

Using the definition of weight fraction, we get the following equation for weight percent primary alpha,

$$w_{\alpha_P} = \frac{W_{\alpha_P}}{W_{\alpha_P} + W_{\alpha_E} + W_{CuAl_2}} * 100 \qquad (6.3)$$

where $\hat{w}_{\alpha_P}$ is the weight percent primary α-Al, $\hat{W}_{\alpha_P}$ is the weight of primary α-Al, $\hat{W}_{\alpha_E}$ is the weight of α-Al in the eutectic and $\hat{W}_{\alpha_{CuAl_2}}$ is the weight of $CuAl_2$. Converting the weights of phases into their respective volume, Eqn. 6.3 can be rewritten as

$$w_{\alpha_P} = \frac{v_{\alpha_P}\rho_\alpha}{v_{\alpha_P}\rho_\alpha + v_{\alpha_E}\rho_\alpha + v_{CuAl_2}\rho_{CuAl_2}} * 100 \qquad (6.4)$$

here v_{α_P} is the volume percent primary phase, v_{α_E} is the volume percent α in the eutectic and v_{CuAl_2} is the volume percent of $CuAl_2$. Note that the terms v_{α_P} etc have been described as "volume percent" and not "actual volume". This does not affect the results, since dividing the numerator and the denominator by the actual volume (whatever that number may be) changes "actual volume" of constituents into "percent (or fraction) volume". The ρ term is the density of the respective phases. The densities of primary α-Al and eutectic α-Al are assumed to be the same and are given by ρ_α. The value was taken to be 2800 kg/m^3 [Smithells1998]. This takes into account the dissolution of Cu in the α-Al. The density of $CuAl_2$ was taken as 4340 kg/m^3 [Conlon2000]. Eqn. 6.4 has the volume terms as unknown. To calculate these terms, a global volume balance equation and a volume balance equation for the eutectic percent is used along with the definition of volume percent of a constituent for $CuAl_2$. The global volume balance equation for the droplet set is given as,

$$v_{\alpha_P} = 100 - v_E \tag{6.5}$$

where v_E is the percentage volume eutectic obtained from stereology on SEM images and v_{α_P} is the volume percent primary α-Al. This equation states that the droplet is composed of eutectic and primary α-Al. Likewise, since eutectic is composed of $CuAl_2$ and α-Al, the volume percent eutectic can be expressed as,

$$v_E = v_{\alpha_E} + v_{CuAl_2} \tag{6.6}$$

Once again, the choice of dividing the right hand and left hand side of the equation by the actual volume permits us to write Eqn. 6.6 in terms of volume percent. The volume percent of $CuAl_2$ is evaluated using the definition of volume of a constituent. This is given as,

$$v_{CuAl_2} = \frac{\dfrac{\hat{w}_{CuAl_2}}{\rho_{CuAl_2}}}{\dfrac{\hat{w}_{CuAl_2}}{\rho_{CuAl_2}} + \dfrac{w_{\alpha_P} + w_{\alpha_E}}{\rho_\alpha}} * 100 \tag{6.7}$$

Dividing the numerator and denominator of Eqn. 6.7 by $\frac{\hat{w}_{CuAl_2}}{\rho_{CuAl_2}}$ and recognizing the global mass balance equation,

$$w_{\alpha_E} + w_{\alpha_P} + \hat{w}_{CuAl_2} = 100 \tag{6.8}$$

the volume percent $CuAl_2$ can be rewritten as,

$$v_{CuAl_2} = \frac{100}{1 + \left(\frac{100}{\hat{w}_{CuAl_2}} - 1 \right) * \frac{\rho_{CuAl_2}}{\rho_{\alpha}}} \tag{6.9}$$

v_{CuAl_2} can be evaluated now from the Neutron diffraction results for $\hat{w}_{CuAl_2}$ and the density values of ρ_α and ρ_{CuAl2} [Conlon2000]. The volume percent $CuAl_2$ is used in Eqn. 6.6 to calculate v_{α_E}. v_{α_P} is calculated using Eqn. 6.5. Substituting these values in Eqn. 6.4 gives the weight percent primary α-Al, w_{α_P}. Note that from the weight percent primary alpha, the weight percent eutectic can be determined from global weight balance (Eqn. 6.8). Furthermore, the weight percent of eutectic α-Al is calculated from the following equation,

$$w_{\alpha_E} + \hat{w}_{CuAl_2} = w_E \tag{6.10}$$

6.3.1 Average Cu content in primary phase

From the calculated weight percent of the different phases, the amount of Cu in each phase can now be determined. The mass balance for Cu in the alloy is used for this calculation.

$$\overline{C}_0 = Cu_{\alpha_P} w_{\alpha_P} + Cu_{\alpha_E} w_{\alpha_E} + Cu_{CuAl_2} w_{CuAl_2} \tag{6.11}$$

where $\overline{C}_0$ is the original alloy composition obtained from ICP technique, and Cu with different subscripts denotes percent Cu in each phase. As the eutectic reaction approaches, it is likely that there would be some undercooling [Takeshita1986] associated with it. Depending upon the degree of undercooling and subsequent growth rate of the eutectic recalescence might also be possible. Because of lack of information on these issues, we have assumed that the eutectic takes place at the equilibrium temperature. With this assumption, the Cu_{CuAl2} and $Cu_{\alpha E}$ can be obtained from the Al-Cu phase diagram. Using the weight percent of different phases from earlier calculations, the Cu content in eutectic α-Al and $CuAl_2$ from the phase diagram, Eqn. 6.11 can be used for calculating the Cu in primary α-Al. The average Cu in the primary phase or the Cu solubility in the primary phase is now given as,

$$\overline{C}_{\alpha_P} = \frac{Cu_{\alpha_P}}{w_{\alpha_P}} \tag{6.12}$$

6.4 Results

The results for weight percent eutectic as a function of droplet size obtained from the derivation are shown in Figure 6.4a, and as a function of alloy composition in Figure 6.4b. The trend follows the same as volume percent eutectic and weight percent $CuAl_2$ (Figures 6.2 and 6.3). The Al-5%Cu shows eutectic values between Gulliver-Scheil and Equilibrium amounts and as the composition is increased, the eutectic amount decreases. For Al-17%Cu, the amount of eutectic goes below the equilibrium line. Furthermore, there is no significant effect of cooling rates on the eutectic amount.

The volume percent eutectic, weight percent $CuAl_2$ and weight percent eutectic data shows that lesser amount of eutectic is formed as the alloy composition is increased. Figure 6.5 shows a typical eutectic structure seen in the droplets. The figure is for an Al-17%Cu droplet, but Al-10%Cu and Al-5%Cu droplets also show similar structures of regular lamellae.

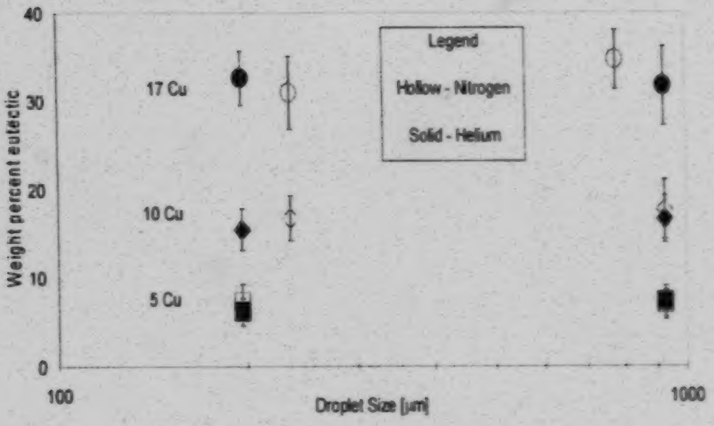

(a)

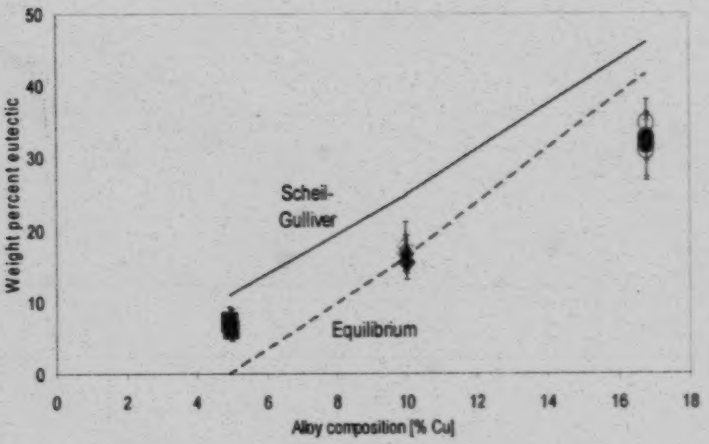

(b)

Figure 6.4: Weight percent of eutectic for droplets of different (a) sizes and (b) compositions. The weight percent was obtained by using volume percent eutectic and weight percent $CuAl_2$.

micrometers

Figure 6.5: Figure showing the eutectic structure with a halo in an Al-17%Cu, 850–710 μm droplet, atomized in N_2 *(Run no. 021021). The halo is the light band surrounding the primary phase and is an evidence of eutectic undercooling.*

Such eutectics are formed when one of the phases nucleate on the other and grow. In Al-Cu system, the $CuAl_2$ nucleates on the primary phase dendrites of α-Al. The similar regular eutectic structure for different droplet sizes, gas types and alloy composition suggests that the eutectic mechanism has not changed with either alloy composition or cooling rate. Also, using the weight percent of eutectic and $CuAl_2$ phase in the eutectic, the ratio of weight percent $CuAl_2$ and weight percent eutectic was calculated. This is shown in Figure 6.6. There is a steady decrease in the amount of $CuAl_2$ in the eutectic as the alloy composition is increased. The lower amount of $CuAl_2$ indicates lesser Cu available to form $CuAl_2$ phase.

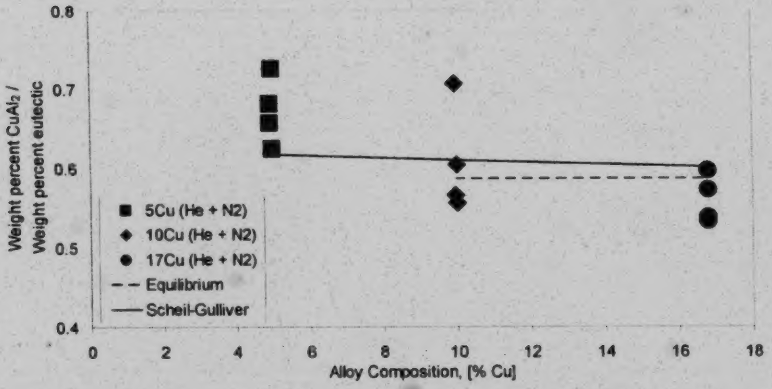

Figure 6.6: Ratio of weight percent $CuAl_2$ and weight percent eutectic plotted as a function of droplet composition. The amount of $CuAl_2$ in the eutectic decreases steadily as the alloy composition is increased.

The Cu content in the alpha phase is shown as total Cu in the primary phase as well as an average Cu in the primary phase. The average Cu in the α-Al is also the average solute solubility of Cu in the primary α. To see the effect of alloy composition on Cu content of primary alpha, the total Cu and solute solubility are plotted as a function of alloy composition. These are shown in Figures 6.7 and 6.8 for total Cu and average solute solubility, respectively.

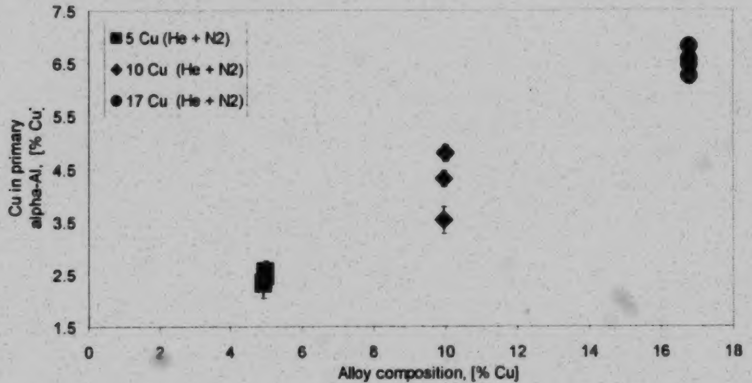

Figure 6.7: Total Cu content in the primary phase plotted for droplets of the three alloy compositions.

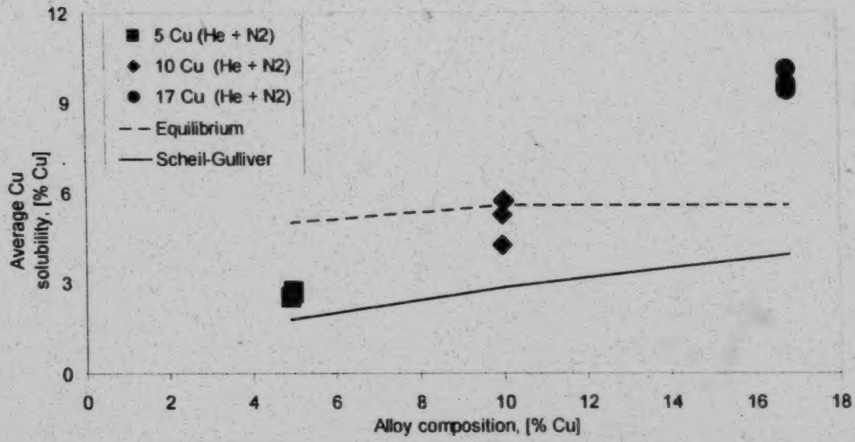

Figure 6.8: Cu solubility in the primary phase plotted for droplets of the three alloy compositions. The strong effect of alloy composition in the solubility is clearly seen.

The data for different gas types and droplet sizes for a given alloy composition are plotted together. The error bars are also plotted in the data, but the error bars are small compared to the size of the data points and are not clearly visible. From the figures, as the alloy composition is increased from Al-5%Cu to Al-17%Cu, the Cu content in the primary phase increases steadily. This increase is much more than the changes seen in Cu in the primary phase when gas type and/or droplet sizes are changed. Thus, there seems to be some effect of alloy composition on solute solubility in the primary phase. This will be further discussed in the next section. Also, with respect to the Scheil-Gulliver predictions, the droplets show higher solute solubility. This deviation further increases as the alloy composition is increased from Al-5%Cu to Al-17%Cu.

The data points in Figure 6.8 show the value of the average Cu solubility in the primary phase along with the error bars. For purposes of clarity, the size of the data points used in the figure are big and the error bars are not visible. The data is shown for two different droplet sizes and the two gas types for all the alloy compositions. This permits one to see the effect of gas type and droplet size more closely. Droplets atomized under He gas always have more Cu content compared to the droplets atomized under N_2 gas. The difference is small and is seen for all the three alloy compositions. Therefore, it might seem that there is a small effect of gas type on the amount of Cu the primary phase can hold. Within a particular gas type (He or N_2), as the droplet size is changed, there seems to be some difference in the Cu content of the primary phase as well.

The error bars were calculated by taking 1 S.D. variance in the volume percent eutectic and weight percent $CuAl_2$ data. The numerical values of the mean and standard deviation values plotted in the figure show that error bars are large enough to cause an overlap between the values plotted for different gas types and droplet sizes. Since statistically, the data can vary from the upper to lower error bar limits, the variations in Cu content in the primary phase with gas type and droplet size is smaller than the error associated with the measurements of the data. This is especially true for Al-5%Cu and Al-17%Cu droplets. Therefore, there may seems to be an effect of cooling rate (gas type and droplet size) on the Cu content in the primary phase, but using the experimental techniques utilized in this work the trend is not definitive.

6.5 Discussion

6.5.1 Solute solubility

Calculated Cu content values represent the average solute content of the primary phase from the start of solidification to the onset of the eutectic reaction. Figure 6.8 shows that as the alloy composition is increased the average solute solubility in the primary phase also increases. Baker and Cahn [Baker1971] have thermodynamically shown that at undercooled temperatures a range of solid compositions can form from a liquid of given composition. This depends on the dendrite growth rate conditions at the time of solidification.

In our X-ray tomography work on atomized samples, we have quantified the volume of recalescence in Al-5%Cu and Al-17%Cu droplets [Prasad2004]. The Al17-%Cu droplet has 1.5-2 times more recalescence volume than Al-5%Cu droplets (34% in 17Cu as compared to 20% in 5Cu). With sufficiently high growth rates following nucleation at some undercooling, it is likely that diffusionless transformation takes place during this initial growth and recalescence regime. Such diffusionless transformations can result in higher solute content of the primary phase formed. Remelting of primary phase formed during recalescence with increased solute content would in turn increases the amount of solute in the liquid. Such dendrite remelting has been predicted by a non-isothermal atomization droplet developed by Heringer et al [Heringer2004]. A higher degree of remelting in Al-5%Cu would result in lower amount of Cu content in the Al-5%Cu primary phase.

For a given amount of nucleation undercooling, Al-5%Cu would have faster growth rates than Al-17%Cu [Lipton1987b] and therefore a higher degree of remelting is indeed feasible in a 5Cu droplet. Moreover, Al-17%Cu droplets also have 5-6 times more eutectic volume as compared to Al-5%Cu droplets, reported earlier in this paper. Therefore, the post-recalescence solidification regime between recalescence and eutectic, which takes place at near-equilibrium Scheil-Gulliver condition, is much smaller in Al-17%Cu compared to Al-5%Cu. During the Scheil-Gulliver regime, the primary solid will form following equilibrium conditions and therefore the dendrites that will form will have a different Cu content as compared to the α-Al that forms during initial growth and recalescence. Since coarsening tends to push the system towards homogenous chemical redistribution, the coarsening phenomena would try to chemically equilibriate the dendrites formed during initial growth plus recalescence and Scheil-Gulliver regime. Thus any metastability caused during recalescence will tend to be reduced. The coarsening depends on the thermal energy and chemical potential for the Cu to diffuse. We have shown in our earlier work [Prasad2004] that there is more coarsening in Al-5%Cu than in Al-17 %Cu. Also, the post-recalescence regime gets smaller with Al-17%Cu and thus further reduces the chances of chemical homogeneity. Based on the above, a combination of higher amount of dendrite remelting and coarsening in the Al-5%Cu droplets tends to lower the Cu content in the primary phase in Al-5%Cu as compared to a Al-17%Cu droplet in Al-17%Cu.

Note that it is very likely that eutectic undercooling is present as well. This phenomenon would also tend to increase the amount of primary phase, the amount of total Cu in the primary phase and eventually lesser amount of eutectic. With lack of experimental data, the degree of undercooling could not be determined from the present set of experiments. However, based on Mondolfo's arguments [Mondolfo1965], the presence of a halo (thin white line) around primary phase dendrites indicates eutectic undercooling. Evidence of eutectic undercooling is seen by the presence of such a halo in the lamellar eutectic of Al-17%Cu as shown in Figure 6.5.

Solid state diffusion can also lead to reduction in amount of $CuAl_2$ and eutectic. But with the cooling rates involved, the solid diffusion is expected to be very limited and is overshadowed by the solute trapping and eutectic undercooling effects. Sarreal et al have shown that in the cooling rates ranging from 10^{-1}-10^{4} K/s, the amount of $CuAl_2$ first increases, goes through a maximum and then decreases again. They have explained the results in terms of solid state diffusion for lower range of cooling rates (up to 200 K/s) and dendrite tip undercooling and eutectic undercooling for higher cooling rates.

To get an estimate of the cooling rates of the atomized droplets, we have used a microsegregation model for the droplet solidified during atomization. The details of this model will be published in a forthcoming article. The simulation was run for all the three compositions. The model predicts cooling rates of the order of

75-3200 K/s for the droplet size range of interest. At such high cooling rates, the effect of solid state diffusion would be negligible.

6.6 Conclusions

We have introduced a simple mathematical model based on mass balance and volume conservation equations to study microsegregation (weight percent eutectic) and solute solubility in the primary phase in rapidly solidified Al-Cu alloys. Al-Cu droplets of three different compositions were atomized under different gases. Microsegregation in these droplets was studied by using Neutron diffraction and stereology. Diffraction experiments gave weight percent $CuAl_2$ data whereas stereology analysis on SEM image, gave volume percent eutectic data. The volume percent eutectic, weight percent $CuAl_2$ and weight percent eutectic showed a steady decrease with respect to Equilibrium and Scheil-Gulliver values when the alloy composition was increased. The droplet size and gas type did not show a significant change in these values.

Using the model formulations, the average primary phase solute solubility could be calculated as a function of alloy composition, gas type and droplet size. The droplets showed an increase in solute solubility as the alloy composition was increased. Also, these effects are more significant with compositional changes in the alloy than with cooling rate changes. The increase in solute solubility and a subsequent decrease in microsegregation can be a result of diffusionless transformation and phenomena like solute trapping may be responsible for the metastability. The metastability can occur during initial growth and recalescence and can result in diffusionless solidification in all alloy compositions. However, it is believed that dendrite remelting and coarsening tends to negate this effect. These phenomena are much more effective in lower alloy composition as compared to alloys with higher solute content.

6.7 References

[Baker1971]:	"Solidification", Baker J.C. and Cahn J.W., American Society for Metals, Pennsylvania, 1971, pp 23-56.
[Cao2000]:	"Microstructural characterization of Co–Sb eutectic alloy droplets solidified in drop tube", Cao C.D., Xie, W.J. and Wei B., Materials Science and Engineering A, v. 283A, 2000, pp 86-93.
[Chadwick1974a]:	"The growth crystallography of unidirectionally solidified Al-Al/sub 3/Ni and Al-Al/sub 2/Cu eutectics", Chadwick G.A. and Cantor B., Journal of crystal growth, v. 23, 1974, pp 12-20.
[Chadwick1974b]:	"Crystallography of Al-Al/sub 3/Ni, Al-Al/sub 2/Cu and Al-zeta (AlAg) eutectics during nucleation and the early stages of growth", Chadwick G.A. and Cantor B., Journal of Crystal growth, v. 30, 1974, pp 101-108.

[Conlon2000]: “Processing and microstructural characterization of Al-Cu alloys produced from rapidly solidified powders”, Conlon K.T., Maire E., Wilkinson D.S. and Henein H., Metallurgical and Materials Transactions, v. 31A, 2000, pp 249-260.

[Croker1973]: “The characteristics of eutectic structures”, Croker M.N., Fidler R.S. and Smith R.W., Proceedings of the Royal Society of London, vol. 335, n. 1600, 1973, pp 15-37.

[DeHoff1968]: “Quantitative Microscopy”, DeHoff R.T. and Rhines F. N., McGraw-Hill Book Company, New York, 1968, pp 50.

[Dreele1994]: “Neutron Diffraction in Materials Science and Technology: A comprehensive treatment”, Von Dreele R.B., v 2B, Wiley-VCH, New York, 1994, pp 562-610.

[Dubey1992]: “Characterization of eutectic microstructures”, Dubey K.S. and Ramachandrarao P., Scripta Metallurgica, v. 26, 1992, pp 709-710.

[Hamar1981]: “Facetting behaviour of Al_2Cu during solidification”, Hamar R. and Lemaignan C., Journal of Crystal growth, v. 53, 1981, pp 586-590.

[Henein2001]: “Single fluid atomization through the application of impulses to a melt”, Henein H., Materials Science and Engineering A, vol. 326, n. 1, 2001, pp 92-100.

[Heringer2004]: “Modélisation de la solidification de gouttes atomisées, Heringer R., Ph. D. Thesis, Institut National Polytechnique de Lorraine, Nancy, France, 2004.

[Hunt1966]: “Binary eutectic solidification”, Hunt J.D. and Jackson K.A., Transactions of the Metallurgical Society of AIME, vol. 236, 1966, pp 843-852.

[Lipton1987b]: “Rapid Dendrite growth in Undercooled Alloys”, Lipton J., Kurz W. and Trivedi R., Acta Metallurgica, 35, n. 4, 1987, 957-964.

[Mondolfo1965]: “Nucleation in eutectic alloys”, Mondolfo L.F., The Journal of the Australian Institute of Metals, vol. 10, n. 2, 1965, pp 169-177.

[Morin1996]: “The Impulse Atomization Process: an economical and flexible process for producing powders with a tailored size distribution”, Morin L.C., Reider M., Meja J. and Henein H., Proceedings of the Int. Symposium on Light Metals 1996, Metallurgical Society of CIM, Montreal, pp. 293-304.

[MPIF92]: “MPIF92.: Standard test methods for Metal Powders and Powder Metallurgy Products”, Metal Powder Industries Federation, 1992.

[Ott1985]: “Understanding Statistics”, Ott L.R. and Mendenhall W., PWS-Kent Publishing Co., Boston, 1985.

[Prasad2004]: “X-Ray Tomography study of atomized Al-Cu droplets”, Prasad A., Henein H., Maire E., and Gandin Ch-A., Canadian Metallurgical Quarterly, vol. 43, n. 2, 2004, pp 273-282.

[Sarreal1986]: “Effect of solidification rate on microsegregation”, Sarreal J.A. and Abbaschian G.J., Metallurgical Transactions A, vol. 17A, 1986, pp 2063-2073.

[Scheil1942]: “Bemerkungen zur Schichtkristallbildung”, Scheil E., Zeitschrift fur Metallkunde, vol. 236, 1942, pp 70-72.

[Smithells1998]: “Smithells metals reference book”, Brandes E.A. and Brooks, G.B. (eds.), Butterworths-Heinemann, London, 1998, pp 14(1)-14(14).

[Takeshita1986]: “The undercooling attainable by the rapid quenching of Al-$CuAl_2$ eutectic alloy melt”, Takeshita K. and Shingu P. H., Transactions of the Japan Institute of Metals, v. 27, n. 3, 1986, pp 180-186.

[Wiskel2002b]: “Solidification study of aluminum alloys using Impulse Atomization: Part II: Effect of cooling rate on microstructure”, Wiskel J.B., Navel K., Henein H. and Maire E., Canadian Metallurgical Quarterly, v. 41, n. 2, 2002, pp 193-204.

[Yao2002]: “Rapid solidification of highly undercooled Co-30wt%Sn alloy”, Yao Y.J., Wang N. and Wei B., Journal of Materials Science Letters, vol. 21, 2002, pp 357-360.

[Young2000]: “The Rietveld Method”, Young R.A. (ed.), International Union of Crystallography, Oxford University Press, New York, 2000, pp 21-28.

Chapter 7

Solidification modeling of Al-Cu Impulse Atomized droplets

7.1 Introduction

The object of this thesis was to study microsegregation for rapid solidification under unconstrained growth conditions with changing alloy chemistry. A combination of experiments and modeling was proposed to achieve this objective. The experimental details and results have been provided in previous chapters (Chapters 3-6). This chapter is devoted to the modeling aspect. The model was developed to predict the microsegregation under unconstrained rapid solidification conditions and to test the theories pertaining to microsegregation, specifically, the dendrite velocity. The theories tested involve the dendrite kinetics and its role in microsegregation through diffusionless transformation (solute drag or solute trapping). These tests are performed by developing a solidification model, which takes into account dendrite kinetics. The experimental results are then used to validate this model. The validation is performed by first establishing the user-defined variables: the nucleation undercooling, nucleation site position and the droplet size. The results from the X-Ray tomography are used to establish the nucleation undercooling achieved. The undercooling is then used in the model to do sensitivity analysis of other variables. Following this analysis, the microsegregation results from neutron diffraction and stereology experiments in terms of weight fraction eutectic are compared with the model results. Subsequently, diffusionless solidification theories are assessed with respect to dendrite velocities and the role of dendrite velocity in microsegregation. The model development is described in this chapter, and the model validation and subsequent analyses are presented in Chapter 8.

A solidification model for Impulse Atomization process was first developed by Ding et al [Ding1997]. The model was developed to generate a thermal history of the droplets by solving the heat balance equation. The heat loss due to convective heat transfer was evaluated using the Whitaker correlation, while a power-law was used to calculate the growth rate of the interface for evaluating the latent heat release. Wiskel et al [Wiskel2002a] later modified the calculations for the Whitaker correlation for the convective heat transfer coefficient. The present work continues this work further, and a microsegregation model for the solidification of the droplets generated by Impulse Atomization is proposed here.

The microsegregation was calculated using the Rappaz-Thevoz (R-T) model [Rappaz1987a, b]. The Rappaz-Thevoz (R-T) model was originally developed for calculating the microsegregation within a spherical grain in a casting with one nucleation site at the center [Rappaz1987a, b]. However, with the help of X-Ray tomography results [Prasad2004, Prasad2005] for Al-Cu droplets, it was shown that a single nucleation event occurs off-center towards the droplet periphery. The tomography results also confirmed that no multiple nucleation events had occurred. The approximate location of this nucleation site was also measured. Therefore, the present model was modified to accommodate off-center nucleation, and the LKT model [Lipton1987b, c] was included for dendrite kinetic formulations to replace the power-law in the previous work.

For the off-center nucleation modification, a geometrical function was developed that enabled the nucleation site within the droplet to be defined anywhere between its center and surface. This chapter describes the complete model development to study the solidification behavior of the droplets produced from Impulse Atomization. Starting with a user-defined off-center nucleation site and initial undercooling for the nucleation of the primary phase, the model simulation predicts the thermal history, fraction solidification and microsegregation in the droplet as a function of time. The simulation results are compared with the experimental results, and this comparison forms the basis for understanding the solidification path of the atomized droplets. This topic is discussed in the next chapter.

7.2 Model formulation

The model is described in two steps. In the first step, the relevant equations are developed to track the thermal history, fraction solid formation and microsegregation in the atomized droplet as a function of time. The thermal history requires formulating the heat balance equation and the expressions for solving various terms in the equation. The fraction solid formation and microsegregation require knowledge of dendrite kinetics. These constitute the relevant equations in the model. In the second step, the modification for off-center nucleation is introduced, and the order in which the equations are solved is described.

The process of atomization can be described as follows. An ensuing metal ligament from the nozzle breaks to form droplets. The physics of a single droplet falling through the stagnant atomization fluid [Chapter 3] is as follows. The droplets formed from the ligament break-up, have some initial velocity and fall through the stagnant gas in the atomization chamber. While falling through the quiescent gas, they lose heat mainly through convection and, to a very small extent, by radiation. A schematic diagram of a droplet falling, the forces acting on the droplet and the energy losses from the droplet is shown in Figure 7.1. The small effect of radiation in the heat loss will be discussed later. The convective heat loss is a result of the relative velocity between the droplet velocity and the atomization gas. The droplet temperature at the start is close to the atomization temperature, and as the droplet loses heat, it cools and at some temperature, nucleation sets in. Typically, the atomization droplets nucleate at temperatures below the equilibrium liquidus temperature of the alloy [Boettinger1985]. This phenomenon is called nucleation undercooling. Subsequent to this nucleation event, the liquid-solid transformation takes place by the movement of the solid-liquid interface in the shape of paraboloids called dendrites, whose velocity is proportional to the nucleation undercooling attained by the droplet [Lipton1987b, c]. The phase transformation results in latent heat release, and the net heat content of the droplet is given by the difference between the latent heat generated and the convective heat loss. This energy balance can be written as

$$C_p \frac{dT}{dt} = -\dot{Q}_c + L\frac{df_s}{dt} \tag{7.1}$$

where C_p is the specific heat and L is the latent heat of fusion of the alloy. $\dot{Q}_c$ is the rate of convective heat loss from the droplet and f_s is the fraction solid formed during phase transformation. The fraction solid is defined as the ratio between the amount of solid and liquid present during the course of solidification. The negative sign in front of $\dot{Q}_c$ indicates the heat loss from the droplet which takes place at the droplet surface.

The latent heat is released until solidification is complete. Following complete solidification, the droplet cools due to convective heat losses only. To solve the energy balance in Eqn. 7.1, the droplet solidification model therefore requires expressions for the convective heat loss $\dot{Q}_c$ and the rate of the fraction solid f_s formed. Note that the convective loss would be a function of the relative velocity between the droplet velocity, v, and the atomization gas. Since it is stagnant in Impulse Atomization, the convective heat loss would be a function of the droplet velocity only. While the droplet velocity and convective heat loss are macroscopic phenomena, the rate of fraction solid formation is microscopic in nature. However, these are intrinsically coupled to each other due to the latent heat release, which depends on the rate of fraction solid formation. Therefore, the development of the solidification model requires using and coupling force and energy balance to evaluate the macroscopic aspect of droplet solidification and using the dendrite growth theories to evaluate the microscopic phenomena. These equations are developed in the following sections.

7.2.1 Macroscopic: Momentum balance

As the droplet falls through the chamber, the relative velocity between the droplet and the gas changes as a result of the net forces acting on the droplet as it falls through the gas atmosphere. The schematic in Figure 7.1 shows the different forces acting on the droplet as well as the energy balance in the droplet. This velocity appears in the Re number in the formula for the convective heat transfer coefficient (described in the following), and, therefore, the heat transfer coefficient also changes with time. The droplet velocity is calculated by doing a force balance on the droplet. As shown in Figure 7.1, the forces acting on the droplet are gravity [=mg], fluid drag force [=f(Re)] and buoyancy [=$m_f g$]. The drag force and buoyancy act in the opposite direction to the gravity as the droplet falls through the atomization gas. Taking into account all these forces, the net force (instantaneous acceleration) on the droplet can be written as

$$\frac{dv}{dt} = \frac{\rho_p - \rho_f}{\rho_p} g - 0.75 \frac{\rho_f}{\rho_p} \frac{C_d}{D_p} v^2 \qquad (7.2)$$

where v is the relative velocity between the droplet and the atomization fluid ($v_{gas} = 0$); ρ_p and ρ_f are the densities of the droplet and atomization gas, respectively; C_d is the drag coefficient; and D_p is the droplet diameter. C_d is calculated from [Yule1994]:

$$C_d = \frac{18.5}{\mathrm{Re}^{0.6}} \qquad (7.3)$$

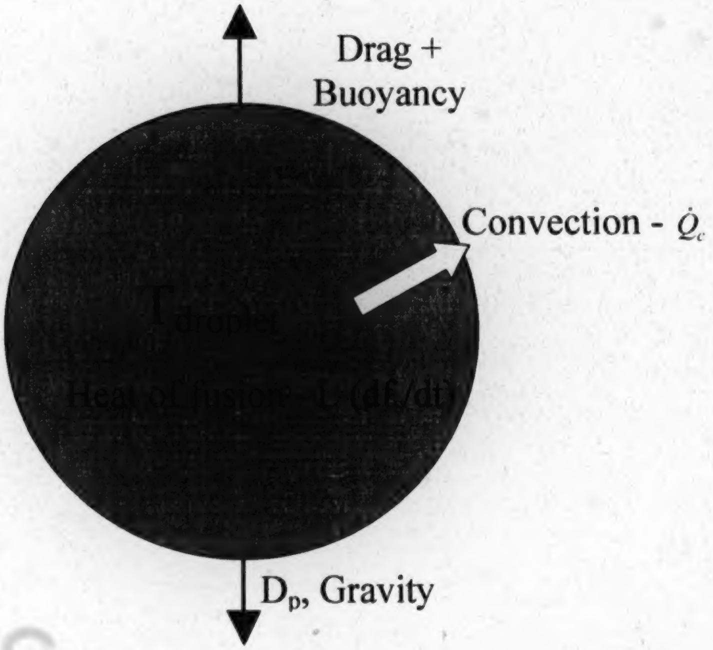
Drag +
Buoyancy
Convection - $\dot{Q}_c$
$T_{droplet}$
Heat of fusion - L (df/dt)
D_p, Gravity

Figure 7.1: Schematic of a droplet during atomization with different forces acting on it. The heat loss due to convection and radiation and latent heat generated due to phase transformation is also shown.

The drag coefficient is valid for Re numbers in the range of 0.1 to 1000. By substituting the expression for C_d in Eqn. 7.2 one gets,

$$\frac{dv}{dt} = \frac{\rho_p - \rho_f}{\rho_p} g - 0.75 \frac{\rho_f}{\rho_p} \frac{18.5}{\mathrm{Re}^{0.6} D_p} v^2 \qquad (7.4)$$

Noting that,

$$\mathrm{Re} = \frac{v D_p \rho_f}{\mu_f} \qquad (7.5)$$

Eqn. 7.4 can be rewritten as

$$\frac{dv}{dt} = \frac{\rho_p - \rho_f}{\rho_p} g - (18.5 * 0.75) \frac{\rho_f^{0.4}}{\rho_p} \frac{\mu_f^{0.6}}{D_p^{1.6}} v^{1.4} \qquad (7.6)$$

Eqn. 7.6 describes the velocity of the droplet as a function of time as the droplet falls through the atomization chamber. The solution of this equation requires an initial velocity, and this value is given in Table 7.4.

7.2.2 Macroscopic: Heat loss from the droplet

The total heat loss from the droplet is by convection and, to a very small extent, by radiation. Using the Stefan-Boltzmann law [Incropera1996] the radiation heat loss can be evaluated. Assuming that a uniform aluminum oxide coating forms instantaneously on the droplet surface, the radiation emissivity of the droplet with an oxide layer can be approximately taken as 0.6 [Incropera1996]. At close to the atomization temperature, the radiation heat loss is ≈3.5% of the total heat loss, which reduces to ≈1.6% at the melting temperature of pure aluminum. Furthermore, as the temperature reduces, the radiation heat loss reduces at the rate of T^4 (Stefan-Boltzmann law). With such small contributions from the radiation heat loss, this term was not taken into account, and the heat loss from the droplet was assumed to come from convection only. The convective heat loss is calculated using the following expression,

$$\dot{Q}_c = h_c\left(T_i - T_f\right) \tag{7.7}$$

where h_c is the convective heat transfer coefficient, T_i is the instantaneous droplet temperature and T_f is the gas temperature (assumed constant). The droplet is assumed isothermal, and, therefore, the droplet temperature is uniform throughout. The assumption of isothermal droplet is justified by the condition of Bi < 0.1 [Jana1986].

The convective heat transfer coefficient, h_c, is calculated by evaluating the Nusselt number, Nu, which is determined from the modified Whitaker correlation [Wiskel2002a] as follows. The modification of the Whitaker correlation is the first term in the parentheses in Eqn. 7.8 which accounts for the properties of the gas at the droplet surface temperature. The rest of the equation containing the Re and Pr number terms is the same as in the original Whitaker correlation.

$$Nu = \frac{h_c D_p}{k_s} = 2\left(\frac{B}{k_s (m+1)} \frac{T_s^{m+1} - T_f^{m+1}}{T_s - T_f} \right) + \left(0.4\,\mathrm{Re}^{1/2} + 0.06\,\mathrm{Re}^{2/3}\right)\mathrm{Pr}^{0.25}\left(\frac{\mu_\infty}{\mu_s}\right)^{1/4} \tag{7.8}$$

Where D_p is the droplet diameter, k_s is the gas thermal conductivity evaluated at the temperature of the droplet surface and T_s is the droplet surface temperature, which is replaced by T_l, based on the assumption of isothermal droplet. T_f is the fluid temperature in the bulk assumed to be constant. Re and Pr are Reynolds and Prandtl numbers, respectively. Finally, μ_∞ and μ_s are the viscosity of the fluid in the bulk and on the droplet surface, respectively, evaluated at the temperature of the bulk fluid, T_∞, and at the droplet temperature. Since Re is a function of the droplet velocity (Eqn.7.5), once the velocity is known, the heat transfer coefficient can be evaluated using Eqn. 7.8. The convective heat loss is then calculated from Eqn. 7.7. Thus, f_s in Eqn. 7.1 remains to be defined and is described next.

7.2.3 Microscopic: Latent heat generation

The calculation of latent heat requires knowledge of nucleation and subsequent phase transformation through the dendrite growth. The nucleation sets in at some undercooling. This undercooling is given by ΔT = $T_l - T_l$, where ΔT is the undercooling, T_l is the equilibrium alloy liquidus temperature and T_l is the droplet temperature. Following nucleation, the dendrites grow at a rate proportional to the undercooling ΔT. Since the dendrite growth represents the rate of phase transformation, the growth results in the release of latent heat, which enters the heat balance equation. The above-mentioned sequence of events is modeled in the R-T model by assuming that the nucleation occurs in the center of the R-T grain.

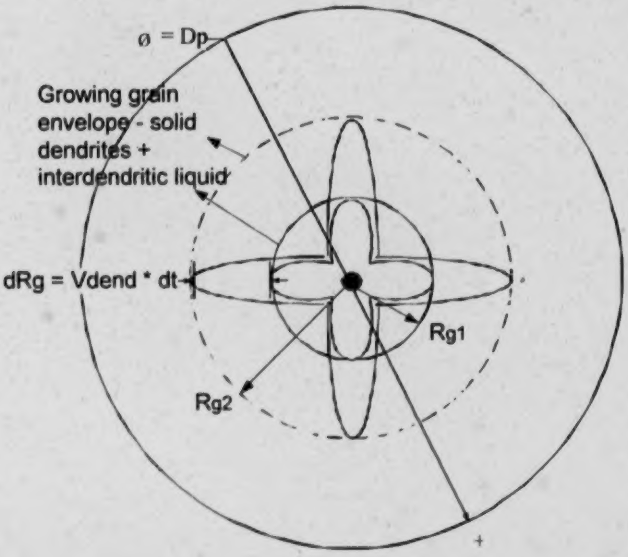
ø = Dp
Growing grain envelope - solid dendrites + interdendritic liquid
dRg = Vdend * dt
Rg1
Rg2

Figure 7.2: Schematic representation of the R-T model with nucleus at the center. The change in grain radius δR_g *in one time step is exaggerated for illustration purposes.*

Shown in Figure 7.2 is an R-T grain, resembling an atomization droplet undergoing solidification. The R-T grain will henceforth be called the atomization droplet with diameter D_p and the nucleus is in the droplet center. The dendrites grow equiaxially from the nucleus at the same speed in all directions. The locus of the tip of the dendrites forms the grain envelope, whose radius is R_g. Within this envelope are solid dendrites as well as interdendritic regions, which are liquid. Between time $t = t_1$ when $R_g = R_{g_1}$ and $t = t_2$ when $R_g = R_{g_2}$, the grain envelope grows at a rate defined by the dendrite growth velocity. The change in the grain envelope radius, dR_g, is given by

$$dR_g = \delta t * V_{dend} \tag{7.9}$$

where V_{dend} is the dendrite velocity and δt is the time step. The envelope grows until the droplet surface is reached. At this point, interdendritic liquid regions are still present and it is assumed that the solidification of this liquid follows a Scheil-Gulliver type of solidification path. The fraction solid calculation (and subsequent latent heat release) from nucleation to the point when the grain envelope reaches the droplet boundary will be called Stage I and the Scheil-Gulliver type of solidification will be called Stage II. The solid dendrites within the grain envelope constitute the solid fraction in Stage I, whereas the fraction solid for Stage II is simply given by the Scheil-Gulliver equation.

7.2.3.1 Fraction solid formed during Stage I

The fraction solid calculation for the R-T model (or atomization droplet) is described next. Diffusion and mass balance equations are applied to different regions within the droplet. These regions are the solid dendrites, the solid-liquid mushy region within the grain envelope and the liquid outside the grain envelope. The solute diffusion equation for the liquid region is

$$D\left[\frac{\partial^2 c}{\partial r^2}+\frac{2}{r}\frac{\partial c}{\partial r}\right]=\frac{\partial c}{\partial t} \tag{7.10}$$

for $R_g \leq r \leq R_{tot}$.

D is the diffusion coefficient and c is the solute concentration. Note that R_{tot} is the droplet radius in the case of the atomized droplet. The initial condition is $c(r,0) = c_0$ for $R_N \leq r \leq R_{tot}$. R_N is the radius of the nucleus. The boundary condition at r = R_g is

$$\left.\frac{\partial c}{\partial r}\right|_{r=R_{tot}}=0 \tag{7.11}$$

while that at r = R_g comes from the solute mass balance. The mass balance equations are based on complete mixing within the interdendritic liquid (finite diffusion) and no back-diffusion in the solid. In radial coordinates, a mass balance equation can be written as

$$\int_{0}^{R_s} k_0 c^{*}(R_s'')4\pi R_s^2 dR_s'' + \frac{4}{3}\pi c^{*}(R_g^3 - R_s^3) + \int_{R_r}^{R_{tot}} c(r,t)4\pi r^2 dr = \frac{4}{3}\pi R_{tot}^3 c_0 \tag{7.12}$$

where k_0 is the equilibrium partition coefficient of the alloy system and determines the amount of segregation of the solute between the liquid and the solid phases. The term f_g is the fraction of grain envelope and is given by

$$f_g = \left(\frac{R_g}{R_p}\right)^3 \tag{7.13}$$

Likewise, R_s is related to the fraction solid f_s,

$$f_s = \frac{4}{3}\pi R_s^3 \tag{7.14}$$

Using the above-mentioned diffusion (Eqn. 7.10) and mass balance (Eqn. 7.12) equations, it can be shown that the fraction solid is given by [Rappaz1987b]

$$f_s = f_g * f_i \tag{7.15}$$

where f_g is the volume of the grain and f_i is the actual amount of solid within the grain. Eqn. 7.16 was derived analytically from the mass balance and solute diffusion equations and it is valid only for the spherical geometry of the grain. f_i is given by

$$f_i = \left(\frac{C_l^* - C_0}{C_l^* - C_s^*} \right) g(P_{gn}) \tag{7.16}$$

where C_l^* and C_s^* are liquid and solid phase concentrations at the instantaneous droplet temperature, T_i, and are determined at the droplet temperature from the phase diagram. $g(P_{gn})$ is a function of the Peclet number of the growing grain. The first part of f_i, described by Eqn. 7.16, is also called the supersaturation. P_{gn} is the Peclet number and, in general, is defined as

$$P_{gn} = \frac{V_{gn} R_{gn}}{2D_{gn}} \tag{7.17}$$

where V_{gn} is the velocity of the advancing front, R_{gn} is the radius of the advancing front and D_{gn} is the diffusion coefficient of the species (solute or thermal). Depending upon the species, thermal or solutal, the general Peclet number will be replaced by subscripts 't' and 'c' to represent thermal and solutal diffusion respectively. The term $g(P_{gn})$ is given as [Rappaz1987b]

$$g(P_{gn}) = (1 + \frac{3}{2} Z + Z^2 + \frac{Z^3}{4}) \tag{7.18}$$

where Z = $1/P_{gn}$. The calculation of both R_g and $g(P_{gn})$ requires that the rate of growth of dendrite velocity V_{dend} be known, and therefore, the fraction solid f_s (Eqn. 7.15) is a function of the dendrite velocity. The dendrite velocity is calculated from the LKT model [Lipton1987b,c] and is described next.

7.2.3.1.1 LKT model

The LKT model was developed for calculating the growth kinetics of an isolated dendrite growing in an undercooled melt. In the atomized droplets, after nucleation at an undercooled temperature, the dendrites grow freely in an undercooled liquid, and, therefore, it is valid to apply the LKT model to calculate the growth rate of dendrites within an atomized droplet.

The basic premise of the LKT model is that the growth rate of dendrites is proportional to the undercooling ahead of them. Following the LGK analysis [Lipton1984], Figure 7.3 schematically shows the undercooling possible in front of the dendrite. The total undercooling is the difference between the equilibrium liquidus temperature of the alloy and the undercooled liquid (droplet) temperature. This total undercooling is the sum of the undercooling caused by solute rejection, heat rejection and the capillary effect. Individually, these undercoolings can be expressed mathematically. Following LKT [Lipton1987b], the non-dimensional forms of these undercoolings are described in the following.

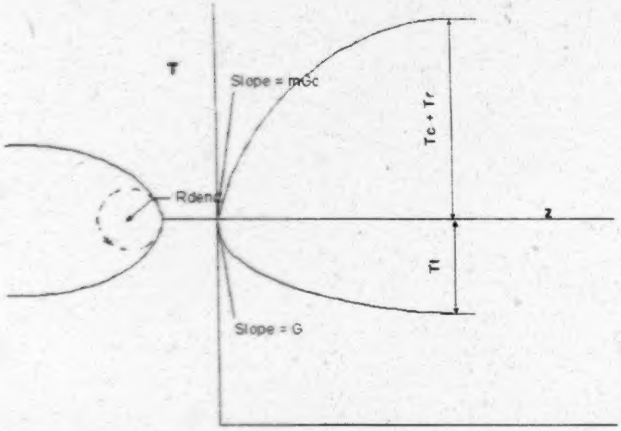

Figure 7.3: Possible undercoolings in front of a growing dendrite [Lipton1984]. The sum of the three undercoolings is the driving force for the dendrites to grow.

(i) Thermal undercooling: It is a result of the rejection of heat across the advancing interface as the liquid-solid transformation is taking place. The solution of the thermal diffusion equation across a dendrite tip (interface) is given by the Ivantsov solution for diffusion of heat for a paraboloid of revolution:

$$\overline{\Delta T_t} = Iv(P_t) \tag{7.19}$$

where $\overline{\Delta T_t}$ is the non-dimensional thermal undercooling, Iv(P_t) is the Ivantsov solution to the diffusion from the tip of a paraboloid of revolution and P_t is the thermal Peclet number. The "bar" at the top signifies a non-dimensional quantity. Note that the introduction of the Peclet number is necessary to include the effect of the rate of growth of dendrite on the heat rejection. The Ivantsov solution to the diffusion (thermal or solutal) from the tip of a paraboloid of revolution is expressed as $Iv(P_{gn}) = P_{gn}e^{P_{gn}}E_1(P_{gn})$, where $P_{gn}e^{P_{gn}}$ is the product between the Peclet number and the exponential raised to the power of the Peclet number and $E_1(P_{gn})$ is the exponential integral function given by [Kurz20000]

$$E_1(P_{gn}) = -0.5772157 - \ln(P_{gn}) - \sum_{n=1}^{\infty}\frac{(-1)^n P_{gn}^n}{n.n!} \tag{7.20}$$

Note that this expression is valid for both thermal as well as solutal Peclet numbers.

(ii) Solutal undercooling: The solutal undercooling is caused by the rejection of solute across the interface. This rejection results from the difference in solute solubility between the solid and the liquid. The relation is given by the phase diagram and mathematically is given as

$$\overline{\Delta T_c} = \overline{C}\left(\frac{1}{1-(1-k_0)Iv(P_c)} - 1\right) \tag{7.21}$$

where $\overline{C}$ is the non-dimensional melt solute composition ($\overline{C} = C_0 \mid m_l \mid C_p / L$), k_0 is the equilibrium partition coefficient as defined before and is a constant. C_0 is the alloy composition, $\mid m \mid$ is the absolute liquidus slope, C_p is the specific heat, L is the latent heat and $Iv(P_c)$is the solutal Ivantsov solution. The form of the Ivantsov solution for solutal diffusion is the same as that for thermal diffusion except that the thermal diffusivity in P_t is replaced by the solutal diffusivity in P_c.

(iii) Curvature undercooling: This is caused by the change in radius of curvature from planar (infinite radius of curvature) to a parabolic shape (finite radius of curvature). The change is a result of the surface tension between the liquid and the solid dendrite that is growing into the liquid ahead of it. Mathematically, the curvature undercooling is written as

$$\overline{\Delta T_r} = \frac{2}{\overline{R}} \tag{7.22}$$

where $\overline{R}$ is the non-dimensional radius of curvature of the growing dendrite. The dimensionless radius of curvature is related to the actual radius of curvature, R, by $R = \overline{R}d_0$, where d_0 is the capillary length.

The sum of these three undercoolings is the total undercooling experienced by the growing dendrite. From the above, it is clear that the Peclet number is an important parameter and it appears in all equations. Therefore, to solve for the total undercooling, the knowledge of the Peclet number is required. There are 5 unknowns: the three undercoolings (thermal, solutal and capillary), the velocity (V_{dend}) and the radius (R_{dend}) of the growing dendrite. However, there are three equations, Eqns. 20-22. A fourth equation is obtained by introducing the definition of the Peclet number, which relates the dendrite radius and velocity. The Peclet number is defined as in Eqn. 7.17 and for the dendrite is given as

$$P_{dend} = \frac{V_{dend} R_{dend}}{2D} \qquad (7.23)$$

where V_{dend} is the velocity of the dendrite, R_{dend} is the radius and D is the diffusivity (thermal or solutal) of the species. To get a fifth equation and therefore a unique solution for the dendrite velocity and radius, LKT used the marginal stability criterion proposed by Mullins-Sekerka. Using this stability criterion, one can relate the radius of curvature of the dendrite tip to the solutal and thermal diffusivity. For a high Peclet number (P>1), the expression is given as [Lipton1987b]

$$\overline{R} = \frac{1}{\sigma^* \left(\overline{G_c}\xi_c - \overline{G}\xi_t\right)} \qquad (7.24)$$

where $\overline{G_c}$ and $\overline{G}$ are the non-dimensional average solutal and the thermal gradients in front of the dendrite tips. These gradients are a result of solute and heat rejection, respectively, as the dendrite grows. The terms $\overline{G_c}$ and $\overline{G}$ are evaluated by using the LGK [Lipton1984, 1987a] analysis. Since the rejection (solute or heat) is dependant on the dendrite velocity, these can be written in terms of the respective (solutal or thermal) Peclet numbers:

$$\overline{G_c} = -\frac{P_c C^* (1-k_0)}{R} \qquad (7.25)$$

$$\overline{G} = -\frac{P_t L}{C_p R} \tag{7.26}$$

L is the latent heat of fusion, C_p is the specific heat and σ^* is a constant ($\cong 1/4\pi^2$) in Eqn. 7.24. ξ_c and ξ_t are the stability parameters given as [Lipton1987b],

$$\xi_c = 1 + \frac{2k_0}{1 - 2k_0 - \sqrt{1 + \frac{1}{\sigma^* P_c^2}}} \tag{7.27}$$

$$\xi_t = 1 + \frac{1}{\sqrt{1 + \frac{1}{\sigma^* P_t^2}}} \tag{7.28}$$

These stability parameters reduce to 1 for P → 0 (low undercooling) which is the original LGK model. Hence, the current LKT model is valid for both low and high undercoolings.

The dendrite velocity is calculated by first fixing the P_c number. For any given P_c number, using equations 7.19-7.28, one can calculate the total undercooling and the radius and velocity of the dendrites, corresponding to that P_c number. The undercooling, dendrite velocity and the radius are unique for a given Peclet number value. For the solidification model, using the relevant equations in a subroutine, and a table of P_c numbers with corresponding total undercooling and dendrite velocity is created. The main program, which calculates the actual undercooling, T_l - T_t, reads the dendrite velocity from this table corresponding to the calculated undercooling. A linear interpolation scheme is used to calculate the actual undercooling not directly found in the table. Thus, for a given undercooling, which comes from the instantaneous droplet temperature, the growth velocity is known. A large range of Peclet number is chosen to ensure that a wide range of undercooling has been taken into account.

Once V_{dend} is calculated, the fraction solid f_s is evaluated using Eqns. 7.13, 7.15-7.16, 7.18. The ${df_s}/{dt}$ term in the heat balance equation (Eqn. 7.1) can now be evaluated for Stage-I of solidification during the growth of the grain envelope with dendrite growth. After mathematical manipulation, the heat balance equation can be written as

$$dT = \frac{-\dot{Q}_c dt + Ldf_g f_i}{C_p - Lf_g df_i g(P)} \tag{7.29}$$

From the start of the nucleation, when the grain begins to grow, to the time when it reaches the droplet boundary, Eqn. 7.29 is used for calculating the change in the droplet temperature. Recall that from the initial melt temperature to the onset of nucleation (given by user defined nucleation undercooling), no fraction solid is formed, and, therefore, the change in temperature is simply given by $dT = -\dot{Q}_c dt$.

7.2.3.2 Fraction solid in Stage II

As the grain envelope reaches the droplet boundary, this envelope can grow no further. The remaining liquid is assumed to solidify by following the Scheil-Gulliver path. Scheil-Gulliver solidification assumes infinite diffusion in the liquid and no diffusion in the solid. The solidification is independent of the geometry of the system. After the grain reaches the droplet boundary, when Scheil-Gulliver solidification takes over, the df_s/dt term is calculated from the Scheil-Gulliver [Scheil1942] equation:

$$df_s = \left[\left(\frac{T_m - T}{T_m - T_l} \right)^{\frac{2-k_0}{k_0-1}} \frac{1}{(T_m - T_l)(k_0 - 1)} \right] dT \tag{7.30}$$

In this case, the change in temperature is evaluated as

$$dT = \frac{\dot{Q}_c dt}{C_p - L df_s} \tag{7.31}$$

where the df_s term is obtained from Eqn. 7.30. Note that Eqn. 7.30 states that the fraction solid is a function of temperature. If the temperature reaches the eutectic temperature and the solidification is still not complete (f_s<1), then eutectic solidification begins to take place. During the eutectic solidification, the temperature does not change, and the change in the fraction solid is given by

$$df_s = \frac{\dot{Q}_c}{L}dt \tag{7.32}$$

After the solidification is complete, $f_s = 1$, and no further latent heat is released.

7.2.4 Off-center nucleation

Experimentally, it was found that the nucleation point is located close to the droplet surface. The distance between the center of the droplet and the nucleation point was measured to be 0.75 R_p and 0.63 R_p for 4.3 Cu and 17 Cu, respectively [Prasad2004]. An attempt was made to incorporate this observation into the droplet model. Since the nucleus is off-center, the grain growth would actually take place as shown in Figure 7.4.

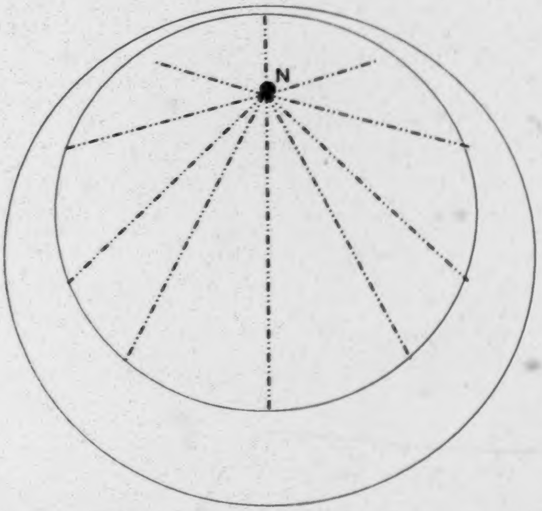

Figure 7.4: Schematic showing the dendrite growth in a droplet with off-center nucleation N.

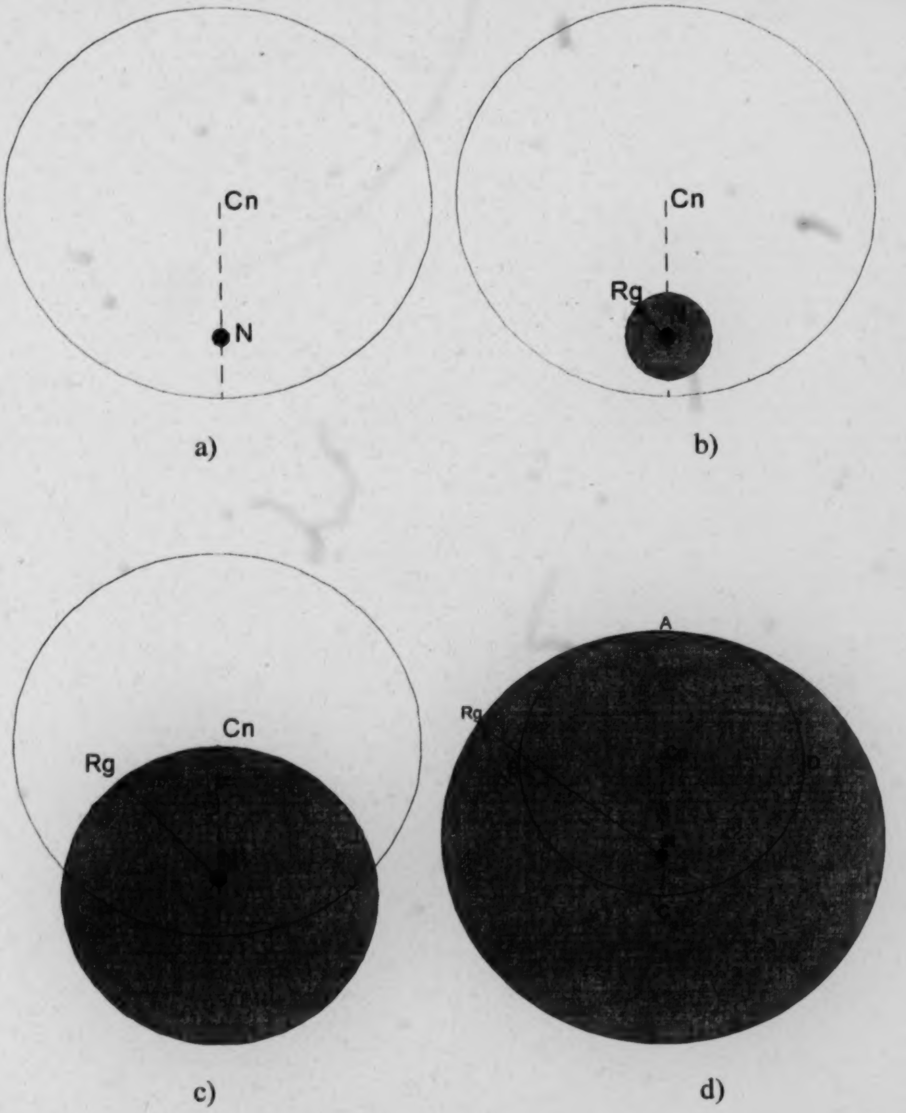

Figure 7.5: Schematic showing the progressive growth of a grain from an off-center nucleation point N within the droplet with center denoted as C_n. The shaded circle is the spherical grain envelope whose radius, R_g, increases with time. Part a) of the figure shows the off-center nucleation site N. This is followed by growth of grain with passing time. In b) the grain is still within the droplet. However with increasing time the grain envelope will grow beyond the droplet as shown in c). Finally, as shown in d) the grain completely covers the original droplet ABCD. The part of the grain envelope outside the droplet does not take part in the latent heat release.

Since the R-T model is valid only for a spherical grain envelope, to be able to account for the growth as shown in Figure 7.4, we attempted a geometrical approach to the problem. The nucleus was geometrically shifted to an off-center position and the grain envelope was assumed to grow spherically as before.

The series of schematics in Figure 7.5 shows in 2D the progressive development of the grain envelope for an off-center nucleus. Starting from the nucleation point, the grain envelope begins to grow. It continues to grow until at some point, it grows beyond the droplet surface. It is clear that the part of the grain which lies outside the droplet cannot take part in the heat balance. Hence, shifting the nucleus to an off-center position requires finding the expression for the volume of the grain which lies within the droplet and takes part in the heat balance. The solution to finding this volume, called the effective volume, is described next. Since the nucleus is now off-center, at some point, a portion of the grain will go beyond the droplet boundary. The condition when the grain envelope has grown beyond the droplet boundary is shown in 2D schematically in Figure 7.6. O is the droplet center whereas point N is the off-center nucleus, which is also the origin of the co-ordinate system. Point A is the grain envelope boundary whereas point B is the droplet boundary along the negative Y-axis. The Y-axis is chosen as such to facilitate mathematical calculations. The boundary of the grain envelope is AKIHFLMA. The portion of this grain which is within the droplet is BJIHFLB, which takes part in the heat balance equation. The grain portion AKIJBLMA is outside the droplet body and does not take part in the heat balance. To be able to calculate the effective grain volume, BJIHFLB, the dimensions of the various points comprising this region are required. The coordinates of these points are given in Table 7.1.

This effective grain envelope is calculated as follows. If a circular strip of thickness δy occupying an area 'A' is integrated along the Y-axis over a distance of 0 to Y, then it generates a cylinder whose volume is given by

$$V_{cyl} = \int_{0}^{Y} A dy \tag{7.33}$$

where V_{cyl} is the volume of the cylinder with base area A.

The same approach was used for calculating the volume BJIHFLB. The volume was divided into the sum of two parts BJIDLB and DIHFLD. For the region BJIDLB, the volume can be calculated by integrating the orthogonal area subscribed by strip I (CJ - thickness δy) along the Y-axis. Mathematically, this volume is given by

$$V_1 = \pi \int_{R_{p0}-R_p}^{Y_D} \left(R_p^2 - R_{p0}^2 + 2yR_{p0} - y^2\right) dy \tag{7.34}$$

where Y_D is the Y-coordinate of point D in Figure 7.6 and is given by

$$Y_D = \frac{R_g^2 - R_p^2 + R_{p0}^2}{2R_{p0}} \tag{7.35}$$

Likewise, by integrating the orthogonal area subscribed by strip II (EH - thickness δy) along the Y-axis, the volume of revolution of plane DIHFD can be expressed as

$$V_2 = \pi \int_{Y_D}^{R_g} \left(R_g^2 - y^2\right) dy \tag{7.36}$$

The sum of these two gives the effective volume of the grain. The terms for the area occupied by strip I and II and the coordinates Y_D (Eqns. 7.34 to 7.36) were calculated using geometry and are explained in Appendix A. The final volume $V_{g_{eff}}$ is obtained by performing the integration in Eqns. 7.34 and 7.36. After mathematical manipulation, the final form of $V_{g_{eff}}$ can be written as a sum of four terms: V_1', V_2', V_3' and V_4'.

$$V_{g_{eff}} = V_1 + V_2 = V_1' + V_2' + V_3' + V_4' \tag{7.37}$$

where V_1', etc., are given by Eqns. 7.37a to 7.37d.

$$V_1' = \pi\left\{(R_p^2 - R_{p0}^2) - R_g^2\right\}Y_D \tag{7.37a}$$

$$V_2' = \pi\left\{Y_D^2 - \left(R_{p_0} - R_p\right)^2\right\}R_{p_0} \tag{7.37b}$$

$$V_3' = \pi\left(R_p^2 - R_{p_0}^2\right)\left(R_p - R_{p_0}\right) \tag{7.37c}$$

$$V_4' = \pi\frac{\left(R_{p_0} - R_p\right)^3 + 2R_g^3}{3} \tag{7.37d}$$

The effective $f_{g_{eff}}$ term in the R-T fraction solid is now given as

$$f_{g_{eff}} = \frac{V_{g_{eff}}}{\frac{4}{3}\pi R_p^3} \tag{7.38}$$

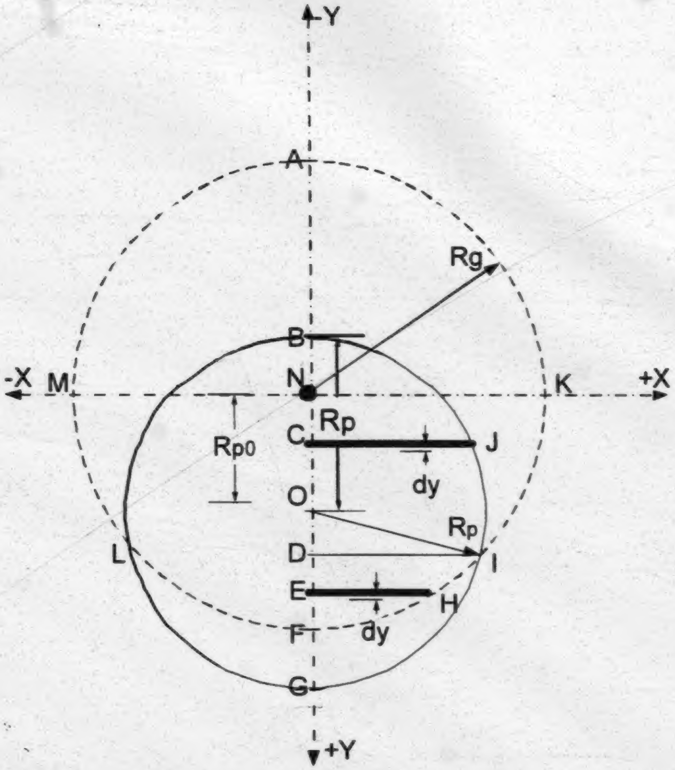

Figure 7.6: Figure showing the schematic of grain growth from off-center nucleation. The effective volume of the grain, EDGF, within the droplet is calculated using calculus.

Note that the volume is dependant only on the grain envelope radius R_g, the droplet radius R_p and the nucleation position R_{p_0}. The nucleation position can be expressed as a ratio of the droplet radius R_p with 1 being the periphery and 0 being the center. Since R_g is calculated based on the dendrite kinetics and R_p is the known droplet diameter, the only information required to calculate the effective grain volume is the position of the nucleation site. This information is available from the tomography experiments explained in the previous chapters.

Table 7.1: Coordinates for evaluating the effective grain volume.

Point	Description	Coordinates
A	Boundary of grain envelope along Y-axis	$(0,-R_g)$
B	Boundary of droplet along Y-axis	$(0, R_{p_0} - R_p)$
C	Intersection of strip-I with the Y-axis	(0,y)
D	Perpendicular projection of the point of intersection between the grain and the droplet, I, on the Y-axis.	$(0, Y_D)$
E	Intersection of strip-II with the Y-axis	(0,y)
F	Boundary of grain envelope along +Y-axis	$(0, R_g)$
G	Boundary of droplet along +Y-axis	$(0, R_p)$
I	Point of intersection between the grain and the droplet.	(X, Y_D)
K	Boundary of grain envelope along +X-axis	$(R_g, 0)$
N	Origin of the Cartesian coordinates	(0,0)
O	Droplet center	$(0, R_{p_0})$

This effective volume is used in the heat balance equation. After making appropriate changes in the original heat balance equation, Eqn. 7.29, the nucleation site modified heat balance equation is written as

$$dT = \frac{\dot{Q}_c dt + L df_{g_{eff}} f_i}{C_p - L f_{g_{eff}} df_i g(P)} \tag{7.39}$$

where the subscript "eff" represents the effective grain envelope volume taking part in the heat balance equation.

7.2.5 Calculation of microsegregation

Time dependant microsegregation calculation requires evaluating the solute concentration of the solid and liquid phases at any given temperature. Therefore, this requires a Temperature-Composition relationship, which is obtained from the phase diagram. Once the temperature is evaluated in the main program, the phase diagram information is used to calculate the liquid and solid phase concentrations at the corresponding temperature. Following these calculations, at any given droplet temperature, the primary phase fraction, f_s and its composition C_s is known. We compare the microsegregation between the model and the experiment by calculating the weight percent eutectic from the model and the average composition of the primary phase. At the equilibrium eutectic temperature, the fraction solid formed is the amount of the primary phase. The amount of eutectic is given by $f_e = 1 - f_s$.

The average Cu content of the primary phase was calculated using the following formula,

$$C_{s_{ave}} = \frac{1}{f_s} \int_0^{f_s} C_s df_s \tag{7.40}$$

where C_s and f_s are obtained from the model. The integration was numerically evaluated using the Trapezoidal rule. Note that the average solute content is defined as the copper content of the pro-eutectic primary phase.

7.3 Solution of heat balance equation

Various physical property values are required to solve the system of equations developed in the previous section. The physical properties of the gases are shown in Table 7.2. The modified Whitaker correlation requires that the temperature-dependant values of viscosity and conductivity be used, since a significant temperature gradient can exist from the droplet surface to the bulk stream. These properties are denoted by the temperature-dependant equations in the table where the temperature is in Kelvin. B and m are the parameters appearing in the modified Whitaker correlation (Eqn. 7.8).

Table 7.2: Physical properties of gases used in the simulation [Wiskel2002a].

Gas properties	He	N_2
ρ_f, [kg/m^3]	5	$335.5T^{-0.9971}$
μ_f x 10^7, [Pa.s]	1.75	$3.79T^{0.6766}$
k_f x 10^4, [J/kg/m^2/^{0}C]	$27.78T^{0.7025}$	$3.44T^{0.7609}$
m	0.7025	0.7609
B	2.778e-3	3.44e-4

The dendrite kinetics and the supersaturation term in the R-T model requires phase diagram information. For modeling purposes, the straight-line approximation of the phase diagram liquidus and solidus is often used [Kurz2000]. We have taken the same approach for our model and used the straight-line approximation of the equilibrium phase diagram. Since the liquidus and the solidus are assumed to be straight, the partition coefficient, k_0, is a constant. The schematic of the linearized phase diagram is shown in Figure 7.7. The partition coefficient k_0 is mathematically defined as

$$k_0 = \frac{m_l}{m_s} \tag{7.41}$$

where, m_s and m_l are the solidus and liquids slopes, respectively. The slope of the liquidus m_l and the solidus m_s are defined as

$$m_l = \frac{T_l - T_E}{C_{lliq} - C_{le}} \tag{7.42}$$

$$m_s = \frac{T_l - T_E}{C_{sliq} - C_{se}} \tag{7.43}$$

respectively. The range of temperature and composition used for calculating the slope was between the liquidus of the alloy, T_l, and the eutectic temperature T_E. These values for different alloy compositions, along with the values of the physical properties of the alloys, are given in Table 7.3. The values given in the table are taken from different sources and are referenced in the table. The conductivity values for the alloy, K, are weighted values. The ratio of the weighting fractions is the same as the ratio of weight percent of the elements in the alloy.

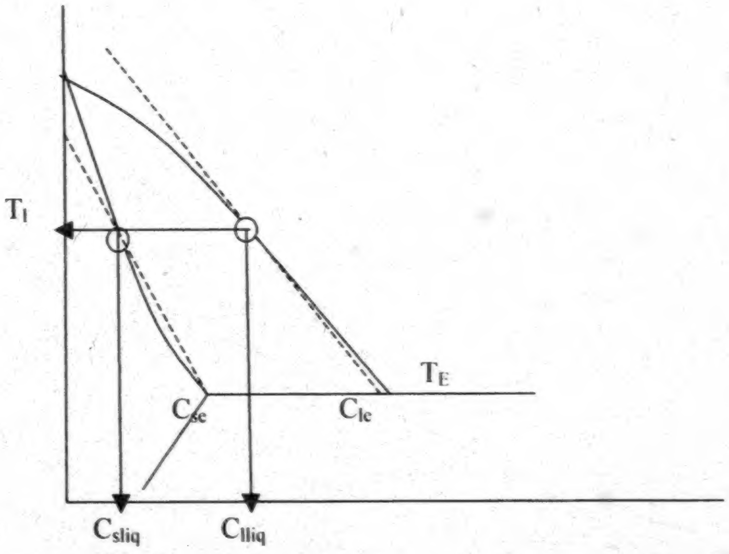

Figure 7.7: Schematic of a linearized phase diagram with straight line approximation of the liquidus and the solidus. Solid lines indicate the actual phase diagram and the dotted lines are the approximations.

Table 7.3: Properties of alloys used in the simulation[a,b,c].

Alloy properties	4.3%Cu	5%Cu	10%Cu	17%Cu
T_l [K]	922	920	907	885
ρ^a [kg/m^3]	2750	2760	2870	3100
$C_p{}^b$ [J/K/m^3]	3.2378e6	3.2465e6	3.3087e6	3.3957e6
K^c [W/K/m] (liquid metal)	278.4	279.3	285.5	294.3
L^b [J/m^3]	10.8113e8	10.8661e8	11.2575e8	11.8054e8
m_l [K/%]	-3.63	-3.66	-3.86	-4.23
k_e [-]	0.177	0.178	0.194	0.224

---

[a] [Smithells1998]
[b] [Kubaschewski1979]
[c] [Guthrie1992]

7.4 Solving the set of equations

The model requires initial values to solve the set of equations. The required initial values are, the melt temperature, droplet velocity, gas temperature, user-defined primary phase nucleation temperature and nucleation position. These values are given in Table 7.4. Depending on the droplet temperature, the position of the grain envelope or the fraction solid formed, the droplet cooling can be divided into 5 steps:

- Step 1: From the initial atomization temperature to start of the nucleation temperature. No latent heat is released and the droplet cools by convection heat loss.

- Step 2: From onset of nucleation and grain envelope formation to the grain envelope reaching the droplet surface. Latent heat is released and enters the heat balance equation. The fraction solid is evaluated as a function of time.
- Step 3: From the grain envelope at the droplet boundary to the eutectic temperature. Solidification follows the Scheil-Gulliver path.
- Step 4: If $f_s < 1$ until Step 3; then eutectic solidification occurs until $f_s = 1$. No change in temperature during the eutectic reaction.
- Step 5: From complete solidification to room temperature.

Following these 5 steps, the entire program is also divided into 5 modules corresponding to each regime of droplet solidification. Each module calculates the change in temperature, fraction solid and solid-liquid phase concentration (microsegregation) depending upon whether the condition exists for fraction solid formation or not. Module 1 represents the droplet cooling from the atomization temperature to the time when nucleation occurs at a user-defined nucleation temperature. Only temperature change is calculated with no fraction solid formation. Module 2 represents the solidification in Stage I when the grain envelope grows from the nucleus to the droplet boundary. The temperature change is calculated from Eqn. 7.29 (or Eqn. 7.38 when off-center nucleation is used). The fraction solid calculation is performed according to the equations developed in the section describing the Stage I solidification. When the grain envelope reaches the droplet boundary, the program moves to Module 3, which is the Scheil-Gulliver type of solidification. The change in temperature is evaluated using Eqn. 7.31 while the change in fraction solid is calculated using Eqn. 7.30. When the eutectic temperature is reached and if the droplet is not completely solidified, the program moves to module 4 which is the eutectic solidification. The temperature remains constant, but the fraction solid changes according to Eqn. 7.32. Module 5 is the post-solidification cooling of the droplet when the temperature change is calculated using Eqn. 7.1 without any latent heat release.

Since the temperature change is calculated in each module, the convective heat loss must be calculated. Therefore, the droplet velocity is first calculated (Eqn. 7.6) by using Milne's predictor-corrector method [Chappra2002], starting with an initial droplet velocity (Table 7.3). Milne's predictor-corrector method is a 2nd-order Runge-Kutta (R-K) technique. For the set of equations that is solved, the accuracy of this technique is the same as the more commonly used 4th-order R-K method. This accuracy is shown in Appendix B. At each time step, δt, a new velocity gives a new Re number, which when substituted in Eqn. 7.8, gives a new heat transfer coefficient, h_c at each time step. Using h_c in Eqn. 7.7 gives the rate of convective heat loss from the droplet. The convective heat loss gives the change in temperature in the droplet and this heat loss is calculated at each time step as the temperature changes.

The choice of time step for the simulation was based on the convergence test. The time step chosen for 4.3Cu is shown in Figure 7.8. The figure shows that at time steps close to 2e-5s and below, the amount of grain volume predicted becomes constant. Based on this plot, the time step chosen was 1e-5s. A similar result for 17Cu was obtained and an identical time step of 1e-5s was chosen for 17Cu as well.

Table 7.4: List of initial values used in the simulation.

Parameters with initial values	Values
Melt Temperature, [K]	From experiment run sheets
Droplet velocity [Ding1997]	0.5 m/s
Gas Temp., [K]	303 K
Nucleation undercooling, [K]	Variable
Nucleation position	Center to Periphery

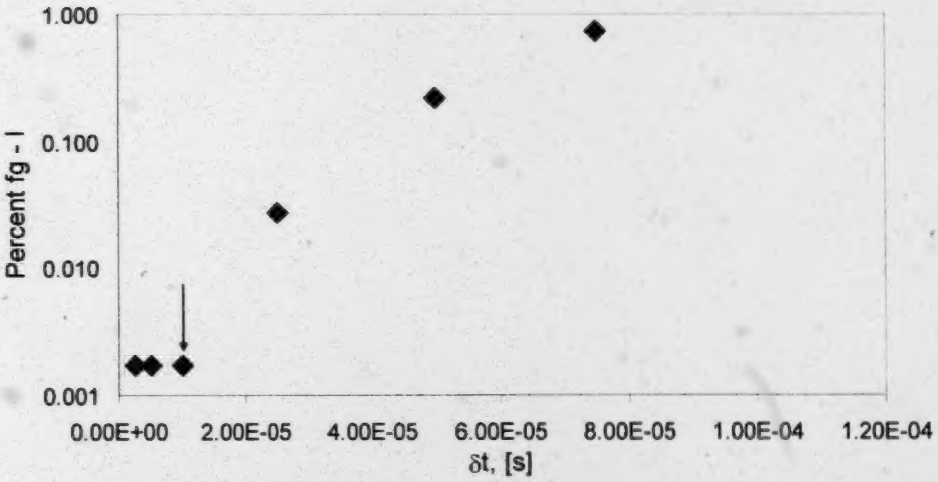

Figure 7.8: Plot for the convergence test for choosing appropriate time step. Test results for Al-4.3%Cu shown with the chosen time step.

7.5 References

[Baker1971]: "Solidification", Baker J.C. and Cahn J.W. American Society for Metals, Pennsylvania, 1971, pp 23.

[Boettinger1985]: Boettinger W.J. and Coriell S.R., In Science and Technology of the Undercooled Melt, (eds.) Sahm P.R, Jones H. and Adam C.M., NATO ASI series, Series E: Applied Sciences - N. 114, 1985, pp 81-110.

[Chappra2002]: "Numerical method for engineers", Chappra S.C. and Cannale R.P. 4th ed., McGraw Hill, U.S.A., 2002, pp 747-748.

[Ding1997]: "Impulse Atomization", Ding Y. Ph.D. Thesis, University of Alberta, Canada, 1997.

[Flemings1974]: "Solidification Processing", Flemings M.C., McGraw Hill, U.S.A., 1974, pp 279-283.

[Guthrie1992]: "Engineering in Process Metallurgy", Guthrie R.I.L., Clarendon Press, Oxford, 1992, pp 484.

[Henein2004]: "Effect of process variables on droplet heat transfer", Henein H., Multiphase Phenomena and CFD Modeling and Simulation in Materials Processes Symposium, 2004, p 131-137.

[Heringer2004]: "Modélisation de la solidification de gouttes atomisées, Heringer R., Ph. D. Thesis, Institut National Polytechnique de Lorraine, Nancy, France, 2004.

[Hillert1977]: "A solute drag treatment of the transition from diffusion controlled to diffusionless solidification", Hillert M. and Sundman B., Acta Metallurgica, v. 25, 1977, pp 11-18.

[Incropera1996]: "Introduction to heat transfer", Incropera F.P. and DeWitt D.P., John Wiley and Sons, New York, 1996, pp 610-619.

[Jana1986]: "Engineering Heat transfer", Jana W.S., PWS Engineering, Boston, 1986, pp 251.

[Kubaschewski1979]: "Metallurgical Thermochemistry", Kubaschewski O. and Alcock C.B., Pergamon Press, New York, 1979, pp 326-328.

[Kurz2000]: "Fundamentals of solidification", Kurz W. and Fisher D.J., Trans Tech Publications, Switzerland, 2000, pp 177.

[Lee1994]: "Solidification progress and heat transfer analysis of gas-atomized alloy droplets during spray forming", Lee E-S. and Ahn S., Acta Metallurgica et Materialia, v. 42, n. 9, 1994, pp 3231-3243.

[Levi1982]: "Heat flow during rapid solidification of undercooled metal droplets", Levi C.G. and Mehrabian R., Metallurgical Transactions A, v. 13A, 1982, pp221-234.

[Lipton1984]: "Dendritic growth into Undercooled Alloy Melts", Lipton J., Glicksmann M.E. and Kurz W., Material Science and Engineering, 65, 1984, 57-63.

[Lipton1987a]: "Equiaxed Dendrite growth at small Supercooling", Lipton J., Glicksmann M. E. and Kurz W., Metallurgical Transactions A, v. 18A, 1987, pp 341-345.

[Lipton1987b]: "Rapid Dendrite growth in Undercooled Alloys", Lipton J., Kurz W. and Trivedi R., Acta Metallurgica, 35, n. 4, 1987, 957-964.

[Lipton1987c]: "Effect of growth rate dependant partition coefficient on the Dendrite growth in Undercooled Melts", Lipton J., Kurz W. and Trivedi R., Acta Metallurgica, 35, n. 4, 1987, 965-970.

[Prasad2002]: "A Study of Microsegregation in Al-Cu alloys Using Impulse Atomization as an RSP", Prasad A, Henein H. and Gandin C-A., Light Metals 2002 Métaux Légers, T. Lewis, Editor, MetSoc of CIM, 2002, pp. 101-114.

[Prasad2004]: "X-Ray Tomography study of atomized Al-Cu droplets", Prasad A., Henein H., Maire E. and Gandin Ch.A., Canadian Metallurgical Quarterly, v. 43, n. 2, 2004, pp 273-282.

[Prasad2005]: "Understanding the rapid solidification of Al-4.3Cu and Al-17Cu using X-Ray Tomography", Prasad A., Henein H., Maire E. and Gandin Ch.A., Metallurgical Transactions A, v. 37, n. 1, 2006, pp 249-257.

[Scheil1942]: "Bemerkungen zur Schichtkristallbildung", Scheil E., Zeitschrift fur Metallkunde, v. 236, 1942, pp 70-72.

[Smittells1998]: "Smithells metals reference book", Brandes E.A. and Brook G.B. (eds.), Butterworths-Heinemann, London, 1998, pp 14(1)-14(14).

[Wiskel2002a]: "Solidification study of aluminum alloys using Impulse Atomization: Part I: Effect of cooling rate on microstructure", Wiskel J.B., Navel K., Henein H. and Maire E., Canadian Metallurgical Quarterly, v. 41, n. 2, 2002, pp 193-204.

[Yule1994]: "Atomization of melts for powder production and spray-deposition", Yule A.J. and Dunkley J.J., Oxford Series on Advanced Manufacturing, Clarendon Press, Oxford, 1994.

Chapter 8

Results and Discussion

The results from the experimental work described in the previous chapters are summarized here. From X-Ray Tomography on Al-4.3%Cu and Al-17%Cu droplets, the 3-D microstructure of the individual droplets could be studied. The images showed a single nucleation site and three different microstructural regions within each individual droplet. Immediately surrounding the nucleation site was an Ultra Fine region (initial growth - Region I) whose details were not clear from the Tomography work. Surrounding this Ultra Fine region, and including it, was the Primary Trunks (recalescence region – Region II) and the third region (post-recalescence solidification – Region III) was a coarse dendritic structure. The three regions have been hypothesized as being formed during the initial growth regime, recalescence regime and post-recalescence regime of solidification. These were termed as Region I, Region II and Region III, respectively, in Chapters 4 and 5. The interdendritic structure as seen in the SEM images was the eutectic. Neutron Diffraction and Stereology analysis on the Al-5%Cu, Al-10%Cu and Al-17%Cu droplets showed that as the alloy composition was increased, the amount of volume percent eutectic decreased with respect to the Scheil-Gulliver and Equilibrium predictions. Similar trends were seen in the weight percent $CuAl_2$ and weight percent eutectic results for these droplets. Also, using simple mass balance equations, the average solute solubility of Cu in primary phase was calculated. These experimental results showed a similar trend of increase in the average Cu content in the primary phase in the droplets as the alloy composition was increased. The eutectic and average Cu content results did not show significant changes with droplet sizes or gas type or a combination of both. In summary, the experiments confirmed that microstructural changes had occurred within individual droplets for all compositions, although the scale was different in the Al-4.3%Cu (coarser) and Al-17%Cu (finer) droplets. The volume fraction of features representing initial growth and recalescence was higher in the Al-17%Cu than in the Al-4.3%Cu. Furthermore, a reduction occurred in the amount of microsegregation in the droplet volume as the composition was increased from Al-5%Cu to Al-17%Cu, suggesting the increasing role of recalescence in affecting the microsegregation as the alloy composition was increased.

An isothermal droplet model was developed to study rapid solidification of the Al-Cu binary alloy during Impulse Atomization. The model uses the Rappaz-Thevoz microsegregation model for equiaxed grains and uses LKT dendrite kinetics with equilibrium conditions. The model takes into account the nucleation undercooling and nucleation position, both of which are used as user-defined parameters. With the help of this model, the effect of alloy composition and position of nucleation site on microsegregation will be studied. This chapter describes the model validation followed by microsegregation predictions of the model compared to the experimental results. Following this, the role of dendrite velocity on microstructure and microsegregation is discussed.

8.1 Model validation and microsegregation results

The model requires a user-defined nucleation position and nucleation undercooling values. Subsequently, the model will yield the thermal as well as the fraction solid history. The simulation was run for an Al-4.3%Cu atomized droplet on which tomography experiments were performed. The atomization conditions were 1123K atomization temperature with a 660 μm diameter droplet atomized in N_2 gas. Henceforth, the droplet will be referred to as the "reference droplet". The nucleation position for the simulation was the same as that calculated by stereology on the tomography images, which was $0.75 R_p$ [Chapter 4]. The nucleation undercooling was chosen as 5K and 30K. Figures 8.1 and 8.2 show a typical result obtained from the model. Figure 8.1 shows the thermal history whereas Figure 8.2 shows the fraction solid f_s and grain envelope volume $\bar{f_g}$ as a function of time. The thermal history plot also shows the alloy liquidus.

In the figure for the thermal history, after nucleation at N at the two defined undercoolings, the initial growth regime is represented by NA (the subscripts 5 and 30 represent the two undercoolings) when the droplet temperature decreases after nucleation. The portion AB is the recalescence. For 5K undercooling, the drop in temperature between nucleation and end of initial growth (N_5A_5) is 8K. The subsequent recalescence temperature rise, A_5B, is 5K. The corresponding values for 30K undercooling are 0.1K during $N_{30}A_{30}$ and 22K for $A_{30}B$. Following recalescence, the droplet undergoes near equilibrium solidification, which is given by the Scheil-Gulliver solidification. This regime is indicated by BC. CD is the eutectic and beyond point D is the post-solidification period. The simulation shows that different initial undercoolings can result in different degrees of recalescence. Note that with an undercooling of 30K, the thermal history catches up to the 5K undercooling thermal history.

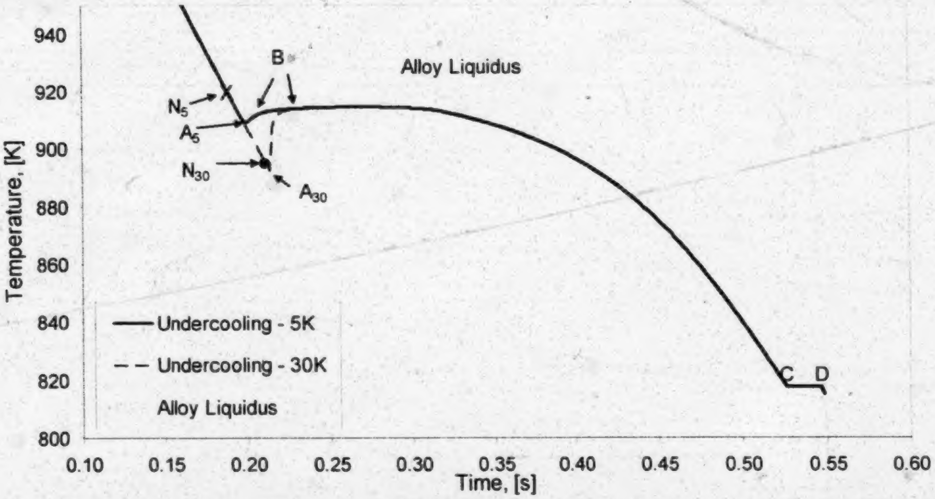

Figure 8.1: Representative thermal history plot for the reference atomized droplet with two undercoolings of 5K and 30K. Higher undercooling (lighter line) results in delayed nucleation and more recalescence.

Figure 8.2 shows the fraction solid f_s and the grain envelope volume fraction, f_g as a function of time. The same legend used in Figure 8.1 is also used in this figure and describes the fraction solid formed during different solidification regimes. The figure shows that by changing the undercooling, the grain volume fraction formed during the initial growth regime, NA, shows a change (see inset). The values of f_s and f_g for 5K undercooling are 0.46% and 0.86%, respectively, at point A_5, and 0.01% and 0.013%, respectively, for 30K undercooling at point A_{30}.

Since f_s is a function of f_g [Eqn. 7.15], the fraction solid formed with different undercoolings during the initial growth will follow a different time history.

These values for the two undercoolings at the end of recalescence (point B) are 25.5% and 66.3%, respectively, for 5K, and 25.9% and 67.3% for 30K. The similar values of f_s and f_g at the end of recalescence can be explained by the fact that the thermal history for 30K undercooling catches up with that of 5K undercooling and the recalescence-end temperature is almost the same. These results show the model is capable of generating results that show the different regimes of solidification.

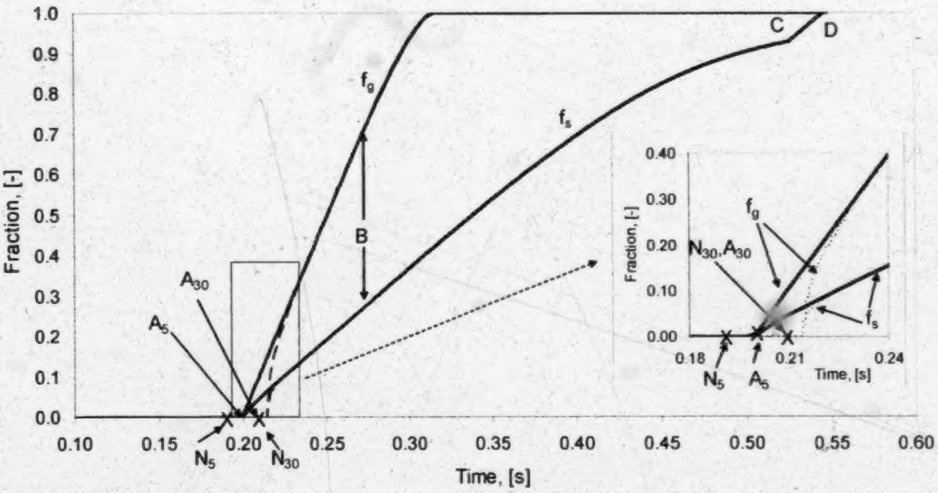

Figure 8.2: Plot for the model results for the same reference droplet as in Figure 8.1 showing the time history profile for fraction solid formed at two different undercoolings. Solid line indicates 5K of undercooling and dotted line indicates 30K of undercooling.

As mentioned earlier, the different microstructural features found in the Tomography images of different droplets were hypothesized to have been formed during different regimes of solidification. Therefore, one can compare and relate the thermal history of Figure 8.1 with the images of the microstructures found in the different regimes. The Ultra-Fine structure called Region I is believed to have formed during the initial growth regime of NA in Figure 8.1, the Primary Trunk region called Region II is believed to have formed during recalescence in the region AB and Region III is believed to have formed during the growth in Scheil-Gulliver regime of BC. Finally, eutectic is formed in the regime described by CD. Using Stereology, the volume fraction of Region I and the eutectic regimes have been quantified [Chapters 4-6]. The experimental results and the results for the fraction solid in Figure 8.2 can thus be compared.

The object of developing the model was to obtain microsegregation predictions for the entire droplet and hence to understand microsegregation in the droplets. Dendrite velocity is central to solidification; hence, microsegregation is assessed by studying the effect of dendrite velocity on partition coefficient. Finally, the effect of nucleation undercooling, nucleation position and cooling rate on microsegregation is studied by analyzing the effect of these variables on dendrite velocity. Note that the volume microsegregation predictions from the model and ND plus stereology results provide information for the entire droplet volume. Hence, time-space based variations in microsegregation within the droplet cannot be studied using the isothermal model.

The model results show a change in the thermal and the fraction solid profile as the undercooling is changed. This change can be explained by considering the effect of undercooling on dendrite velocity. Figure 8.3 shows the change in velocity with undercooling for a Al-4.3%Cu alloy obtained from the LKT dendrite kinetic model. The velocity increases as the undercooling increases. The same trend is also seen for the Al-17%Cu alloy. Based on this result, one would expect the velocity to change when the undercooling is changed for the reference droplet.

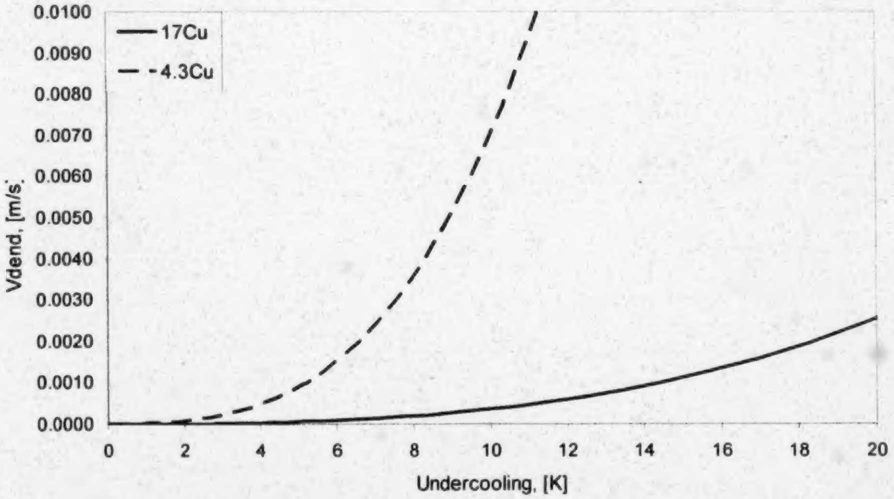

Figure 8.3: Dendrite velocities in Al-4.3%Cu and Al-17%Cu droplets as a function of undercooling calculated from the LKT model.

Since the interface velocity determines the grain envelope growth, R_g, which in turn determines the latent heat release via f_g and f_s, the temperature profile would change as a function of time when the undercooling was changed. In Figure 8.4, the dendrite velocity, V_{dend}, is plotted as a function of time for the two undercoolings for the reference droplet. This figure shows the change in temperature with V_{dend}. The nucleation is represented as N and NA is the initial growth during which the droplet temperature decreases and the undercooling increases. This results in an increase in the interface velocity. For 5K of undercooling, the velocity at the end of initial growth (point A_5) is 0.016 m/s. This value is almost an order of magnitude higher for the 30K undercooling at 0.21 m/s. Note that while the growth velocity increases slowly in the case of 5K undercooling, the rise in velocity is extremely rapid for 30K. This result can be understood with the help of Figure 8.3, which shows that the velocity increases as the undercooling increases.

As the velocity increases, the rate of latent heat released also increases, which eventually results in recalescence at point A. During recalescence (AB), the undercooling decreases with a consequent decrease in the velocity. The portion AB has a steady decrease for both the undercoolings. Thus, different undercoolings would result in different velocities, which would affect the final recalescence. The magnitude of recalescence depends on the velocity-dependant rate of the latent heat released, and, therefore, the velocity plays an important role in defining the recalescence.

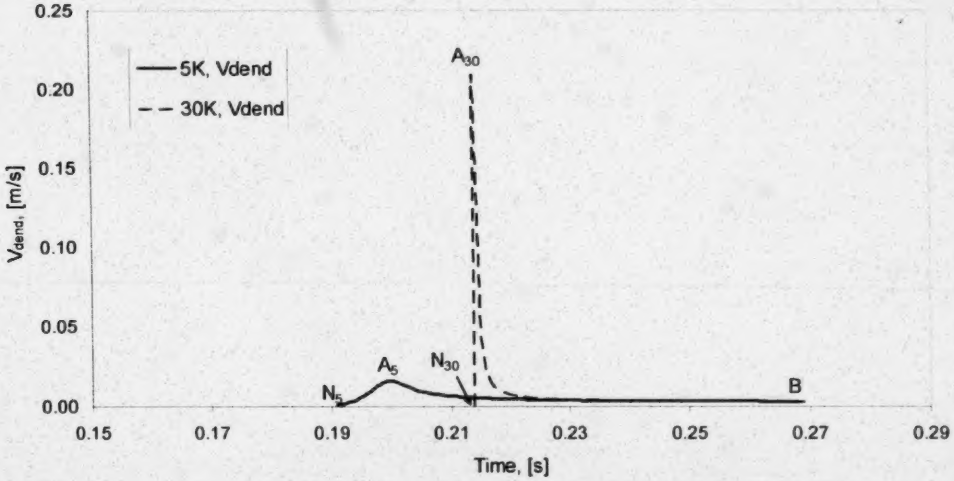

Figure 8.4: Dendrite velocity in the reference droplet for two undercoolings. The change in velocity results in a corresponding change in temperature.

As seen from the Tomography results in Chapters 4 and 5 and microsegregation results in Chapter 6, as the amount of recalescence increases in the Al-17%Cu alloy, the microsegregation decreases in the Al-17%Cu alloy. This suggests that recalescence plays an important role in microsegregation. Since recalescence is governed by dendrite velocity, it plays an important role in microsegregation. Therefore, the model is used to generate dendrite velocity results to analyze microsegregation vis-à-vis the relation between the dendrite velocities and the effective partition coefficient. Furthermore, the microsegregation assessment based on dendrite velocity is also focused on the variables that can affect the dendrite velocity. However, to make the aforementioned assessment, the existing model must first be validated. This is done by comparing the model predictions of eutectic weight percent with the weight percent eutectic data of 5Cu obtained from neutron diffraction and stereology experiments.

8.1.1 Model validation

Validation with Al-5%Cu eutectic results requires model predictions for the amount of eutectic in Al-5%Cu. The model requires user-defined nucleation position values and nucleation undercooling and these two parameters need to be established first. The nucleation position was ascertained by using tomography experiments for the Al-4.3%Cu and Al-17%Cu droplets only. Therefore, to be able to extrapolate the nucleation position of Al-4.3%Cu and Al-17%Cu on the Al-5%Cu, two pieces of information are required. First, a region of high probability of nucleation position within the droplet volume during atomization needs to be identified, and secondly, a sensitivity analysis for the nucleation position with respect to eutectic weight percent needs to be performed. The statistically possible nucleation region within an atomized droplet can be ascertained from the heat transfer analysis explained in Chapter 4.

8.1.1.1 Stochastic position of nucleation

From a previous work [Prasad2004 - Chapter 4], it was shown that the nucleation in an Impulse Atomized droplet is a result of variation in the heat transfer across the droplet surface from the stagnation point. In Figure 5.1, the position of highest heat transfer was placed at 120 ^{0} from the stagnation point (two points at 120 ^{0} each from the stagnation point). Based on the Reynolds number ranging from Re = 20 to 100 experienced by the droplet (size range of 200 to 1000 μm), 120 ^{0} is the maximum range of polar angle relative to the stagnation point for Re=20. At 120 ^{0}, Figure 4.8 shows a minimum in surface pressure and, therefore, maximum velocity. This means that the relative velocity between the droplet and the fluid increases from the stagnation point and reaches a maximum at 120 ^{0} at these two points.

For the reference droplet, the model predicts the Reynolds number of the reference droplet to be approximately 85 near the nucleation temperature. Using the same concept as described in the previous paragraph, Figure 4.8 shows that Re=85 would give the highest heat transfer at a polar angle of approximately 90 ^{0} from the stagnation point. This is shown in Figure 8.5. Point S is the stagnation point, and points A and B are 90 ^{0} apart from it. Along SA and SB, the fluid velocity on the droplet surface will continuously increase from point S and result in the highest heat transfer at points A and B. Noting that this higher heat transfer occurs in the lower half of the droplet along ABS and assuming that the droplet is isothermal, the nucleation can occur anywhere in the cone formed by revolving the sector ABS in Figure 8.5. This volume covers half the droplet volume (lower half) and includes both the surface and the droplet center. Recall that the average distance of the nucleation position in the 4.3Cu and 17Cu droplet is $0.75\,R_p$ and $0.63\,R_p$, respectively.

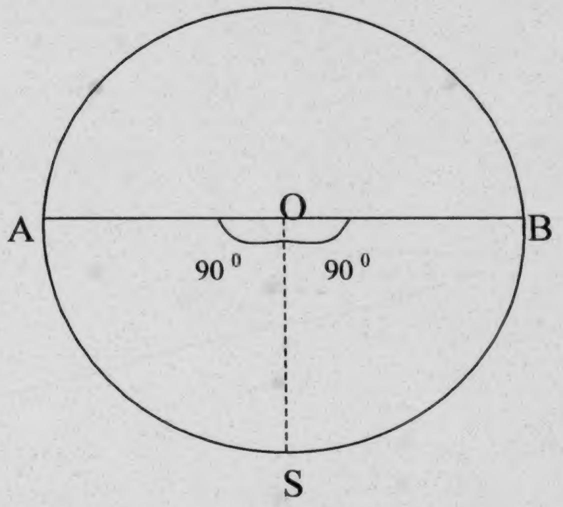

Figure 8.5: Schematic of the volume within an atomized droplet that represents the highest heat transfer region in an atomized droplet. S is the stagnation point and ABS represents the volume covering the range of highest heat transfer.

8.1.1.2 Sensitivity analysis of nucleation position

To determine the effect of nucleation position, simulations were run for the reference droplet with a fixed undercooling and the nucleation positions were changed between 0 R_p and 1.0 R_p. The effect of changing the nucleation position as a function of eutectic was then analyzed. The results are given in Table 8.1.

The results show that very small changes occur in the eutectic weight percent, f_{s_E}, values as the nucleation position is changed. The f_{s_E} value decreases very slightly as the nucleation site is moved towards the surface. The difference of 0.08% from 0 R_p to 1.0 R_p is negligible when compared to the standard deviation expected in experimental results. For example, the standard deviation of weight percent eutectic measurement for the 5Cu droplet is 1.5%. Thus it can be assumed that the change in nucleation position from $0\,R_p$ to $1.0\,R_p$ does not have a significant effect on the eutectic amount. The nucleation site is therefore assumed to be $0.5\,R_p$ for all the droplets without tomography results on which simulations were performed for comparison with the eutectic weight percent results.

8.1.1.3 Droplet undercooling analysis

The model, when run with different initial undercoolings on a given droplet size and atomization gas type for a given alloy composition, would yield different values for the volume of initial growth, as shown in Figure 8.2. Thus, by comparing and matching the tomography results for the growth volume with the model results of initial growth at different undercoolings, the undercooling attained by the droplet can be estimated. This technique was employed on the reference droplet. The model was run with different user-defined nucleation undercooling values ranging from 5K to 35K.

To ascertain the undercooling attained by the 4.3Cu droplet, the volume of $(f_g)_I$ versus initial undercooling for the 4.3Cu droplet is shown in Figure 8.6. The plot shows the change in $(f_g)_I$ with undercooling for the reference droplet with nucleation position at $0.75\,R_p$. The $(f_g)_I$ values are compared to the experimental values of volume percent of Region I (0.1% - Chapter 4).

Table 8.1: Summary of simulation results for the reference droplet for different nucleation positions.

Nucleation Position, X* R_p	Weight percent eutectic f_{s_E} - [%]
0 (i.e. Center)	7.24
0.5	7.22
0.6	7.20
0.70	7.19
0.80	7.17
0.90	7.17
0.95	7.16
1.0 (i.e. Surface)	7.16

Figure 8.6 shows that as the undercooling increases, the initial growth volume decreases. This trend can be explained by the fact that the volume percent of grain envelope is a strong function of the dendrite velocity and that the change in the initial undercooling results in significant changes in the dendrite velocity. Higher undercooling would result in faster growth rates of the dendrite, and, therefore, higher rates of latent heat would be released. This results in recalescence setting in faster and subsequently decreasing the volume of the initial growth regime. Thus, the trend seen in the figure is evidence of the importance of velocity during droplet solidification. The comparison with the experimental results at approximately 20K undercooling, the volume percent of Region I between the model and the experiment matches for the Al-4.3%Cu. Therefore, it is believed that

the Al-4.3%Cu 660 μm droplet attained a nucleation undercooling of approximately 20K.

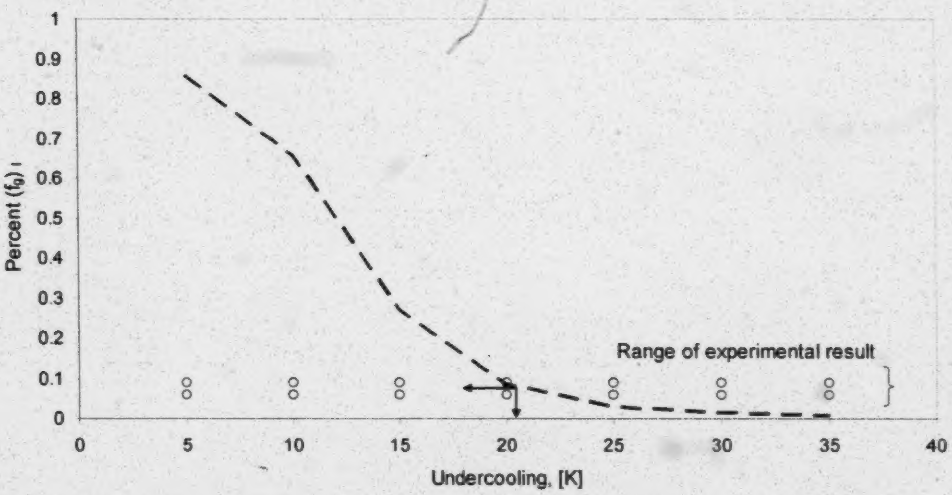

Figure 8.6: Comparison between experimental and model results for volume percent of Region I in the Al-4.3%Cu droplet. As explained in the text, an increase in the nucleation undercooling results in a decrease in the volume of initial growth regime.

Based on this estimate and following Lee and Ahn's [Lee1994] transient nucleation analysis, it is clear that the droplets undergo heterogeneous nucleation. Using Hirth's analysis of homogeneous nucleation under transient conditions, Lee and Ahn have estimated the nucleation temperature for Al-4.5%Cu alloy droplets of different sizes under different contact angles (different heterogeneous substrates). The results showed that in the presence of heterogeneous nucleating agent, the droplet size/cooling rate did not play an important role in the nucleation temperature. These factors are more dominant in the case of homogeneous nucleation. For a droplet size range between 10-180 μm, under homogeneous nucleation conditions, the undercooling temperature varies from 300-240 K, respectively. Under homogeneous nucleation situation, one would expect similar high undercooling in nucleation temperatures for the Impulse atomized droplets as well.

8.1.1.4 Sensitivity analysis of nucleation undercooling and droplet size

Note that depending upon the heterogeneous agent, the undercooling value for particles smaller than 660 μm can be expected to have more than 20K of undercooling and that the droplets bigger than 660 μm can be expected to have undercoolings lower than 20K. Thus, a sensitivity analysis was performed to determine the effect of undercooling and droplet size on the amount of weight percent eutectic. The simulations were run for the reference droplet with different undercoolings (5K to 35K), different droplet sizes (196 μm and 925 μm) and different gas types (N_2 and He gas). Note that since the model is based on equilibrium phase diagram, high undercoolings surpassing the equilibrium alloy freezing range cannot be used. The results are shown in Table 8.2.

Table 8.2: Effect of changing undercooling, droplet size and gas type on the eutectic formed with nucleation at the same position in all cases. Simulations were run for the reference droplet with nucleation at $0.75\,R_p$.

Droplet Size / Gas type	Undercooling, [K]	f_{s_E} -[%]
196 μm / N_2	5	6.53
196 μm / N_2	20	6.53
196 μm / N_2	35	6.53
925 μm / N_2	5	7.31
925 μm / N_2	20	7.31
925 μm / N_2	35	7.31
196 μm / He	20	5.76
925 μm / He	20	6.86

The change in undercooling from 5K to 35K shows a negligible change in the eutectic either with respect to a change in the gas type or droplet size. A decrease in the droplet size for a given undercooling in N_2 gas shows a small decrease (0.8%) in the eutectic amount. A change in the gas type between N_2 and He shows a change of 0.8% (absolute) for the smaller droplet size and a change of 0.5% (absolute) for the bigger droplet. Since the droplet size and gas type represent cooling rate, the model results show a trend as a function of cooling rate. The effect of cooling rate is discussed later. For the present, we will explain that a such small change in the eutectic weight percent with a change in the droplet size was also seen experimentally in the Al-5%Cu, Al-10%Cu and Al-17%Cu droplets (Chapter 6). As seen in Chapter 6, the experimental results also show a small dependence of eutectic percent on the droplet size and gas type. The results in the table show that, for a given droplet size, the change in gas type results in about 0.5 to 0.7% (absolute) difference in the eutectic. From the smallest droplet size in He gas to the biggest droplet size in N_2, the droplets show a maximum of 1.5% (absolute) difference in the weight percent eutectic. A combination of both gas types and droplet sizes results in a maximum of only 1.5% eutectic.

Note that these analyses were performed on Al-4.3%Cu droplets. The closest composition on which eutectic was measured was Al-5%Cu. The Al-4.3%Cu and Al-5%Cu droplets differ slightly in composition and therefore, one would expect a difference in the amount of eutectic found in the droplets of the two compositions. Based on the Scheil-Gulliver calculations, this absolute difference in eutectic between the Al-4.3%Cu (5.6%) and the Al-5%Cu (6.8%) is only 1.2%, which is within the difference of 1.5% seen in the case of Al-4.3%Cu for differences in gas type and droplet size. The Scheil-Gulliver model is independent of the cooling rate, assumes zero undercooling and predicts maximum segregation. This small amount of difference is comparable to the differences seen between different droplet sizes and gas types. Therefore, similar trends can be expected in the weight percent in the Al-5%Cu droplets as are observed in that of the Al-4.3%Cu droplets. Furthermore, since the nucleation undercooling and the position of the nucleation site does not significantly affect the eutectic amount, the same degree of nucleation undercooling of 20K with the nucleation site at $0.5\,R_p$ is assumed for the Al-5%Cu droplets for validation purposes.

The simulation results and experimental results for weight percent eutectic in Al-5%Cu are shown in Table 8.3. The model results show that as the droplet size increases, the eutectic amount also increases. Also, when the gas type is changed from He to N_2, a similar increase occurs in the eutectic amount. Thus, a small trend seems to exist with respect to gas type and droplet size (cooling rate). Such a trend is not clearly seen in the experimental results.

Table 8.3: Comparison of weight percent eutectic for Al-5%Cu droplet between the model and the experimental results.

Alloy composition	Experiment	Model
	f_{s_E} -[%]	f_{s_E} -[%]
5Cu,196 μm / He	7.29 ± 1.77	7.70
5Cu, 925 μm / He	6.14 ± 1.52	8.75
5Cu, 196 μm / N_2	6.92 ± 1.65	8.44
5Cu, 925 μm / N_2	7.20 ± 2.04	9.18

The experimental results show that for the He gas, the average eutectic amount decreases when the droplet size is changed from 196 μm to 925 μm. On the other hand, the trend reverses when the gas type is changed to N_2. However, since the values of standard deviation are higher than the difference between the minimum and maximum values of the weight percent eutectic resulting from a change in the gas type and droplet size, any trend present in the experimental data with respect to the droplet size or gas type will not be readily apparent. The model results are slightly higher than the experimental results but well within the experimental standard deviation. Hence, the model predicts the eutectic weight percent in the Al-5%Cu within the range of the experimental errors.

8.1.1.5 Sensitivity analysis of phase diagram approximation

In the present model, an equilibrium diagram is used with an assumption of linearized liquidus and solidus slopes. The linearization approximation used in the model was explained in Chapter 7. Similar linearizations can be approximated by making other assumptions as well. An example of an alternative approximation is shown in Figure 8.7 along with the comparison for the original approximation.

The different approximations result in slightly different partition coefficient values. By referring to the original approximation as Approximation I and the new approximation as Approximation II, the partition coefficient values for the Al-5%Cu, Al-10%Cu and Al-17%Cu are given in Table 8.4. It can be shown that the partition coefficient for Approximation II is always C_{s_e} / C_{l_e}, whereas the partition coefficient from Approximation I is given by Eqns. 7.41 to 7.43 in Chapter 7. The affect of different partition coefficient values on the average solute solubility will be assessed for the three alloys. The average Cu solubility resulting from the two approximations, along with the experimental values are compared in Table 8.5. It is clear that Approximation I give results that are closer to the experimental values.

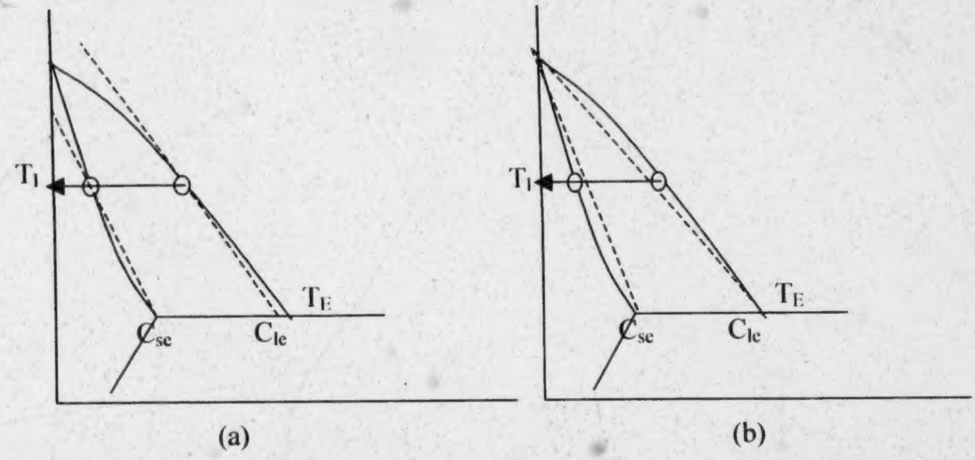

Figure 8.7: Schematic of two different linearization schemes that can be used for approximating the phase diagram. The figure in (a) has been called Approximation I and that in (b) has been called Approximation II.

Table 8.4: Partition coefficient values from the two different phase diagram approximations.

Alloy Composition	Partition Coefficient Values	
	Approximation I	Approximation II
5Cu	0.179	0.167
10Cu	0.194	0.167
17Cu	0.224	0.167

In summary, a model was successfully developed to study the solidification of individual droplets during atomization. The model assumes an isothermal droplet and uses the Rappaz-Thevoz microsegregation model with the LKT (constant k) model for dendrite growth kinetics. The thermal history from the model clearly shows the initial growth, recalescence, Scheil-Gulliver and eutectic regions. Using calculus, a geometrical function was developed. With its help, the nucleation site within the droplet could be changed from the surface to the center. Therefore, the model also incorporates the position of the nucleation site within the droplets. The model is therefore capable of capturing the effect of changing the nucleation undercooling, droplet size and position of nucleation site on the dendrite velocity, and, in turn, on microsegregation.

Table 8.5: Comparison of average Cu solubility obtained from the different approximations and the experiment.

Alloy Composition	Average Cu solubility			
	Experiment	Approximation I	Approximation II	% Diff. (App.I-App.II)
5Cu, 196 μm, He	2.7±0.17	2.2	2.0	9.1
10Cu, 196 μm, He	5.7±0.09	3.7	3.2	13.5
17Cu, 196 μm, He	10.1±0.19	6.3	4.5	28.6

From the model results for the reference droplet, a change in the initial undercooling and nucleation position showed that the effect of undercooling (and, therefore, the dendrite velocity) is important. It has been shown that the position of nucleus site does not affect the amount of eutectic. Furthermore, changing the nucleation undercooling and droplet size in the range of sizes studied in this work, does not change the eutectic significantly. Comparing the model result of volume percent of Region I in the Al-4.3%Cu droplet with the experimental values, a 20K nucleation undercooling was estimated. By extrapolating the nucleation undercooling and nucleation position of the Al-4.3%Cu on the Al-5%Cu alloy composition, simulations were run for the Al-5%Cu with droplet sizes and gas types that were analyzed with ND and stereology for eutectic analysis. The microsegregation results from the model compares well with those from the Al-5%Cu alloy concentration. The model predictions are now extended to the Al-10%Cu and Al-17%Cu alloy compositions and are described next.

8.2 Comparison of weight percent eutectic

The results from these simulations are shown in Figure 8.8. Each data point for the model predictions represents droplets for each size range and a given gas type. The results show that the model agrees fairly well with the experimental results for the Al-5%Cu droplets, but overestimates the amount of eutectic for the Al-10%Cu and Al-17%Cu droplets.

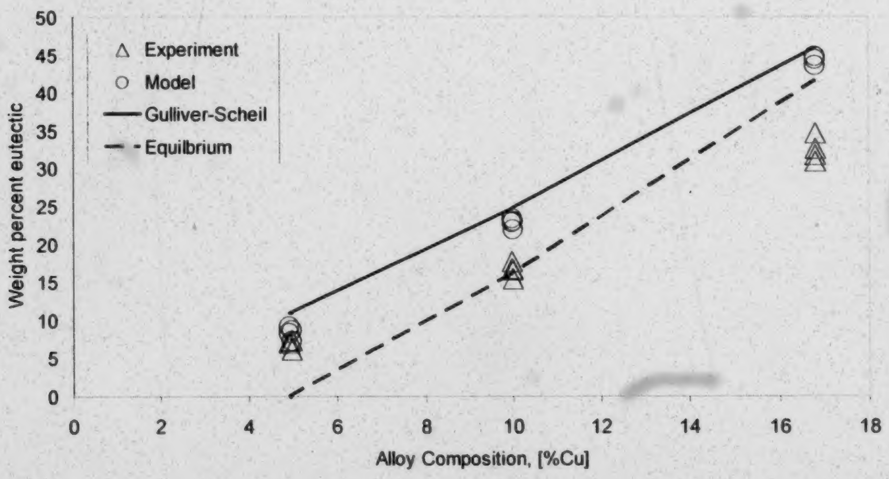

Figure 8.8: Figure comparing the weight percent eutectic from experiments and model. The model was run with eutectic assumed to occur at equilibrium.

8.3 Comparison of average solute solubility

Microsegregation can also be tested by comparing the solute content of the primary phase. Figure 8.9 shows this comparison with the average Cu solubility evaluated from the experimental results of weight percent eutectic (Chapter 6) and calculated from the model. Scheil-Gulliver and Equilibrium predictions are also shown in the same figure. Since Scheil-Gulliver predicts maximum microsegregation, the Cu solubility is the least, as shown by the dark solid line. The experimental results are published in a previous work by Prasad et al [Prasad2005b]. These results show a steady increase in Cu solubility with an increase in alloy composition. The model results also show a similar trend with alloy composition. The model predictions are in good agreement with the lower alloy compositions (i.e. 5wt%Cu), but as the alloy composition is increased, the model prediction deviates to lower values compared to the experimental value.

The deviation between the model prediction and the experimental results increases as the composition increases from Al-5%Cu to Al-17%Cu. Recall that the volume of recalescence in the Al-17%Cu is much higher than that in the Al-4.3%Cu, as reported in Chapters 4 and 5, suggesting the role of recalescence in deciding the microsegregation found in the droplets. The importance of the amount of recalescence regime can be seen from the fact that the model predicts that the time spent by the Al-17%Cu droplet in Regions I and II is about 20% of the total solidification time. Since recalescence depends strongly on the dendrite velocity, dendrite velocity plays an important role in the amount of final microsegregation found in the droplets, and a non-equilibrium affect may be taking place at the interface during recalescence.

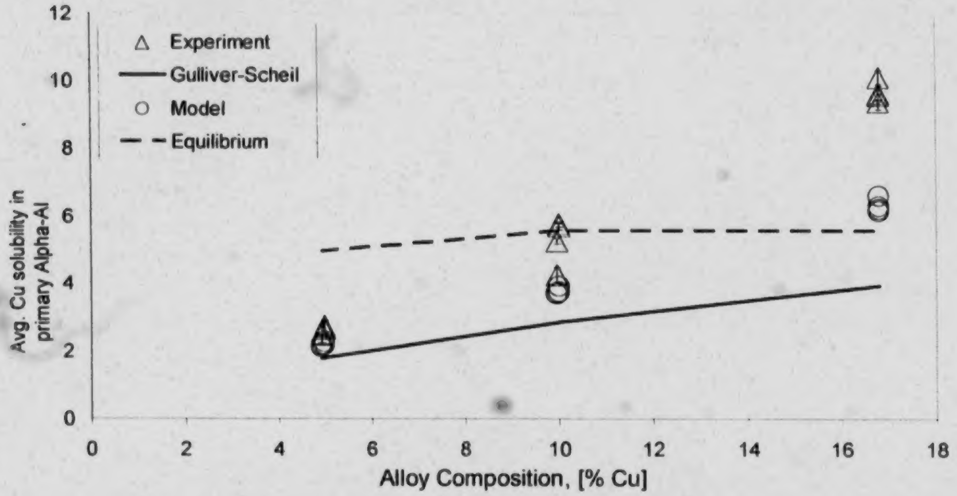

Figure 8.9: Comparison of Cu solubility in the primary phase from experimental calculations and model.

The metastable effects of velocity on solute segregation have been studied before. Baker and Cahn [Baker1971] have shown the thermodynamically possible boundary of solute content for the solid phase. Following Baker and Cahn, Flemings [Flemings1974] has shown the same limitations by using a free-energy-composition diagram. According to the Baker-Cahn analysis, the solute content boundary is a function of the interface velocity and the solute content of the primary phase can be a result of solute diffusion or diffusionless transformation.

The role of dendrite velocity in microstructure and microsegregation is discussed next. Microstructure gradation within the droplet is analyzed with respect to the dendrite velocity, followed by the analysis of the effect of the dendrite velocity on solute trapping, solute drag or dendrite remelting, which affect microsegregation. Lastly, the variables that can affect the dendrite velocity are discussed: nucleation position, nucleation undercooling and alloy chemistry.

8.4 Microstructural features in the atomized droplets

As stated in Chapters 4 & 5, the tomography work on the Al-4.3Cu and Al-17Cu droplets show a gradation in the microstructures and a general solidification path of Nucleation–initial growth–recalescence–Scheil-Gulliver growth followed by interdendritic eutectic was proposed for the alloy droplets of both compositions. However, the quantification of Regions I and II also revealed important differences. The main difference between the Al-4.3%Cu and the Al-17%Cu droplet was the extremely small volume of Region I in the Al-4.3%Cu droplet (0.1% in Al-4.3%Cu and 14% in Al-17%Cu). Furthermore, the Al-17%Cu droplet shows a distinct variation in the scale of the microstructure between Region I plus Region II and Region III. Although a similar change occurs in the microstructure between Region I and Region II plus III in the Al-4.3%Cu, the scale of the structure between Region II and Region III is fairly uniform. Based on the LKT model of dendrite growth in an undercooled melt, Boettinger [Boettinger1986] and Fleming [Flemings1987] showed that differences in the scale of the structure were caused by the changing undercooling within the droplet due to recalescence. Though such a distinct gradation is not seen in Al-4.3%Cu, the presence of Region I and II confirms the presence of recalescence in the droplets. A further analysis of this situation in terms of the velocity – undercooling relationship suggests that the individual components of the total undercooling – solutal, thermal and capillary undercooling – have an important role in the interface morphology and scale of the microstructure [Boettinger1985].

The evidence of the changing structure in Al-17%Cu was confirmed by the tomography images. A further confirmation was found in the FESEM images. These are shown in Figures 8.10 and 8.11 for the Al-17%Cu droplet. Figure 8.10 shows the full droplet area. The triangular white enclosure is the finer recalescence region (Region I + II) and outside this area is the post-recalescence Scheil-Gulliver region. The figures reveal a clear change in morphology from a finer to a coarser structure. The area bounded by the white triangle in Figure 8.10 shows a finer structure.

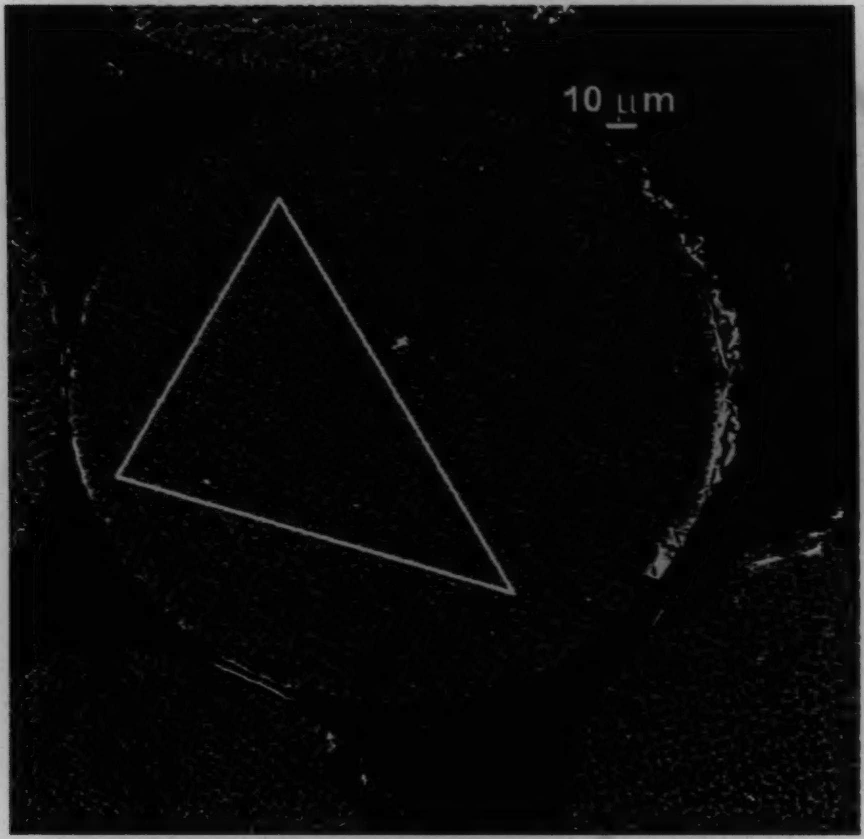

Figure 8.10: FESEM images of the droplet cross-section for the Al-17%Cu droplet. The white lines indicate the enclosed recalescence region, which has a different morphology than the post-recalescence region outside the white lines.

This difference is shown more clearly in Figure 8.11, which shows the region within the triangle in Figure 8.11(a), and the structure from outside the triangle in Figure 8.11(b). This change in scale has been explained in terms of changing undercooling (with a concomitant change in the velocity and, hence, a change in scale) during recalescence. Such a gradation in the morphology and scale has been reported by Boettinger ([Boettinegr1986], Al-Fe) and Trivedi ([Trivedi2003], Al-Si) in their gas atomized droplets. Similar structural variation is also shown for the Al-10%Cu in Figure 8.12. Finding such regions in 2–D microscopy is a highly statistical process and the probability of finding such areas depends on the volume of recalescence in the droplet.

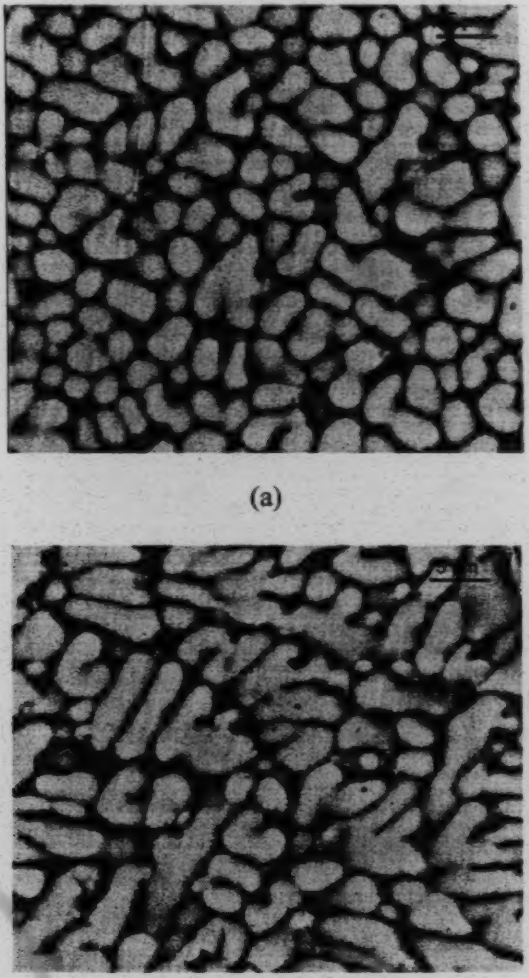

(a)

(b)

Figure 8.11: Magnified FESEM images of the (a) region within white lines and (b) region outside white lines for the Al-17% Cu droplet. The images are inverted for clarity so that the lighter regions are primary phase and the darker regions are the $CuAl_2$ phase.

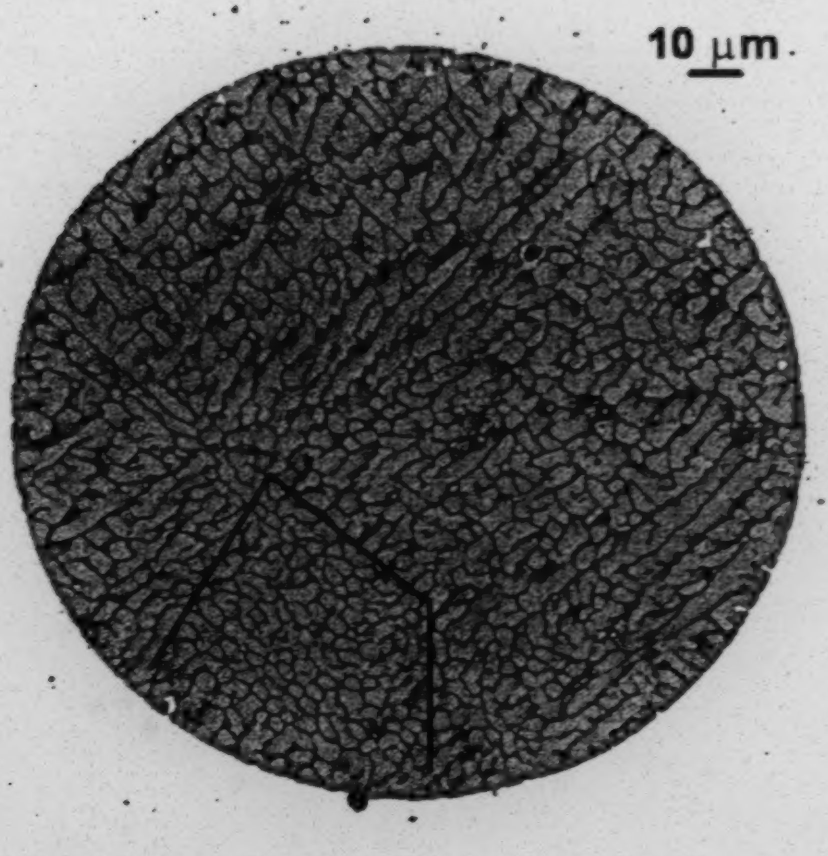

Figure 8.12: Microstructure gradation in a Al-10%Cu droplet very similar to that seen in the Al-17%Cu droplets.

Using the analysis performed by Boettinger et al [Boettinger1985], the role of dendrite kinetics in generating microstructural gradation in the droplets can be assessed. Boettinger et al [Boettinger1985] calculated the three components of the undercooling for a hypothetical metallic alloy system of varying composition solidifying in an undercooled melt. The dimensionless melt undercooling was 0.1 (≅35K for Al-Cu alloy), the partition coefficient was chosen as 0.1 and the ratio of the thermal to the solutal diffusion coefficient was chosen as 10^4. Since Al-Cu alloys have a similar thermal to solutal diffusivity ratio [Kurz2000], this result can be directly used with Al-Cu alloys. Moreover, several values of partition coefficient give similar results, and, therefore, the choice of 0.1 does not compromise the comparison with Al-Cu alloys, which have a partition coefficient value close to 0.17, as calculated from the Al-Cu phase diagram.

The results from Boettinger et al [Boettinger1985] are reproduced in Figure 8.13. It shows a phase diagram on which the values of the calculated undercooling components are superimposed. Also superimposed are the Al-Cu alloy compositions 5%Cu, 10%Cu and 17%Cu, respectively. This figure clearly shows that for the growth of dendrites in Al-5%Cu (or Al-4.3%Cu), thermal and solutal undercooling contribute approximately 45-50% each and thus, play a dominant role. On the other hand, the growth for the Al-10%Cu and Al-17%Cu is approximately 65-70% controlled by the solutal undercooling alone, and the thermal undercooling makes a minimal contribution. Because of the extremely high thermal diffusivity relative to the solutal diffusivity, the thermally controlled dendrite will have faster growth rates (Figure 8.3).

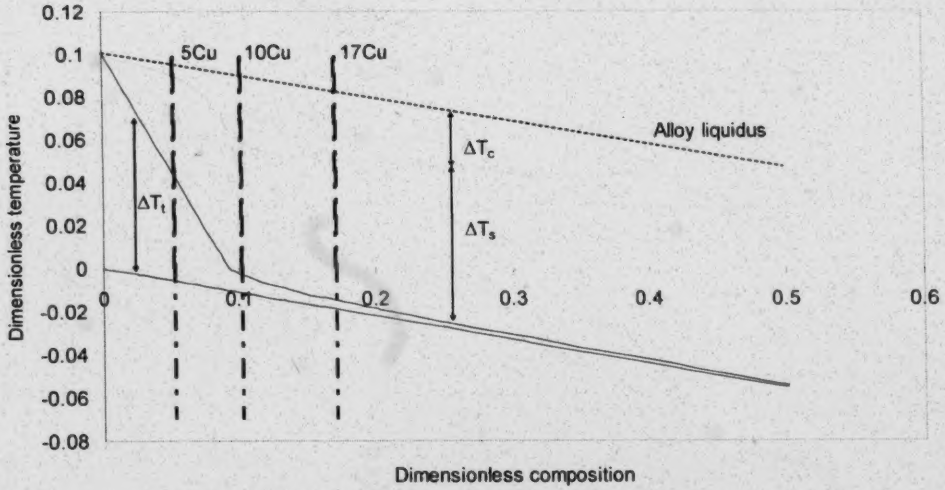

Figure 8.13: The three calculated undercoolings, capillary, solutal and thermal, presented in a dimensionless temperature-composition diagram. Data taken from Boettinger et al [Boettinger1985] with k=0.1 and α/D = 10000.

Based on the evidence of changing morphology and dendrite velocity analysis, the structure in Al-5%Cu appears to be a mix of solutal (Ultra-Fine region) and thermal (similar microstructural scale in Region II and III) dendrites, whereas the structure in Al-17%Cu is dominated by solutal dendrite. Furthermore, the dendrites in the Al-10%Cu droplet are also believed to be solutal controlled as well. This validates the LKT theory and also shows the difference in the "type" (solutal / thermal or a mix thereof) of dendrite as the alloy composition is changed. The difference in the "type" of dendrite also explains the difference in velocity evaluated for the Al-4.3%Cu and Al-17%Cu in Figure 8.3. Being solutal controlled, the dendrites of 17Cu depend on the solute diffusion and are slow compared to the thermal-diffusion-controlled 4.3Cu dendrite, which is much faster.

8.5 Dendrite velocity and effective partition coefficient

Microsegregation is quantified by the partition coefficient (C_s^*/C_l^*). Hence, a change in this ratio will change the microsegregation. As the experimental results show, the average Cu in the primary α-Al increases with respect to the equilibrium values (Figure 8.9). Therefore, an increase in the effective partition coefficient seems to occur during solidification as the alloy composition is increased from Al-5%Cu to Al-17%Cu. Such a change in partition coefficient can be caused by solute trapping, solute drag, dendrite remelting or a combination of all three but all of these parameters are dependent on the dendrite velocity. Therefore, using the dendrite velocity data predicted from the simulation, one can assess the weightage of each of these parameters that might be at play in changing the partition coefficient for the higher alloy composition droplet. This assessment is described next.

8.5.1 Solute trapping

Solute trapping occurs when the dendrite velocity is so high that solute rejection has no time to take place, and solute remains "trapped" in the solid, resulting in diffusionless transformation. The solute-trapping effect in the droplet solidification is seen by comparing the average dendrite velocity obtained from the solidification model results for the partition coefficient-velocity (k-v) plots obtained from the velocity-dependant partition coefficient LKT model. A typical partition coefficient-dendrite velocity plot obtained from the velocity dependant partition coefficient LKT model is shown in Figure 8.15. The partition coefficient calculation was carried out by using the Aziz model, which was described in Chapter 2. As mentioned in that chapter, the model predicts a monotonous increase in partition coefficient with an increase in velocity representing the solute-trapping effect with an increase in velocity.

Figure 8.14 suggests two important points. Firstly, the starting k value does not affect the velocity when the solute trapping begins, resulting in a similar increase in the value of k, and secondly, the velocity shown in the plot is related to the dimensionless velocity by the following relation [Lipton1987c],

$$\upsilon_d = \eta \varepsilon \bar{V} \tag{8.1}$$

where $\bar{V}$ is the dimensionless velocity, η is the ratio of the thermal to the solutal diffusivity and ε is the ratio of the interatomic jump distance and capillary length. Since both the jump distance and the capillary length are of nanometer magnitude, ε becomes close to unity [Lipton1987c]. Lipton et al [Lipton1987c] used $\eta = 10000$ for their simulation, and, therefore, the dimensionless velocity where the effect of velocity begins to take place is approximately 10^{-6}.

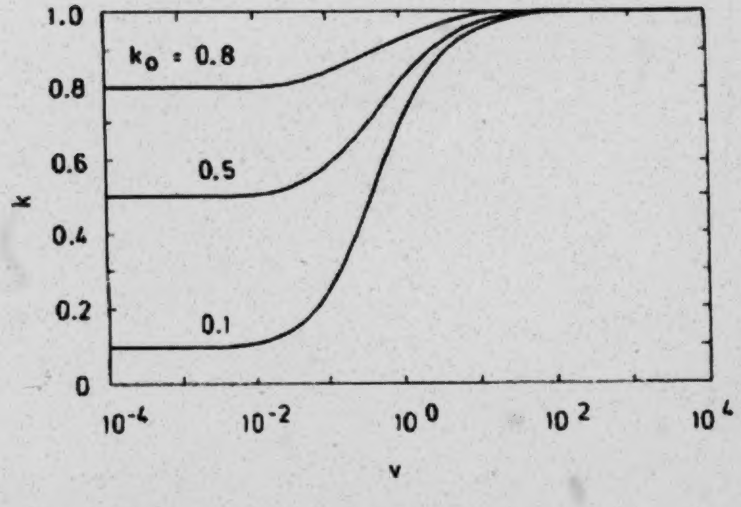

Figure 8.14: Variation in partition coefficient with dendrite velocity from velocity-dependant partition coefficient LKT model [Lipton1987c].

For our purposes, the above analysis is valid because the value of k (0.17 for the Al-Cu system) does not affect the velocity at which the deviation of k starts, and secondly, the ratio of the thermal to the solutal diffusivity for the Al-Cu system is approximately 10500, which is the same order of magnitude as that used in the model by Lipton et al [Trivedi1987c]. However, to determine if solute trapping exists in the droplets, one needs to convert the dimensionless velocity from Figure 8.14 to the actual dendrite velocity and then compare it with the dendrite velocity in the atomized droplets. The results for dendrite velocities are given in Table 8.6 for the droplets for all compositions. The dimensionless velocity and actual velocity are related according to the following equation [Lipton1987c]:

$$\bar{V} = V_{dend} \frac{d_0}{2a} \qquad (8.2)$$

where d_0 is the interatomic jump distance and 'a' is the thermal diffusivity. The value of d_0 can vary from 0.5 to 5 nm [Lipton1987c] and the thermal diffusivity in the Al system is of the order of 10^{-5} [Kurz2000]. Therefore, the actual dendrite velocity can vary from $\bar{V}*10^4$ or $\bar{V}*10^5$ m/s.

After appropriate conversion, the actual dendrite velocity versus the partition coefficient is shown in Figure 8.15. A comparison between the dendrite velocity values from the figure and from Table 8.6, it can be clearly seen that solute trapping will not be active for any alloy composition. With $\bar{V}*10^4$, 5Cu tends to show some solute trapping only in the initial growth regime, but due to the small time spent by the droplet in that regime, the effect of solute trapping, will be negligible. The value of the ratio $d_0/2a$ does not significantly affect the result.

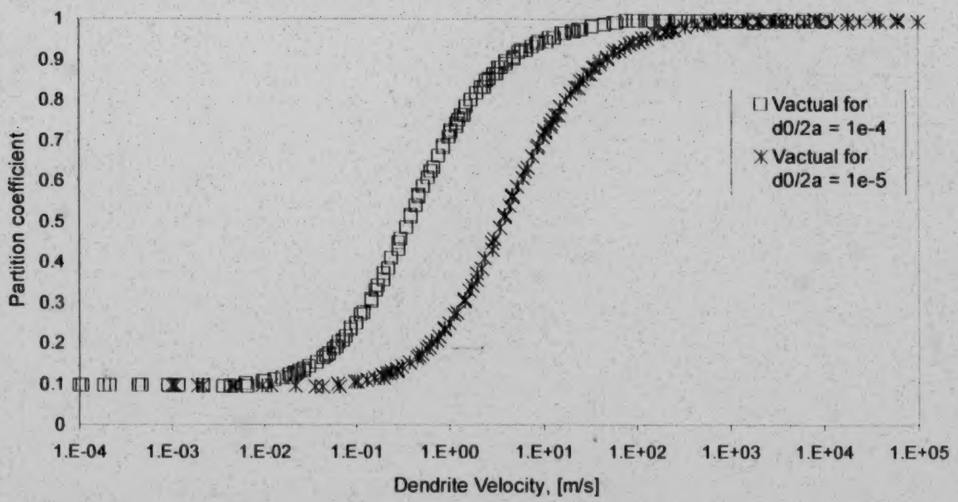

Figure 8.15: Variation in partition coefficient with dendrite velocity attained in the droplets during atomization [Lipton1987c].

Table 8.6: Average dendrite velocities in initial growth and recalescence periods for Al-5%Cu, Al-10%Cu and Al-17%Cu atomized droplets.

Alloy	Size / Gas	$(V_{dend})_{IG}$	$(V_{dend})_{Recal}$
5Cu, 20K, 0.5Rd	196μm, He	6.45 cm/s	1.82 cm/s
5Cu, 20K, 0.5Rd	925μm, He	4.89 cm/s	0.86 cm/s
5Cu, 20K, 0.5Rd	196μm, N_2	4.64 cm/s	0.68 cm/s
5Cu, 20K, 0.5Rd	925μm, N_2	4.46 cm/s	0.51 cm/s
10Cu, 20K, 0.5Rd	196μm, He	2.90 cm/s	1.82 cm/s
10Cu, 20K, 0.5Rd	925μm, He	1.71 cm/s	0.84 cm/s
10Cu, 20K, 0.5Rd	234μm, He	1.47 cm/s	0.62 cm/s
10Cu, 20K, 0.5Rd	925μm, N_2	1.29 cm/s	0.49 cm/s
17Cu, 20K, 0.5Rd	196μm, N_2	1.75 cm/s	1.78 cm/s
17Cu, 20K, 0.5Rd	925μm, He	0.95 cm/s	0.83 cm/s
17Cu, 20K, 0.5Rd	234μm, N_2	0.77 cm/s	0.60 cm/s
17Cu, 20K, 0.5Rd	780μm, N_2	0.65 cm/s	0.48 cm/s

8.5.2 Solute drag

Since solute trapping seems to be inoperative, the effective partition coefficient may be affected by solute drag. When the rejected solute from the solid does not diffuse away into the liquid, solute piles up in front of the advancing solid-liquid interface. This pile exerts an attractive force on the neighboring solute atoms in the melt. As the interface advances, the attractive force from the solute pile, “drags” the neighboring solute atoms with it. Thus solute drag results from the solute pile-up in front of the advancing interface. Hillert et al [Hillert1976] have generated a Solute Drag Parameter (SDP) as a function of velocity for different alloy compositions. The SDP gives an estimate of the degree of pile-up in front of the interface, and, hence, it gives a qualitative estimate of the amount of solute-drag that is present. Therefore, it also gives an estimate of the effect of solute drag. Hence, the basic difference between solute trapping and solute drag is that very high velocities may be required for solute trapping to take place, whereas solute drag can take place even with slower growth rates.

To evaluate the SDP, the velocity was kept constant, and the alloy composition changed. This was repeated for a range of velocities, and, thus, a map could be drawn out relating the alloy composition, interface velocity and the SDP to each other. Since dimensionless alloy compositions were used, their data can be used in the case of Al-Cu alloys. The plot in Figure 8.14 shows the change in the SDP with velocity for different Cu compositions in the Al-Cu system.

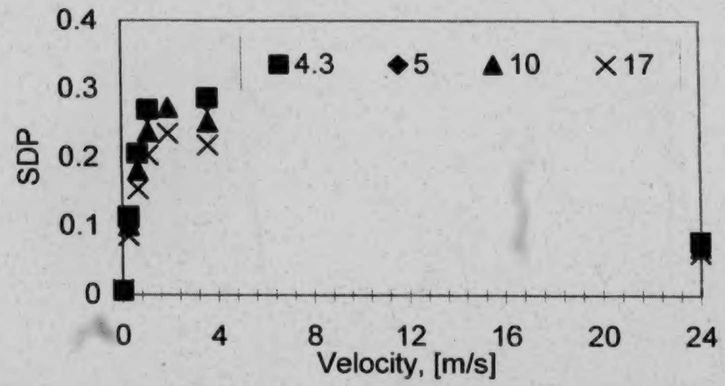

Figure 8.16: Solute Drag Parameter for Al-Cu system following the analysis of Hillert et al [Hillert1976].

The shape of the curve can be explained as follows. At very low velocities, 0.012 m/s or lower, no pile-up occurs, and, hence, no solute drag is present. On the other hand, with extremely high velocities in the order of 5 m/s and above, the solute rejection is limited, and solute trapping is dominant. Consequently, a limited pile-up occurs at high velocities. Thus, at intermediate velocity values between 1 to 4 m/s, a peak in the solute drag can be expected, as seen in the figure. The pile-up in front of the interface would affect the rejection of the solute across the solid-liquid interface from solid into the liquid. This result would change the effective partition coefficient, and a very high pile-up or solute drag would result in no or very little solute being transferred. Hence, diffusionless transformation may result [Hillert1977].

To see the effect of solute drag on Al-Cu solidification, the dendrite velocities obtained from the droplet solidification model were compared to the data in the plot in Figure 8.16. This analysis provided a qualitative information on how much solute drag effect is taking place when the alloy composition is changed and also when the solidification proceeds from nucleation to the end of recalescence for a given alloy composition. Note that the quantitative effect of solute drag on velocity is not available in the literature, and, therefore, these velocities cannot be modified to take into account the presence of solute drag. Therefore, the velocities obtained from the LKT model have to be used.

To check the solute drag effect as the alloy composition is changed, the following tables were generated. Tables 8.7 to 8.9 show the average values of LKT dendrite velocities for Al-5%Cu, Al-10%Cu and Al-17%Cu during the initial growth and recalescence periods. The droplets used in these simulations are the same as those analyzed for measuring the eutectic weight percent and calculating the Cu content in the primary phase. The average dendrite velocities were calculated by using the Trapezoidal rule, as described by Eqn. 7.40 in Chapter 7 for the average solute solubility calculation. For the solute solubility, the average was evaluated over a range of fraction solid values whereas for the velocities, the average was evaluated over time. Using the data shown in Figure 8.16, the SDP was evaluated against the average velocity in the initial growth and recalescence regimes for the three alloy compositions. Since the maximum velocity occurs at the end of the initial growth regime (points A_5 and A_{30} in Figure 8.4), the average velocity is higher in the initial growth regime than in the Recalescence regime.

Table 8.7: Solute Drag parameter calculated (from Hillert et al [Hillert1976]) for dendrite velocities obtained from LKT dendrite kinetics for Al-5%Cu atomized droplets.

Alloy	Size / Gas	$(V_{dend})_{IG}$	SDP	$(V_{dend})_{Recal}$	SDP
5Cu, 20K, 0.5Rd	196μm, He	6.45 cm/s	0.03	1.82 cm/s	0.008
5Cu, 20K, 0.5Rd	925μm, He	4.89 cm/s	0.02	0.86 cm/s	0.004
5Cu, 20K, 0.5Rd	196μm, N_2	4.64 cm/s	0.02	0.68 cm/s	0.003
5Cu, 20K, 0.5Rd	925μm, N_2	4.46 cm/s	0.02	0.51 cm/s	0.002

Table 8.8: Solute Drag parameter calculated (from Hillert et al [Hillert1976]) for dendrite velocities obtained from LKT dendrite kinetics for Al-10%Cu atomized droplets.

Alloy	Size / Gas	$(V_{dend})_{IG}$	SDP	$(V_{dend})_{Recal}$.	SDP
10Cu, 20K, 0.5Rd	196μm, He	2.90 cm/s	0.01	1.82 cm/s	0.009
10Cu, 20K, 0.5Rd	925μm, He	1.71 cm/s	0.009	0.84 cm/s	0.005
10Cu, 20K, 0.5Rd	234μm, He	1.47 cm/s	0.008	0.62 cm/s	0.004
10Cu, 20K, 0.5Rd	925μm, N_2	1.29 cm/s	0.007	0.49 cm/s	0.003

Following points can be noted from the tables. For a droplet size of any given composition, the initial growth regime has a higher velocity than that of the recalescence regime. This can be explained by the fact that during initial growth, the droplet temperature is still falling, resulting in increasing undercooling. Corresponding with the higher velocities in the initial growth regime, the SDP is also higher. For the Al-5%Cu droplet, the SDP is almost an order of magnitude higher in the initial growth regime compared to that of the recalescence regime.

This ratio reduces for the Al-10%Cu and Al-17%Cu droplets. In fact, for the 17Cu droplet, the SDP remains almost the same between the initial growth and the recalescence regimes. Thirdly, the value of the SDP is higher for Al-5%Cu compared to Al-10%Cu and Al-17%Cu droplets.

Table 8.9: Solute Drag parameter calculated (from Hillert et al [Hillert1976]) for dendrite velocities obtained from LKT dendrite kinetics for Al-17%Cu atomized droplets.

Alloy	Size / Gas	$(V_{dend})_{IG}$	SDP	$(V_{dend})_{Recal}$	SDP
17Cu, 20K, 0.5Rd	196μm, N_2	1.75 cm/s	0.009	1.78 cm/s	0.009
17Cu, 20K, 0.5Rd	925μm, He	0.95 cm/s	0.006	0.83 cm/s	0.005
17Cu, 20K, 0.5Rd	234μm, N_2	0.77 cm/s	0.005	0.60 cm/s	0.004
17Cu, 20K, 0.5Rd	780μm, N_2	0.65 cm/s	0.004	0.48 cm/s	0.003

The observed experimental results suggest that for the Al-10%Cu and Al-17%Cu droplets, an SDP in the range of 1e-3 results in an increase in the partition coefficient during the phase transformation. For Al-5%Cu, however, even a higher range of SDP values is seemingly not enough to cause a change in the partition coefficient. Some of the possible reasons for this are discussed next.

Owing to high dendrite velocities, the time spent in the initial growth regime by a Al-5%Cu droplet is much smaller compared to the time spent by the Al-10%Cu and Al-17%Cu droplets in the same regime. Furthermore, relative to the time spent by Al-10%Cu and Al-17%Cu, that spent by the Al-5%Cu droplet from the onset of nucleation to end of recalescence is very small compared to the total solidification time. Moreover, with a higher degree of coarsening in the Al-5%Cu, which tends to push the system towards equilibrium, any change in the partition coefficient may be lost. Lastly, different alloy compositions may have different solute drag effects for a given dendrite velocity. In other words, the effect of solute drag on velocity may be composition-dependant.

Hillert et al [Hillert1976] also performed calculations on the solute drag effect to study diffusion – to – diffusionless solidification for binary alloys. The approach taken was to fix the solute drag parameter and plot a map of dendrite velocity versus dendrite radius for a range of alloy composition. The solute drag parameter was fixed at 0.1, which is much higher than that calculated for the atomized droplets. Therefore, a direct comparison cannot be made. However, solute drag is dependant on the alloy composition, as well as the dendrite velocity, and, therefore, a coupling effect between the dendrite velocity and solute drag might exist. This is so because solute pile-up would depend on the alloy composition. During solute drag, when a pile-up of solute occurs across the interface, the partition coefficient may be affected. This effect, in turn, would affect the interface growth rate. Hence, the change in partition coefficient due to solute drag requires knowledge of this coupling effect. No such information is available in the literature, therefore, this area needs to be studied to understand the effect of solute drag in more detail.

Based on the above analysis, the solute drag seems to have some effect on the Al-10%Cu and Al-17%Cu droplet solidification, but the dendrite velocities are not high enough to cause solute trapping in any of the alloys. This may be due primarily to the low heterogeneous nucleation undercooling whereby the dendrite velocity is too low for solute trapping to set in. The Al-5%Cu droplets do indeed show the possibility for solute trapping, but only during the initial growth regime which has been evaluated to range from 0.1 to 0.8 volume percent. Such a low amount would not have any effect on the final eutectic fraction or the Cu content of the primary phase. Recall the poor comparison between the model and the experimental results for higher alloy compositions. With solute drag playing a role in promoting diffusionless solidification, the effect of solute drag on partition coefficient needs to be considered.

8.5.3 Dendrite remelting

Another important consequence of dendrite velocity and recalescence is dendrite remelting. At the end of recalescence, if the dendrite temperature exceeds the equilibrium liquidus temperature of the alloy, then dendrite remelting may take place. Note that this would be a local effect, and only a small fraction of a solid dendrite (in the tip region) would melt. A fraction of dendrite that melts, with larger amount of Cu in it from diffusionless solidification, will result in the Cu going into the liquid. Thus, dendrite remelting will push the system towards higher microsegregation as opposed to what occurs with diffusionless solidification. The non-isothermal atomization droplet solidification model predictions by Heringer et al [Heringer2004] showed that dendrite remelting is possible. Since Al-5%Cu would have a higher dendrite velocity than that of Al-17%Cu for a given undercooling (Figure 8.3), the Al-5%Cu droplet would undergo more dendrite remelting. However, the amount of solute in the primary phase would depend on the degree of diffusionless solidification, which requires an analysis of the effect of solute trapping and solute drag on the dendrite velocity. This analysis is qualitative since the dendrite remelting phenomenon cannot be modeled for an isothermal case as local fluctuations in the dendrite temperature need to be tracked, which is beyond the capability of the model proposed in this work.

The effect of velocity on the microsegregation has been assessed. The solute trapping appears to have little effect, and solute drag may be the active phenomenon in increasing the average solute solubility of the primary phase in the alloys with higher Cu content. The rest of this chapter is devoted to assessing the variables that can affect the dendrite velocity, and, consequently, microsegregation.

8.6 Center-Surface nucleation

8.6.1 Effect on recalescence

One of the factors that can affect the dendrite velocity is the position of the nucleation site within the atomized droplet. Figures 8.17 and 8.18 show the simulation results for a Al-17%Cu, 460 μm droplet, atomized in He. The undercooling was assumed to be 20K, and the two limiting nucleation site positions were placed at the center ($0\,R_p$) and the surface ($1.0\,R_p$), respectively. The thermal history is shown in Figure 8.17 whereas the fraction solid profile is shown in Figure 8.18. The legends on the figures are the same as those explained in Figure 8.1. From Figure 8.17 it is clear that the degree of recalescence changes when the nucleation position is changed. The difference in the final temperature at the end of recalescence for the two nucleation positions is 8K, with the center nucleation showing a higher recalescence-end temperature. The magnitude of the recalescence (temperature difference between points A and B in Figure 8.17) is also higher for the center nucleation (17K as compared to 12K). This change is due to the difference in heat balance as a different grain volume fraction, f_g, is formed for the two nucleation positions.

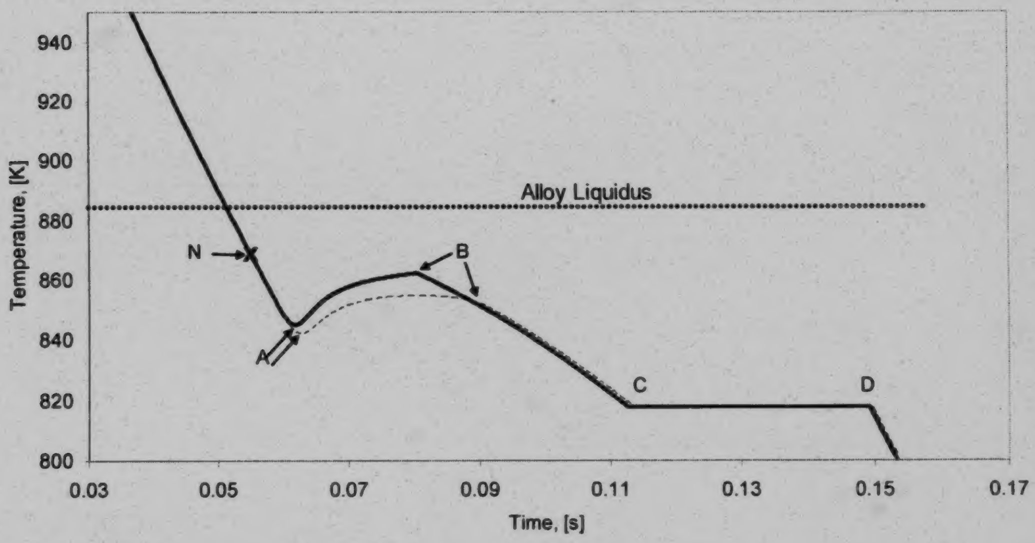

Figure 8.17: Thermal history for a Al-17%Cu droplet atomized in He. Undercooling is 20K and the nucleation position is chosen to be at the center (bold line) and the surface (lighter lines).

The plot for the fraction solid f_s and its components f_g and f_i is shown in Figure 8.18. In Figure 8.18, soon after nucleation, f_i shows a value of 1 for both the cases. This value represents the nucleus with a supersaturation of unity. The result shows that as the nucleation position changes, some change occurs in f_s and its components, f_g and f_i, from the start of the nucleation to the end of recalescence. For off-center nucleation, for example, f_g shows a slower rate of growth because of the difference in the f_g volume that takes part in the heat balance equation. This result can be understood with the aid of Figure 7.5 in Chapter 7, which shows the progressive growth of a grain envelope from an off-center nucleus. By visualizing a nucleus at the droplet surface, one can see that only a fraction of the grain volume would take part in the heat balance as compared to that of a grain growing from the center. This would result in a difference in the velocity and, subsequently, also in the amount of recalescence. The difference in the recalescence fraction solid for the two nucleation positions is 2.5%, with a higher amount found in the center nucleation. The reason for these differences is the dendrite velocity attained in the droplet when the nucleation position is changed.

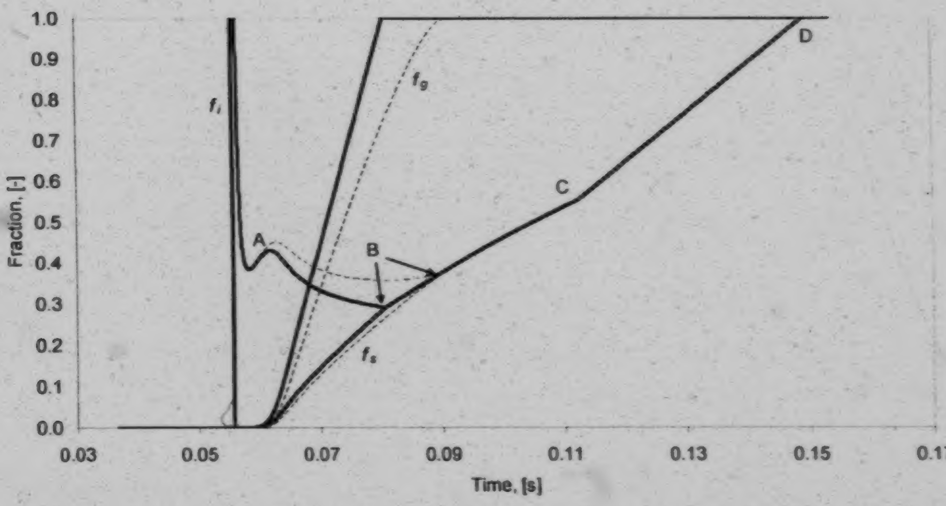

Figure 8.18: Fraction solid history for the same droplet as shown in Figure 8.17. The lighter lines represent surface nucleation while the darker lines represent center nucleation.

8.6.2 Effect on eutectic

Table 8.1 showed the sensitivity analysis of changing the nucleation position on weight percent eutectic. The results in Table 8.1 clearly show that the amount of eutectic changes in Al-4.3%Cu is minimal, as the nucleation position is changed from $0\,R_p$ to $1.0\,R_p$. To assess the role of dendrite velocity, the average dendrite velocity in the region between nucleation and recalescence for the two cases was evaluated. For the center nucleation, the average velocity was 0.92 cm/s while the average velocity for the surface nucleation was 1.3 cm/s. These velocity values are similar in magnitude to the dendrite velocity values presented in Tables 8.6 to 8.9 for the solute drag and solute trapping analysis. From that analysis, this change in velocity between the center and surface nucleation is not high enough for the solute trapping or solute drag effect to be substantially different. Hence, no change in eutectic is expected with a change in the nucleation position. Recall that the experimental observation of a change in the eutectic with nucleation position was not possible with low resolution of the tomography. Such experimental data can provide a very useful validation of the effect of nucleation position on microsegregation.

8.7 Effect of undercooling

8.7.1 Nucleation undercooling

The effect of small changes in undercooling for Al-4.3%Cu has been shown in Table 8.2. It clearly shows no change in the eutectic amount as the undercooling is changed by 40K. To test the effect of dendrite velocity on microsegregation for the Al-17%Cu, the undercooling was changed for the Al-17%Cu droplets also. The equilibrium alloy freezing range for the 17Cu is about 65K, and, therefore, the undercooling was changed from 5K to 65K. The current model is based on equilibrium phase diagram, and, therefore, a higher range of undercooling values could not be considered.

It was found that increasing the undercooling from 5K to 65K for the 17Cu alloy droplets increases the solubility in the primary phase. However, the increase was only of 2% (relative). Although the average dendrite velocity would increase with increasing undercooling, however, on varying the undercooling from 5K to 65K, the change in velocity did not affect the microsegregation significantly. The average velocity for 5K of undercooling was 1.3 cm/s while that for 65K of undercooling was 2.3 cm/s. The distinct increase in velocity with increasing undercooling is to be expected. At higher undercoolings, the dendrite velocity will be higher, and will result in more recalescence, with perhaps higher degree of solute trapping, and, subsequently, increased solute solubility of the alloy. Therefore, some effect of velocity is expected in the case of higher undercooling. With equilibrium phase diagram approximation, this effect of velocity on solute trapping will not be visible. A velocity-dependant partition coefficient expression, as developed by Lipton et al [Lipton1987c], would be useful for testing the sensitivity of undercooling in the higher range. Note that the velocity at 65K undercooling is higher in magnitude than the velocity values given in Table 8.6 for the 17Cu. Thus, the effect of solute drag might also change with the undercooling (and therefore, with dendrite velocity). However, no expression, like the one for solute trapping effect, is available that can relate the coupled effect of velocity and solute drag and its subsequent effect on partition coefficient.

8.7.1.1 Effect of cooling rate

The product of thermal gradient and dendrite velocity has units of cooling rates [Lavernia1989], and the thermal gradient is a result of the undercooling. Therefore, the effect of undercooling and dendrite velocity on microsegregation can also be expressed by plotting microsegregation as a function of cooling rate. As mentioned before, cooling rate has been an integral part of representing the atomization experiment results, and, therefore, such a plot would be of interest. The eutectic data for Al-5%Cu has been validated (comparison between model and experiment), and, therefore, the microsegregation result from the experiment for Al-5%Cu is plotted as a function of cooling rate. The cooling rate is calculated from the model and is defined as the temperature difference between point N and point D in the thermal history plot (Figure 8.1) divided by the time corresponding to these two points in that plot. The results for the weight percent eutectic versus cooling rate and the average Cu solubility versus cooling rate are shown in Figures 8.19 and 8.20, respectively. Each data point represents a set of droplets of a given size atomized under a given atomization gas. The small droplet under He gas shows the highest cooling rate while the larger droplet under N_2 shows the lowest cooling rate. Thus, the model shows the effect of droplet size as well as gas type.

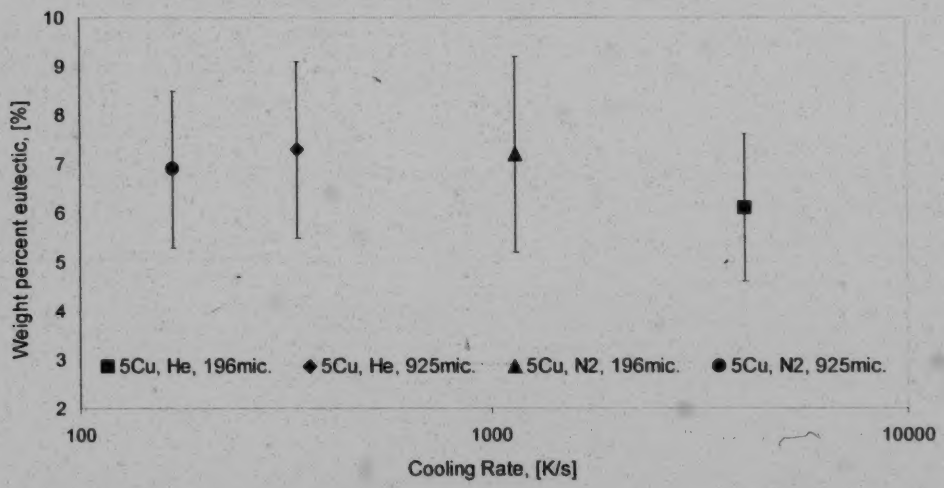

Figure 8.19: Effect of cooling rate on the weight percent eutectic. The cooling rates were evaluated from the model.

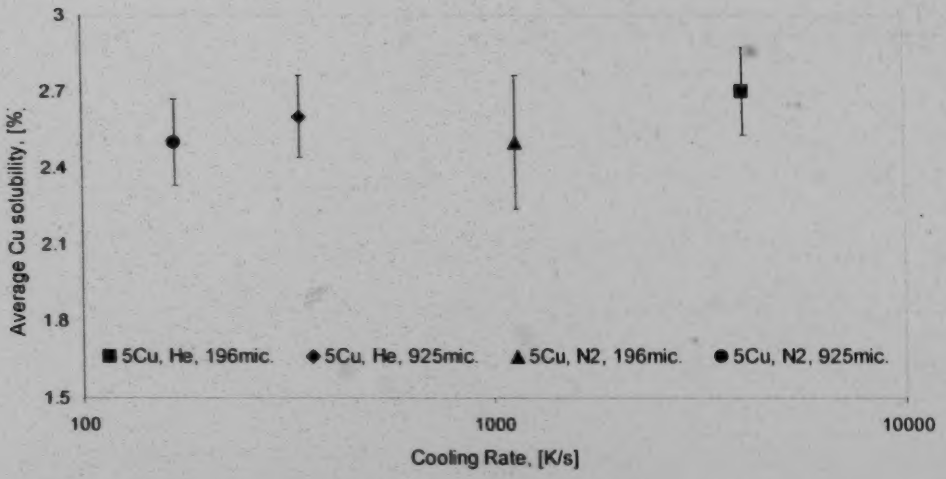

Figure 8.20: Effect of cooling rate on the average Cu content of the primary phase. The cooling rates were evaluated from the model.

From Fig. 8.19, the cooling rates experienced by the droplets vary from 10^2 to 10^3 K/s. In this range, the figure shows a small decrease in the amount of eutectic. Sarreal and Abbaschian [Sarreal1986] have studied microsegregation in Al-4.9%Cu alloy over a range of cooling rates (10^{-1} to 10^4 K/s) obtained from constrained growth conditions. For the range of cooling rates between 10^2 to 10^3 K/s, their results showed an appreciable decrease in the amount of $CuAl_2$ (hence the eutectic) as the cooling rate increased. Since their experiments were based on constrained growth, a direct comparison with this work cannot be made. However, the Al-5%Cu atomized droplet shows a small decrease in the amount of eutectic, which is the same trend as has been reported by Sarreal and Abbaschian. Thus, the cooling rates in the range of 10^2 to 10^3 K/s during atomization have a small effect on microsegregation.

As the cooling rate increases, corresponding to the decrease in the eutectic amount, a small increase seems to occur in the average solubility of Cu in the primary phase (Fig. 8.20). In this case too, the cooling rate does not has a very significant effect. Lavernia and coworkers [Ruhr1990] have studied the solubility of Mn in Al for cooling rates in the range of 10^4 to 10^5 K/s through gas atomization experiments. They have reported that the solubility of Mn increased by about 10% (relative) as the cooling rate increased. In the present work, the increase in Cu solubility is about 8% for a cooling rate in the range of 10^2 to 10^3 K/s. Thus, the present work confirms the effect of faster cooling rate with a consequent, albeit small, decrease in microsegregation. It should be noted, however, that this analysis is based on mean values of the volume eutectic and average Cu solubility without taking into account the error bars.

Extending the notion of undercooling – cooling rate relationship further, the effect of changing the undercooling on the cooling rate can be determined. Model simulations were run for a 196 μm Al-5%Cu droplet atomized in He and the undercooling was changed from 5K to 50K. At an undercooling of 5K, the cooling rate was 4670 K/s, which decreased to 2830 K/s at 50K. Thus, the change in undercooling from 5K to 50K, shows an approximately 40% change in the cooling rate. The cooling rate is defined according to Eqn. 1.1. At low undercoolings, the nucleation start temperature is reached sooner. However, because of the slower growth rates at the lower undercoolings, the time spent by the droplet in the initial growth and recalescence region will be longer than that at higher undercoolings.

Recall that the recalescence-end temperature and fraction solid formed in the nucleation to recalescence-end period is almost the same even when the undercooling is changed (Section 8.1 – reference droplet). Therefore, the time spent by the droplet from the end of recalescence to complete solidification will be similar for any undercooling. However, the total solidification time spent by the droplet under higher undercooling will be smaller than that of the droplet under lower undercooling because the time spent from onset of nucleation to the end of recalescence by the droplet under higher undercooling is smaller compared to that spent by the droplet undergoing a lower undercooling. There is also a difference in the freezing range of the alloy at different undercoolings. For the same solidification-end temperature (same eutectic temperature), the droplet with a higher undercooling will have a smaller freezing range. This difference in the total solidification time and freezing range for different undercoolings, results in different cooling rates. The total solidification time for 5K undercooling is 21 ms and that for 50K is 19 ms. This solidification time appears in the denominator of Eqn. 1.1. The freezing range for 5K undercooling is 98K while that for 50K undercooling is only 53K and appears in the numerator of Eqn. 1.1. Therefore, with an increase in undercooling, the values in both the numerator and denominator decrease. However, since the decrease in numerator value is much more than the decrease in denominator value, there is a net decrease in the cooling rate for a higher undercooling.

Similar results were obtained for droplets of different sizes, different gas types and droplets of different alloy compositions. On changing the gas type to N_2, a similar 40% decrease in cooling rate was obtained as the undercooling was increased from 5K to 50K. Likewise, for a 925 μm droplet under He, increasing the undercooling again resulted in a 40% decrease in the cooling rate. For the Al-17%Cu droplet, a 925 μm droplet atomized under He showed a 67% change in the cooling rate. In all the cases, the higher undercooling droplet always had a smaller cooling rate. Hence, the microsegregation model shows that the change in undercooling has some effect on the cooling rate.

The aforementioned result has two implications. Firstly, the alloy composition has some effect on the undercooling – cooling rate relationship. According to the result for a change in the cooling rate for the Al-17%Cu droplet, a higher alloy composition has more effect of undercooling on the cooling rate. This can be understood by the fact that for a given undercooling, differences in alloy chemistry result in different dendrite velocities (Figure 8.3). Secondly, if coarsening is taken into account, then a droplet with higher undercooling should have a finer scale since the total solidification time is smaller (Section 2.3.1.2.2). However, the cooling rate for a higher undercooled droplet is smaller, and according to equation 2.1, it should have a coarser scale. Thus, the SDAS trends are contradictory, when considered with respect to (a) the cooling rate and (b) the solidification time. This implies that some parameter apart from the SDAS – Cooling Rate relationship may be required to assess solidification processes.

8.7.1.1.1 Macrosegregation

It was shown in the previous section that the effect of cooling rate is not readily apparent because of the large error bars. Their presence is briefly discussed in this section. The Cu solubility calculations were performed by using the volume percent eutectic data and the weight percent $CuAl_2$ data (Chapter 6). While the eutectic volume percent was measured using stereology on randomly sectioned individual droplets, the $CuAl_2$ data were measured by using Neutron Diffraction (Chapter 3). With a high depth of penetration of the neutron beams, the $CuAl_2$ weight percent was measured for the entire droplet volume. To measure the volume of the eutectic for the entire droplet, individual droplets were sectioned and stereology calculations performed on each section. It was pointed out in Section 3.4 that the stereological analysis assumes a random distribution of the eutectic within the droplet volume. However, in the presence of macrosegregation, the eutectic distribution within the droplet volume may not be random, and some local areas of higher (or lower) eutectic amount may exist within a droplet. In such a case, the stereology results will depend on which sections of the droplet have been analyzed. Since the droplet sectioning was random (Section 3.1), the presence of macrosegregation can result in large standard deviations in the measured volume percent eutectic. These deviations in turn, would propagate to weight percent eutectic and Cu-solubility calculations. Recall that large error bars have indeed been obtained for weight percent eutectic and Cu solubility results, thus indicating the presence of macrosegregation in the droplets.

Statistically, a random distribution of the eutectic within the total droplet volume would be defined as equal amount of eutectic present in any given sub-volume of the droplet. Therefore, stereology on a randomly distributed eutectic would not be affected by the section selected for analysis. Macrosegregation, on the other hand, can render the distribution to be not random. The effect of macrosegregation on Stereology was analyzed by generating a Quantile-Quantile (Q-Q) plot for the volume percent eutectic from each individual section for a given set of droplets. The Q-Q plot compares the experimental values of the eutectic with a theoretical normal distribution (for a perfectly random distribution). Therefore, a random distribution in the experimental eutectic would yield a straight line at $45\ ^0$ and the absence of random distribution would result in a line with a slope other than $45\ ^0$.

A typical Q-Q plot for an Al-10%Cu droplet set is shown in Figure 8.21. The plot is for a 1000 μm droplet atomized in He. The equation for the straight line clearly shows that the line is not at $45\ ^0$ (the slope is not equal to 1), thus indicating the presence of macrosegregation in the droplet. Based on Electron Back Scattered Diffraction (EBSD) experiment on an Impulse Atomized Al-10%Cu droplet, Heringer et al [Heringer2004] show the presence of macrosegregation.

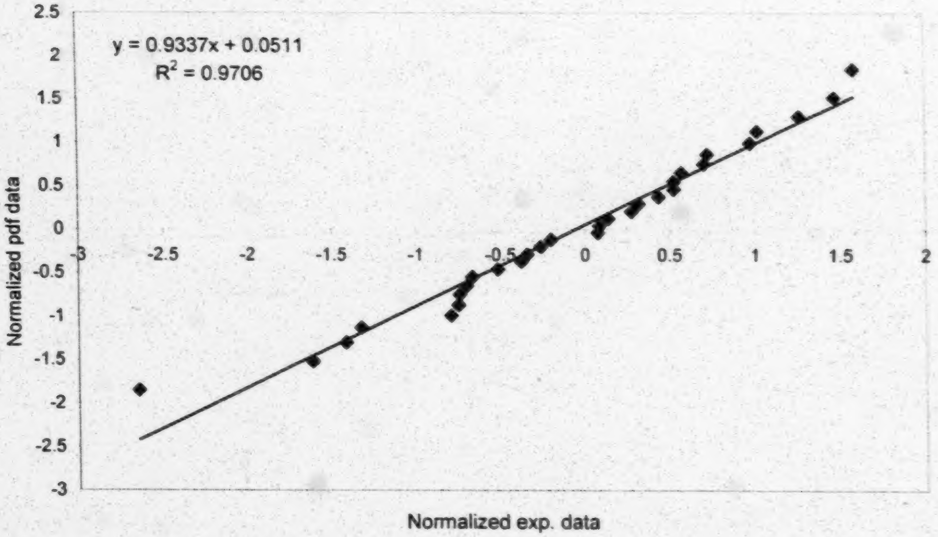

Figure 8.21: Q-Q plot for an Al-10%Cu alloy 1000μm droplet atomized in He gas. The slope of the line is not equal to 1, indicating the deviation from normalcy as a result of macrosegregation.

Moreover, the model result for f_i as a function of time is shown in Figure 8.22 for the reference droplet. The result is for an undercooling of 5K. Recall that f_i is the supersaturation term in the model, which represents the chemistry of the liquid phase. The peak showing $f_i = 1$ represents the onset of nucleation, following which, f_i decreases drastically to some value and subsequently increases during the initial growth regime. At the end of initial growth period when recalescence sets in and the temperature rises, f_i decreases continuously. After recalescence, the temperature continuously decreases with a corresponding increase in the value of f_i. According to the phase diagram, the supersaturation, or the amount of Cu in the liquid (or solid), would decrease as temperature increases. The change in f_i with time clearly shows that different volumes of the droplet would have different chemistries. Also shown in the figure is the average f_l value, which further confirms that f_l values (or chemistry, and, hence, the amount of eutectic) different from the average value can exist within the droplet. Thus, the model qualitatively describes the presence of macrosegregation within the droplet.

Based on the above, the evidence of the presence of macrosegregation within the droplets is quite strong. Therefore, the lack of trend seen in weight percent eutectic and Cu solubility with change in cooling rates can be attributed to macrosegregation. Since the dendrite growth velocity plays an important role in the period between onset of nucleation and end of recalescence, the change in f_l reflects the role of dendrite growth velocity in causing macrosegregation. Consequently, since growth rates can vary with alloy composition, macrosegregation can also vary with the changes in alloy composition. The presence of macrosegregation and the effect of dendrite growth velocity on macrosegregation also suggest that the position of nucleus could affect segregation patterns across the droplet volume. In other words, the presence of macrosegregation is an evidence of spatial variation in microsegregation that can be affected by the nucleation position. Of course, a non-isothermal model can provide more quantitative information about this phenomenon.

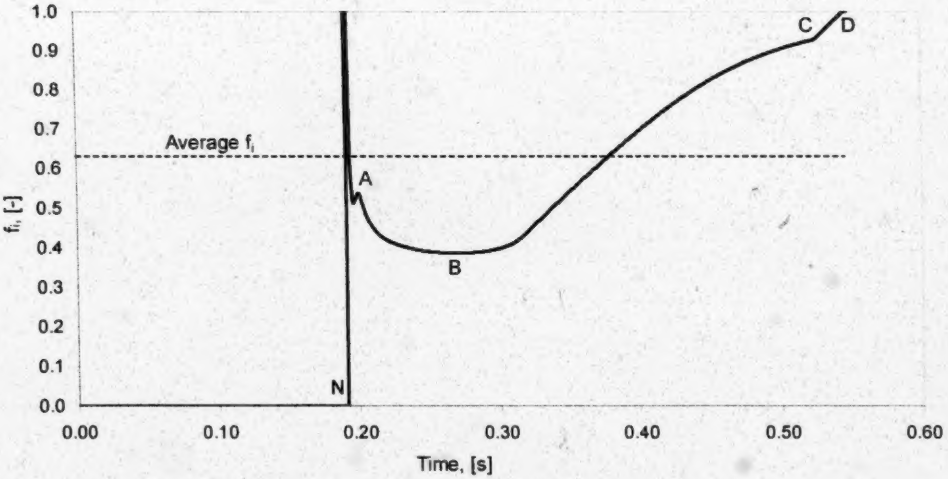

Figure 8.22: Time history of the supersaturation term f_i.

8.8 Effect of alloy composition

The microsegregation results show that the alloy composition seems to have more effect than the cooling rate. A simple way to understand this is that as the composition increases from Al-5%Cu to Al-17%Cu, the amount of eutectic falls below the Equilibrium amount for the higher composition (Figure 8.7). If the effect of composition were not present, the data points would have been positioned between Scheil-Gulliver and Equilibrium (as seen in the Al-5%Cu droplets) for all the compositions. Furthermore, these data points lie below the Equilibrium value for the entire range of droplet sizes and gas types even when the error bars are included. Hence, the alloy composition has more effect than the cooling rate.

The effect of alloy composition on microsegregation can also be understood in terms of the dendrite velocity. Microsegregation depends on the dendrite velocity, which, in turn, is controlled by different components of undercooling, thermal+solutal for Al-5%Cu and solutal for the Al-17%Cu. Furthermore, with the alloy composition effects on solute drag, a change in the degree of segregation with the alloy composition can be expected.

Moreover, the phase diagram approximation also reveals the importance of the alloy composition in microsegregation and the partition coefficient values as the alloy composition is changed. With Approximation I, the partition coefficient changes from 0.18 to 0.22, corresponding to the composition change from Al-5%Cu to Al-17%Cu. With these partition coefficient values, the model results are closer to the experimental values as compared to the results from Approximation II with constant partition coefficient. Thus, the partition coefficient of the droplets during solidification must have increased with respect to equilibrium value, with a subsequent increase in the primary phase Cu content (or a decrease in the volume percent eutectic). Such an increase in the partition coefficient also suggests that, for Al-10%Cu and Al-17%Cu, some degree of diffusionless solidification seems to result in an increase in the effective partition coefficient. Therefore, an equilibrium approximation is not enough to model microsegregation for 10Cu and 17Cu alloy droplets. On the other hand, the Al-5%Cu droplets seem to have solidified with partition coefficient values close to equilibrium, and, therefore, these droplets can be modeled with linear approximations. The percentage difference in average Cu solubility, due to the different phase diagram linearization technique (shown in Table 8.5), increases as the alloy composition increases. Therefore, the microsegregation results are more sensitive to the choice of linear approximation method as the alloy composition is increased.

Based on the analysis presented above, the Al-5%Cu droplet appears to solidify with solute diffusion whereas when the alloy composition is increased to Al-10%Cu and Al-17%Cu, an increasing amount of diffusionless transformation occurs. Thus, the change in the partition coefficient needs to be captured. Since velocity plays an important role during solidification, a velocity-dependent partition coefficient value is required for modeling Al-10%Cu and Al-17%Cu droplets. To obtain this value, in the case of solute drag, its effect on dendrite velocity and subsequent effect on the partition coefficient need to be established first. The solute trapping, on the other hand, has been well researched, and Lipton et al [Lipton1987c] have developed dendrite kinetic model based on a velocity-dependant partition coefficient. As a second step, the linearized approximation of the phase diagram can be replaced by the composition-temperature relationship from the actual phase diagram.

8.9 References

[Baker1971]: "Solidification", Baker J.C. and Cahn J.W., American Society for Metals, 1971, pp 23-56.

[Boettinger1985]: Boettinger W.J. and Coriell S.R., In Science and Technology of the Undercooled Melt, (eds.) Sahm P.R, Jones H. and

Adam C.M., NATO ASI series, Series E: Applied Sciences - N. 114, 1985, pp 81-110.

[Boettinger1986]: "An analysis of the microstructure of rapidly solidified Al-8wt percent Fe powder", Boettinger W.J., Bendersky L. and Early G., Metallurgical Transactions A, v. 17A, n. 5, 1986, pp 781-790.

[Flemings1987]: "Dendritic growth of an undercooled Nickel Tin alloy", Flemings M.C., Shiohara Y., Wu Y. and Piccone T.J., In "Undercooled Alloy Phases", Collings E.W. and Koch C.C (eds.), The Metallurgical Society, pp 321-334.

[Heringer2004]: "Modélisation de la solidification de gouttes atomisées, Heringer R., Ph. D. Thesis, Institut National Polytechnique de Lorraine, Nancy, France, 2004.

[Hillert1976]: "A treatment of the solute drag on moving grain boundaries and phase interfaces in binary alloys", Hillert M. and Sundman B., Acta Metallurgica, v.24. 1976, pp 731-743.

[Hillert1977]: "A solute drag treatment of the transition from diffusion-controlled to diffusionless solidification", Hillert M. and Sundman B., Acta Metallurgica, v.25. 1977, pp 11-18.

[Kurz2000]: "Fundamentals of Solidification", Kurz W. and Fisher D.J., TransTech Publications, Switzerland, 2000, pp 293-294.

[Lavernia1989]: "On quenching rates, secondary dendrite arm spacings and particle size in gas atomization", Lavernia E.J. and Baram

J.C., Journal of Materials Science Letters, v. 8, 1989, pp 612-614.

[Lee1994]: "Solidification progress and heat transfer analysis of gas-atomized alloy droplets during spray forming", Lee E-S. and Ahn S., Acta Metallurgica et Materialia, v. 42, n. 9, 1994, pp 3231-3243.

[Lipton1987c]: "Effect of growth rate dependant partition coefficient on the Dendrite growth in Undercooled Melts", Lipton J., Kurz W. and Trivedi R., Acta Metallurgica, 35, n. 4, 1987, 965-970.

[Prasad2004]: "X-Ray Tomography study of atomized Al-Cu droplets", Prasad A., Henein H., Maire E. and Gandin Ch.A., Canadian Metallurgical Quarterly, v. 43, n. 2, 2004, pp 273-282.

[Prasad2005b]: "Quantification of microsegregation during rapid solidification of Al-Cu powders", Prasad A., Henein H., and Conlon K.T., Metallurgical Transactions A, In Press.

[Ruhr1990]: "Extended Al(Mn) solution in a rapidly solidified Al-Li-Mn-Zr alloy", Ruhr M., Lavernia E.J. and Baram J.C., Metallurgical Transactions A, v. 21A, 1990, pp. 1785-1789.

[Sarreal1986]: "The effect of solidification rate on microsegregation", Sarreal J.A. and Abbaschian G.J., Metallurgical Transactions A, v. 17A, 1986, pp 2063-2073.

Conclusions

The purpose of the current thesis work was to study the microsegregation and microstructure evolution in rapidly solidified Al-Cu alloys. This involved both experimental and modeling efforts. The experimental work involved producing rapidly solidified droplets generated from Impulse Atomization. Several techniques were then employed to characterize the microstructure and measure the microsegregation in the droplets. Modeling involved developing a set of equations that describes the thermal history of the solidifying droplet as well as the microsegregation within the individual droplets. Both the experimental and modeling work are summarized below, followed by the observations that can be drawn from this research.

9.1 Summary

- X-Ray tomography was used to characterize the microstructure of rapidly solidified droplets of Al-4.3%Cu and Al-17%Cu. From the images and movies obtained from tomography, the nucleation site was identified in each droplet. A single nucleation site was found within each droplet volume and its location was quantified for Al-4.3%Cu and Al-17%Cu.

- Individual droplets showed a gradation of morphology with three distinct microstructural features. These features were designated as Region I, Region II and Region III. Region I showed Ultra-Fine structure. Surrounding Region I, and including it, was Region II, which consisted of Primary Trunks. The rest of the droplet volume was called Region III, consisting of coarse dendrite. An interdendritic eutectic was also observed with the help of electron microscopy. Using techniques of stereology, the volume percentages of the Ultra Fine and the Primary Trunk regions were evaluated.

- The nucleation undercooling was estimated to be approximately 20K. The undercooling was estimated by comparing the experimentally obtained volume percent of Region I with model results of volume percent for Region I calculated under different undercoolings. Based on this undercooling value and homogeneous nucleation temperature values from the literature, this nucleation appears to be heterogeneous in nature.

- Extended study of the microstructure formation included studies on coarsening and porosity distribution. The porosity distribution was studied using X-ray tomography in Al-4.3%Cu and Al-17%Cu droplets. Al-4.3%Cu droplets showed an even distribution, whereas the Al-17%Cu droplets showed an uneven distribution. The porosities in both droplets, and more so in Al-17%Cu droplets, were always away from the nucleation and recalescence site. This suggests that the nucleation and fast dendrite growth during recalescence affect the porosity distribution.

- Coarsening was studied by doing dendrite arm spacing measurements on 2-D images of droplet cross-section. There were marked differences in the arm spacing (or coarsening) in droplets of different alloy compositions and different sizes. As the composition of the alloy increased, the arm spacing decreased. On the other hand, for any given alloy composition, the arm spacing decreased with decreasing droplet size. The difference in coarsening in different alloy compositions was attributed to the differences in freezing ranges and higher solute diffusion at higher temperatures.

- Neutron Diffraction was used to quantify the second phase formed in the Al-Cu eutectic. Weight percent of $CuAl_2$ was measured for Al-5%Cu, Al-10%Cu and Al-17%Cu droplets atomized in He and N_2 gas. The droplets studied were in the size range of 200 to 960 μm. The droplets that were analyzed for weight percent $CuAl_2$ were also analyzed for volume percent eutectic. These measurements were made for the entire droplet volume. By combining the weight percent $CuAl_2$ and volume percent eutectic data, weight percent eutectic in these droplets was evaluated. Furthermore, using mass balance equations on the weight percent eutectic and the chemical composition of the alloys, the average amount of Cu in the primary phase was calculated. Thus, this work introduces a new technique to estimate the average solute solubility in the primary phase.

- Microsegregation results from the experiments show that the weight percent of eutectic lies between Scheil-Gulliver and Equilibrium values for low alloy concentration (Al-5%Cu). As the alloy concentration was increased to higher compositions (Al-17%Cu), the weight percent eutectic value fell below the Equilibrium value. Data points for a given alloy composition were comprised of weight percent eutectic values for all droplet sizes and gas types. A similar trend was observed for average Cu solubility in the primary phase. For low alloy concentrations, the average Cu solubility was found to be between the Scheil-Gulliver and Equilibrium limits. As the alloy composition was increased, the average Cu solubility was found to exceed the Equilibrium limit.

- A microsegregation model was developed for a droplet solidifying during atomization. The Rappaz-Thevoz (R-T) microsegregation model for equiaxed growth was used in an isothermal droplet. The model couples the LKT dendrite kinetic and Scheil-Gulliver models for fraction solid calculations. A geometrical expression was developed for specifying the nucleation position within the droplet. Thus, the model also takes into account the position of the nucleation site. The model was validated against experimental results for the weight percent eutectic in Al-5%Cu droplets.

- Based on weight percent eutectic and average solute solubility data, the microsegregation trends from model and experiments were found to be the same, though the model results deviated from the experiment results at higher alloy compositions.

- Cooling rates from the model show that within the range of 10^2 to 10^3 K/s, cooling rate has a small effect on microsegregation. There is a marginal decrease in microsegregation as the cooling rate is increased in the range mentioned above. Also, the model qualitatively showed the presence of macrosegregation in the droplets.

- Changing the nucleation site has no effect on microsegregation. On the other hand, the range of recalescence temperature increases when the nucleation site is moved from the surface to the droplet center.

9.2 Observations

- The current work has clearly demonstrated that techniques like X-Ray tomography, Neutron Diffraction and Stereology can yield unique and useful data for the solidifying volume.

- Using the data from X-Ray tomography and Neutron Diffraction, a new technique was developed to estimate the undercooling in atomized droplets.

The droplets undergo a relatively lesser degree of undercooling possibly because of the presence of heterogeneous substrates.

- Dendrite velocity plays an important role during microstructure formation as well as microsegregation. Following nucleation, the solid-liquid growth front advances, resulting in different morphologies within the droplet. The Ultra Fine structure is believed to have formed during the initial growth regime when the droplet temperature is still decreasing. During this time the growth velocity increases as a result of increasing undercooling and eventually recalescence sets in when the dendrite velocity becomes high enough. The Primary Trunks are believed to have formed during this period. At the end of recalescence, the dendrites grow slowly at near equilibrium conditions while following the Gulliver-Scheil solidification path. Finally, the remaining liquid solidifies as eutectic. Gradation in microstructure shows the evidence of spatial variations in morphology within the droplet. This is a result of recalescence, which results in a change in undercooling and consequently in the dendrite growth rate.

- Microsegregation trends indicate that increasing alloy composition leads to an increased degree of diffusionless solidification. The quantified volume fraction of both initial growth and recalescence was more in the case of higher alloy composition (Al-17%Cu) than the lower alloy composition (Al-4.3%Cu) droplet. Therefore, it is believed that diffusionless solidification takes place during initial growth and recalescence periods and that dendrite velocity plays an important role. Furthermore, based on the effects of alloy composition and cooling rate on microsegregation, the results indicate that changing the alloy composition has more effect on the final microsegregation than changing the droplet size or the gas type.

- The effect of dendrite velocity on microsegregation seems to be via solute drag. For low undercoolings, the dendrite velocity is not high enough for solute trapping to take place. The dendrite velocity in lower alloy compositions is mainly controlled by thermal+solutal undercooling, whereas dendrite velocity in higher alloy compositions is mainly controlled by solutal undercooling. Thus the dendrite growth rate changes with alloy composition. Therefore, the effect of solute drag can also be expected to be alloy composition dependent with increased diffusionless transformation at higher alloy chemistry.

- In the presence of diffusionless transformation, linear phase diagram approximations are not sufficient to model microsegregation. This is especially true for higher alloy compositions with increased diffusionless transformation, when the deviation between the model and the experiment becomes greater.

- Velocity dependent partition coefficient expressions are required in the model. Such expressions are available for solute trapping but not for solute drag. Modification of the model, therefore, constitutes a major area for future research. However, this requires quantitatively establishing the affect of solute drag on partition coefficient.

- The cooling rate experienced by a droplet changes with droplet undercooling. The SDAS – cooling rate correlation and SDAS – solidification time correlation show opposite trends. Hence, this research suggests that cooling rate may not be a reliable parameter to assess the scale of the microstructure. Furthermore, because of the presence of macrosegregation within the droplets, the trend in eutectic and average Cu solubility with respect to cooling rates is not apparent.

9.3 Future Work

The current work suggests that the following areas of rapid solidification need future work.

9.3.1 A reliable parameter

In the past, the scale of the microstructure and/or microsegregation has been studied in terms of cooling rates. However, as shown in Chapter 8, the sole dependence on cooling rates as the parameter can be misleading. Cooling rates change with undercooling which in turn can change with the type of nucleation agent. In other words, two droplets of the same size atomized under the same gas can have different cooling rates if they experience different undercoolings. In the current work, the undercooling was evaluated by comparing the results from the model to the experimental results in terms of volume percent of Region I. As explained in Chapters 4 and 5, this requires demarcating the boundary between Ultra Fine structure (Region I) and Primary Trunks. A fine scaled structure, as seen in Al-17%Cu alloy droplets, can result in uncertainty in the demarcation. The large error associated with Region I and Region II volume percent measurements for Al-17%Cu (Table 5.1 and 5.2) is a result of this uncertainty. Consequently, the undercooling number obtained is affected by the resolution limitations of the characterization tool. Hence, if the resolution limits of the techniques can be improved, more accurate undercooling temperature evaluations can be made. Better resolution limits of the characterization techniques can also help in performing macrosegregation measurements in the atomized droplets, which has not been quantified in great detail. For example, X-Ray tomography with a resolution limit of 0.1 μm used on an Al-5%Cu droplet will provide better demarcation between Ultra Fine structure and Primary trunks, and therefore more accuracy in undercooling values. Thus, undercooling can be used as a parameter provided the characterization tools have good resolution. Alternatively, a new parameter, other than undercooling or cooling rate, may be identified which can be obtained relatively easily and accurately. However, with a better resolution of tomography, it will also be possible to perform an interdendritic eutectic measurement for the entire droplet volume, thus yielding macrosegregation information within the droplet. Moreover, the eutectic measurement as a function of distance from nucleation site will also provide useful information about macrosegregation.

9.3.2 Solute drag

Solute drag has been less studied relative to its counterpart, solute trapping. The current work suggests that solute drag can also alter the partition coefficient and thus result in diffusionless transformation. Correlations exist for modeling the affect of solute trapping, where partition coefficients are related to interface growth rates. However, there is no empirical relationship that correlates partition coefficient with interface velocity based on the affect of solute drag. Hillert and coworkers have developed models (referred to in previous chapters) for estimating the effect of interface velocity on solute drag. A convenient starting point in developing such an empirical relationship would, therefore, be the modification of the Hillert model.

9.3.2 Improvements in the model

There are two areas in which the present microsegregation model can be improved. First, the model may be improved by introducing velocity-dependent partition coefficients. Velocity-dependent partition coefficients using solute trapping model would be useful to study the effects of higher ranges of undercooling. For lower ranges of undercooling, velocity-dependent partition coefficient using solute drag model would be useful. Also, the linear approximations of the phase diagram could be replaced by Temperature-Composition relationships from the phase diagram.

Second, macrosegregation can be better understood by a non-isothermal microsegregation model. In such a model, both the temperature and the composition can be tracked within different regions of the droplet. Furthermore, by accommodating for the nucleation position, the temporal as well as the spatial thermal gradient and interface velocity can be tracked, thus giving important information about the microstructure evolution and microsegregation with off-center nucleation.

Equations for growth of grain envelope during off-center nucleation

The equations developed for finding the volume of the effective grain envelope requires finding the area on which the integration is performed. The integrands with the appropriate limits were described by Eqns. 7.34 to 7.36. The calculation of integrands and the limits require geometry and are described in the following. Figure 7.7 has been reproduced here (Figure A.1) and for clarity only half of the droplet and grain envelope along the Y-axis is shown. The same nomenclature is used as in the original figure and the coordinates are the same as described in Table 7.1.

The volume of the cylinder mentioned in Eqn. 7.34 is the area of a circle, A ($=\pi R^2$), integrated along the Y-axis. In this case the radius, R, of the cylinder remains a constant and the volume is simply given as $\pi R^2(\Delta Y)$, where ΔY is the height of the cylinder along the Y-axis. In the case of the grain envelope within the droplet droplet, the radii are CJ and EH corresponding to the regions BJIDB and DIHFD respectively. These radii subscribe a circular area when rotated along the Y-axis and this area when integrated between B to D (for BJIDB) and D to F (for DIHFD) gives the volume between BJIDB and DIHFD respectively. The addition of these two volumes then gives the total effective grain envelope volume. However, in this case the two radii are not constant and is a function of their position along the Y-axis. Therefore, the problem is to find the radius of the two strips $r_1(y)$ and $r_2(y)$ respectively as a function of the position along Y-axis. The corresponding volumes are then, $V_1 = \pi \int (r_1(y))^2 dy$ and $V_2 = \pi \int (r_2(y))^2 dy$ respectively, where $r_1(y)$ and $r_2(y)$ are the radii of CJ and EH as a function of their position along the Y-axis and are rotated around the Y-axis orthogonal to the plane shown in Figure A.1.

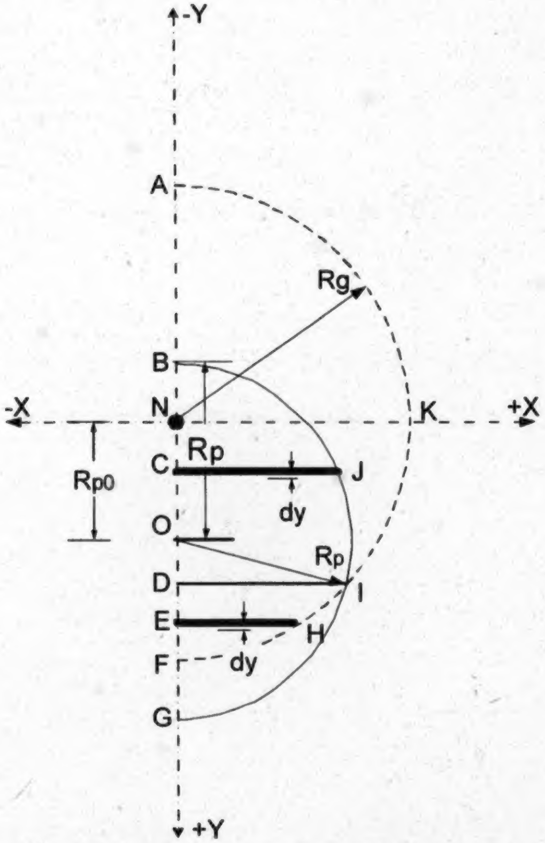

Figure A.1: Schematic of the grain envelope growing from an off-center nucleation. Solid semi-circle represents the actual droplet and the dashed semi-circle is the grain envelope.

Volume of BJIDB

The volume evaluations are based on using Pythagoras theorem on appropriate right angled triangles. For clarity in the figure only few of these triangles are marked. Using Pythagoras theorem on triangle CJO we get,

$$r_1(y)^2 = CJ^2 = OJ^2 - OC^2 \tag{A.1}$$

But, OJ = R_p and OC = ON – CN = R_{p_0} – y. Therefore,

$$r_1(y)^2 = R_p^2 - R_{p_0}^2 + 2yR_{p_0} - y^2 \tag{A.2}$$

The limits for this volume are between points B and D. The coordinates of B are (0, R_{p_0} - R_p) whereas that of D can be evaluated using geometry. The coordinates of the point D, Y_D, would be the distance ND since N coincides with the origin of the coordinate axis. Using Pythagoras theorem again on triangle NDI,

$$ND^2 = NI^2 - DI^2 \tag{A.3}$$

where NI = R_g and DI can be found using Pythagoras theorem on triangle ODI.

$$DI^2 = R_p^2 - (R_{p_0} - ND)^2 \tag{A.4}$$

Substituting the expression for DI in Eqn. A.3, we get,

$$ND^2 = R_g^2 - [R_p^2 - (R_{p_0} - ND)^2] \tag{A.5}$$

$$ND = Y_D = \frac{R_g^2 - R_p^2 + R_{p_0}^2}{2R_{p_0}} \tag{A.6}$$

Substituting the expressions for $r_1(y)^2$ and Y_D gives the volume V_1 of the region BJIDB,

$$V_1 = \pi \int_{R_{p_0} - R_p}^{Y_D} (R_p^2 - R_{p_0}^2 + 2yR_{p_0} - y^2)dy \tag{A.7}$$

Volume of DIHFD

Likewise, using Pythagoras theorem on triangle NHE gives the radius EH.

$$r_2(y)^2 = EH^2 = NH^2 - y^2 \tag{A.8}$$

Since NH = R_g, the volume of the region, V_2, would be,

$$V_2 = \pi \int_{Y_D}^{R_g} (R_g^2 - y^2)dy \tag{A.9}$$

Appendix B

Accuracy analysis of model results

This section describes the analysis performed on the model results to check its accuracy. The model equations developed for simulating the droplet solidification is given in the paper. The set of equations leading to the final heat balance equation can be solved analytically and therefore the model is analytical in nature. To solve these equations, a FORTRAN code using "Implicit Double-Precision" scheme was used.

One of the terms in the final heat balance equation is the convective heat transfer coefficient which requires time-dependant solution of the droplet velocity. This equation is rewritten here for convenience.

$$\frac{dv}{dt} = \frac{\rho_d - \rho_f}{\rho_d} g - 0.75 \frac{C_d}{D_p v^2} \qquad \text{(B.1)}$$

The solution of this equation requires that an initial value of the velocity be known ($V(t=0) = V_i$) and the velocity at later time periods is evaluated by a numerical integration scheme. The numerical schemes inherently have errors associated with them depending upon the technique used and the interval for the independent variable used. The independent variable in our case is 'time' and a global time step, δt = 1e-5s, was chosen for the FORTRAN program. Runga-Kutta

(R-K) methods are the most commonly used technique for solving equations of the type presented in Eqn. B.1. We have used Milne's predictor-corrector method [Chappra2002] which is a 2nd order R-K method. The technique can be mathematically written as,

$$v_{i+1} = v_i + \frac{1}{2}(k_1 + k_2)\delta t \tag{B.2}$$

where v_{i+1} is the velocity in the $(i+1)^{th}$ time, v_i is the velocity in the i^{th} time, δt is the time interval and k_1 and k_2 are functions of velocity and time. The 4th order R-K method in general is more accurate and is mathematically given as,

$$v_{i+1} = v_i + \frac{1}{6}(k_1 + 2k_2 + 2k_3 + k_4)\delta t \tag{B.3}$$

To ensure that the Milne's method gave accurate results, the velocity output from Milne's method was compared to the results from the 4th order R-K technique. An initial velocity of 0.5 m/s was used and two different time steps of $\delta t = 0.01$s and 0.0001s were chosen for comparison. The result from R-K 4th order is plotted against Milne's method and shown in Figure B.1.

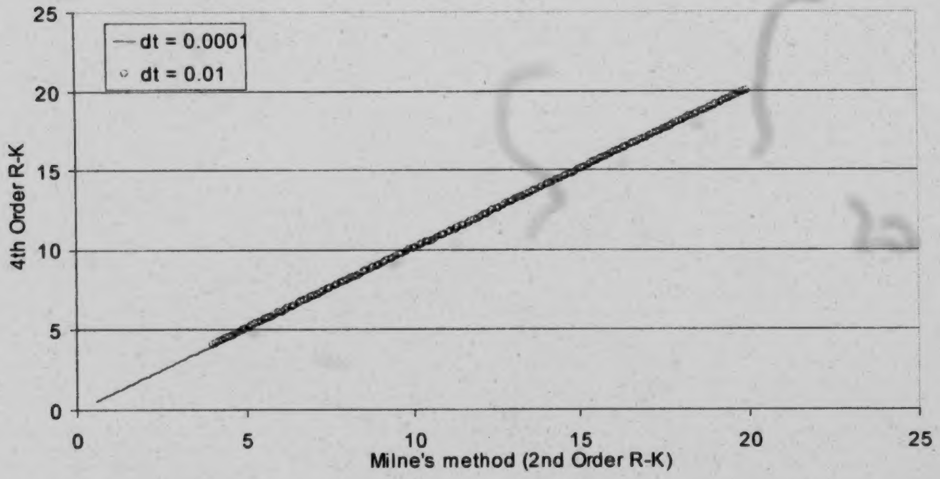

Figure B.1: Simulation results for droplet velocity calculated and compared using Milne's and 4th order R-K techniques. The straight line at 45^0 shows that the two techniques give same results with both the time steps used.

With no difference between the two techniques, it is clear that the Milne's method gives accurate results even with a time step of 0.01s. This shows that the numerical technique employed in Eqn. B.1 gives accurate results.

References

[Chappra2002]: "Numerical method for engineers", Chappra S.C. and Cannale R.P., McGraw Hill, U.S.A., 2002, pp 747-748.